

AD-A034 722

NIELSEN ENGINEERING AND RESEARCH INC MOUNTAIN VIEW CALIF F/G 16/4
CALCULATION OF COMPONENT FORCES AND MOMENTS OF ARBITRARILY BANK--ETC(U)
NOV 76 M J HEMSCH, C A SMITH, J N NIELSEN N00014-74-C-0050

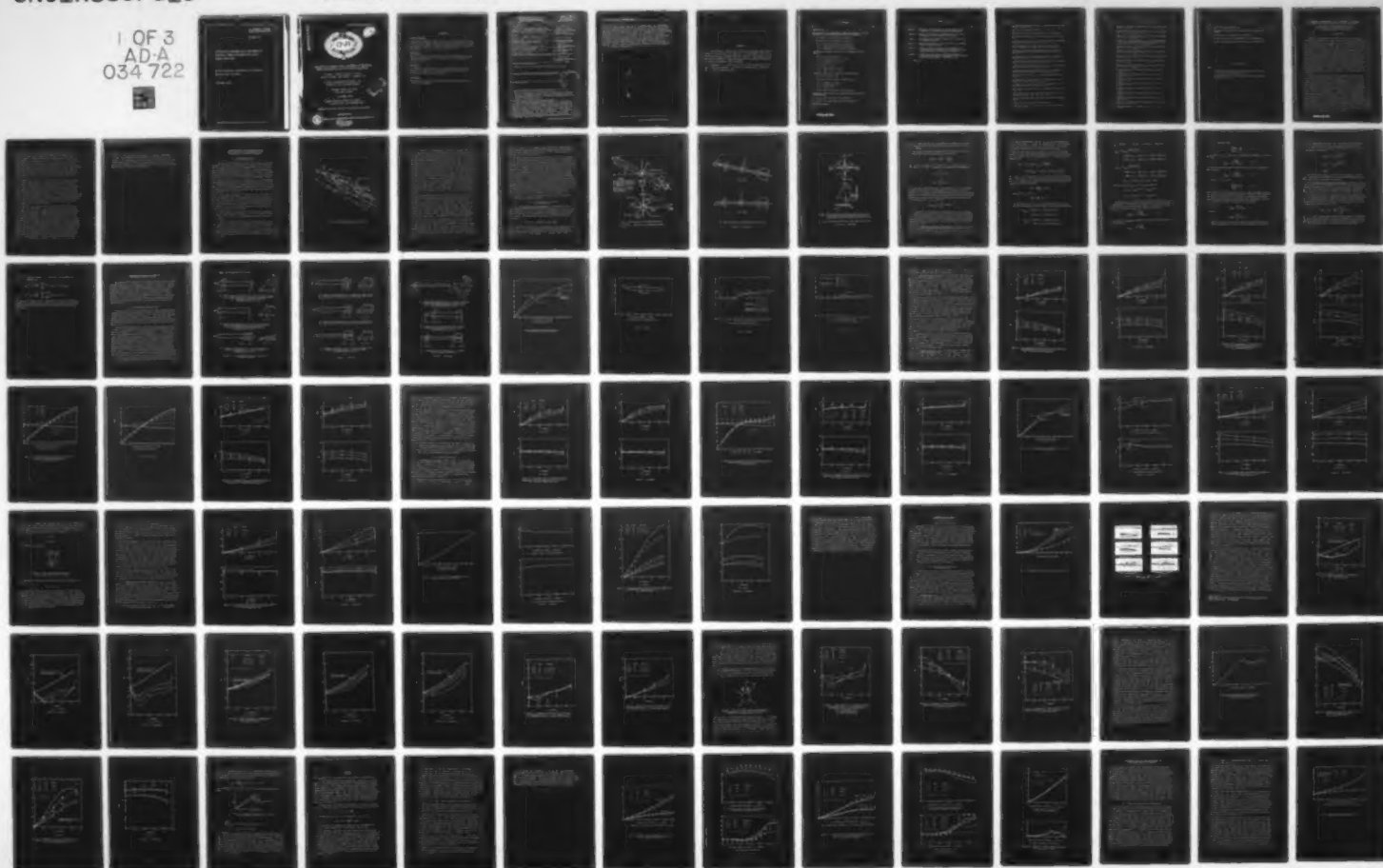
UNCLASSIFIED

NEAR-TR-125

ONR-CR215-226-3

NL

1 OF 3
AD-A
034 722



U.S. DEPARTMENT OF COMMERCE
National Technical Information Service

AD-A034 722

CALCULATION OF COMPONENT FORCES AND MOMENTS OF
ARBITRARILY BANKED CRUCIFORM MISSILES WITH
CONTROL DEFLECTIONS

NIELSON ENGINEERING AND RESEARCH, INCORPORATED
MOUNTAIN VIEW, CALIFORNIA

1 NOVEMBER 1976

026080

REPORT ONR-CR215-226-3

ADA034722



CALCULATION OF COMPONENT FORCES AND MOMENTS OF ARBITRARILY
BANKED CRUCIFORM MISSILES WITH CONTROL DEFLECTIONS

MICHAEL J. HEMSCH, CHARLES A. SMITH,
JACK N. NIELSEN, AND STANLEY C. PERKINS, JR.

NIELSEN ENGINEERING & RESEARCH, INC.
MOUNTAIN VIEW, CALIFORNIA 94043

CONTRACT N00014-74-C-0050
ONR TASK 215-226

1 NOVEMBER 1976

ANNUAL TECHNICAL REPORT FOR PERIOD
1 OCTOBER 1975 - 30 SEPTEMBER 1976

APPROVED FOR PUBLIC RELEASE; DISTRIBUTION UNLIMITED



PREPARED FOR THE

OFFICE OF NAVAL RESEARCH 600 N. QUINCY ST. ARLINGTON VA 22217

REPRODUCED BY
NATIONAL TECHNICAL
INFORMATION SERVICE
U. S. DEPARTMENT OF COMMERCE
SPRINGFIELD, VA. 22161

NOTICES

Change of Address

Organizations receiving reports on the initial distribution list should confirm correct address. This list is located at the end of the report. Any change of address or distribution should be conveyed to the Office of Naval Research, Code 211, Arlington, Virginia 22217.

Disposition

When this report is no longer needed, it may be transmitted to other authorized organizations. Do not return it to the originator or the monitoring office.

Disclaimer

The findings in this report are not to be construed as an official Department of Defense or Military Department position unless so designated by other official documents.

Reproduction

Reproduction in whole or in part is permitted for any purpose of the United States Government.

UNCLASSIFIED

COPY NO. 20

SECURITY CLASSIFICATION OF THIS PAGE (When Data Entered)

REPORT DOCUMENTATION PAGE		READ INSTRUCTIONS BEFORE COMPLETING FORM
1. REPORT NUMBER ONR-CR215-226-3	2. GOVT ACCESSION NO.	3. RECIPIENT'S CATALOG NUMBER
4. TITLE (and Subtitle) CALCULATION OF COMPONENT FORCES AND MOMENTS OF ARBITRARILY BANKED CRUCIFORM MISSILES WITH CONTROL DEFLECTIONS		5. TYPE OF REPORT & PERIOD COVERED Technical Report 10-01-75 to 9-30-76
7. AUTHOR(s) Michael J. Hensch, Charles A. Smith, Jack N. Nielsen, and Stanley C. Perkins, Jr.		6. PERFORMING ORG. REPORT NUMBER NEAR TR 125
9. PERFORMING ORGANIZATION NAME AND ADDRESS Nielsen Engineering & Research, Inc. 510 Clyde Avenue Mountain View, California 94043		8. CONTRACT OR GRANT NUMBER(s) N00014-74-C-0050
11. CONTROLLING OFFICE NAME AND ADDRESS Office of Naval Research (Code 211) 800 N. Quincy Street Arlington, VA 22217		10. PROGRAM ELEMENT, PROJECT, TASK AREA & WORK UNIT NUMBERS 61153N-14 RR014-11-84, 1-12 ONR Task NR 215-226
14. MONITORING AGENCY NAME & ADDRESS (if different from Controlling Office)		12. REPORT DATE 1 November 1976
		13. NUMBER OF PAGES 229
		15. SECURITY CLASS. (of this report) Unclassified
		15a. DECLASSIFICATION/DOWNGRADING SCHEDULE N/A
16. DISTRIBUTION STATEMENT (of this Report) Approved for public release; distribution unlimited.		
17. DISTRIBUTION STATEMENT (of the abstract entered in Block 20, if different from Report)		
18. SUPPLEMENTARY NOTES		
19. KEY WORDS (Continue on reverse side if necessary and identify by block number) Missile Aerodynamics; Guided Missiles; Aerodynamic Character- istics; Aerodynamic Canard Control; Aerodynamic Empirical Techniques; Aerodynamic Flow Patterns; Aerodynamic Vortices; Missile Aerodynamic Loads		
20. ABSTRACT (Continue on reverse side if necessary and identify by block number) This report describes the development of a preliminary version of a single comprehensive code for the engineering calculation of all missile component aerodynamic forces and moments, except minimum drag, for angles of attack up to the unsteady regime. The engineering method to be described in this report is composed of five basic procedures: (1) computation of forces and moments, with no external vortices present, for individual fins in the presence of a body at arbitrary angle of		

DD FORM 1473

1 JAN 73

EDITION OF 1 NOV 65 IS OBSOLETE

SECURITY CLASSIFICATION OF THIS PAGE (When Data Entered)

Block No. 20 (Concluded)

attack and bank angle with control deflections; (2) computation of forces and moments induced on individual fins due to the presence of external vortices; (3) calculation, using an empirical method, of the strengths and positions of body vortices generated upstream of the first set of fins; (4) computation, using a vortex tracking method, of the strengths and positions of vortices between the first and second sets of fins; and (5) determination of body forces and moments due to the presence of the fins and vortices. Detailed comparisons between data and theory for determining the effectiveness of the above procedures are presented. Several important phenomena which are not accounted for in the present method are discussed and appropriate improvements to the code are recommended.

☒ Main Section
☐ Ref Section
 INDEXED
 SERIALIZED
 FILED
 OCT 1964
 A

PREFACE

This technical report covers the work performed under Contract N00014-74-C-0050 from 1 October 1975 to 30 September 1976, and is the third report published under the program. The program is sponsored by the Office of Naval Research with significant assistance provided by NASA/Ames Research Center.

Commander P. R. (Bob) Hite, Office of Naval Research, is the Navy Scientific Officer. Dr. Gary T. Chapman and Mr. Gerald N. Malcolm are the NASA advisors.

TABLE OF CONTENTS

<u>Section</u>	<u>Page</u>
1. INTRODUCTION	9
2. INTRODUCTION TO THE ENGINEERING METHOD AND DESCRIPTION OF THE EXTENSIONS FOR CALCULATING BODY FORCES AND MOMENTS	12
2.1 Introduction to the Engineering Method	12
2.2 Description of Extensions to the Method	15
2.2.1 Nose section forces and moments	15
2.2.2 Finned section forces and moments	19
2.2.3 Afterbody section forces and moments	23
3. COMPARISONS WITH DATA FOR FINS WITH NO EXTERNAL VORTICES PRESENT	25
3.1 Moderate Aspect-Ratio Fins	25
3.1.1 Supersonic flow, $M_{\infty} = 1.75$	33
3.1.2 Subsonic flow, $M_{\infty} = 0.8$	33
3.2 Low-Aspect-Ratio Fins	42
3.2.1 Aspect ratio 1.3 fins	42
3.2.2 Aspect ratio 1.0 fins	53
4. COMPARISONS WITH DATA FOR BODY-TAIL CONFIGURATIONS	61
4.1 Results for Bodies Alone	61
4.2 Fin Loads in the Presence of Body Vortices	61
4.2.1 Leeward fins, fin 1	61
4.2.2 Leeward fins, fin 2	73
4.2.3 Windward fins	77
4.3 Total Loads for Body-Tail Configurations	84
5. COMPARISONS WITH DATA FOR BODY-CANARD AND BODY-CANARD-TAIL CONFIGURATIONS	91
5.1 Results for Body-Canard Configurations	91
5.2 Results for Body-Canard-Tail Configurations	100
6. CONCLUDING REMARKS	110
REFERENCES	112

Preceding page blank

TABLE OF CONTENTS (CONCLUDED)

<u>Section</u>	<u>Page</u>
APPENDIX A - PROCEDURE FOR COMPUTATION OF VORTEX PATHS IN THE PRESENCE OF A CRUCIFORM WING-BODY COMBINATION	115
APPENDIX B - REVERSE FLOW METHOD FOR COMPUTATION OF FIN FORCES AND MOMENTS IN THE PRESENCE OF VORTICES	123
APPENDIX C - PROCEDURE FOR COMPUTING STRENGTHS AND POSITIONS OF FIN TRAILING VORTICES	137
APPENDIX D - METHOD FOR COMPUTING VORTEX POSITIONS AND STRENGTHS OVER AFTERBODY SECTION	143
APPENDIX E - MLOADS, A COMPUTER PROGRAM FOR CALCULATING THE COMPONENT FORCES AND MOMENTS OF ARBITRARILY BANKED CRUCIFORM MISSILES WITH CONTROL DEFLECTIONS	149
APPENDIX F - MODIFICATIONS TO CRFWBD, A COMPUTER PROGRAM FOR CALCULATING AERODYNAMIC CHARACTERISTICS OF CRUCIFORM WING-BODY COMBINATIONS IN SUPERSONIC FLOW	217
LIST OF SYMBOLS	231

LIST OF ILLUSTRATIONS

<u>Figure</u>		<u>Page</u>
1	Banked canard-cruciform missile at angle of attack showing typical vortex field.	13
2	Definition of coordinate systems.	16
3	Configurations used for comparisons of data and theory.	26
4	Wing-alone characteristics for moderate-aspect-ratio fins (C_6).	29
5	Fin normal force for bank with no fin deflection, moderate-aspect-ratio fins (C_6), BC 1, $M_\infty = 1.75$.	34
6	Fin rolling moment for bank with no fin deflection, moderate-aspect-ratio fins (C_6), BC 1, $M_\infty = 1.75$.	36
7	Fin normal force and rolling moment for fin deflection with no bank, moderate-aspect-ratio fins (C_6), BC 1, $M_\infty = 1.75$.	38
8	Fin normal force for combined bank and fin deflection, moderate-aspect-ratio fins (C_6), BC 1, $M_\infty = 1.75$.	40
9	Fin normal force for bank with no fin deflection, moderate-aspect-ratio fins (C_6), BC 1, $M_\infty = 0.8$.	43
10	Fin normal force for fin deflection with no bank, moderate-aspect-ratio fins (C_6), BC 1, $M_\infty = 0.8$.	45
11	Fin normal force for combined bank and fin deflection, moderate-aspect-ratio fins (C_6), BC 1, $M_\infty = 0.8$.	46
12	Wing-alone characteristics for low-aspect-ratio fins (C_7 and T_2).	48
13	Fin normal force for bank with no fin deflection, low-aspect-ratio fins (C_7), BC 2, $M_\infty = 1.75$.	50
14	Fin normal force for bank with no fin deflection, low-aspect-ratio fins (C_7), BC 2, $M_\infty = 0.8$.	54
15	Wing-alone characteristics for low-aspect-ratio fins (T_{14}), $M_\infty = 2.0$.	56
16	Fin normal force for bank with no fin deflection, low-aspect-ratio fins (T_{14}), BT 1, $M_\infty = 2.0$.	58
17	Comparison between theory and data for body-alone normal force.	62
18	Illustration of vortex-wing interference.	63
19	Effect of V_{\max}/V_∞ on prediction of fin 1 normal force, BT 2, $M_\infty = 1.75$.	65

LIST OF ILLUSTRATIONS (CONTINUED)

Figure		Page
20	Effect of V_{\max}/V_{∞} on prediction of fin 1 normal force, BT 2, $M_{\infty} = 0.8$.	68
21	Comparison of data and theory for fin 1 rolling moment, BT 2, $M_{\infty} = 1.75$, $V_{\max}/V_{\infty} = 0.4$.	71
22	Comparison of data and theory for fin 1 rolling moment, BT 2, $M_{\infty} = 0.8$, $V_{\max}/V_{\infty} = 0.1$.	72
23	Comparison of data and theory for fin 1 rolling moment using α_{eq} to compute lateral position of center of pressure, BT 2, $M_{\infty} = 1.75$, $V_{\max}/V_{\infty} = 0.4$.	74
24	Comparison of data and theory for fin 2 normal force, BT 2, $M_{\infty} = 1.75$, $V_{\max}/V_{\infty} = 0.4$.	75
25	Comparison of data and theory for fin 2 normal force, BT 2, $M_{\infty} = 0.8$, $V_{\max}/V_{\infty} = 0.1$.	76
26	Wing-alone normal-force coefficient for low-aspect-ratio fins (T_{15}), $M_{\infty} = 0.8$.	78
27	Comparison of data and theory for fin 2 normal force, BT 3, $M_{\infty} = 0.8$.	79
28	Comparison of data and theory for fin 3 normal force, BT 2, $M_{\infty} = 0.8$, $V_{\max}/V_{\infty} = 0.1$.	80
29	Comparison of data and theory for PT 2, $M_{\infty} = 1.75$, $V_{\max}/V_{\infty} = 0.4$.	86
30	Comparison of data and theory for BT 2, $M_{\infty} = 0.8$, $V_{\max}/V_{\infty} = 0.1$.	88
31	Comparison of data and theory for BT 4, $M_{\infty} = 0.8$, $V_{\max}/V_{\infty} = 0.4$.	90
32	Comparison of data and theory for BC 1, $M_{\infty} = 1.75$, $V_{\max}/V_{\infty} = 0.4$.	93
33	Comparison of data and theory for BC 2, $M_{\infty} = 1.75$, $V_{\max}/V_{\infty} = 0.4$.	95
34	Comparison of data and theory for BC 3, $M_{\infty} = 0.8$, $V_{\max}/V_{\infty} = 0.1$.	97
35	Comparison of data and theory for BCT 1, $M_{\infty} = 1.75$, $V_{\max}/V_{\infty} = 0.4$.	101
36	Measured and predicted vortex positions at $x/a = 17.2$ for BCT 1, $M_{\infty} = 1.75$.	106
37	Comparison of data and theory for BCT 2, $M_{\infty} = 0.8$, $V_{\max}/V_{\infty} = 0.1$.	108

LIST OF ILLUSTRATIONS (CONCLUDED)

<u>Figure</u>		<u>Page</u>
E.1	Flow of program computations.	153
E.2	Schematic description of control of MLOADS operations by NFIN.	154
E.3	Input formats for computer program MLOADS.	165
E.4	Input for sample case; body-canard-tail configuration.	183
E.5	Output for sample case; body-canard-tail configuration.	184

LIST OF TABLES

<u>Table</u>		<u>Page</u>
1	Predicted Contribution of Vortices to Afterbody Loading for Body-Canard Configuration No. 1.	99
2	Analysis of Error in Rolling Moment for Body-Canard-Tail Configuration No. 1.	104

CALCULATION OF COMPONENT FORCES AND MOMENTS OF ARBITRARILY
BANKED CRUCIFORM MISSILES WITH CONTROL DEFLECTIONS

by Michael J. Hemsch, Charles A. Smith,
Jack N. Nielsen, and Stanley C. Perkins, Jr.
Nielsen Engineering & Research, Inc.

1. INTRODUCTION

Under the sponsorship of the Office of Naval Research (ONR), Nielsen Engineering & Research, Inc. (NEAR) has been developing computer programs for the prediction of the aerodynamics of arbitrarily banked cruciform missiles at high angles of attack. The first two years of the work were devoted to the development of a computer code based on linear supersonic flow theory for the calculation of loadings on cruciform wing-body combinations. The results are reported in references 1 and 2. In 1974-1975, under the sponsorship of the Naval Weapons Center (NWC), China Lake, CA, NEAR developed an engineering method for calculating the induced rolling moments of cruciform missiles at angles of attack up to 20° . At the same time, under the joint sponsorship of NWC and NASA/Ames Research Center, NEAR obtained a systematic set of component-buildup data on a cruciform body-canard-tail missile up to 24° angle of attack at transonic and supersonic speeds. The data included individual fin loads. The engineering method is reported in reference 3. The data are presented in references 4 and 5.

Under the co-sponsorship of ONR and NASA/ARC, NEAR is continuing and extending the work reported in reference 3. The work involves two tasks: (1) development of a single comprehensive code for the engineering calculation of all missile component aerodynamic forces and moments, except minimum drag, for angles of attack up to the unsteady regime; and (2) comprehensive comparison of predicted results with systematic data from a variety of configurations. The work is to be accomplished in two phases. The first phase includes development of a preliminary version of the new code based on the method of reference 3. The new code is then to be compared with available systematic data up to approximately 20° angle of attack. This report describes that work. The work planned for the second phase is: (1) correction of deficiencies in the method which were uncovered in the first phase through comparison of experiment and theory, (2) extension of the method to angles of attack up to the unsteady regime, and (3) comparison of the extended method with systematic high angle of attack data obtained for that purpose.

When the work reported herein was in the planning stage, it was thought that in the first phase a comprehensive comparison between theoretical predictions and data for a number of different missile configurations and Mach numbers would be appropriate. However, detailed comparisons of theory and experiment for individual fin loads were found to be essential for uncovering and sorting out the many and varied phenomena involved. As a result, the comparisons are directed principally toward systematic data which include individual fin loads. Where discrepancies between theory and data are found, remedies are suggested and further work outlined. To insure that the phenomena uncovered are not the result of isolated cases, several different configurations are studied.

The engineering method to be described in this report is composed of five basic procedures: (1) computation of forces and moments, with no external vortices present, for individual fins in the presence of a body at arbitrary angle of attack and bank angle with control deflections; (2) computation of forces and moments induced on individual fins due to the presence of external vortices; (3) calculation, using an empirical method, of the strengths and positions of body vortices generated upstream of the first set of fins; (4) computation, using a vortex tracking method, of the strengths and positions of vortices between the first and second sets of fins; and (5) determination of body forces and moments due to the presence of the fins and vortices.

This report and reference 3 are intended to be sufficient for an understanding of the method. Reference 3 gives a detailed description of procedures (1) and (3). Although detailed descriptions of procedures (2) and (4) are available in reports published prior to reference 3, for the sake of completeness, that work is made available in this report in Appendices A through D. Section 2 of this report presents an overall introduction to the method and describes procedure (5), the development of which is Task 1 of the present effort. Detailed comparisons between data and theory for determining the effectiveness of the above procedures (Task 2) are presented in sections 3 to 5. Section 3 is concerned with cases in which external vortex effects are unimportant (procedure (1)). Section 4 considers situations for which the effects of body vortices are important (procedures (2) and (3)) but do not require the vortex tracking of procedure (4). Section 5 compares theory and data for cases in which all of the above procedures are required. A user's manual for

the Task 1 code is presented in Appendix E. Appendix F contains extensions made to a computer code developed earlier by NEAR for ONR (refs. 1, 2, and 3). The additions were necessary for the computation of certain interference quantities used for the calculation of body forces in the presence of cruciform fins. Appendix F also includes a study of optimum panel spacing to be used for that program.

2. INTRODUCTION TO THE ENGINEERING METHOD AND DESCRIPTION OF THE EXTENSIONS FOR CALCULATING BODY FORCES AND MOMENTS

2.1 Introduction to the Engineering Method

In developing the computer program, we have adopted an analytical approach to the maximum extent possible compatible with obtaining a complete program for all forces and moments acting on the missile components except for minimum drag. However, it has been necessary to adopt semi-empirical techniques for parts of the method. By comparisons of systematic data with theoretical predictions, the shortcomings and limitations can be determined and necessary improvements identified.

To place the present method in perspective, a brief description of the phenomena involved in flow over cruciform missiles is presented. Consider the body-canard-tail configuration shown in figure 1. Experimental work on such configurations has shown that the following sources of component interference can be important for included angles of attack in the range of $0 \leq \alpha_c \leq 20^\circ$.

1. Panel-panel interference: Consider a set of opposing fins at angle of attack and roll joined together at their root chords. We will call such a configuration a "wing alone." A body can be inserted between the fins and another set of fins can be added perpendicular to the first set. Any change in loading experienced by a fin due to changes in loading of another fin is said to be due to panel-panel interference and is affected by the presence of the body.

2. Nose vortex-fin interference: At sufficiently high angles of attack, separated flow will develop on the missile upstream of the first set of fins. The presence of the separated flow over the fins will alter their loading.

3. Canard vortex-tail interference: Each of the fins in the first finned section will shed trailing vorticity. That vorticity passing the tail section will alter the loading experienced by the tail fins.

4. Afterbody vortex-tail interference: At sufficiently high angles of attack, the afterbody boundary layer will separate. The shed vorticity will roll up and interact with the tail fins altering the loadings they will experience.

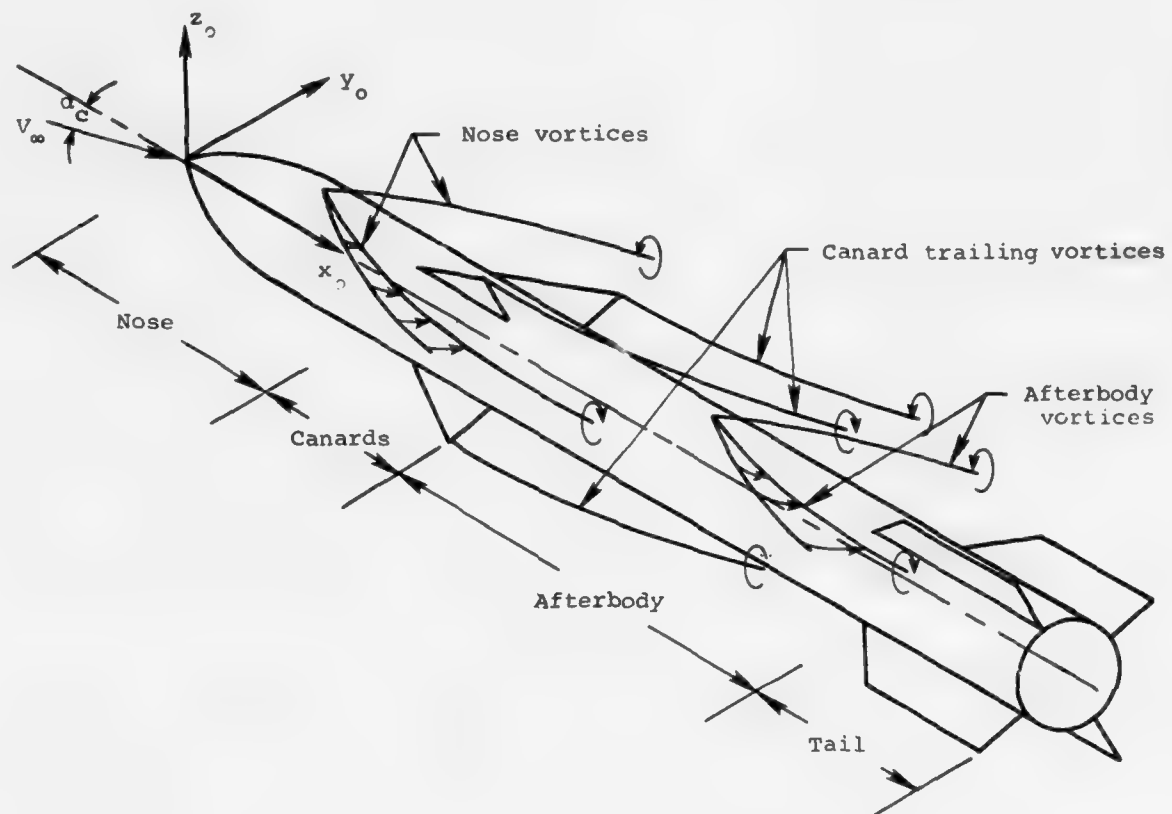


Figure 1. Banked canard-cruciform missile at angle of attack showing typical vortex field.

As discussed in the introduction, the present method models the above phenomena with five basic procedures. The first procedure computes fin forces and moments when no external vortices are present; that is, no vorticity generated upstream of the fins is present. To do this we have developed a correlation method based on the concept of an "equivalent angle of attack." The equivalent angle of attack, α_{eq} , is defined to be the angle of attack of a wing alone such that the normal force of the wing alone is twice* the actual normal force on a fin mounted on a body with arbitrary deflection and roll orientation. The various interference factors which account for fin deflection, roll orientation and ratio of fin span to body radius are described in reference 3. The Task 1 computer code requires that the wing-alone characteristics of normal force and center of pressure location be input as functions of angle of attack. The usefulness of the α_{eq} concept is demonstrated in reference 6, pages 21 to 25. The present version of this procedure is limited to symmetric deflection of opposing fins. Furthermore, only the first set of fins may be deflected. Both of these limitations are easily removed and may be during the second phase of the work. The fins must not be cambered or twisted.

The second procedure mentioned above is concerned with the changes in fin forces and moments when vortices generated upstream of the fins are present. A full description of the method used is given in Appendices A and B and will not be repeated here. However, the reader should be aware that the procedure assumes that the flow induced by the vortices can be described by linear theory and uses reverse flow methods to obtain the appropriate equivalent angle of attack increment due to the vortices. Because of the flow modeling used to track upstream vortices over a finned section, some restrictions on fin leading-edge and trailing-edge sweep exist. See Appendix A for further discussion.

For the third procedure the separated flow over the body upstream of the first set of fins is modeled as two symmetric potential line vortices. The body is assumed to be axisymmetric. It is also assumed to be cylindrical downstream of the nose. The missile station at which separation begins, that is, the station at which the vorticity is rolled up, is estimated from an empirical correlation. The vortex positions on the nose are also obtained from an empirical correlation. The strengths

*Recall that the wing alone is composed of two opposing fins.

of the nose vortices at the leading edge of the first finned section are then calculated using the vortex impulse theorem and two-dimensional crossflow drag coefficient correlations. A full description of this procedure is given in reference 3.

The fourth procedure is concerned with the wake over the afterbody section. The afterbody is assumed to be cylindrical. In this region, all the vortices present are tracked using slender-body theory from the trailing edge of the first set of fins to the leading edge of the second set of fins. Appendix C describes the method used to obtain the initial strengths and positions of the vortices shed by the first set of fins. Criteria for determining the axial location of the onset of boundary-layer separation and roll up of the shed vorticity from the afterbody are based on the local crossflow velocities and the presence or absence of nose vortices. If afterbody vortices form, they are assumed to grow as two potential line vortices under the influence of the vorticity shed upstream. They are allowed to grow unsymmetrically if the local flow is unsymmetrical about the plane containing the body and wind axes. The strengths of the afterbody vortices are assumed to be given by the vortex impulse theorem and two-dimensional crossflow drag correlations. A complete description of this procedure is given in Appendix D.

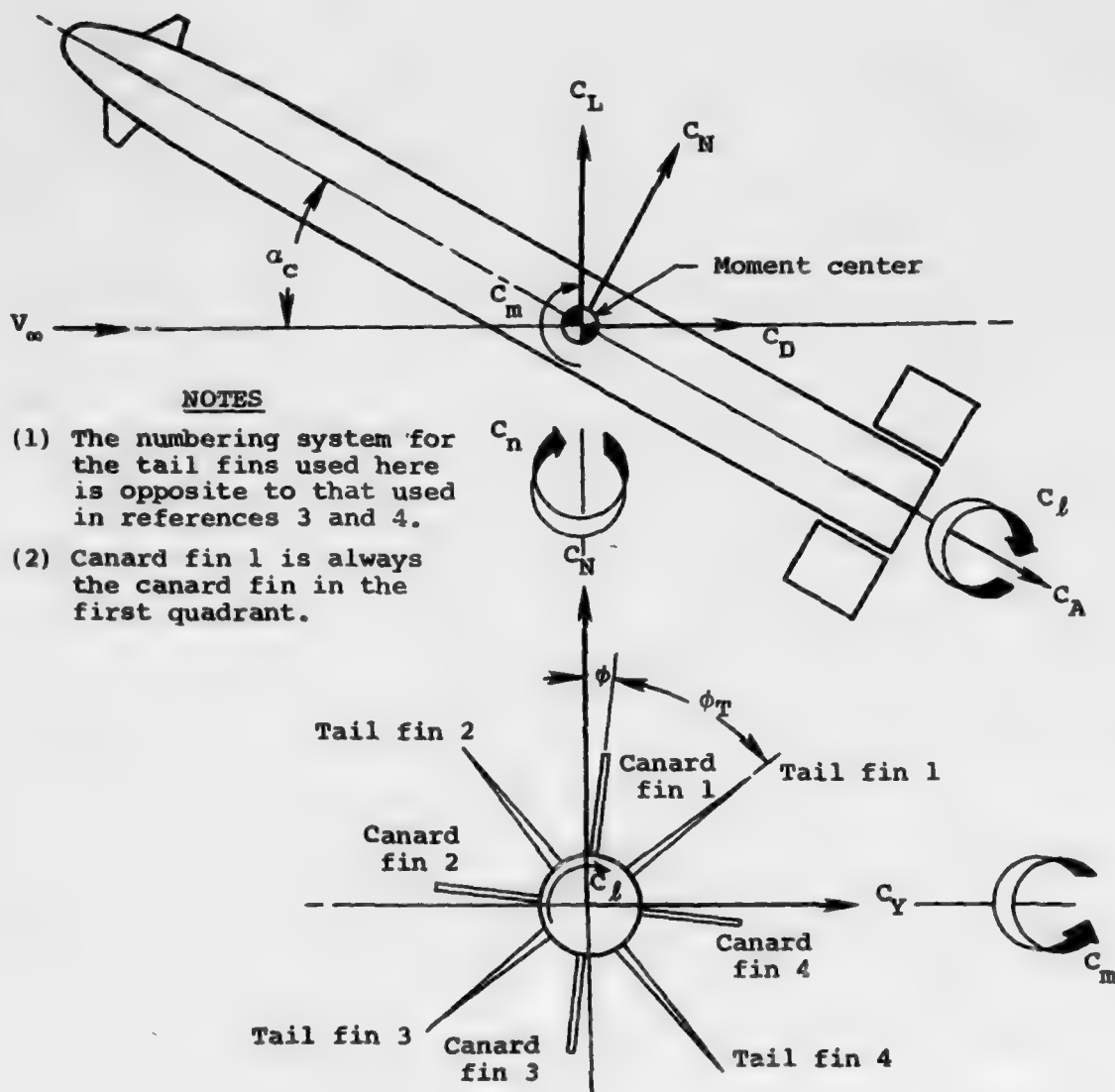
Procedure (5) which is concerned with body forces and moments is described in the remainder of section 2.

2.2 Description of Extensions to the Method

2.2.1 Nose section forces and moments.- The present version of the method assumes that the nose vortices are symmetrical. Hence, in unrolled body coordinates, the nose side force, yawing moment and rolling moment are zero (see fig. 2 for a description of the coordinate system used in this report). The normal-force coefficient is determined from the expression

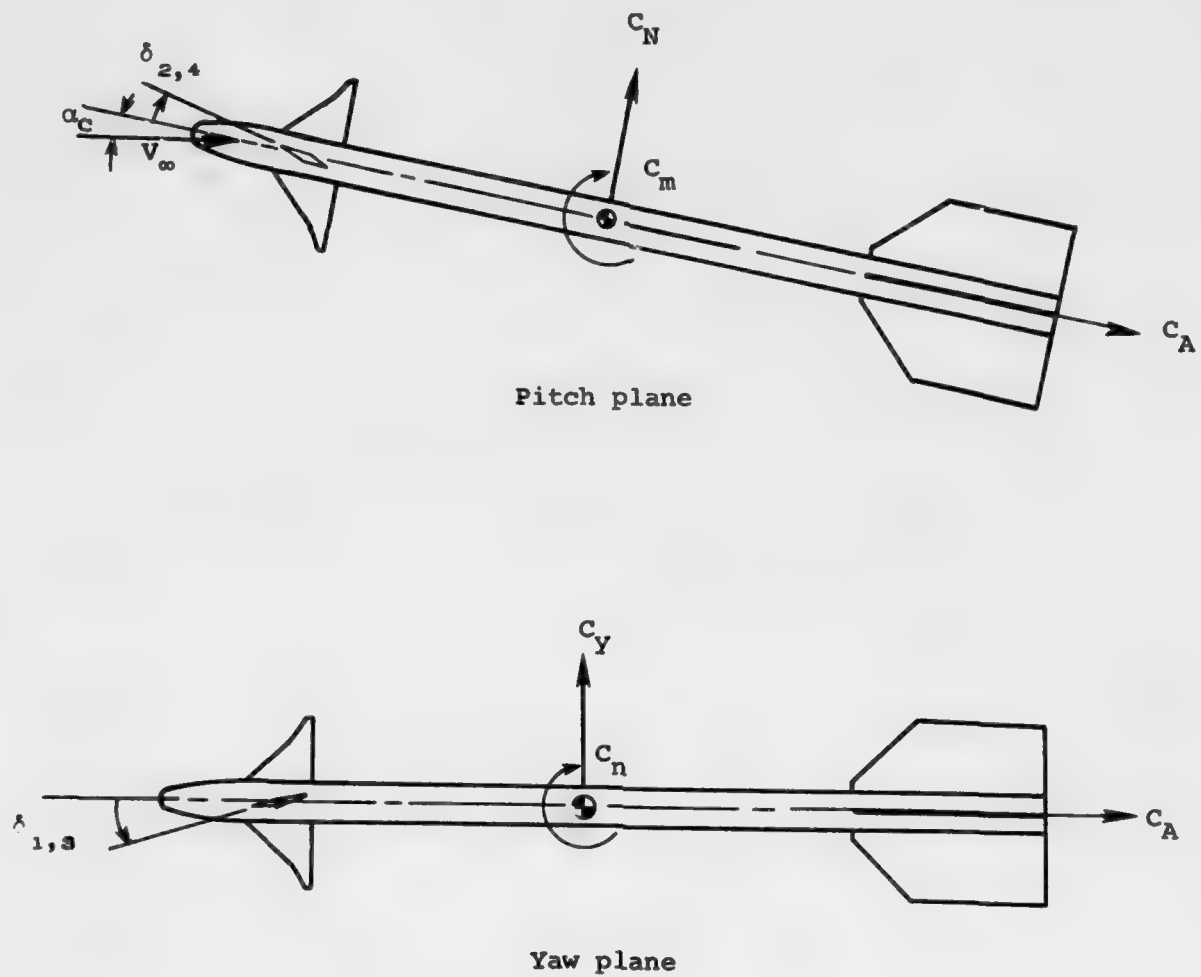
$$C_N = C_{N_\alpha} \sin \alpha_c \frac{\pi a^2}{S_R} + c_{d_c} \sin^2 \alpha_c \frac{S_C}{S_R} \quad (1)$$

If the user does not input C_{N_α} , the program uses the slender-body theory result, $C_{N_\alpha} = 2$. The two-dimensional crossflow drag coefficient is obtained from Fidler's correlations (ref. 7) for crossflow Mach numbers, M_C , less than 0.7 and from Jorgensen's correlation (ref. 8) for



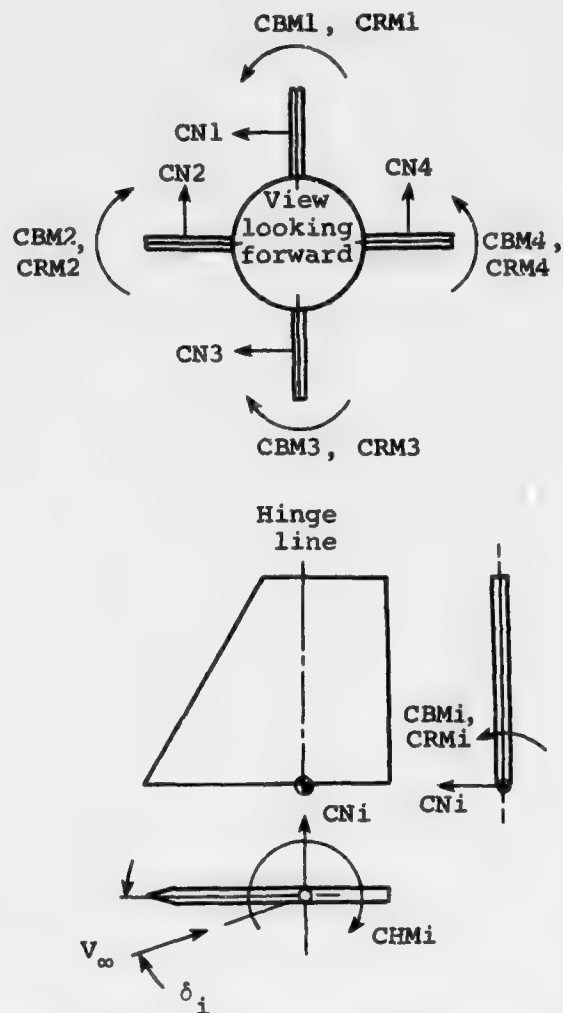
(a) Total loads and fin numbering system.

Figure 2. Definition of coordinate systems.



(b) Sign convention for canard deflection angles.

Figure 2. Continued.



NOTE: Normal forces are measured perpendicular to the fin planform and are considered to act at the intersection of the fin hinge line and root chord.

(c) Axis systems and positive sign convention for fins.

Figure 2. Concluded.

$M_c > 0.7$. Note that the usual formulation of equation (1) includes a multiplicative factor for finite length effects which is not used in the present method.

The center of pressure position for the linear term of equation (1) is obtained from the slender-body theory expression

$$\bar{x}_{\text{linear}} = x_N \left(1 - \frac{V_N}{\pi a^2 x_N} \right) \quad (2)$$

where x_N is the length of the nose and V_N is the nose volume. The code obtains S_C and V_N by numerically integrating the expressions:

$$S_C = 2 \int_{x_s}^{x_N} r(x) dx \quad (3)$$

$$V_N = \pi \int_0^{x_N} r^2(x) dx \quad (4)$$

using the input nose coordinates. The quantity x_s is the estimated initial axial position of flow separation on the nose (see ref. 3, pp. 10-11). Since the crossflow drag coefficient as used in the present method is not a function of axial position on the body, the axial center of pressure location of the viscous portion of the nose normal force (second term of eq. (1)) is given by

$$\bar{x}_{\text{viscous}} = \frac{2}{S_C} \int_{x_s}^{x_N} x r(x) dx \quad (5)$$

In reference 3, two methods for computing nose vortex strengths were used depending upon the length of the body up to the leading edge of the first finned section. During the course of the work for Phase I (reported herein), it was found that the method based on the crossflow drag coefficient was sufficient. The code uses only that method (see ref. 3, pp. 12-13).

2.2.2 Finned section forces and moments.— In reference 3, a method was presented for computing the normal-force coefficient for a rolled fin at angle of attack including the effects of panel-panel interference

and vortex-fin interference (see ref. 3, pp. 14-24 and Appendices A and B of this report). A method for computing the fin rolling-moment coefficient was also given (see ref. 3, pp. 29-30). This section describes the computation of all fin forces and moments.

Once the equivalent angle of attack for a given fin has been computed, the fin normal-force coefficient and center of pressure location can be found. The rolling moment for fin i has been given in reference 3 as

$$\begin{aligned} CRM_i = \cos \delta_i \left\{ CN_i(\alpha_{eq,p}) \frac{\bar{y}_i(\alpha_{eq,p})}{\ell_r} \right. \\ \left. + \left[CN_i(\alpha_{eq,p} + (\Delta\alpha_{eq})_v) - CN_i(\alpha_{eq,p}) \right] \frac{\bar{y}_v}{\ell_r} \right\} \end{aligned} \quad (6)$$

where $\alpha_{eq,p}$ is the equivalent angle of attack without the vortices present and $(\Delta\alpha_{eq})_v$ is the angle of attack induced on the fin by the vortices. The fin bending moment at the root chord follows from the normal force and rolling moment

$$CBM_i = \frac{CRM_i}{\cos \delta_i} - CN_i \frac{a}{\ell_r} \quad (7)$$

The hinge moment is given by

$$CHM_i = \frac{CN_i}{\ell_r} (x_{HL} - \bar{x}_i) \quad (8)$$

The contributions of the fin forces and moments to the total missile forces and moments are given next in unrolled body coordinates.

$$\begin{aligned} C_{N_{fins}} &= (CN_2 \cos \delta_2 + CN_4 \cos \delta_4) \cos \phi \\ &+ (CN_1 \cos \delta_1 + CN_3 \cos \delta_3) \sin \phi \end{aligned} \quad (9)$$

$$\begin{aligned} C_{Y_{fins}} &= (CN_2 \cos \delta_2 + CN_4 \cos \delta_4) \sin \phi \\ &- (CN_1 \cos \delta_1 + CN_3 \cos \delta_3) \cos \phi \end{aligned} \quad (10)$$

$$C_{A_{fins}} = CN1 \sin \delta_1 + CN2 \sin \delta_2 + CN3 \sin \delta_3 + CN4 \sin \delta_4 \quad (11)$$

$$C_{m_{fins}} = C_{N_{fins}} \left(\frac{x_{MC} - x_{HL}}{l_r} \right) + (CBM2 \sin \delta_2 - CBM4 \sin \delta_4 + CHM1 + CHM3) \sin \phi + (CBM1 \sin \delta_1 - CBM3 \sin \delta_3 + CHM2 + CHM4) \cos \phi \quad (12)$$

$$C_{n_{fins}} = C_{Y_{fins}} \left(\frac{x_{MC} - x_{HL}}{l_r} \right) - (CBM2 \sin \delta_2 - CBM4 \sin \delta_4 + CHM1 + CHM3) \cos \phi + (CBM1 \sin \delta_1 - CBM3 \sin \delta_3 + CHM2 + CHM4) \sin \phi \quad (13)$$

$$C_{l_{fins}} = -CRM1 + CRM2 + CRM3 - CRM4 \quad (14)$$

The total lift and drag due to lift for the fins are

$$C_{L_{fins}} = C_{N_{fins}} \cos \alpha_c - C_{A_{fins}} \sin \alpha_c \quad (15)$$

$$C_{D_{fins}} = C_{N_{fins}} \sin \alpha_c + C_{A_{fins}} \cos \alpha_c \quad (16)$$

In reference 9, a method based on slender-body theory is presented for computing the interference lift produced on a body at zero bank in the presence of a set of all-movable fins. For the case of $\alpha_c \neq 0$ and $\delta = 0$, an interference factor, K_B , is defined such that

$$C_{N_{B(W)}} = K_B \left. \frac{dC_{N_W}}{d\alpha} \right|_{\alpha=0} \cdot \alpha_c, \quad \delta = 0 \quad (17)$$

The normal-force coefficient produced on the fins in the presence of the body is given by

$$C_{N_{W(B)}} = K_W \left. \frac{dC_{N_W}}{d\alpha} \right|_{\alpha=0} \cdot \alpha_c, \quad \delta = 0 \quad (18)$$

Dividing (17) by (18) gives

$$\frac{C_{N_{B(W)}}}{C_{N_{W(B)}}} = \frac{K_B}{K_W}, \quad \delta = 0 \quad (19)$$

For the case of $\alpha_c = 0$ and $\delta \neq 0$, an interference factor, k_B , is defined such that

$$C_{N_{B(W)}} = k_B \left. \frac{dC_{N_W}}{d\alpha} \right|_{\alpha=0} \cdot \delta, \quad \alpha_c = 0 \quad (20)$$

The normal-force coefficient produced on the fins in the presence of the body is given by

$$C_{N_{W(B)}} = k_W \left. \frac{dC_{N_W}}{d\alpha} \right|_{\alpha=0} \cdot \delta, \quad \alpha_c = 0 \quad (21)$$

Dividing (20) by (21) gives

$$\frac{C_{N_{B(W)}}}{C_{N_{W(B)}}} = \frac{k_B}{k_W}, \quad \alpha_c = 0 \quad (22)$$

Nielsen (ref. 9) has shown that the ratios K_B/K_W and k_B/k_W differ by less than 5 percent over the entire range of the radius to semispan ratio. This result indicates that the fraction of wing normal force which is carried over onto the body can be assumed to be independent of the means of lift production. Hence, the present method assumes

$$C_{N_{body}} = \frac{K_B}{K_W} C_{N_{fins}} \quad (23)$$

Similarly,

$$C_{Y_{body}} = \frac{K_B}{K_W} C_{Y_{fins}} \quad (24)$$

Reference 10 gives a method for computing the axial location of the center of pressure, \bar{x}_B , for the force on the body due to the fins

for zero fin deflection and zero roll. We assume for the present method that \bar{x}_B gives the correct value independent of the means of lift production on the fins. The moments created by the body force due to the presence of the fins are

$$C_{m_{body}} = C_{N_{body}} \frac{x_{MC} - \bar{x}_B}{l_r} \quad (25)$$

$$C_{n_{body}} = C_{Y_{body}} \frac{x_{MC} - \bar{x}_B}{l_r} \quad (26)$$

$$C_{l_{body}} = 0 \quad (27)$$

The user has the option of having the code compute K_B and \bar{x}_B using the methods of reference 10 or of using values obtained by some other method such as the code of Appendix F.

2.2.3 Afterbody section forces and moments.— The model used in the present method for vortex tracking over the afterbody section has been discussed previously in reference 3, pages 24-28, and in reference 11, pages 6-11. The discussion is repeated and extended in Appendix D. The present code does not account for tearing of afterbody vortices.

The afterbody loading is computed from the vortex impulse theorem using the vortex strengths and positions computed by the tracking method. The vortex impulse theorem for moderate angles of attack gives the following expression for the loading on an infinitesimal length of the afterbody in the presence of vortices

$$dC_N - i dC_Y = \frac{4\pi a^2}{S_R} \sum_{j=1}^{NV(x)} d(\Gamma' \sigma') \quad (28)$$

where σ' is the nondimensional complex distance between a vortex and its image inside the cylinder. Since the afterbody vortices may form anywhere between the canard trailing edge and the tail leading edge, the number of vortices NV is a function of axial position.

We can integrate equation (28) to obtain the afterbody forces and moments. The results are

$$C_N - iC_Y = \frac{4\pi a^2}{S_R} \sum_{j=1}^{NV(x)} [(\Gamma'\sigma')_{XTLE} - (\Gamma'\sigma')_{XCTE}] \quad (29)$$

$$C_m - iC_n = \frac{4\pi a^2}{S_R} \sum_{j=1}^{NV(x)} \int_{XCTE}^{XTLE} (x_{MC} - x) d(\Gamma'\sigma') \quad (30)$$

The integral in equation (30) is approximated by numerical quadrature in the code. The lower and upper limits of the integral are the trailing edge of the canard section and the leading edge of the tail section respectively.

3. COMPARISONS WITH DATA FOR FINS WITH NO EXTERNAL VORTICES PRESENT

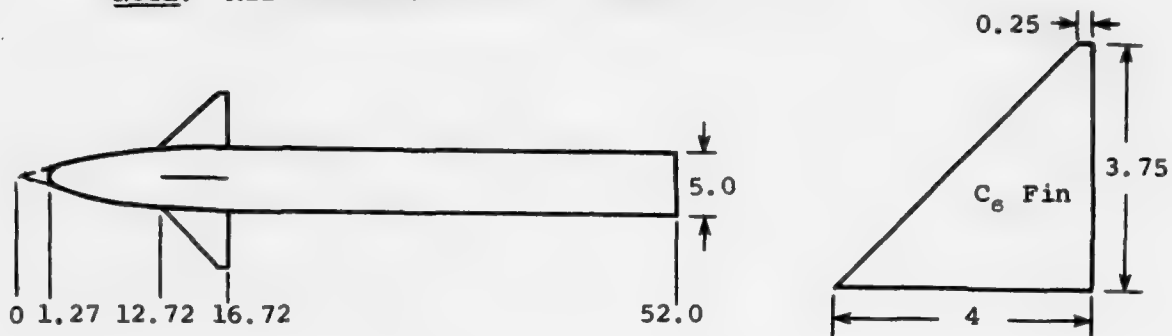
The purpose of this section is to evaluate the ability of the method to predict fin loads in the absence of external vortices. The fins and fin-body combinations to be considered are shown in figure 3. Section 3.1 considers clipped delta fins with a leading-edge sweep of 45° and a taper ratio of 0.06 (aspect ratio = 3.5). According to reference 12, such fins should have very little leading-edge vortex lift. Hence, section 3.1 is an evaluation of the method for fins with no significant vortex lift. Section 3.2 considers two sets of low-aspect-ratio fins for which fin-generated vortex lift is a substantial fraction of the total fin lift.

3.1 Moderate-Aspect-Ratio Fins

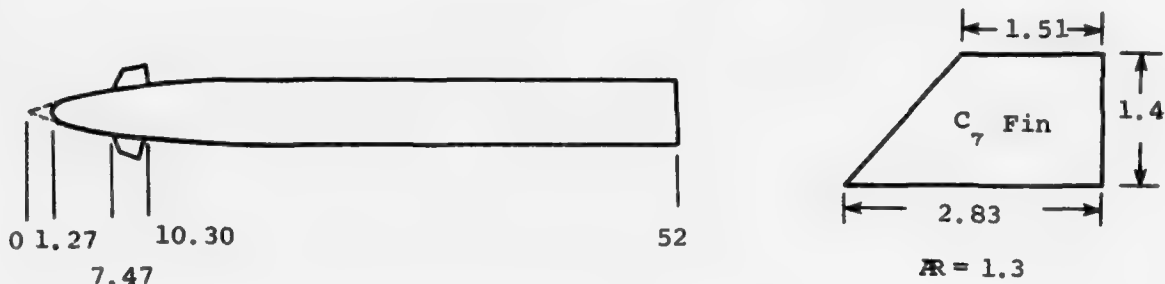
Data for this set of fins (C_δ) mounted as shown in figure 3(a) were obtained for several Mach numbers, bank angles, and fin deflections for included angles of attack up to 24° (ref. 4). The tests were conducted in such a way that the effects of bank only, deflection only, and combinations of both could be studied. A small amount of nose vorticity was observed to be present (ref. 5) that may slightly affect the fin loads.

The wing-alone characteristics used for the predictions are shown in figure 4. The normal force and lateral location of center of pressure data were obtained for $\alpha_c < 30^\circ$ from reference 4. The wing-alone values were computed from fin loads measured for $\phi = 0$, no yaw control and various values of pitch control. A description and experimental verification of this procedure is given in reference 6, pages 21-25. The results were extrapolated to higher angles of attack using a procedure given by Aiello (ref. 13). The axial location of the fin center of pressure was estimated as follows. Axial locations of the center of pressure for several sets of closely related fins tested alone and on bodies (refs. 4, 14, and 15) were compared for equivalent angles of attack up to 45° (see fig. 4). A linear best fit was applied to the data whenever the scatter was not large. For $M_\infty = 0.8$, the scatter was too large to fit for $\alpha_c < 14^\circ$ and \bar{x}/c_r was arbitrarily set equal to 0.55. In each of the subsections below the discussion centers first on the effects

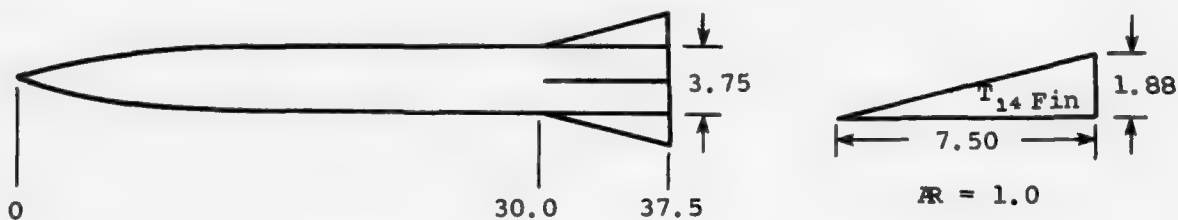
NOTE: All dimensions are in inches.



- (a) Body-canard configuration no. 1 (BC 1); moderate-aspect-ratio C_6 fins mounted on 3-caliber tangent ogive nose with 7-caliber cylindrical afterbody (MICOM-NWC tests, ref. 4).

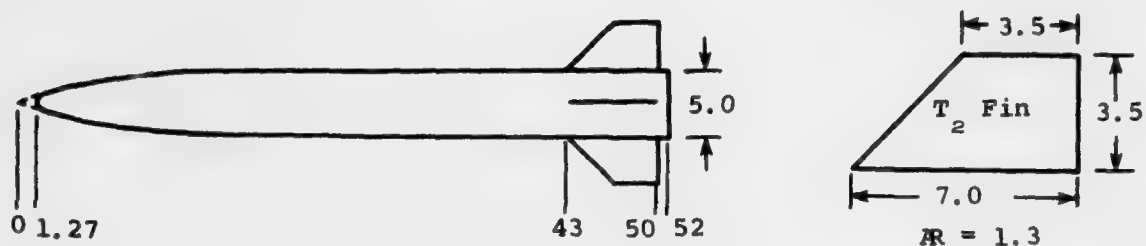


- (b) Body-canard configuration no. 2 (BC 2); low-aspect-ratio C_7 fins mounted on 3-caliber tangent ogive nose with 7-caliber cylindrical afterbody (MICOM-NWC tests, ref. 4).

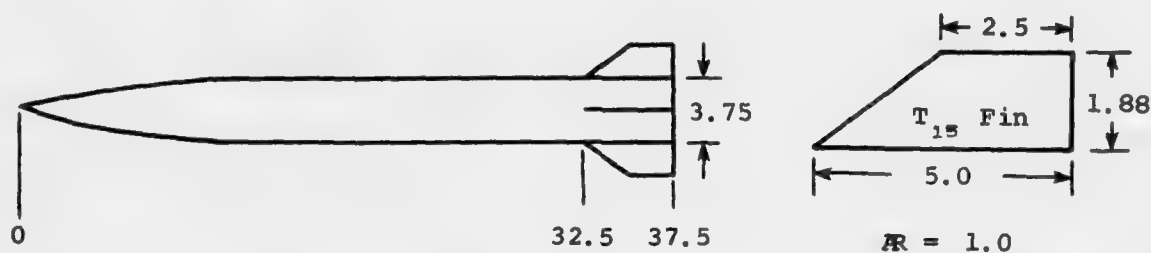


- (c) Body-tail configuration no. 1 (BT 1); low-aspect-ratio T_{14} fins mounted on 10-caliber body (MICOM tests, ref. 16).

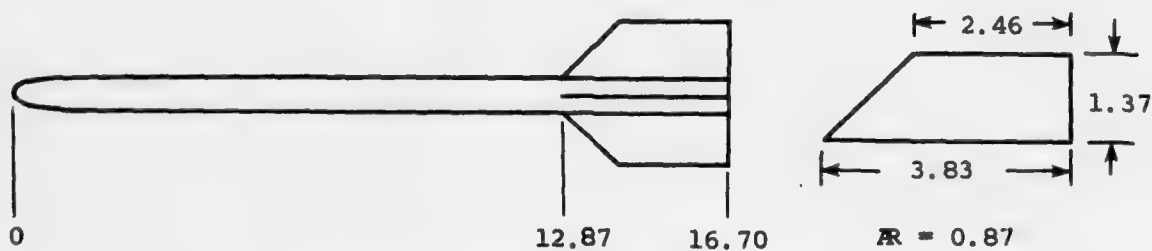
Figure 3. Configurations used for comparisons of data and theory.



(d) Body-tail configuration no. 2 (BT 2); low-aspect-ratio T_2 fins mounted on 10-caliber body (MICOM-NWC tests, ref. 4).

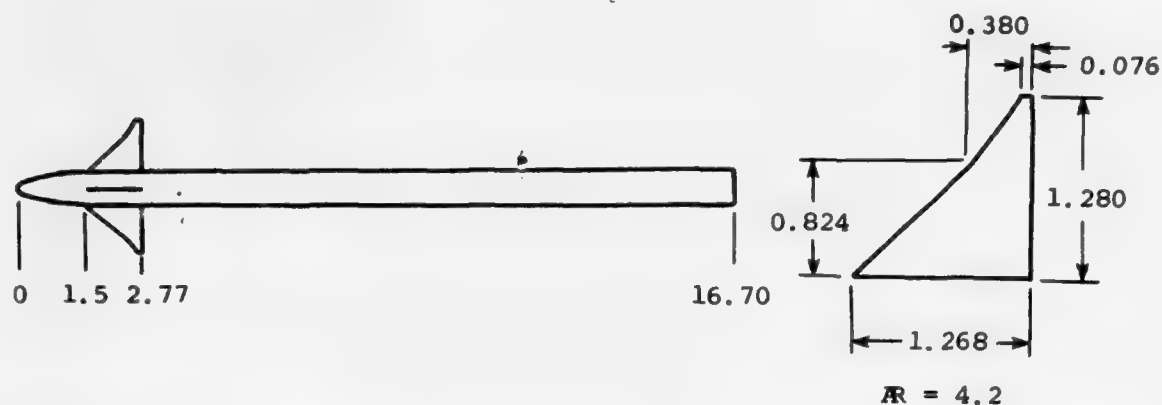


(e) Body-tail configuration no. 3 (BT 3); low-aspect-ratio T_{15} fins mounted on 10-caliber body (MICOM tests, ref. 16).

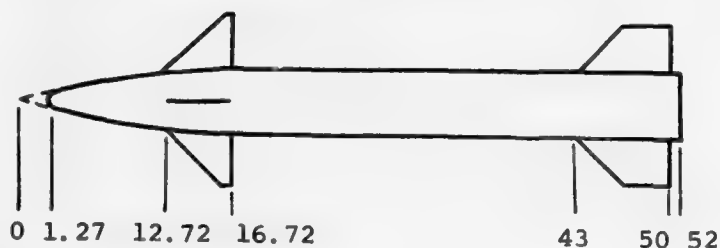


(f) Body-tail configuration no. 4 (BT 4); low-aspect-ratio AIM-9L tail fins mounted on 22-caliber body (AIM-9L tests, ref. 14).

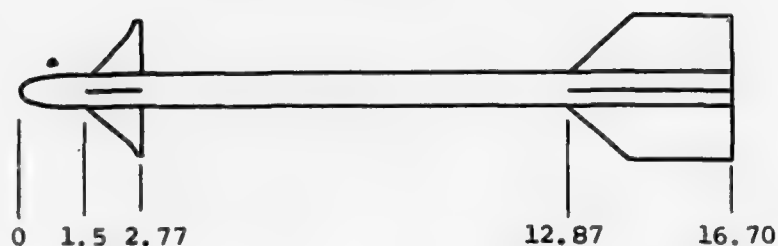
Figure 3. Continued.



- (g) Body-canard configuration no. 3 (BC 3); moderate-aspect-ratio AIM-9L canard fins mounted on 20-caliber cylindrical afterbody with 2-caliber nose (AIM-9L tests, ref. 14).



- (h) Body-canard-tail configuration no. 1 (BCT 1); C_e and T_2 fins mounted on 10-caliber body. (MICOM-NWC tests, ref. 4).



- (i) Body-canard-tail configuration no. 2 (BCT 2); AIM-9L model, reference 14.

Figure 3. Concluded.

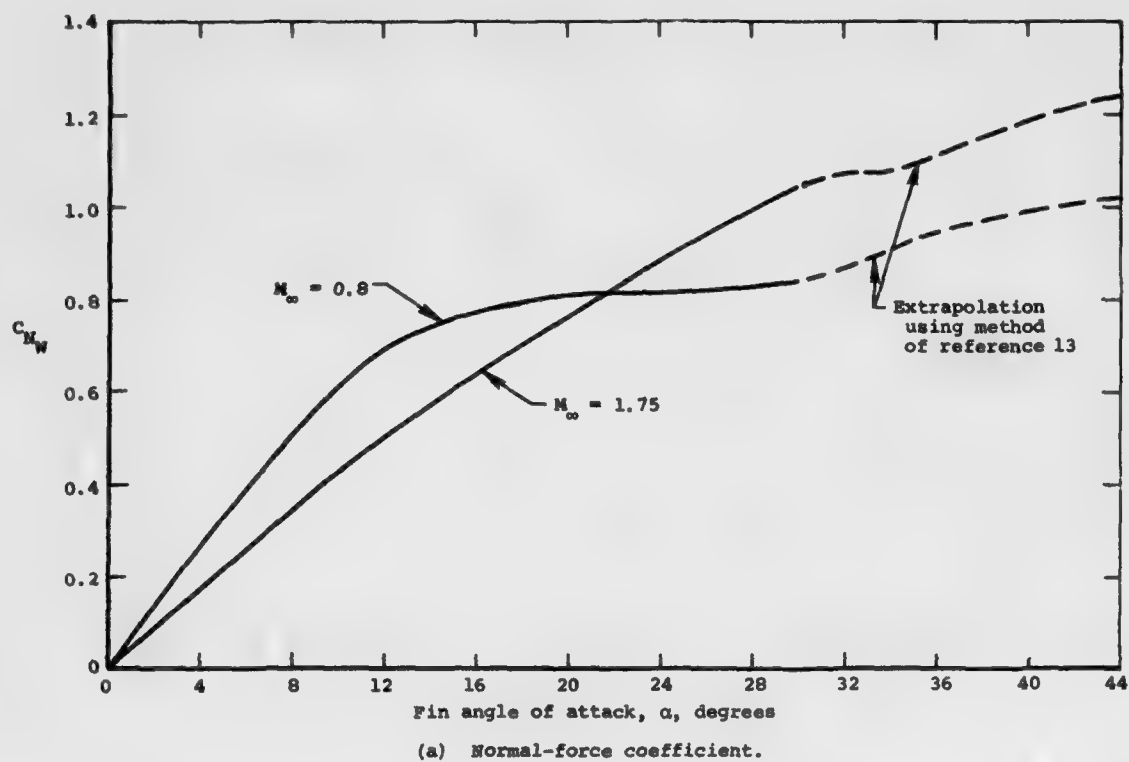
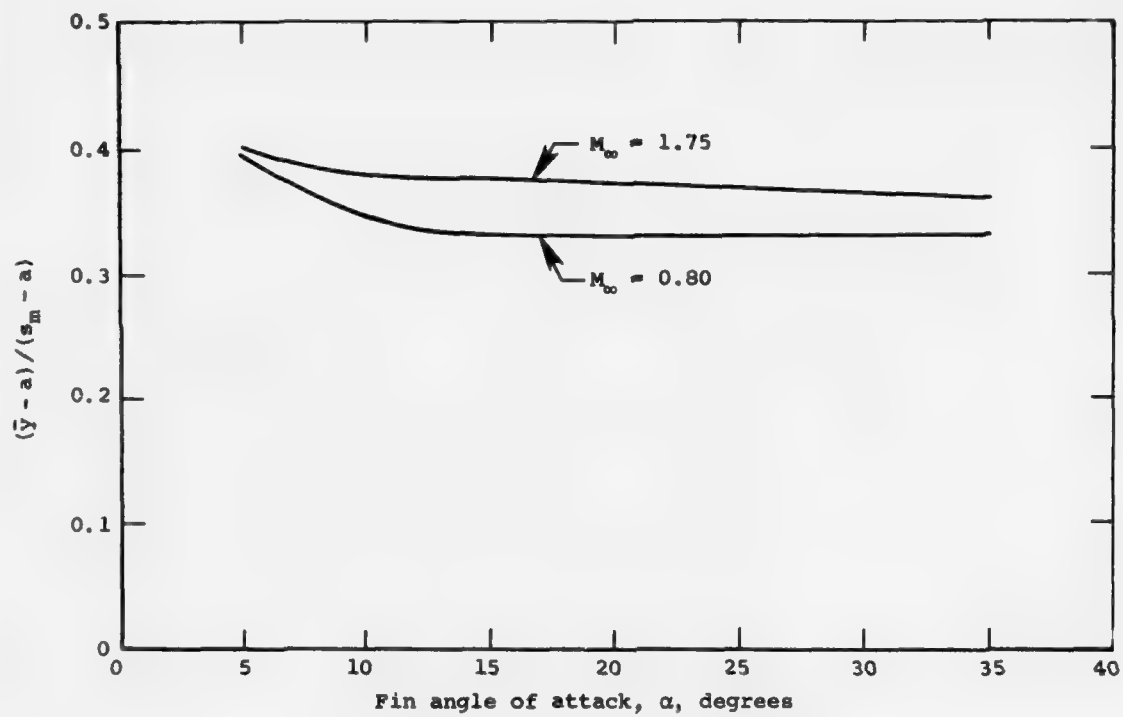
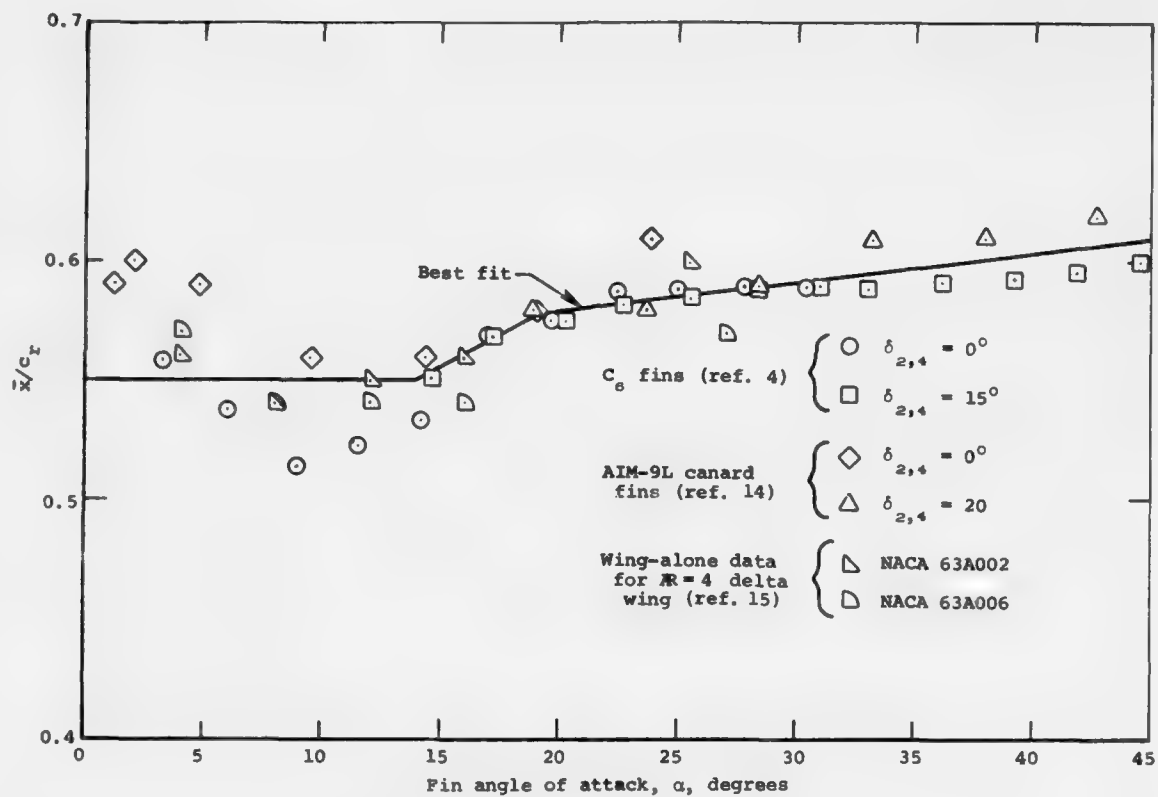


Figure 4. Wing-alone characteristics for moderate-aspect-ratio fins (C_e); S_R = planform area.



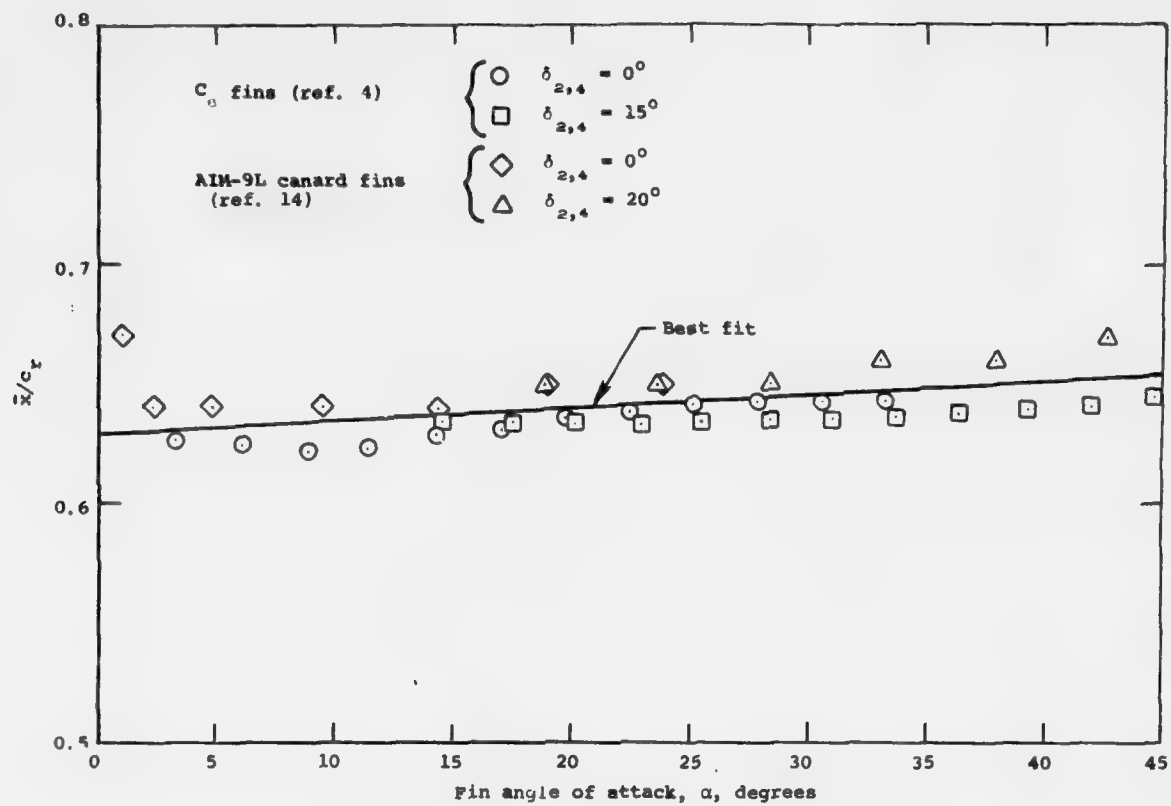
(b) Lateral center of pressure position.

Figure 4. Continued.



(c) Axial center of pressure position for $M_\infty = 0.8$.

Figure 4. Continued.



(d) Axial center of pressure position for $M_\infty = 1.75$.

Figure 4. Concluded.

of bank only, second on the effects of fin deflection only, and third on the combined effects of bank and fin deflection.

3.1.1 Supersonic flow, $M_\infty = 1.75$.— For this Mach number the leading edges of the fins are supersonic for $\alpha_c = 0$ and $\phi = 0$. The effects of bank only are presented first for several angles of attack. Fin normal forces are shown in figure 5 with the corresponding fin rolling moments shown in figure 6. The agreement is good. However, a comparison of the data for fins 1 and 2 at $\phi = 45^\circ$ reveals some discrepancy. The two fins should have the same loads at $\phi = 45^\circ$. Since the normal-force coefficients of fins 2 and 4 agree at $\phi = 0$, it seems likely that the data for fin 1 are slightly too high.

For the case of bank with no fin deflections and no external vortices, the equivalent angle of attack for each fin depends only on the K_W and $K_{\alpha\beta}$ terms of equations (23) to (26) of reference 3. For fins 1 and 2 at $\phi = 45^\circ$, the fraction of the total fin load for the case under discussion represented by the $K_{\alpha\beta}$ term ranges from 25 percent at $\alpha_c = 12.5^\circ$ to 40 percent at $\alpha_c = 20.6^\circ$. Thus, the generally good agreement exhibited in figure 5 suggests that the present method adequately accounts for bank angle when no fin vorticity is generated. The agreement for fin rolling moment is similar to that for fin normal force.

The fin loads with fin deflection and no bank are shown for $M_\infty = 1.75$ in figure 7. The data are shown as open symbols. Predictions using the Task 1 code are shown as solid and dashed lines. The agreement between data and predictions using the present method is good except for fin 3. For fin 3 the rate of change of normal force with α_c , although small, is about twice as great as predicted.

The combined effects of fin deflection and bank are shown in figure 8. The agreement is about what one would expect from a comparison with figures 5 and 7. The theory assumes that fin deflection and bank effects can be linearly superposed and figures 5, 7, and 8 seem to confirm that assumption. Note from figures 5, 6, and 7 that the behavior of the fin rolling moment in the absence of free vortices closely follows that of the fin normal force.

3.1.2 Subsonic Flow, $M_\infty = 0.8$.— At high angles of attack, the flow about body-canard configuration no. 1 (see fig. 3(a)) at $M_\infty = 0.8$ is transonic. Hence, the results of this section represent an evaluation of the method for extreme transonic flow conditions. The effects of

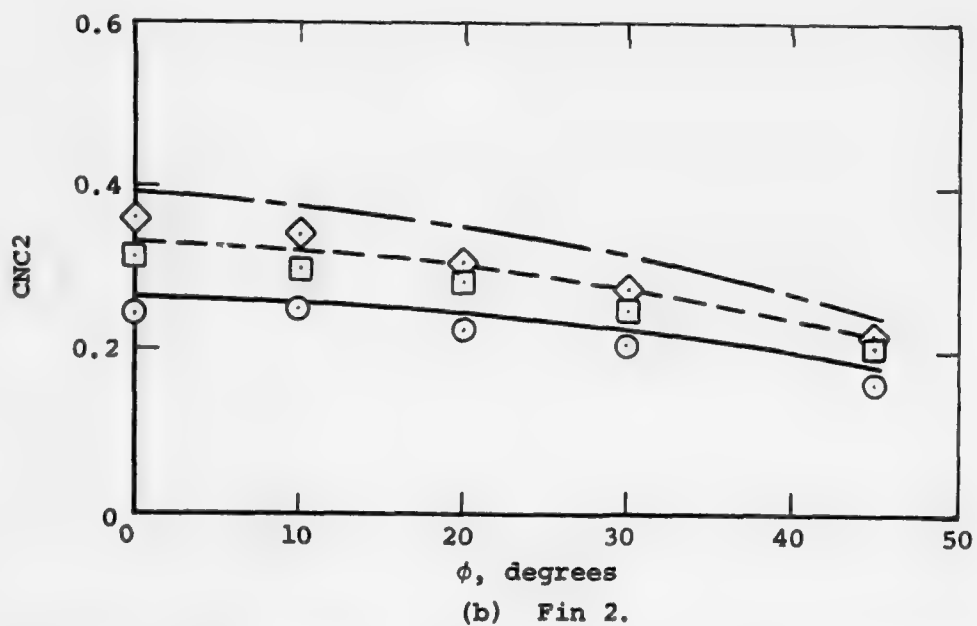
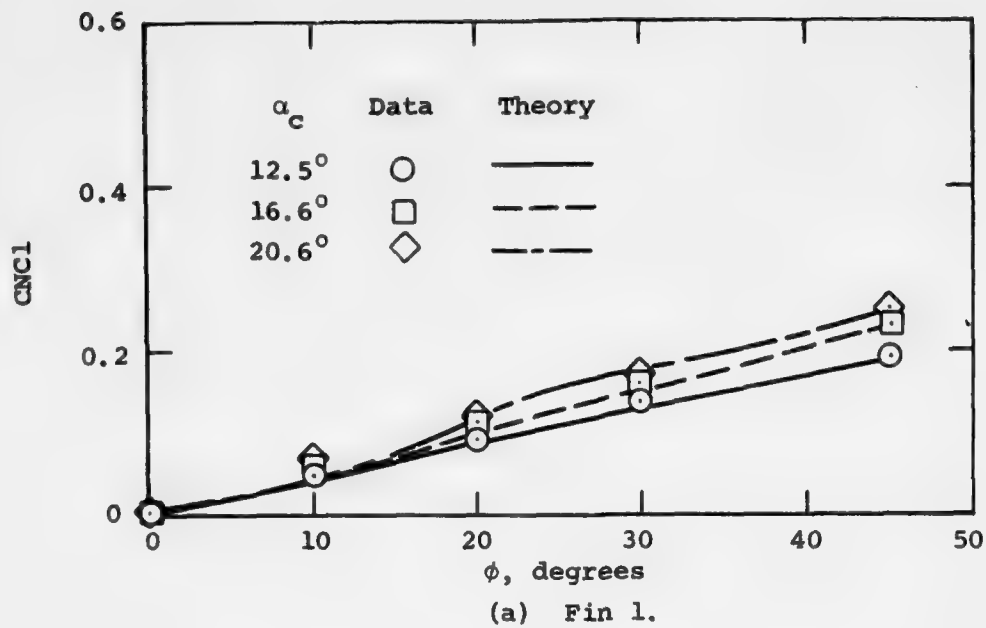


Figure 5. Fin normal force for bank with no fin deflection, moderate-aspect-ratio fins (C_δ), BC 1, $M_\infty = 1.75$; S_R = model base area.

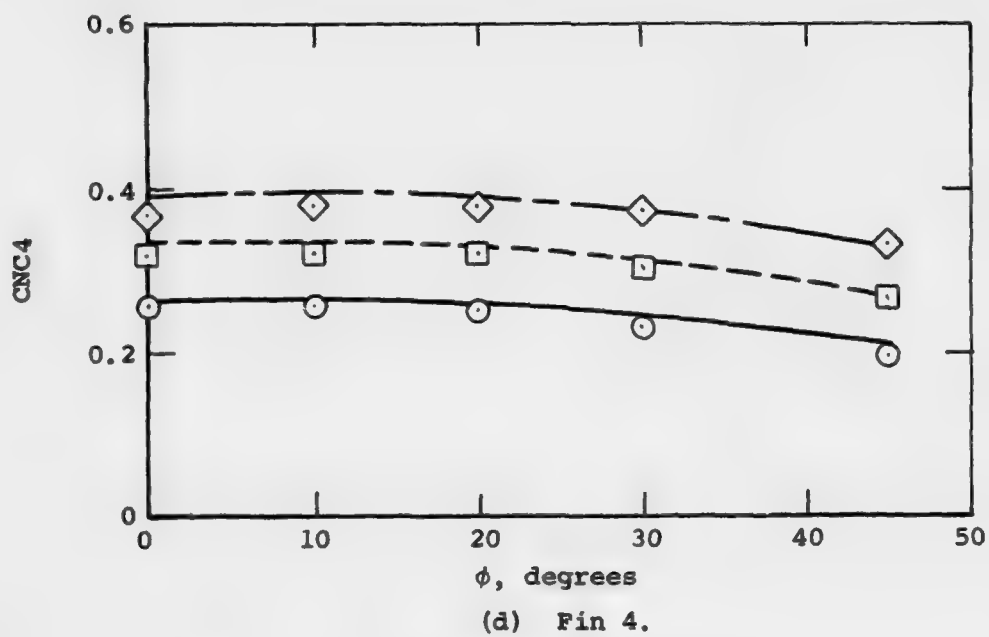
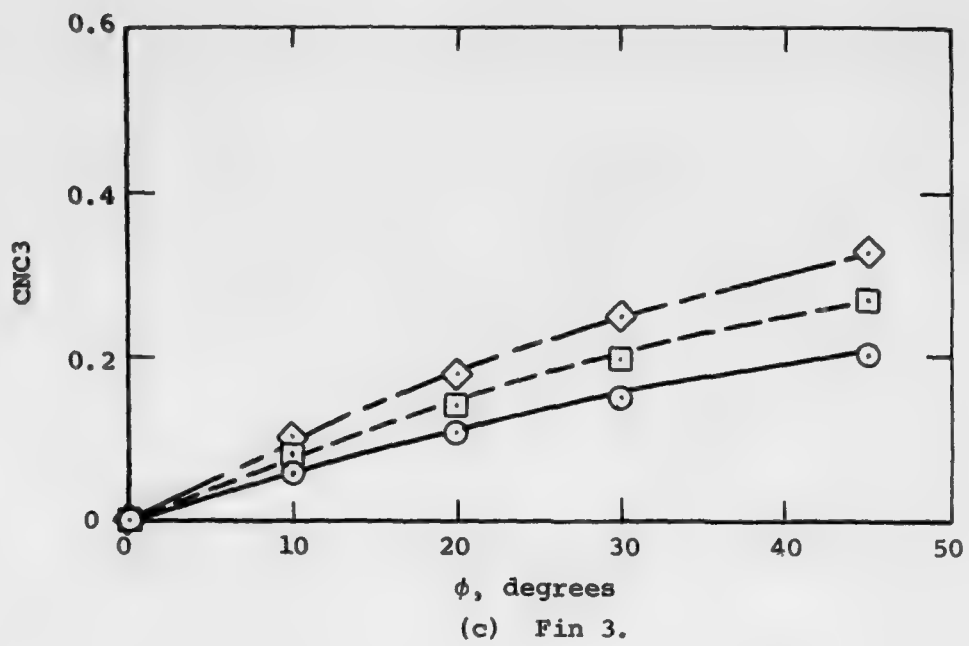
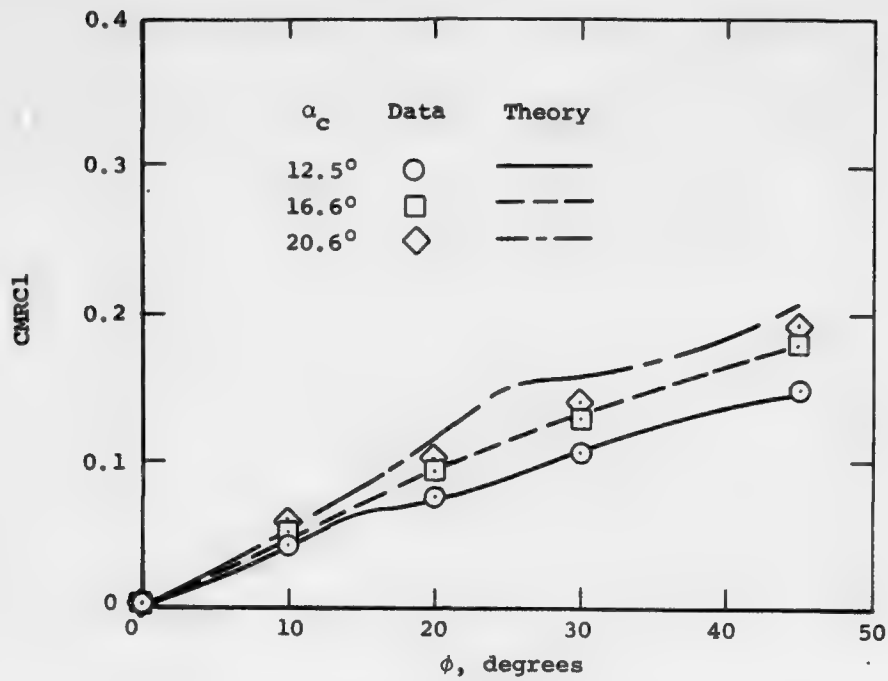
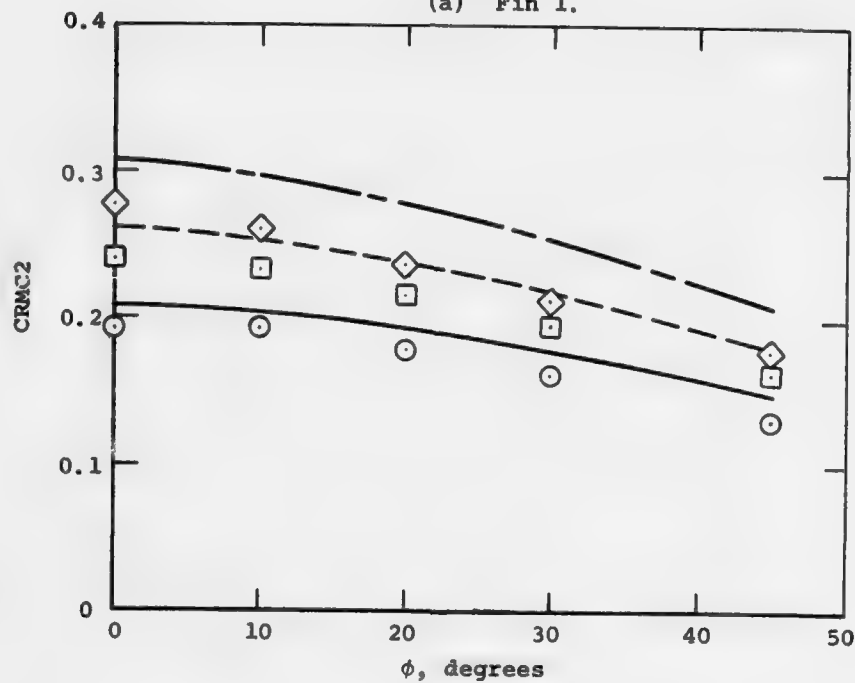


Figure 5. Concluded.

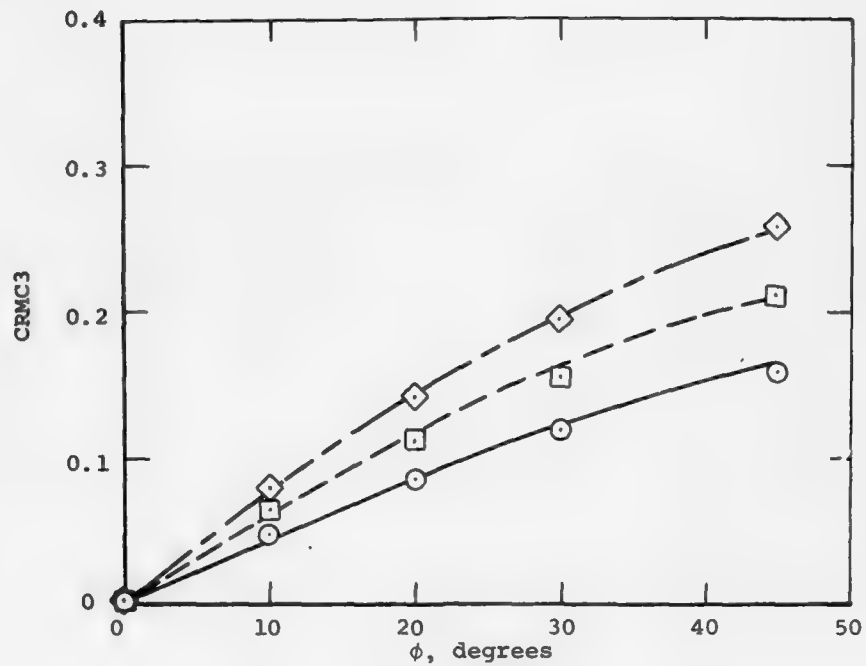


(a) Fin 1.

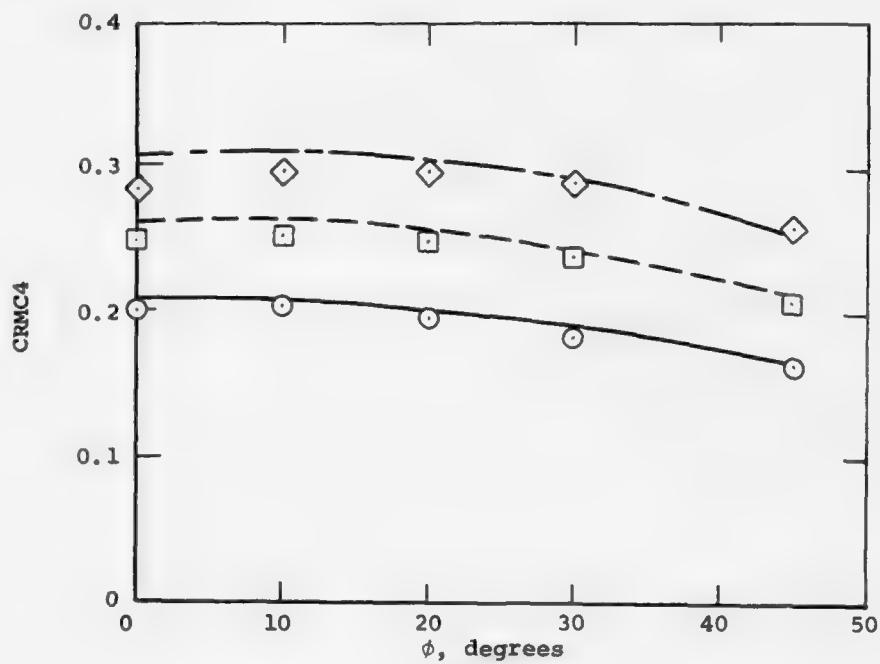


(b) Fin 2.

Figure 6. Fin rolling moment for bank with no fin deflection, moderate-aspect-ratio fins (C_e), BC 1, $M_\infty = 1.75$; S_R = model base area, r_R = model base diameter.



(c) Fin 3.



(d) Fin 4.

Figure 6. Concluded.

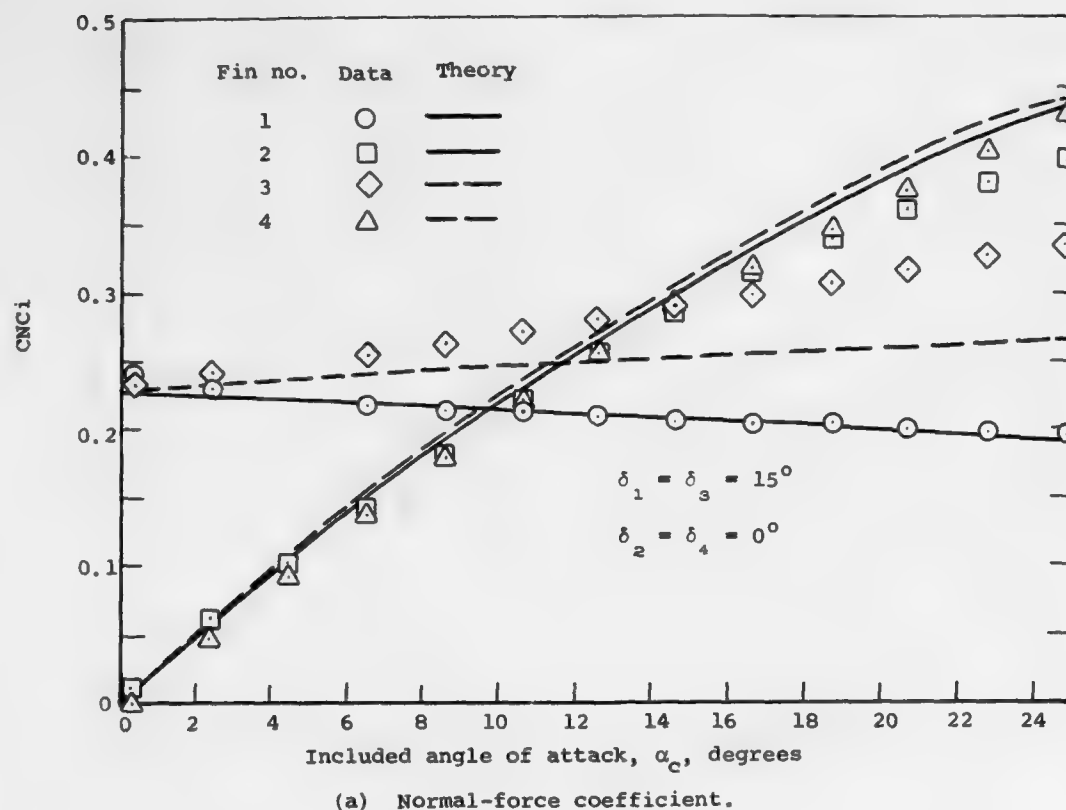
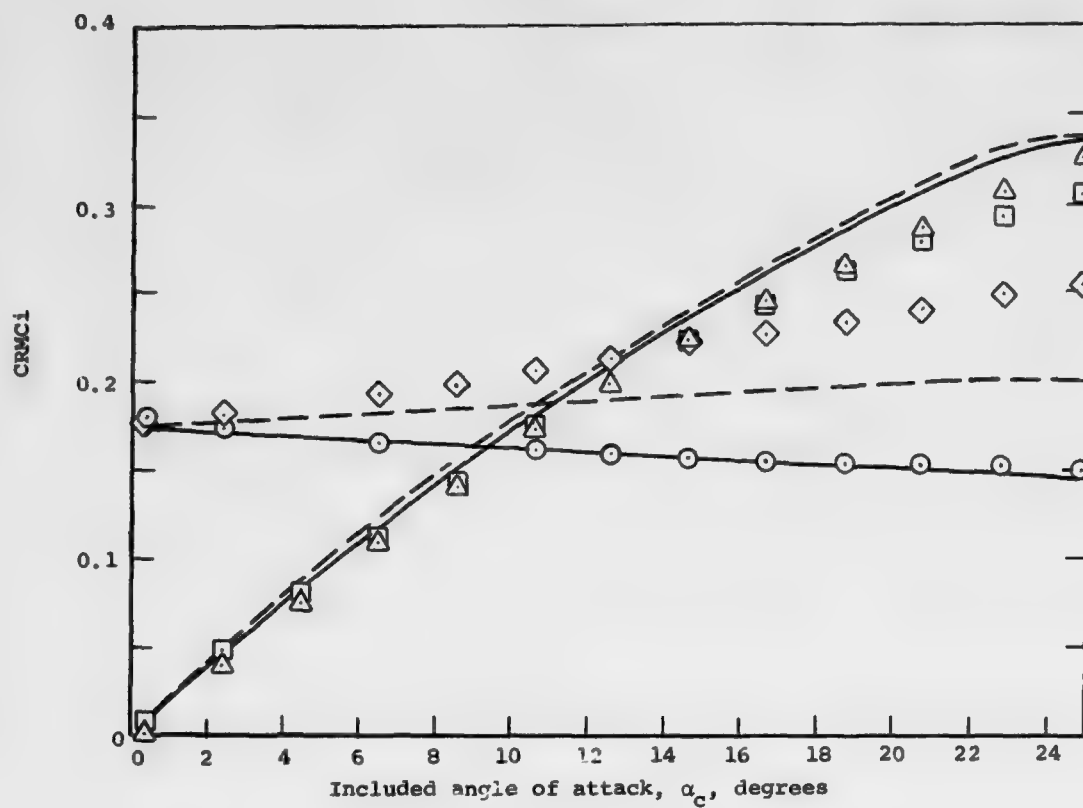
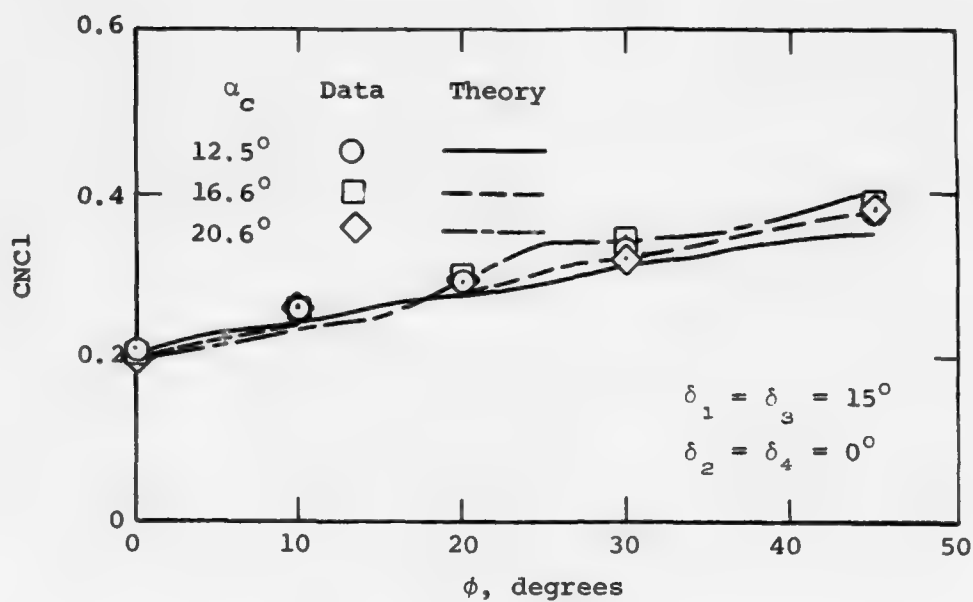


Figure 7. Fin normal force and rolling moment for fin deflection with no bank, moderate-aspect-ratio fins (C_e), BC 1, $M_\infty = 1.75$; S_R = model base area, ℓ_r = model base diameter.

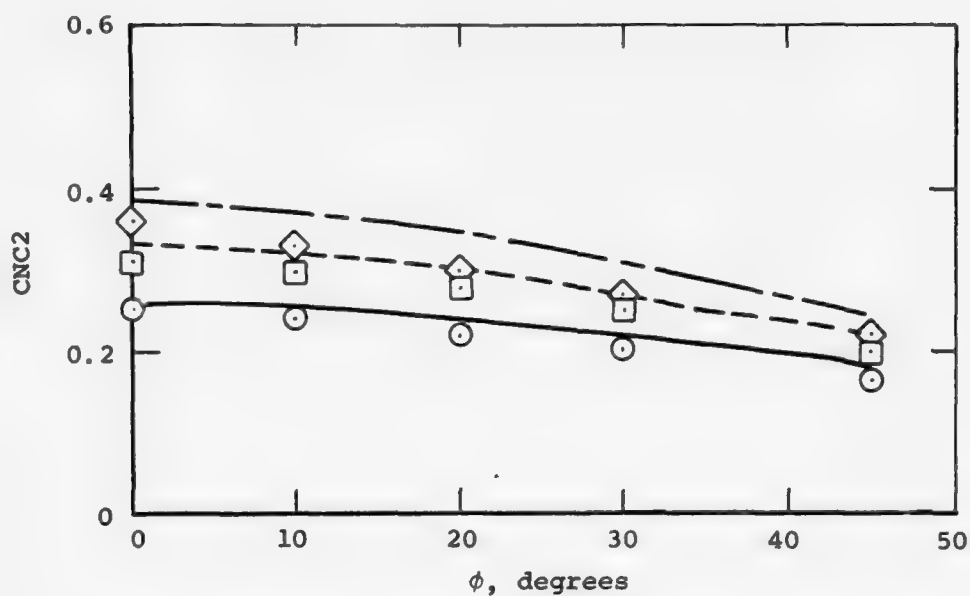


(b) Rolling-moment coefficient.

Figure 7. Concluded.

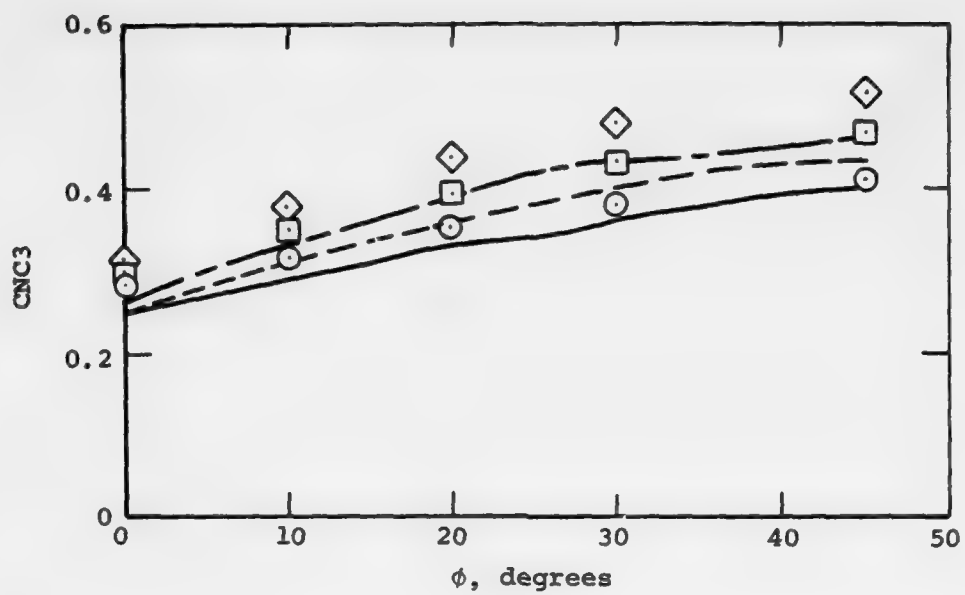


(a) Fin 1.

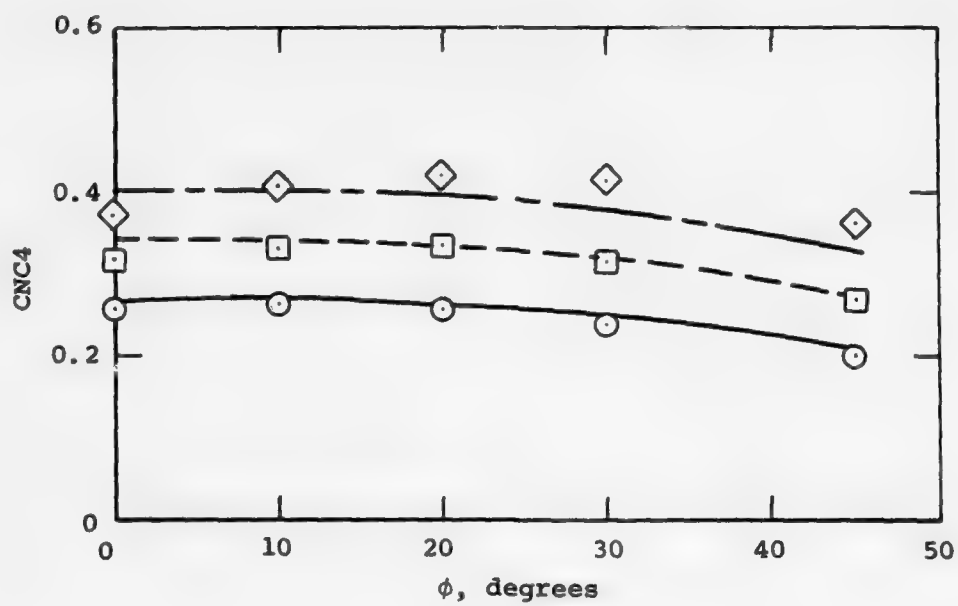


(b) Fin 2.

Figure 8. Fin normal force for combined bank and fin deflection, moderate-aspect-ratio fins (C_e), BC 1, $M_\infty = 1.75$; S_R = model base area.



(c) Fin 3.



(d) Fin 4.

Figure 8. Concluded.

bank only are presented in figure 9. The agreement is generally very good except for fin 1. Again, the data for fin 1 and fin 2 do not agree at $\phi = 0$. It seems likely that, for this case too, the fin 1 data are too high. Adjusting the fin 1 data so that they agree with the fin 2 data at $\phi = 45^\circ$ gives very good agreement with the theory.

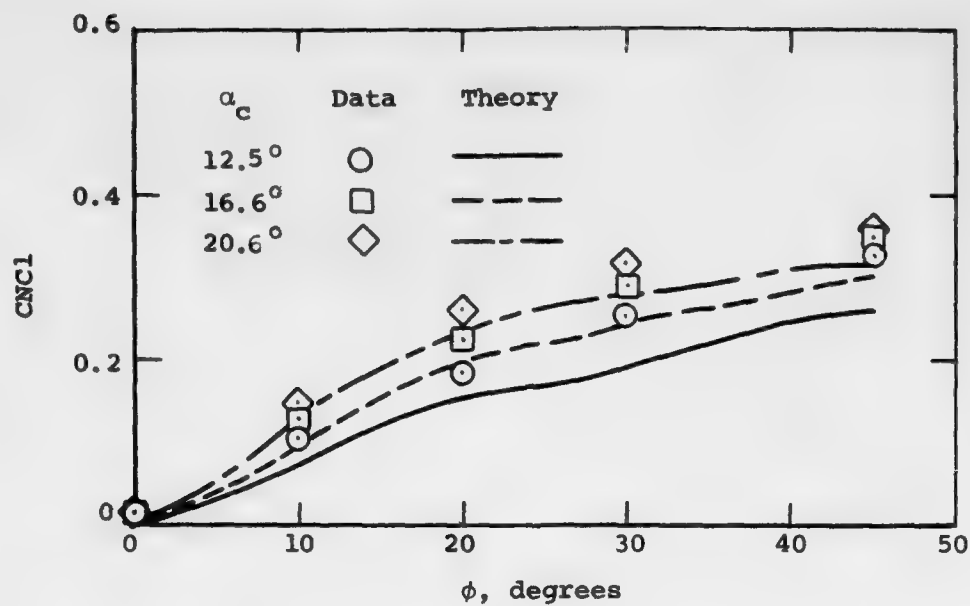
The fin loads due to fin deflection with no bank are shown in figure 10. The agreement is good except for fin 1. Since fin 1 should have the same load at $\alpha_c = 0^\circ$ as fin 3, it appears that the data for at least one of the fins are in error. If the data for fin 1 are adjusted so as to agree with fin 3 at $\alpha_c = 0^\circ$, it is found that the theory slightly overpredicts the decrease in fin normal force as α_c increases for $\alpha_c > 6^\circ$. A possible explanation for this discrepancy may be the change in fin leading-edge sweep with α_c . At $\phi = 0$ and $\alpha_c = 0$, the leading edge of fin 1 is swept 45° . As α_c increases, the effective sweep of the leading edge increases. It seems likely that the fin picks up significant vortex lift as α_c increases. This point will be discussed further in section 3.2. Note that for $\alpha_c > 16^\circ$, fin 1 seems to be favorably affected by the nose vorticity. This point will be discussed further in section 4.

The combined effects of fin deflection and bank are shown in figure 11. Again, the agreement is good except for fin 1. The discrepancy for fin 1 is about what would be expected from the results of the bank only (fig. 9) and fin deflection only (fig. 10) comparisons as discussed above. The data for fin deflection only are suspect.

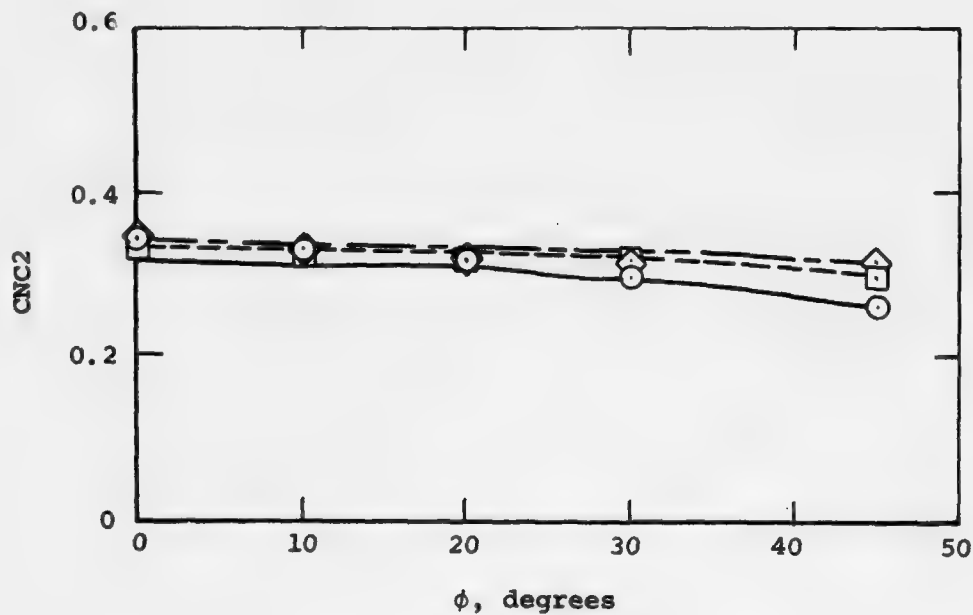
3.2 Low-Aspect-Ratio Fins

3.2.1 Aspect ratio 1.3 fins.— Data for the C_7 set of fins (see fig. 3(b)) were obtained for several Mach numbers and bank angles for model angles of attack up to 24° (ref. 4). The fins were not deflected except in pitch at $\phi = 0^\circ$. The wing-alone normal force was computed using the same procedure used for the moderate-aspect-ratio fins (see section 3.1). The axial and lateral locations of the center of pressure were estimated by the methods of reference 13. The wing-alone characteristics are given in figure 12.

Comparisons of theory and data for $M_\infty = 1.75$ for nose-canard configuration no. 2 (C_7 fins) are presented in figure 13. The data trends are similar to those observed in figure 5 for the moderate-aspect-

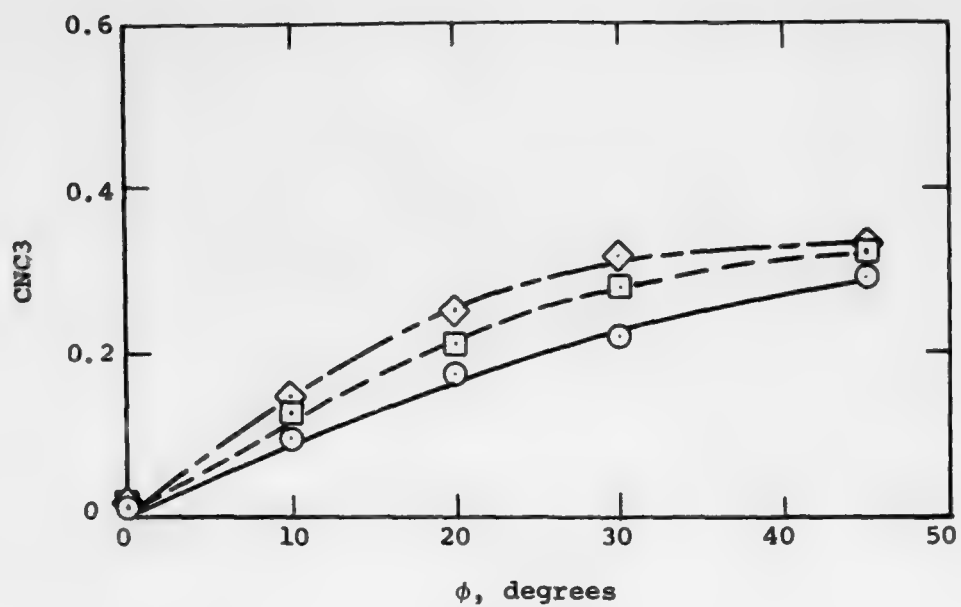


(a) Fin 1.

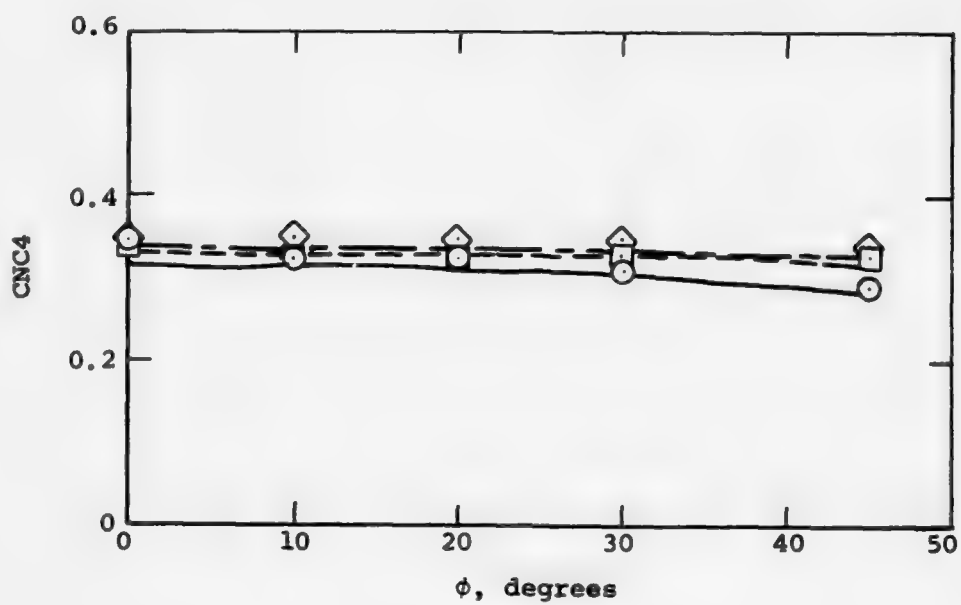


(b) Fin 2.

Figure 9. Fin normal force for bank with no fin deflection, moderate-aspect-ratio fins (C_e), BC 1, $M_\infty = 0.8$; S_R = model base area.



(c) Fin 3.



(d) Fin 4.

Figure 9. Concluded.

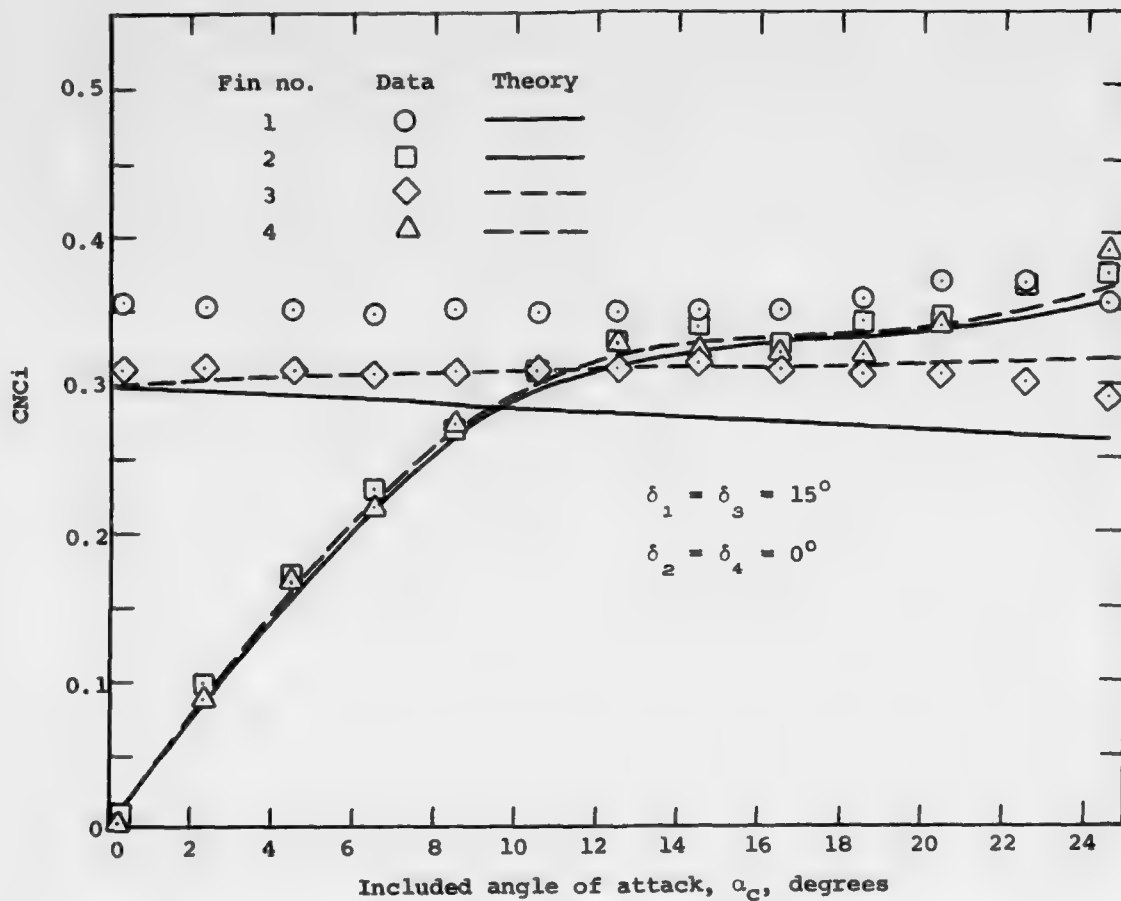


Figure 10. Fin normal force for fin deflection with no bank, moderate-aspect-ratio fins (C_e), BC 1, $M_\infty = 0.8$; S_R = model base area.

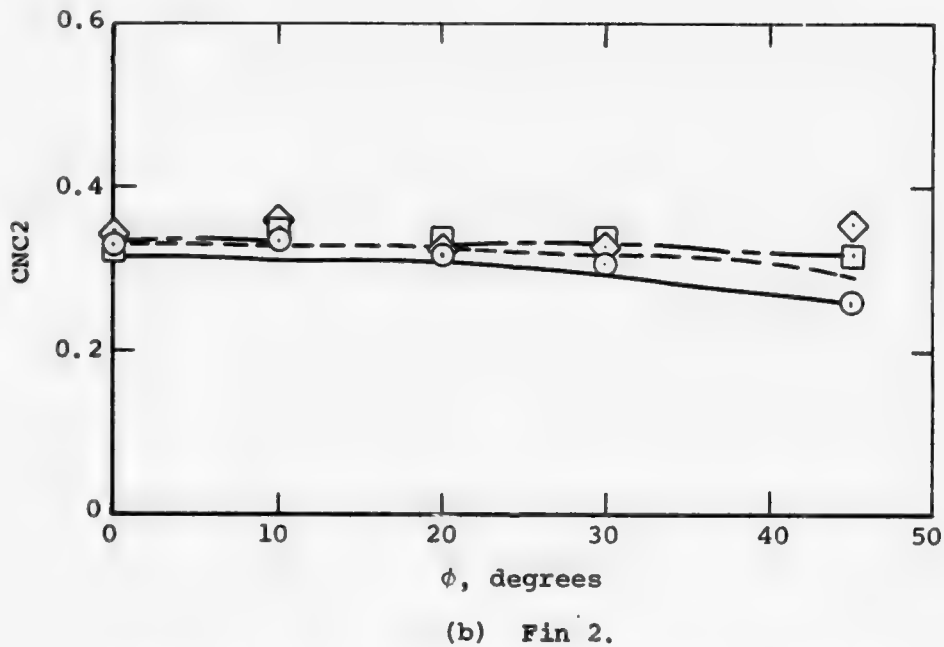
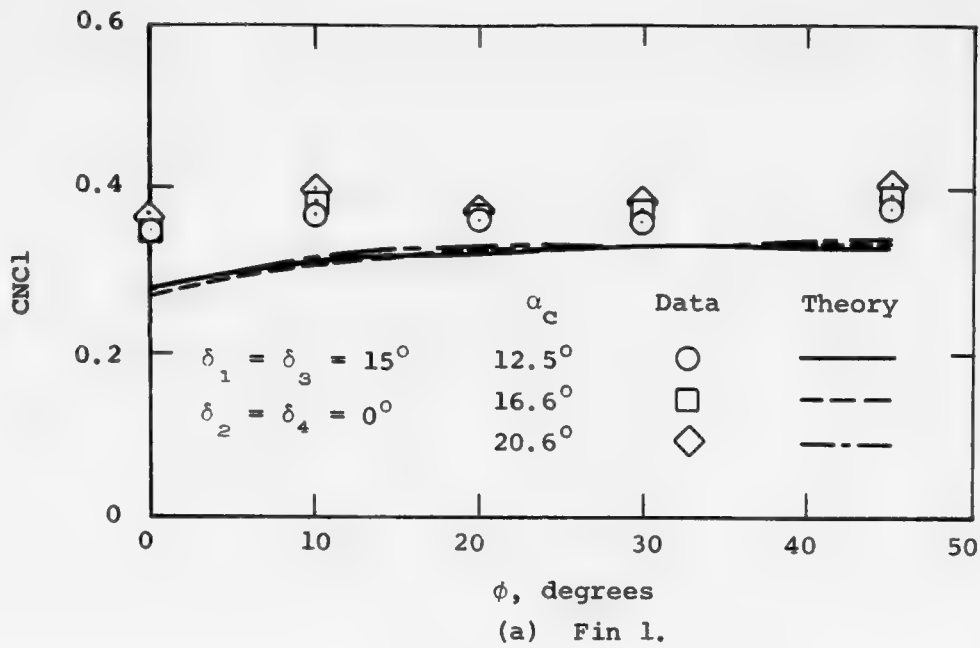
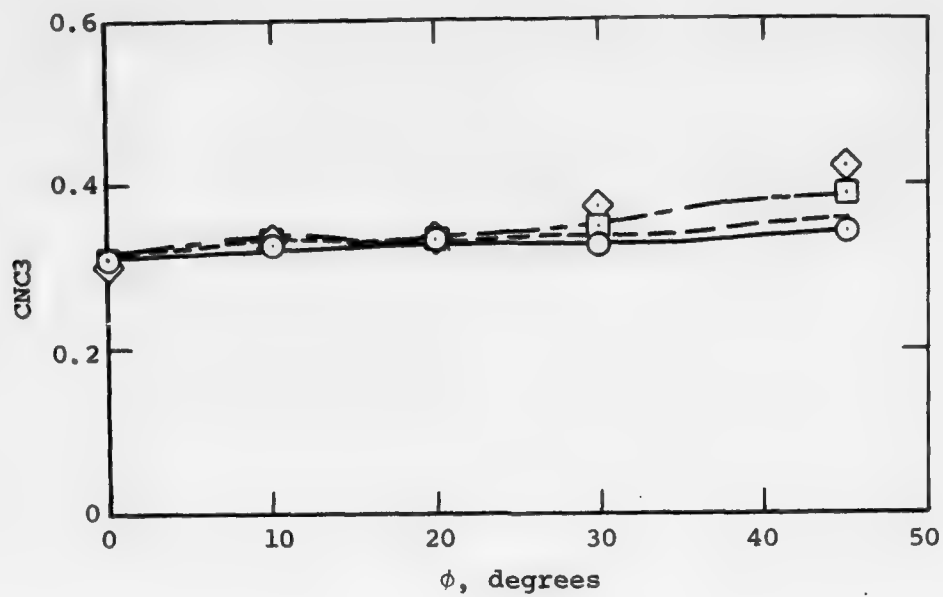
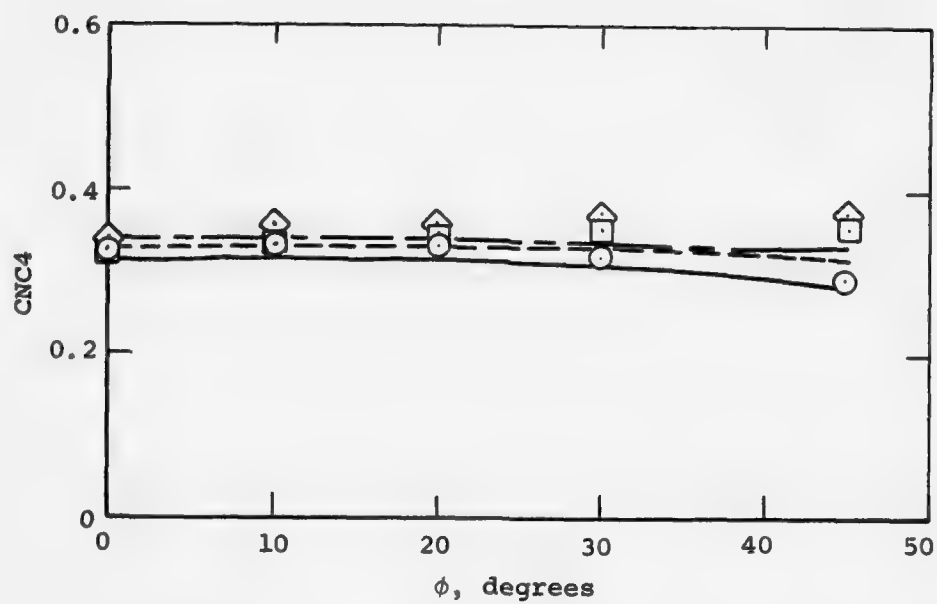


Figure 11. Fin normal force for combined bank and fin deflection, moderate-aspect-ratio fins (C_δ), BC 1, $M_\infty = 0.8$; S_R = model base area.



(c) Fin 3.



(d) Fin 4.

Figure 11. Concluded.

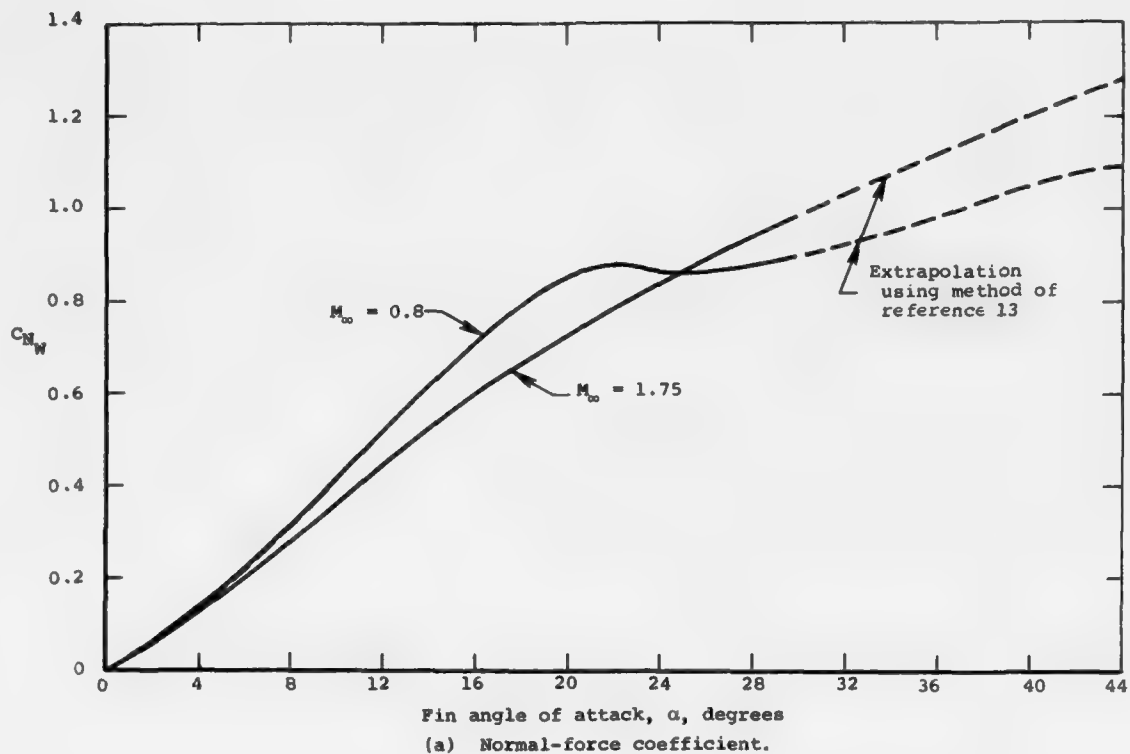
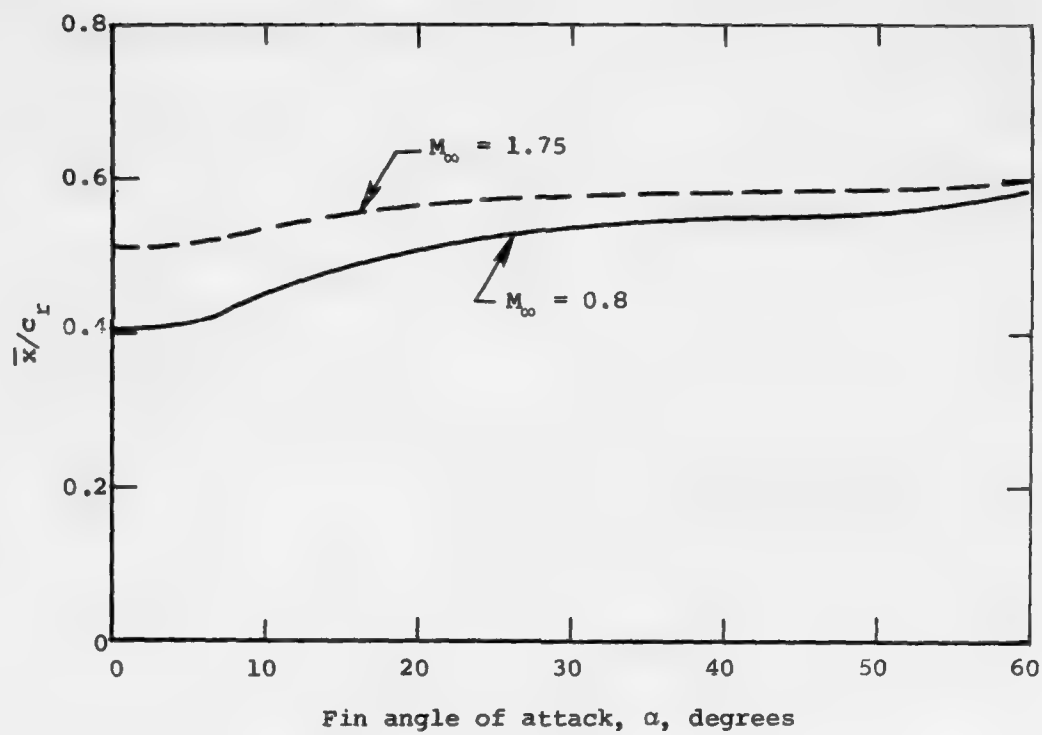
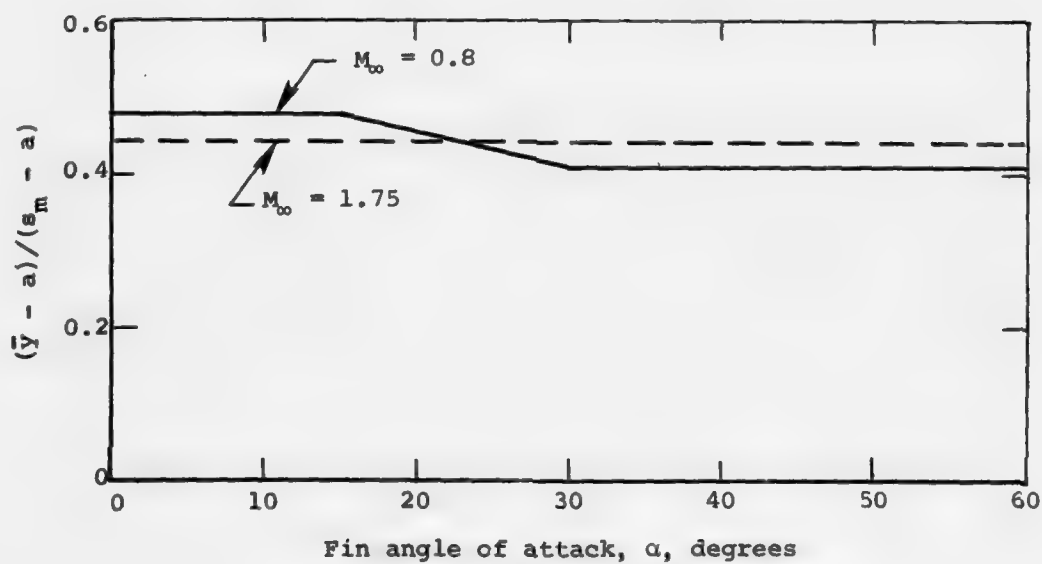


Figure 12. Wing-alone characteristics for low-aspect-ratio fins (C_7 and T_E); $R = 1.3$, S_R = planform area.

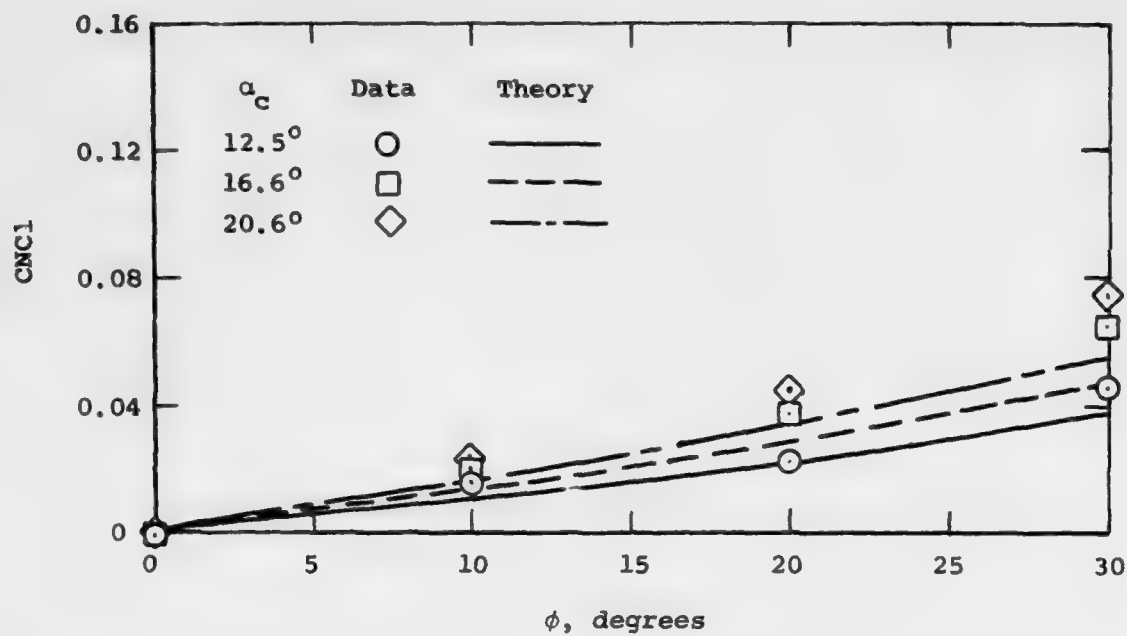


(b) Axial center of pressure position.

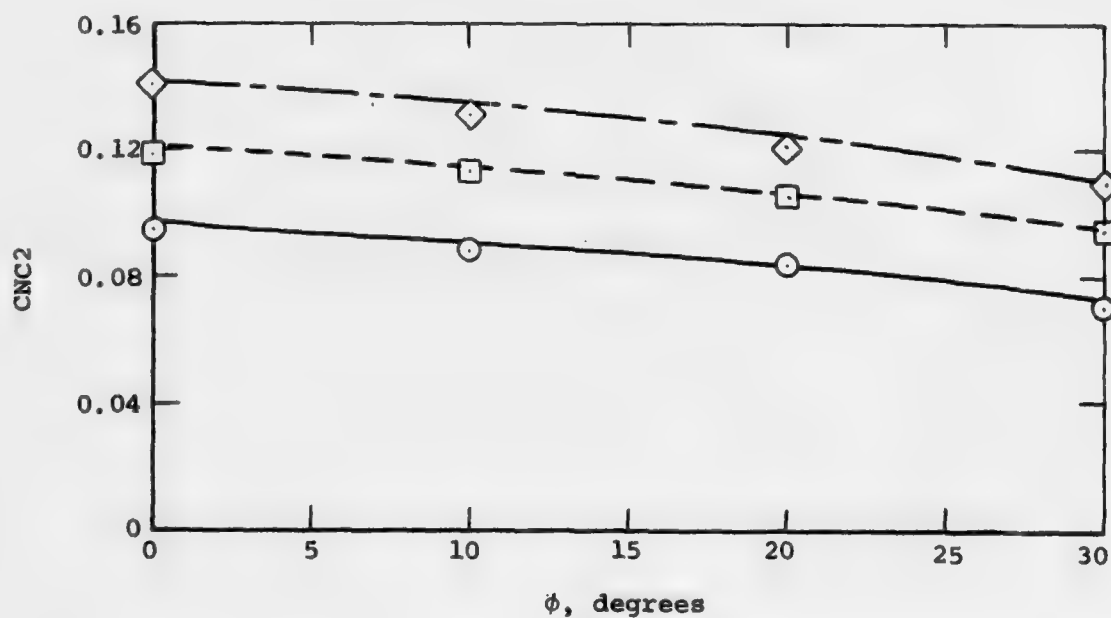


(c) Lateral center of pressure position.

Figure 12. Concluded.

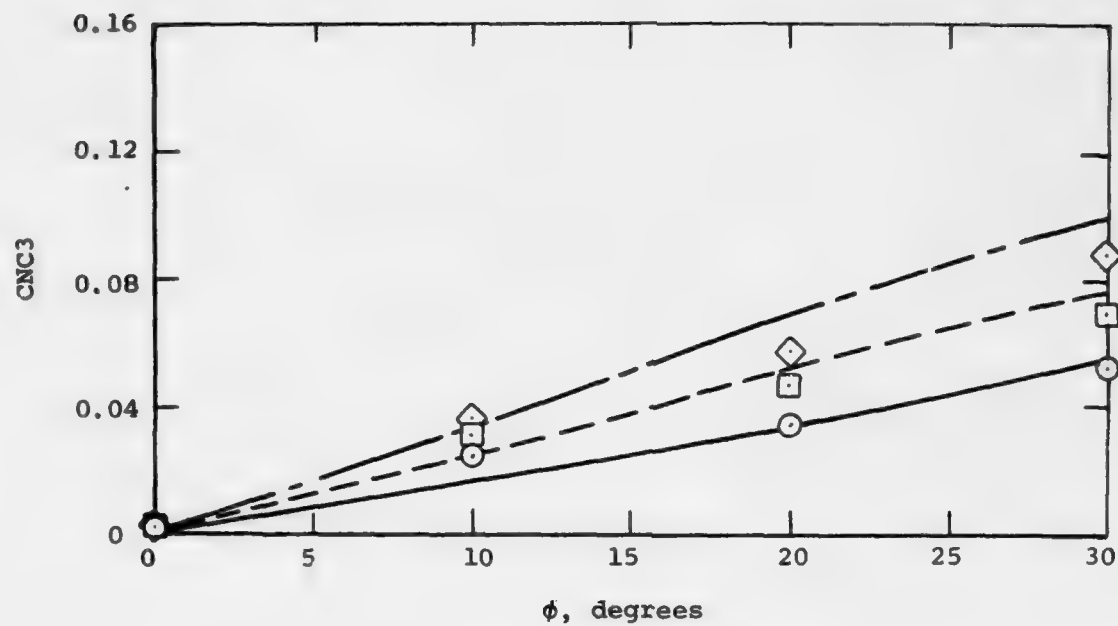


(a) Fin 1.

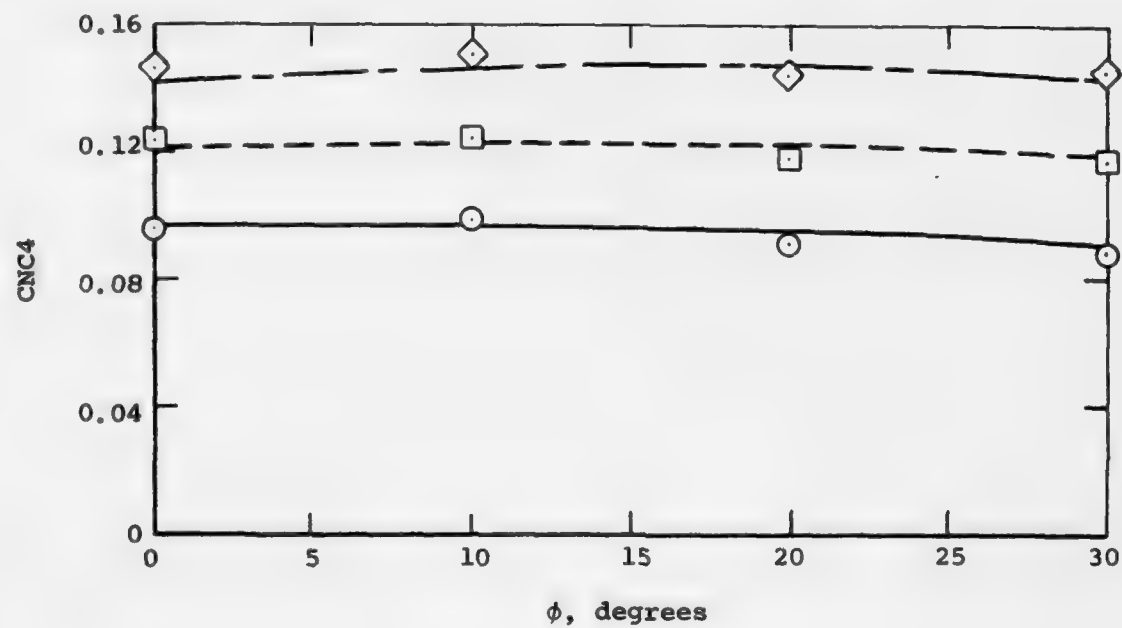


(b) Fin 2.

Figure 13. Fin normal force for bank with no fin deflection, low-aspect-ratio fins (C_7), BC 2, $M_\infty = 1.75$; S_R = model base area.



(c) Fin 3.



(d) Fin 4.

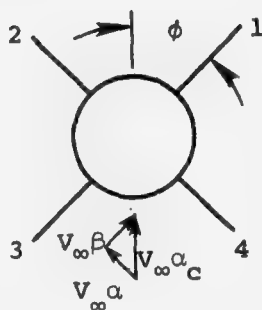
Figure 13. Concluded.

ratio fins (C_g). However, the predictions are low for fin 1 and high for fin 3. Since no such effect was observed for the C_g fins, we are led to attribute the anomaly to the difference in fin aspect ratio. The present method uses the small angle definitions of angle of attack and angle of sideslip. Hence, for fins 1 and 3, we have

$$\alpha = \alpha_c \sin \phi \quad (31)$$

$$\beta = \alpha_c \cos \phi \quad (32)$$

as shown in the sketch below.



Sketch 1. Small angle definitions of fin 3 angle of attack and angle of sideslip.

(For high angle of attack, these definitions must be modified.) Note that

$$\frac{\beta}{\alpha} = \cot \phi \quad (33)$$

which means that when fins 1 and 3 are undeflected, the fin sideslip angle is greater than the fin angle of attack for $\phi < 45^\circ$. For the low-aspect-ratio fins under discussion in this section, it seems likely that the leading-edge and side-edge vortex lift is strongly influenced by the sideslip under such conditions. The theory used in this report does not take this phenomenon into account. In fact, the present method assumes that the ratio of vortex lift to total lift at a given angle of attack does not change with angle of sideslip.

Comparisons of theory and data for the C_7 fins for $M_\infty = 0.8$ are presented in figure 14. Note that the comparisons for fins 1 and 3 are similar to those for $M_\infty = 1.75$. The theory indicates that the equivalent angles of attack for fins 1 and 3 are less than 20° . Hence, considering the wing-alone force characteristics of figure 12, we can assume that the flow over the fins is essentially attached except for edge vortices. As discussed above, the effect of sideslip on edge vortex lift may be an important phenomenon.

For discussion purposes, let us consider a fin with aspect ratio 1.3 but with a delta planform. For such a fin, all the vortex lift is due to the leading edge. It has been shown for such fins in incompressible flow at a given angle of attack with no sideslip that the ratio of vortex lift to attached flow lift decreases as the wing leading-edge sweep decreases (ref. 12). It seems likely that a similar result occurs for changes in leading-edge sweep due to sideslip. The present method assumes that, for a given angle of attack, the vortex lift remains a constant fraction of the attached flow lift as the effective leading-edge sweep changes. Hence, for fin 1, which has an increasing effective leading-edge sweep as α_c increases, the theory would underpredict the data. For the same reasons, the theory would overpredict the data for fin 3.

The discrepancy between data and theory shown in figure 14 for fins 2 and 4 can be traced to measurement error. Fins 2 and 4 should have the same lift at $\phi = 0$. If the data of fin 4 are adjusted so that they match the data of fin 2 at $\phi = 0$, the agreement for fin 4 is good. The agreement for fin 2 is within the apparent measurement error.

3.2.2 Aspect ratio 1.0 fins.— Data for the T_{14} set of fins of body-tail configuration no. 1 were obtained for several Mach numbers and bank angles for model angles of attack up to 45° (ref. 16). Since the body length in front of the fins was large enough to produce strong body vortices, we will give results for the windward fins only. The fins were not deflected. The wing-alone characteristics for angles of attack up to 30° were obtained by interpolation of data at several Mach numbers for fins mounted on a reflection plane (ref. 17). The data were extrapolated to higher angles of attack using the methods of reference 13. The wing-alone results are given in figure 15.

Comparisons of theory and data for $M_\infty = 2.0$ are presented in figure 16. The phenomena discussed above for the 1.3 aspect ratio fins

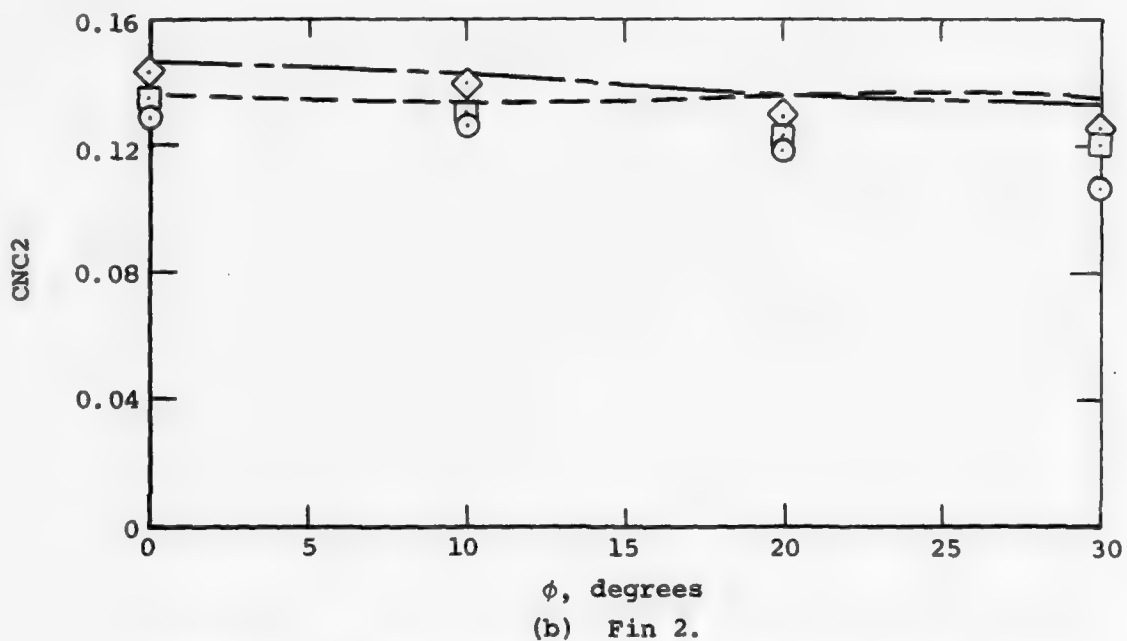
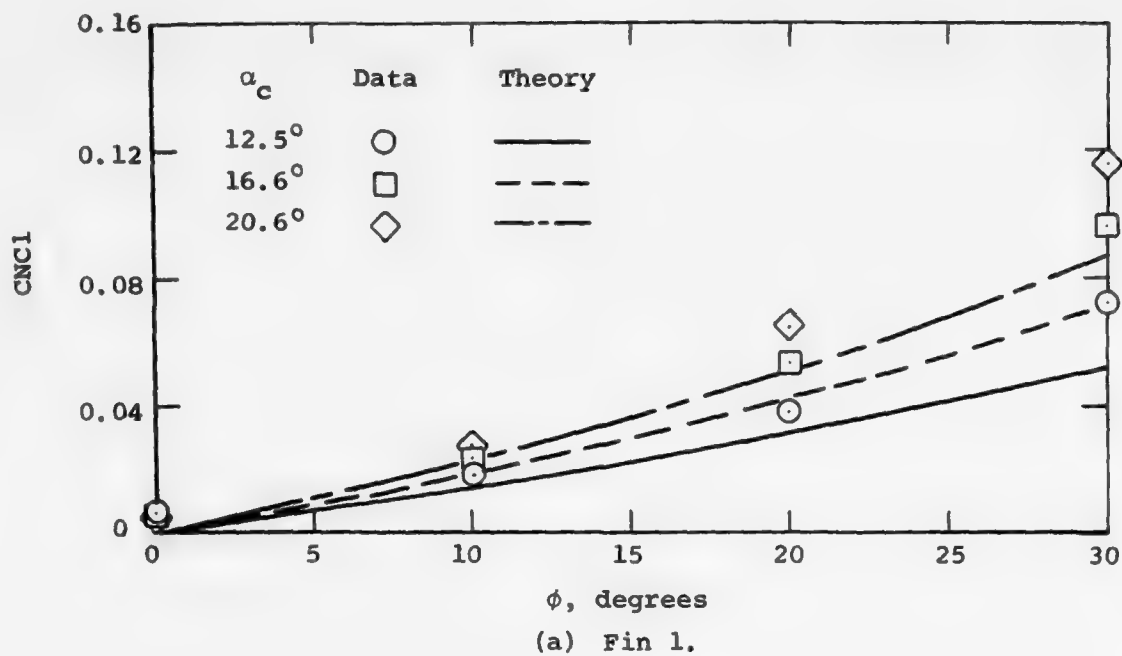
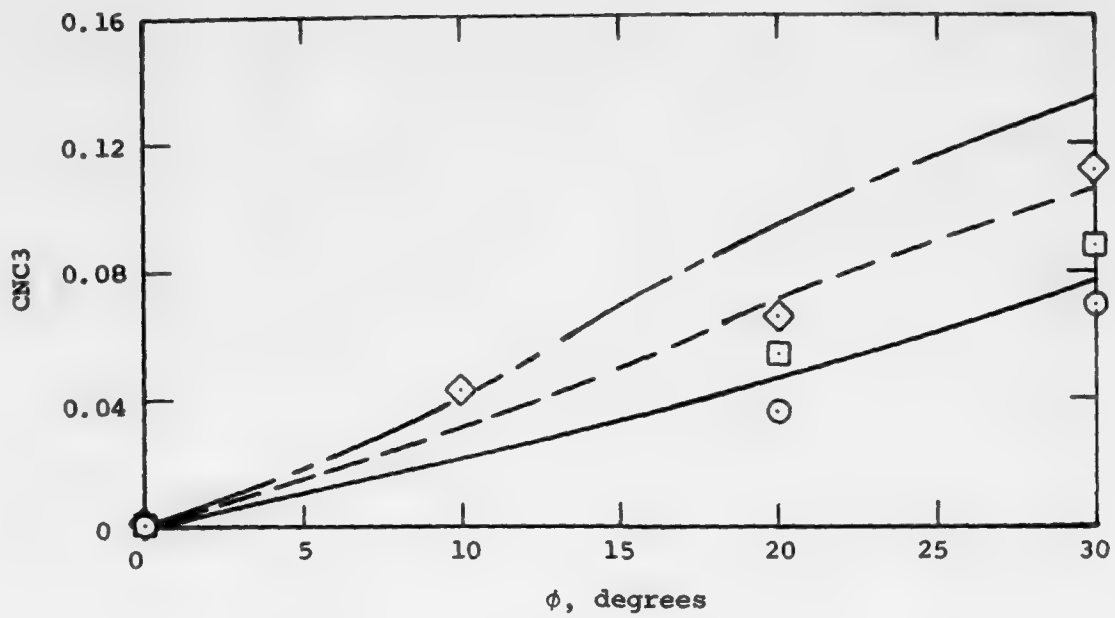
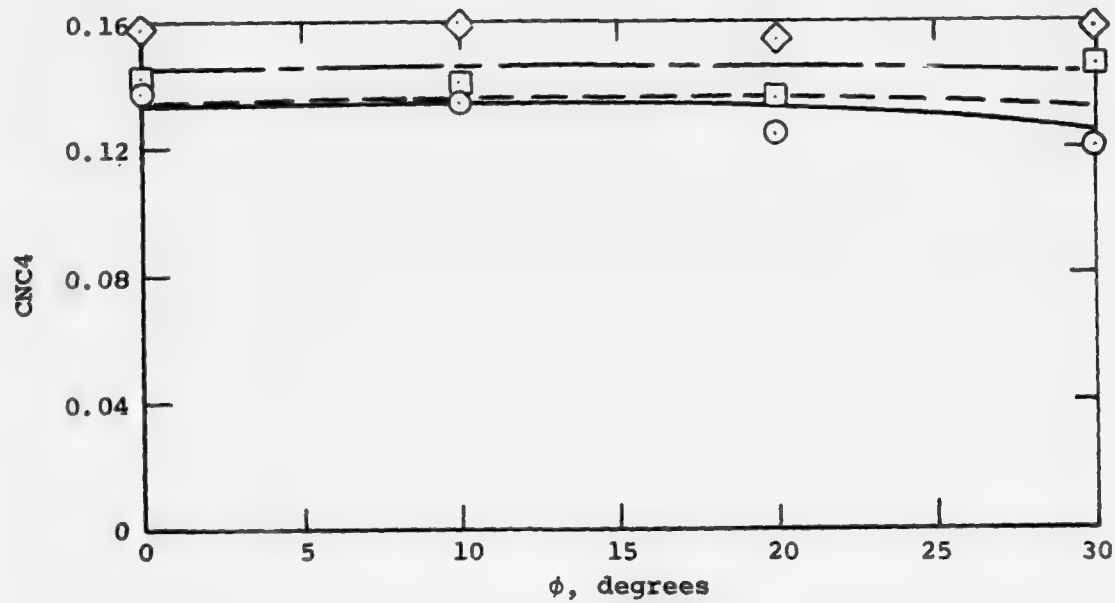


Figure 14. Fin normal force for bank with no fin deflection, low-aspect-ratio fins (C_7), BC 2, $M_\infty = 0.8$; S_R = model base area.



(c) Fin 3.



(d) Fin 4.

Figure 14. Concluded.

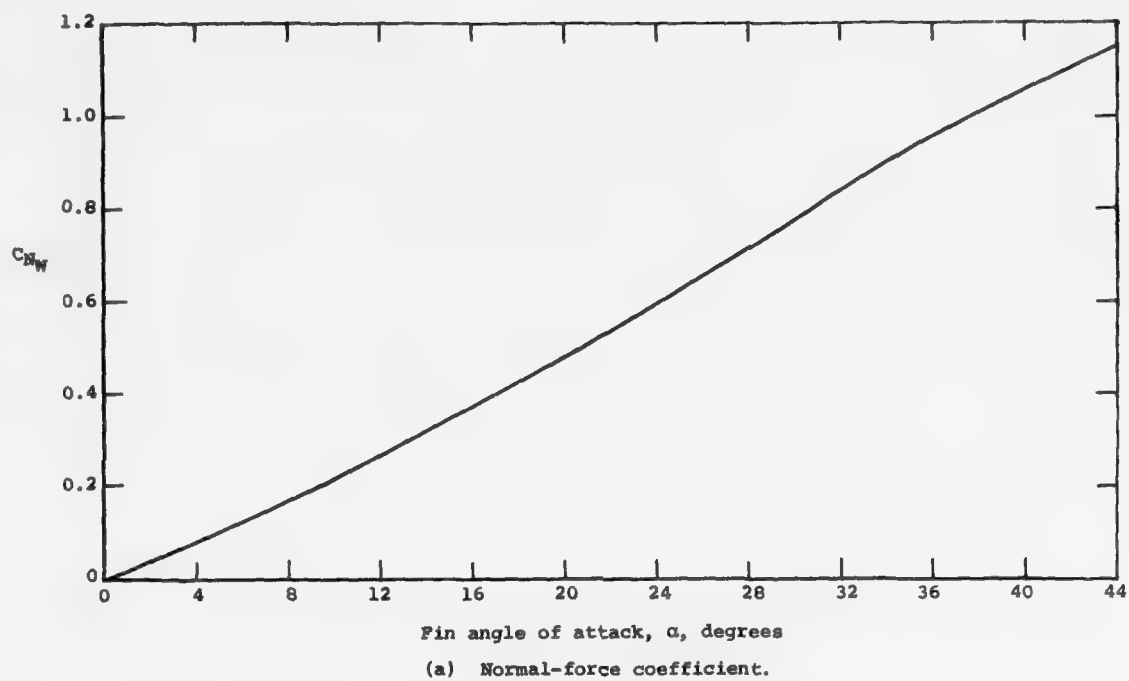
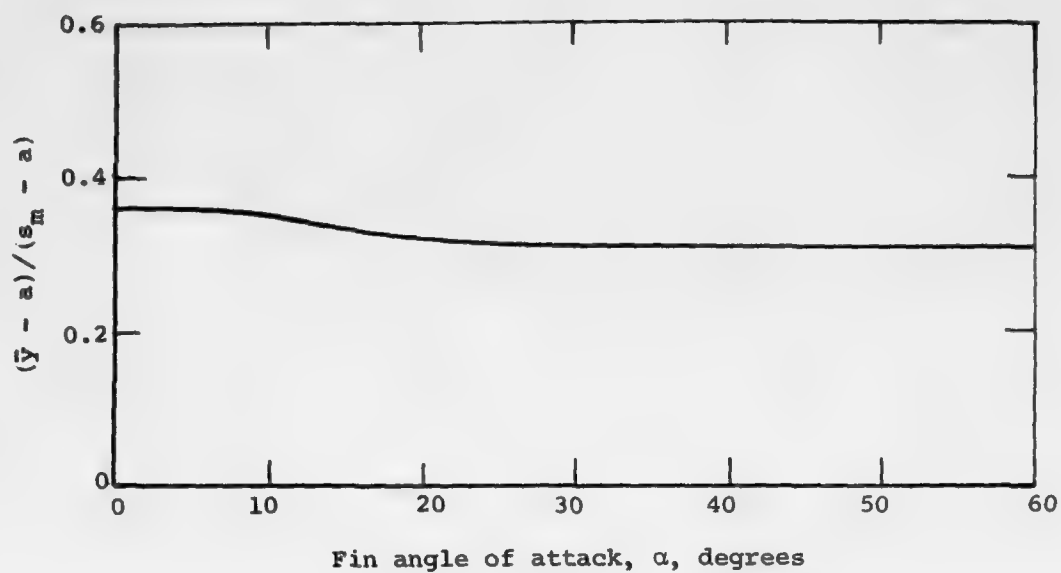
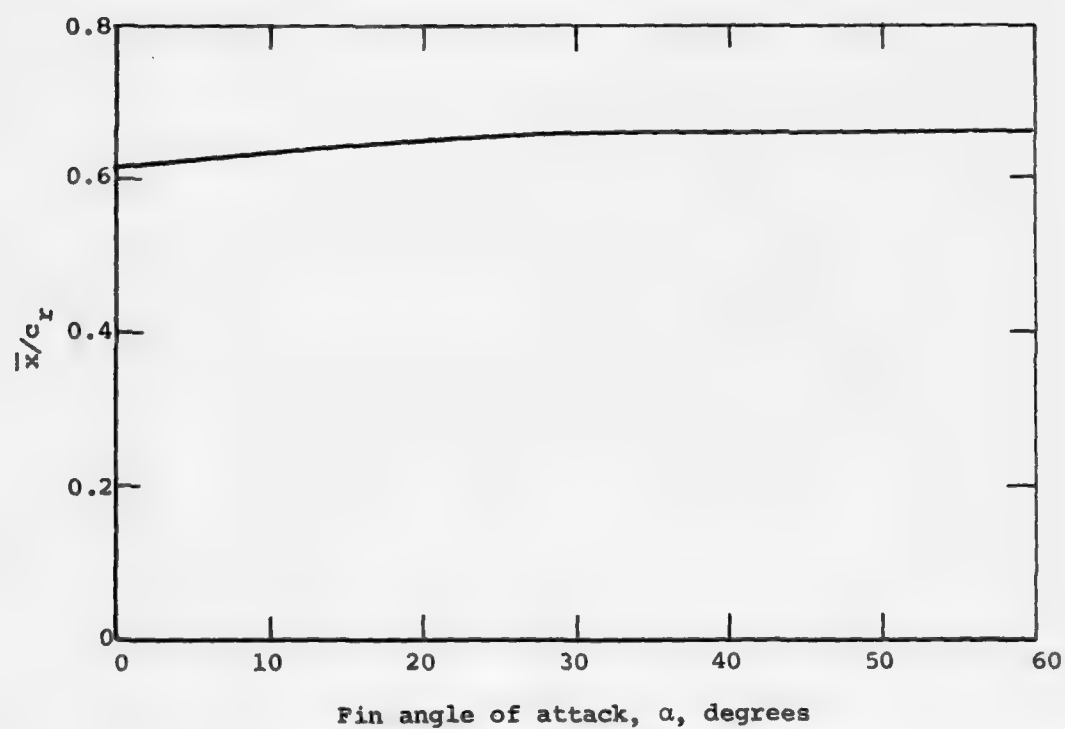


Figure 15. Wing-alone characteristics for low-aspect-ratio fins (T_{14}),
 $M_\infty = 2.0$; $R = 1.0$, S_R = planform area.

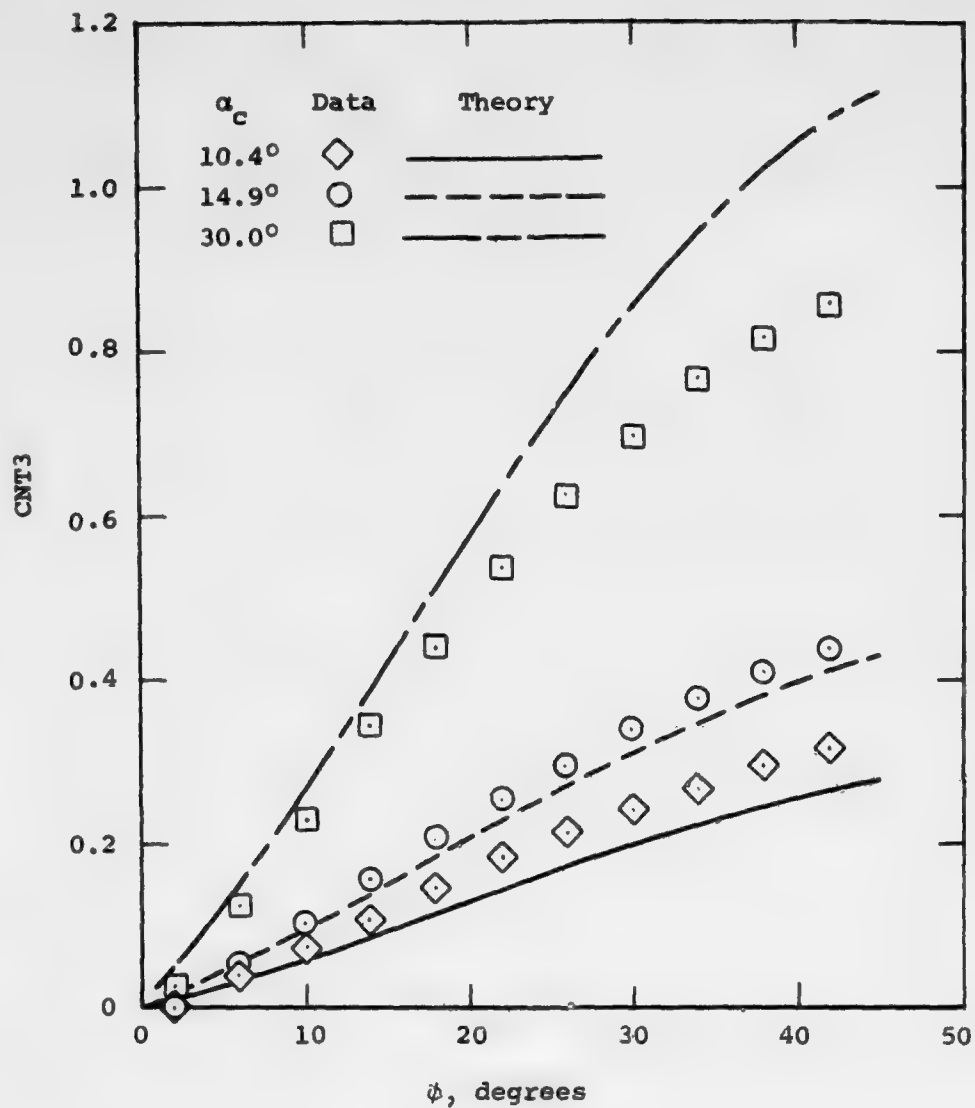


(b) Lateral center of pressure position.



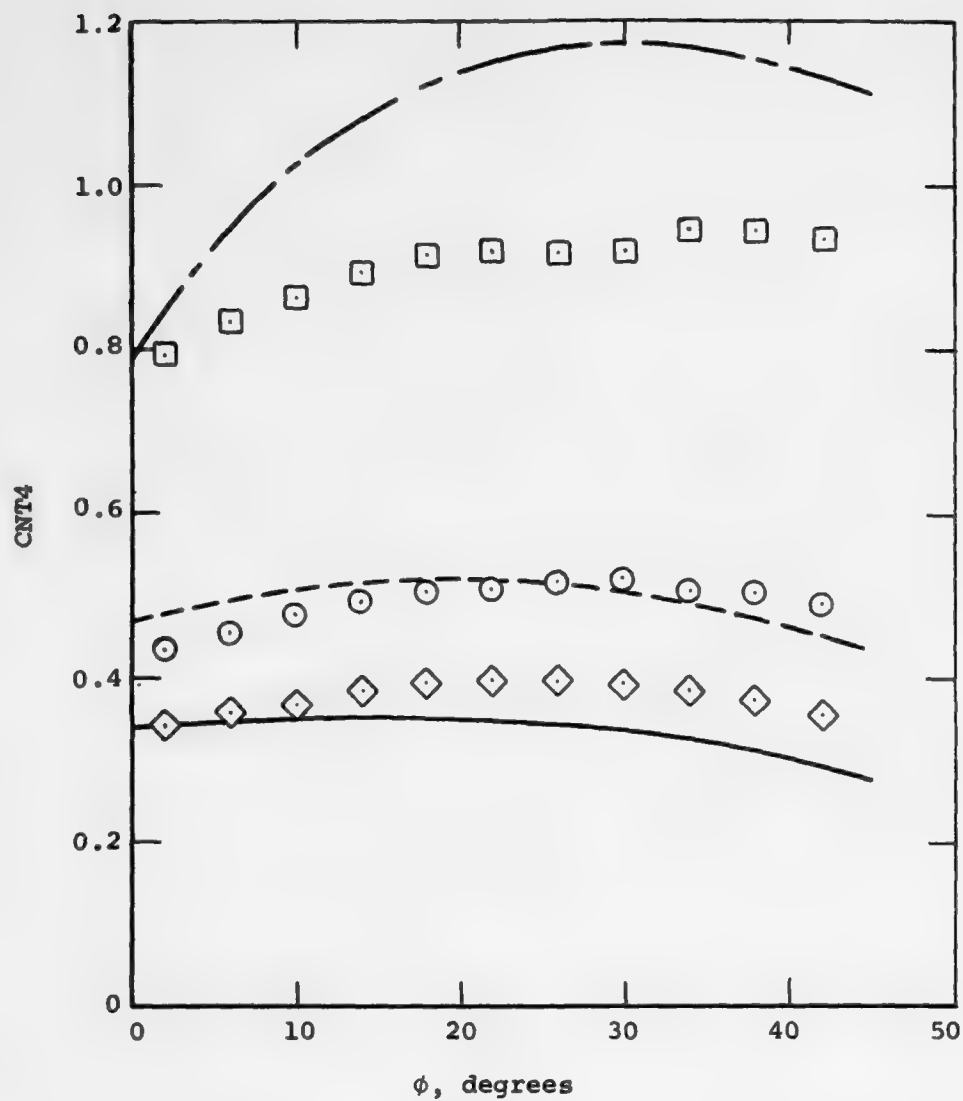
(c) Axial center of pressure position.

Figure 15. Concluded.



(a) Fin 3.

Figure 16. Fin normal force for bank with no fin deflection, low-aspect-ratio fins (T_{14}), BT 1, $M_\infty = 2.0$; S_R = planform area.



(b) Fin 4.

Figure 16. Concluded.

are apparent here also. Since the T_{14} fins have delta planforms, the discussion above concerning leading-edge vortex lift is applicable. It is interesting to note that for $\alpha_c = 30^\circ$ and $\phi = 30^\circ$ fin 4 is side-slipped 15° . Since the fin leading-edge sweep is 76° , the effective sweep is 51° . For $M_\infty = 2.0$, it seems likely that the flow over the leading edge is supersonic. Under such conditions no vortex lift could be generated. Thus, the correct wing-alone normal-force curve for this case would be for the attached flow only. For fin 4 at $\alpha_c = 30^\circ$ and $\phi = 30^\circ$, $\alpha_{eq} = 45^\circ$. If we extrapolate the slope at $\alpha_c = 0$ of the curve of figure 15(a), we obtain an attached flow C_{Nw} of 0.9 rather than the value of 1.15 predicted by the present method. The improvement in the agreement between data and theory indicates that the above explanation accounts for the discrepancies shown in figure 16. It thus appears necessary for very low-aspect-ratio fins to consider the change in leading-edge and side-edge sweep angles in calculating vortex lift.

4. COMPARISONS WITH DATA FOR BODY-TAIL CONFIGURATIONS

4.1 Results for Bodies Alone

Comparisons of the theory, which uses equation (1), with data for bodies alone have been made for various fineness ratios at several Mach numbers. The results shown in figure 17 are typical. The data shown are from references 16 and 18. Agreement is generally good except when the crossflow Mach number is transonic. Either the full two-dimensional crossflow drag is not applicable for yawed bodies at transonic speeds or the transonic C_{dc} values are suspect. Recent experimental results obtained at NASA/Ames Research Center (ref. 19) indicate that the C_{dc} values are reasonable. Hence, the former explanation appears most likely.

In the present method the body vortex strengths and positions are based on a model of two concentrated vortices. Recently, however, Fidler, Schwind, and Nielsen (ref. 20) have shown that such a model is an oversimplification since the body vorticity can be distributed over a large area. The reader should keep this in mind when interpreting the results given below for vortex-fin interaction.

4.2 Fin Loads in the Presence of Body Vortices

The purpose of this section is to uncover phenomena not included or not properly accounted for in the present method by systematic comparison of data and theory. We will be especially interested in phenomena which become more important at higher angles of attack since they will be pertinent to the second year's work. Results for each of the leeward fins and for the windward fins are presented separately below to facilitate discussion of the various phenomena of interest. Note that fin 1 rolls through the starboard body vortex as ϕ increases. Fin 2 rolls up from a horizontal position. It is never "in" a vortex. Fins 3 and 4 should be weakly affected by the body vorticity for positive roll angles up to 45° .

4.2.1 Leeward fins, fin 1.- In addition to problems involving the use of a two-vortex model to represent distributed body vorticity, the prediction of vortex-fin interference effects must take into account the proximity of the vortex to the fin. Figure 18 illustrates this phenomenon for a rectangular wing near a free vortex which was generated upstream by

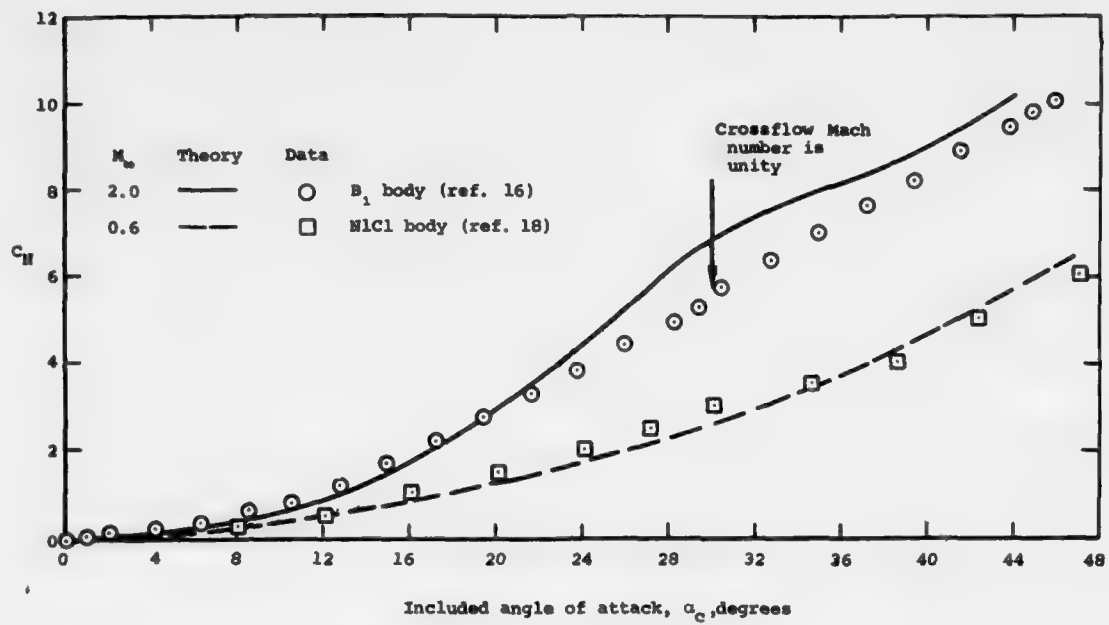
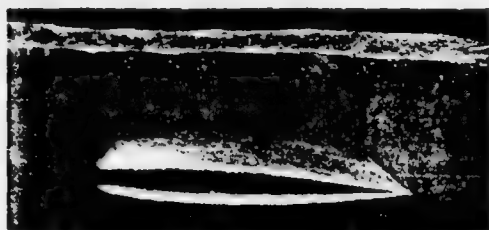


Figure 17. Comparison between theory and data for body-alone normal force.



(a) Vortex far from wing; large wing thickness



(b) Vortex close to wing; large wing thickness



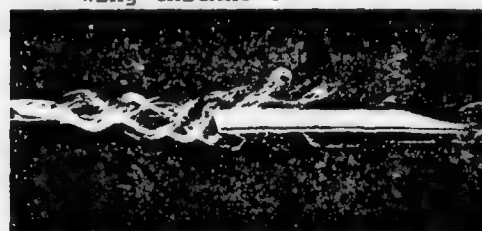
(c) Vortex intersecting wing; large wing thickness



(d) Vortex far from wing; small wing thickness



(e) Vortex close to wing; small wing thickness



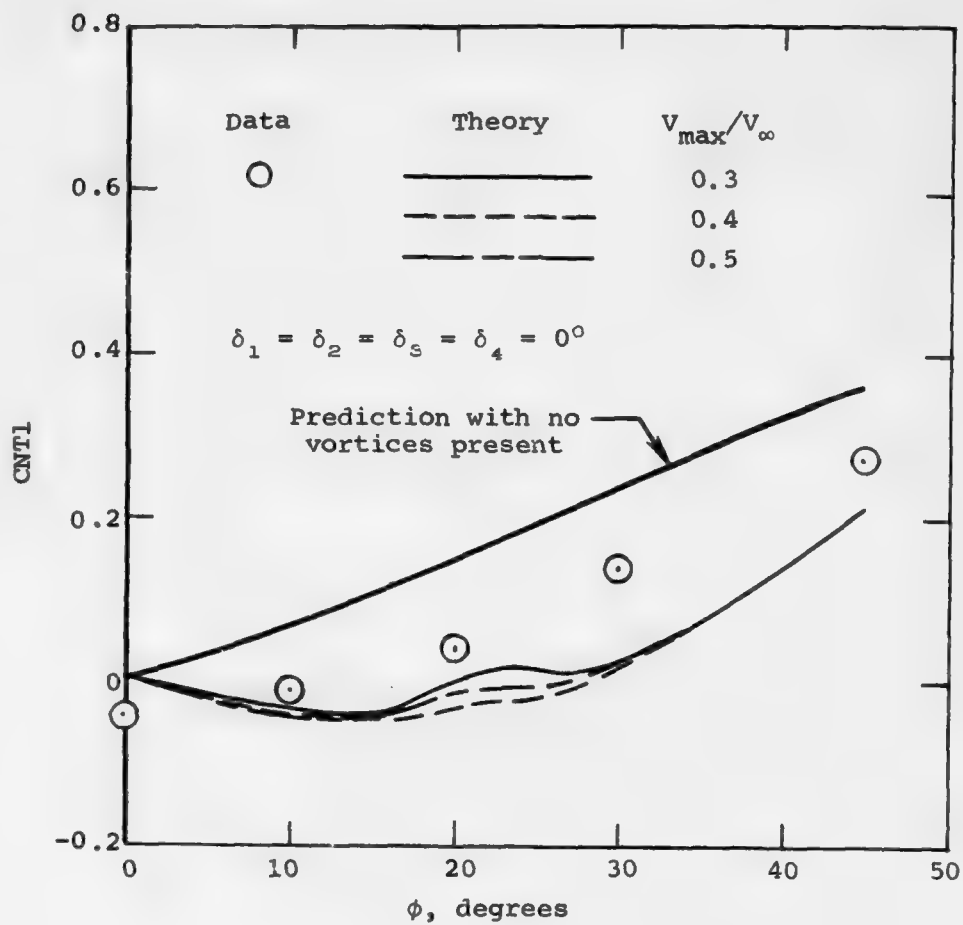
(f) Vortex intersecting wing; small wing thickness

Figure 18. Illustration of vortex-wing interference (photographs taken from ref. 21).

another wing (ref. 21). The possibility of vortex bursting and/or local wing stall is handled in the present method by limiting the maximum velocity nearby vortices can induce on the fin. A study was conducted to determine the best value of V_{\max}/V_{∞} for body-tail configuration no. 2 shown in figure 3(d). The wing-alone characteristics for the C_7 fins (fig. 12) were used since the T_2 fins closely approximate them in planform. The results of the study for fin 1, which rolls through the right body vortex as ϕ increases, are shown in figure 19 for $M_{\infty} = 1.75$ and in figure 20 for $M_{\infty} = 0.8$ for several angles of attack. The two cases show the effects of the simple expedient of limiting the velocity induced on the fins by the vortices. The best values of V_{\max}/V_{∞} appear to be 0.4 for $M_{\infty} = 1.75$ and 0.1 for $M_{\infty} = 0.8$. Since V_{\max}/V_{∞} may be thought of as a local stall angle (in radians), these values imply subsonic stall at low angles of attack and supersonic stall at much higher angles of attack.

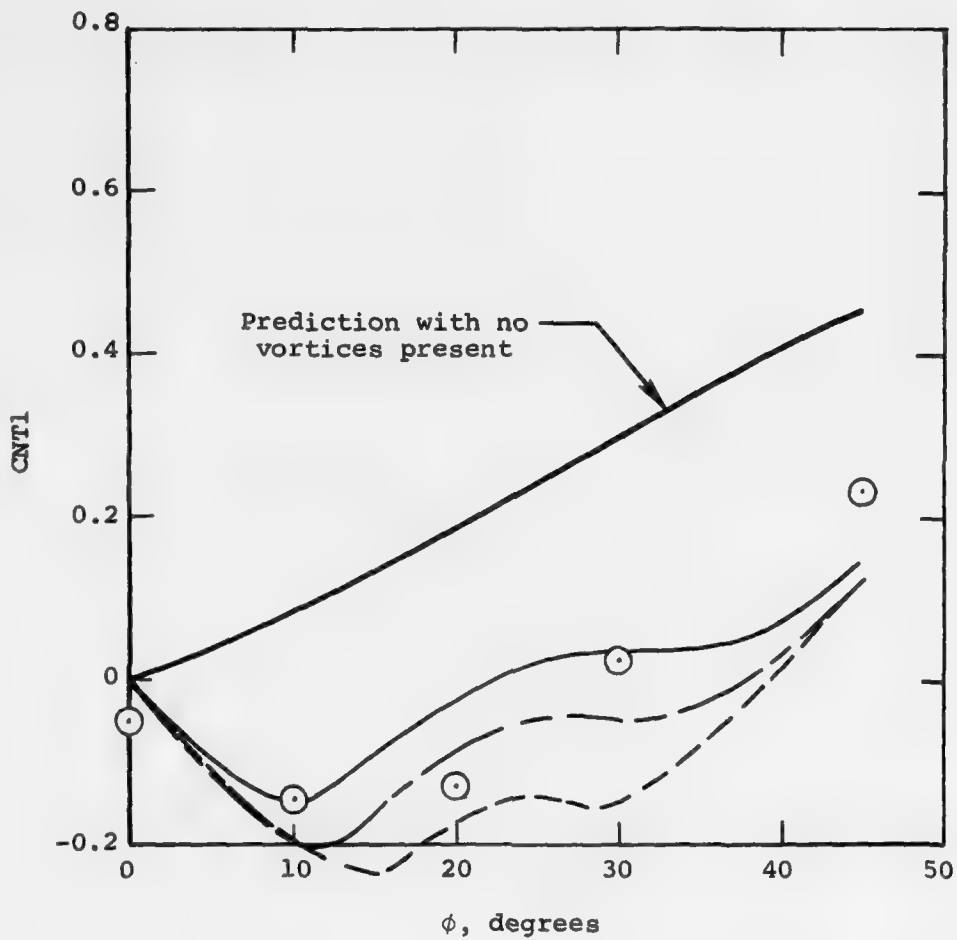
It is interesting to note that the fin 1 normal force without body vortices present is underpredicted for both $M_{\infty} = 1.75$ and $M_{\infty} = 0.8$ for the nearly identical C_7 fins (see figs. 13(a) and 14(a)). Hence, we cannot use figure 19 and 20 to determine the best choice of V_{\max}/V_{∞} . The fin 1 results for rolling moment using $V_{\max}/V_{\infty} = 0.4$ for $M_{\infty} = 1.75$ and 0.1 for $M_{\infty} = 0.8$ are presented in figures 21 and 22. The comparisons for the $M_{\infty} = 0.8$ case are satisfactory. However, the rolling moments for $M_{\infty} = 1.75$ are not well predicted. The rolling moment together with the normal force of a fin in a strong encounter with a vortex is a sensitive indicator of the performance of an analytical model since it requires accurate computations of the center of pressure location as well as normal force. As explained in reference 3 and in Appendix B, the present theory computes the location of the center of pressure using reverse flow theory and would be exact if the flow characteristics were linear.* Unknown nonlinear effects not accounted for by reverse flow theory may be present. Some possible effects not now included in the method are (1) vortex bursting, (2) lateral movement of a vortex as it travels over a fin, (3) increased suction due to the greater axial velocity in the vortex core, and (4) nonlinear terms in the Bernoulli pressure equation.

*Note, however, that the present code assumes that the interaction coefficients, k_{ij} , are zero when $i \neq j$. The coefficient, k_{ii} , is assumed to be one. See Appendix F.



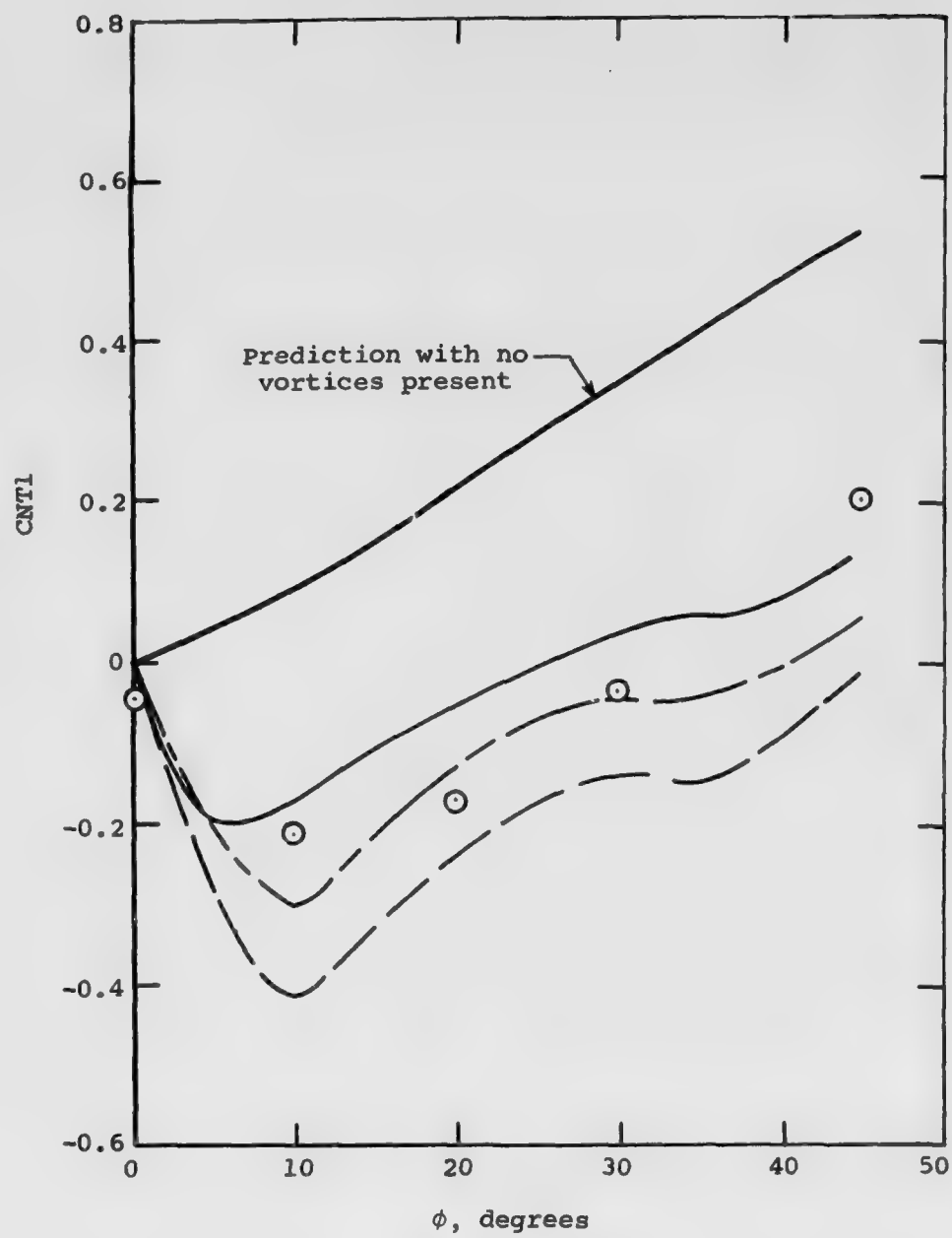
(a) $\alpha_c = 12.5^\circ$.

Figure 19. Effect of V_{max}/V_{∞} on prediction of fin 1 normal force, BT 2, $M_{\infty} = 1.75$; S_R = model base area.



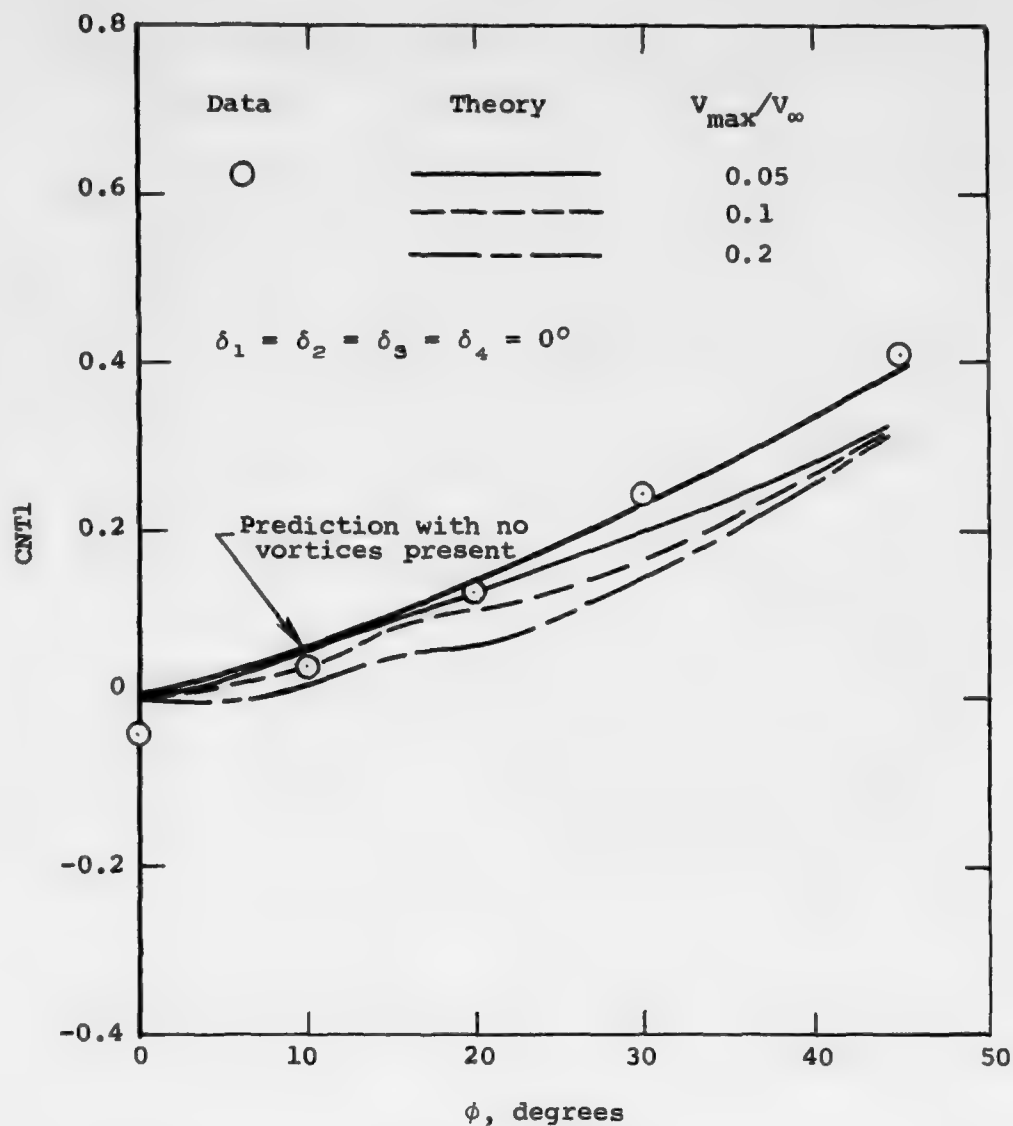
(b) $\alpha_c = 16.6^\circ$.

Figure 19. Continued.



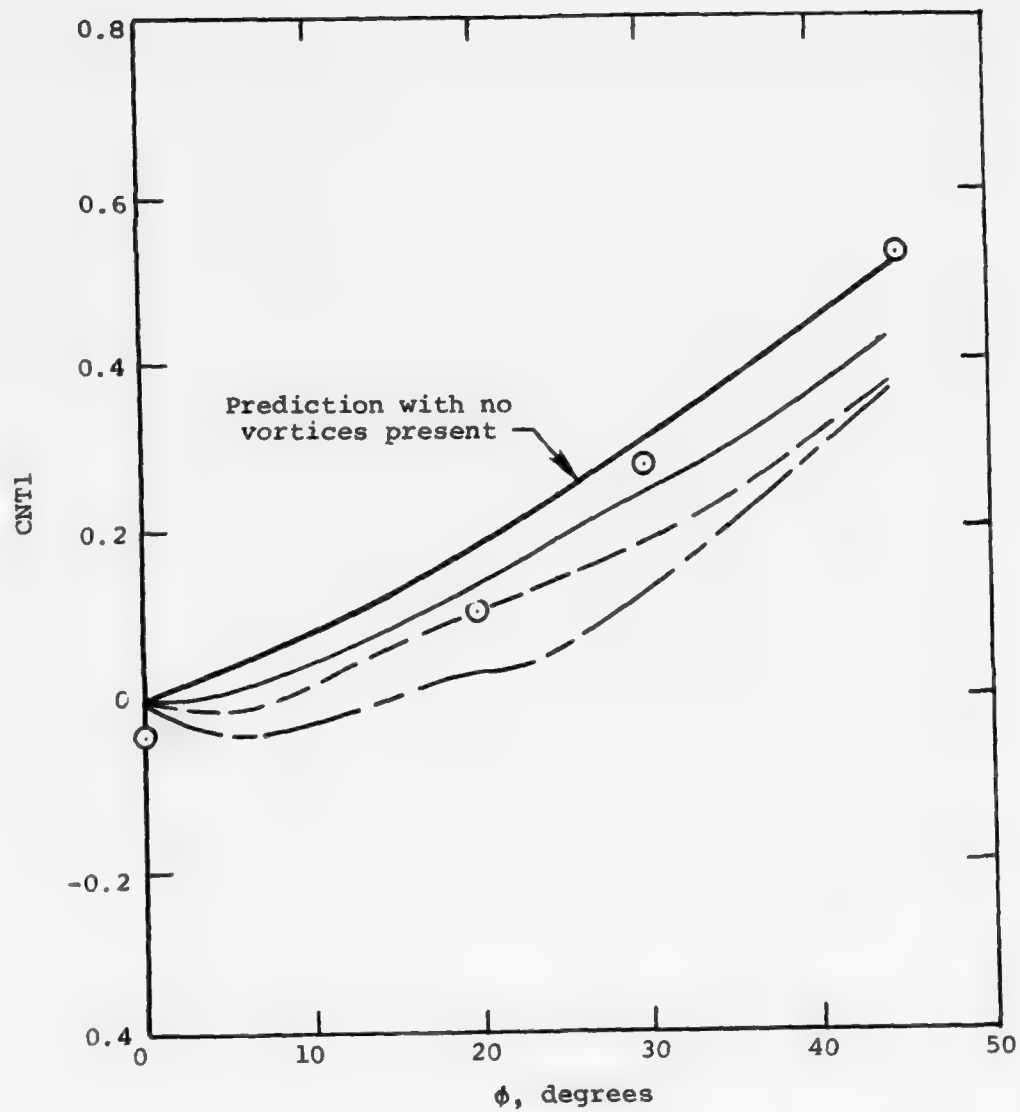
(c) $\alpha_c = 20.6^\circ$.

Figure 19.- Concluded.



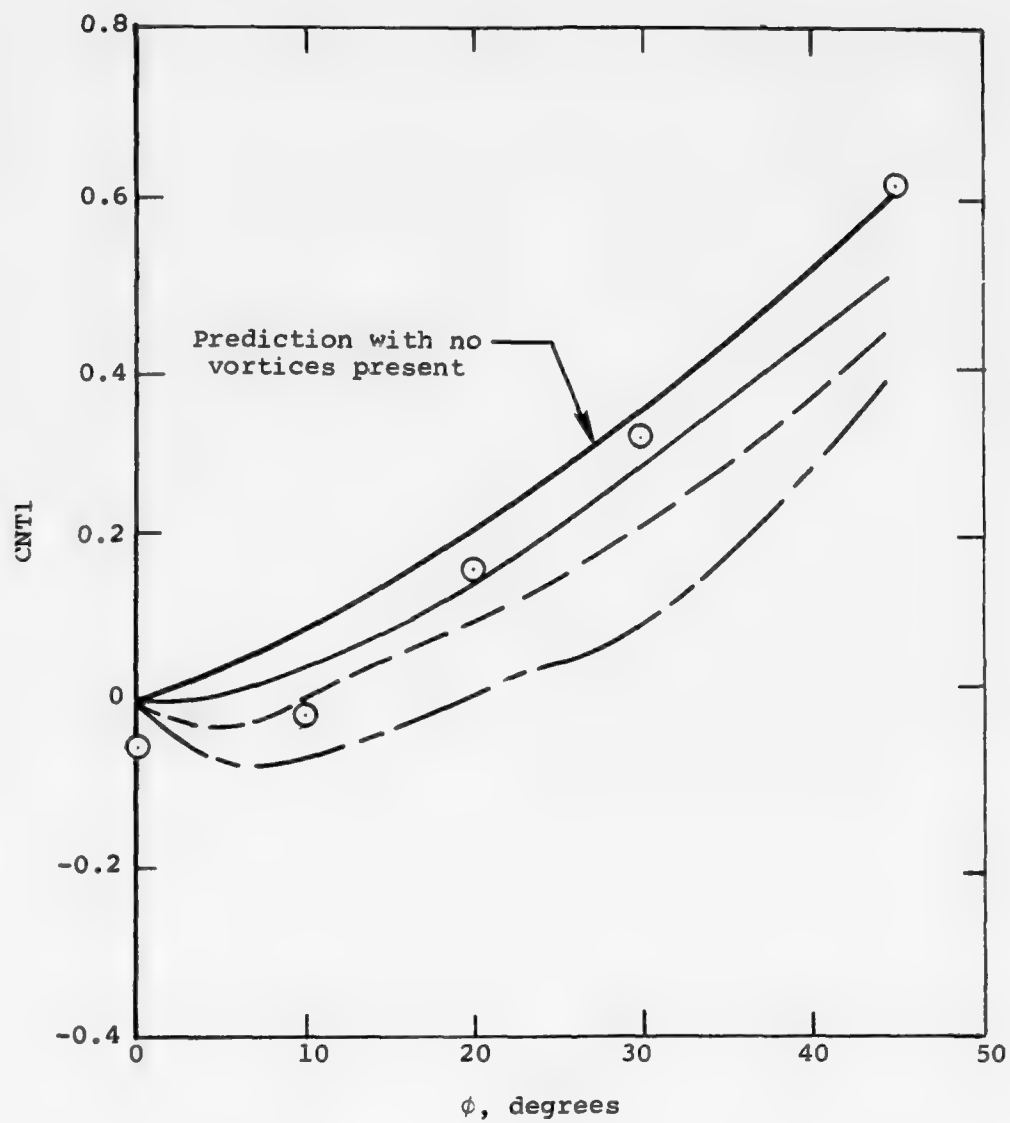
(a) $\alpha_c = 12.5^\circ$.

Figure 20. Effect of V_{\max}/V_{∞} on prediction of fin 1 normal force, BT 2, $M_{\infty} = 0.8$; S_R = model base area.



(b) $\alpha_c = 16.6^\circ$.

Figure 20. Continued.



(c) $\alpha_c = 20.6^\circ$.

Figure 20. Concluded.

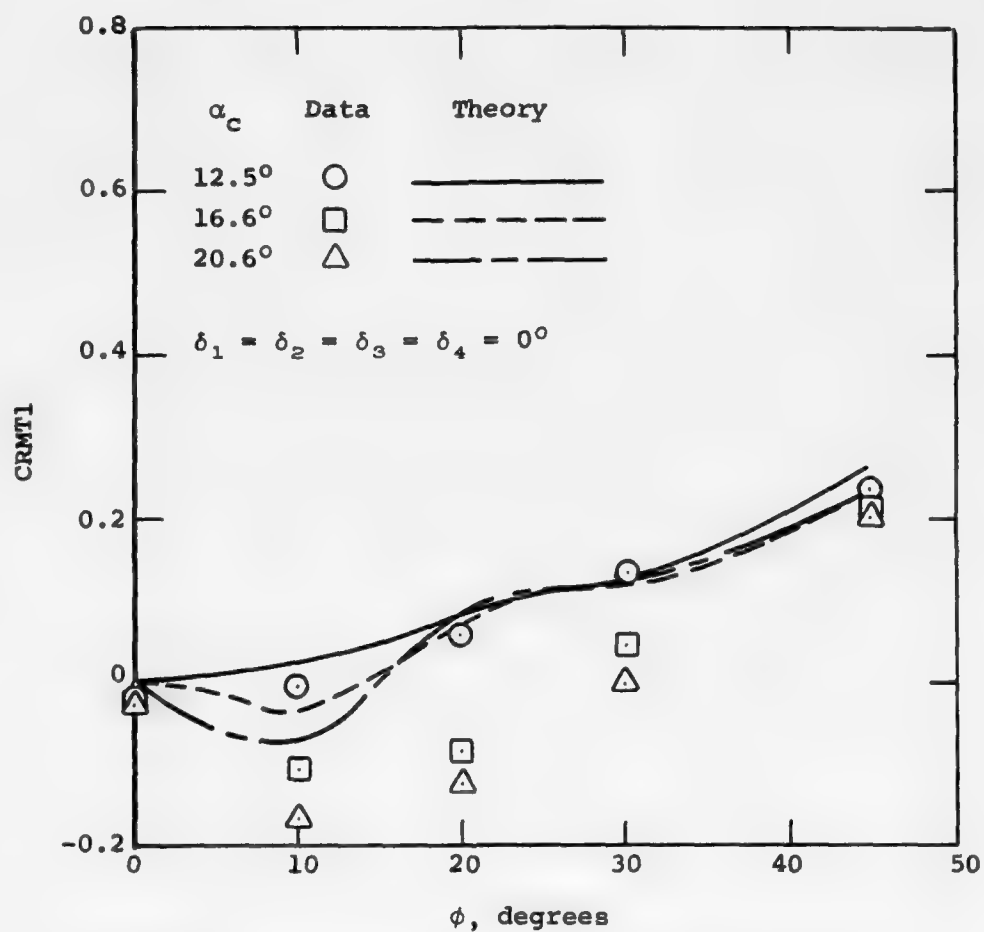


Figure 21. Comparison of data and theory for fin 1
 rolling moment, BT 2, $M_\infty = 1.75$, $V_{\max}/V_\infty = 0.4$;
 S_R = model base area, l_r = model base diameter.

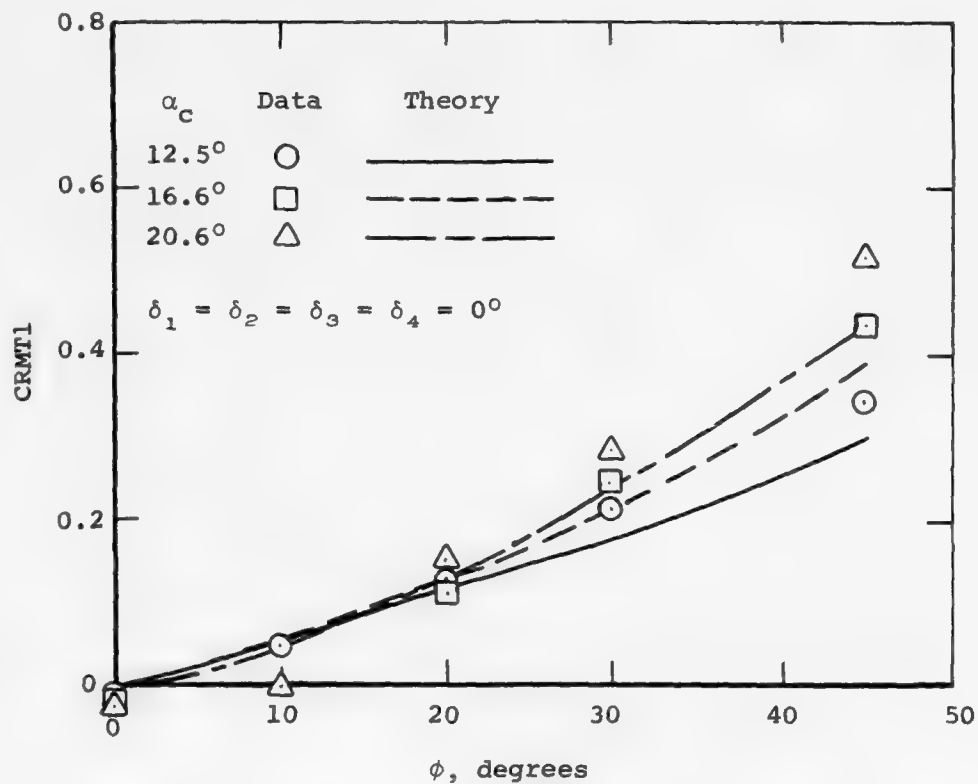
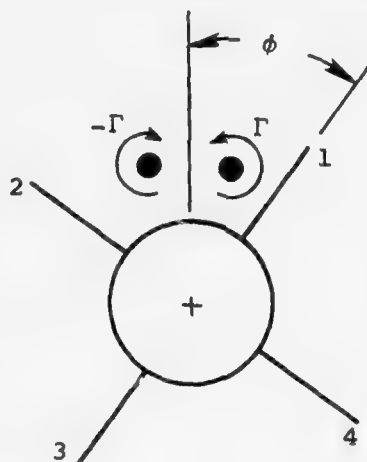


Figure 22. Comparison of data and theory for fin 1 rolling moment, BT 2, $M_\infty = 0.8$, $V_{\max}/V_\infty = 0.1$; S_R = model base area, l_r = model base diameter.

It was noted that the measured values of rolling moment shown in figure 21 varied with ϕ in a manner similar to those for normal force (fig. 19). An attempt was made to improve the rolling-moment predictions for $M_\infty = 1.75$ by using the wing-alone center of pressure location given by α_{eq} . The results are shown in figure 23. Note that the agreement between data and theory improved for the higher angles of attack. These results seem to indicate that the present method of Appendix B is appropriate if the vortex-fin interaction is weak. But, if the interaction is strong, additional factors are present which should be included in the theory.

4.2.2 Leeward fins, fin 2.- Comparisons between data and theory for fin 2 of body-tail configuration no. 2 which rolls up from a horizontal position closer to the port body vortex are given in figure 24 for $M_\infty = 1.75$ and in figure 25 for $M_\infty = 0.8$. See sketch 2 below. For the



Sketch 2. Rear view of body-tail configuration no. 2 showing position of body vortices in crossflow plane at the leading edge of the tail.

supersonic case, the predictions are somewhat high for $\phi = 0^\circ$. However, the trends are well predicted including the fact that at $\phi = 45^\circ$, the normal force on fin 2 decreases with increasing body angle of attack.

For the subsonic case, the agreement is good for $\alpha_c = 12.5^\circ$, but for the higher angles of attack some new phenomenon not accounted for in the theory seems to be present. In an attempt to isolate the cause of the discrepancy, the fin normal force was calculated for the case of no

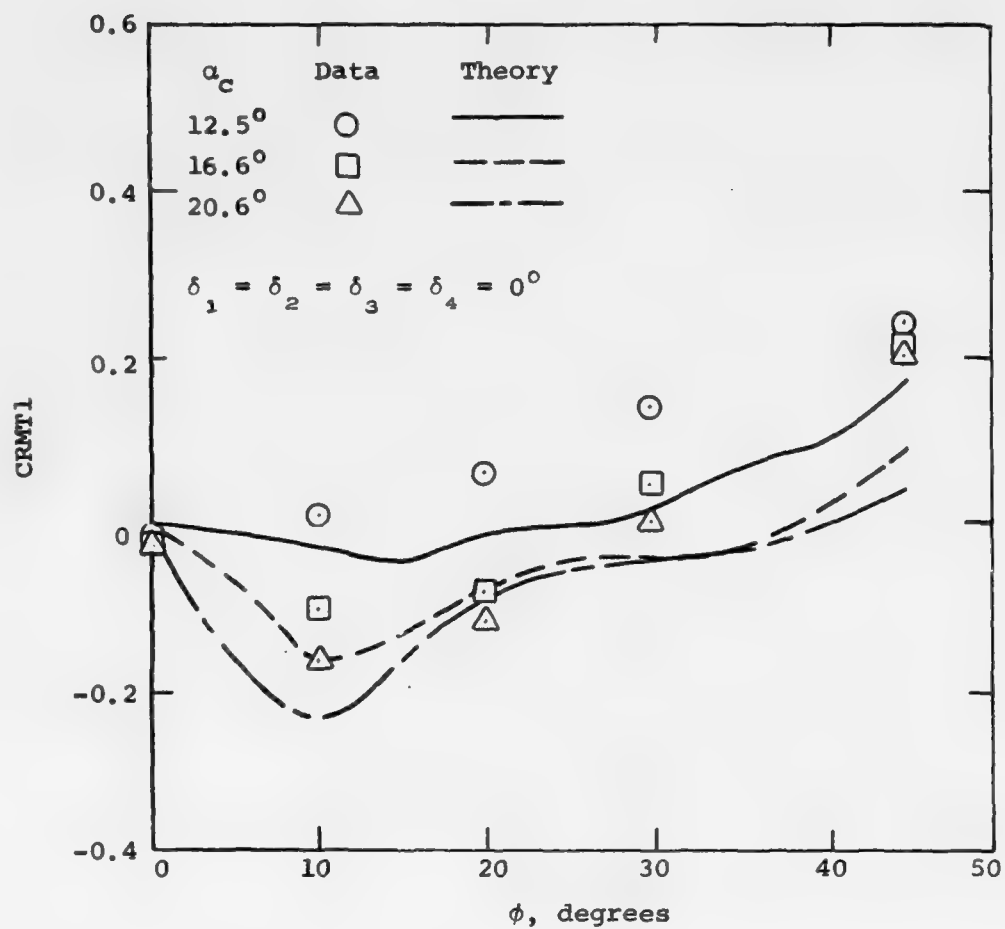


Figure 23. Comparison of data and theory for fin 1 rolling moment using α_{eq} to compute lateral position of center of pressure, BT 2,
 $M_\infty = 1.75$, $V_{max}/V_\infty = 0.4$;
 S_R = model base area,
 l_r = model base diameter.

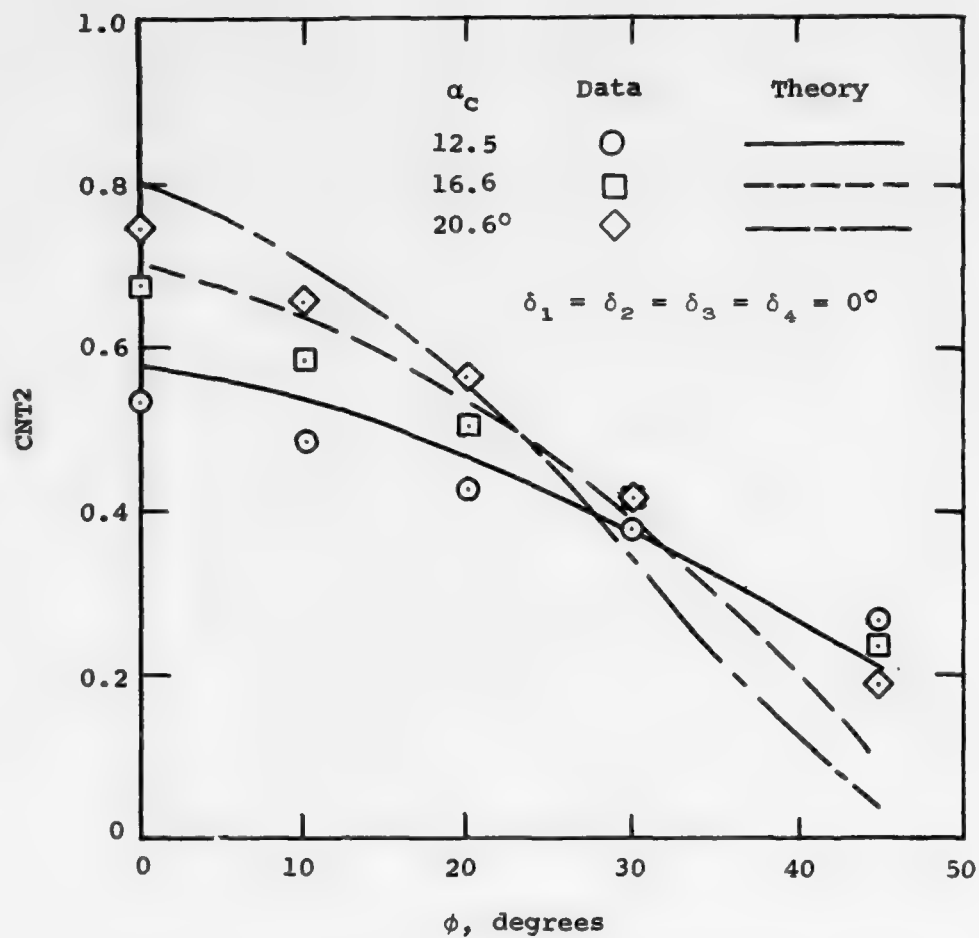


Figure 24. Comparison of data and theory for fin 2
normal force, BT 2, $M_\infty = 1.75$, $V_{\max}/V_\infty = 0.4$;
 S_R = model base area.

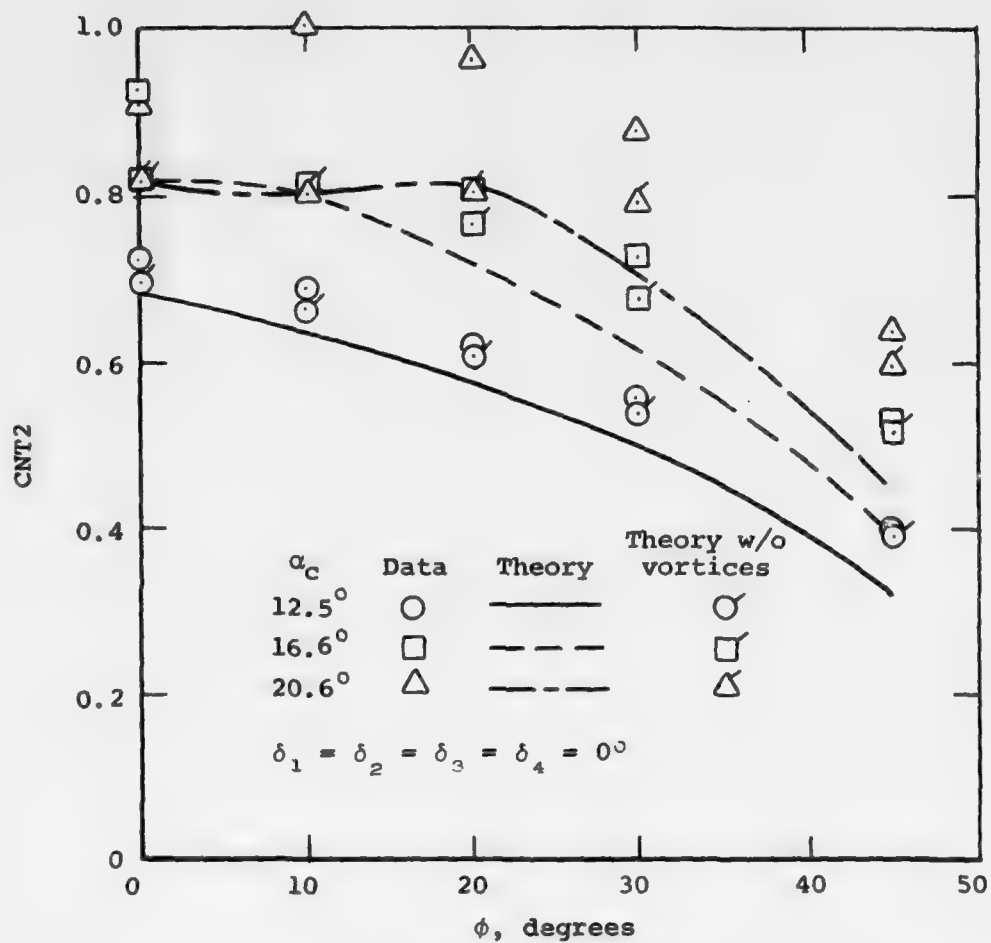


Figure 25. Comparison of data and theory for fin 2
normal force, BT 2, $M_\infty = 0.8$, $V_{\max}/V_\infty = 0.1$;
 S_R = model base area.

body vortices present. The results are shown in figure 25 as flagged symbols. The agreement is improved somewhat especially at $\phi = 45^\circ$. However, for the smaller values of ϕ and for $\alpha_c = 16.6^\circ$ and 20.6° , the normal force is still underpredicted by a significant amount. It appears that a source of favorable lift interference is present. That this is so can be seen by referring to figure 12. (Note that the reference area for figure 12 is the planform area, 18.38 in.^2 , and for figure 25 it is the model base area, 19.64 in.^2 .) At $\phi = 10^\circ$ in figure 24, the measured normal force for $\alpha_c = 20.6^\circ$ is 25 percent higher than the wing-alone curve would give for the equivalent angle of attack indicated. It appears, then, that the discrepancy is due to favorable body vortex-fin interference which was unsuspected and was not included in the method.

To confirm the existence of the phenomenon, another configuration with a different ratio of fin semispan to body radius was examined also at $M_\infty = 0.8$. The configuration is body-tail configuration no. 3 shown in figure 3(e). The wing-alone normal force was taken from reference 22 and is presented in figure 26. The data were taken from reference 16 and are presented for several angles of attack in figure 27. Note the similarity between these data and the data of figure 25. The values of fin normal force which would be predicted if no body vortices were present are also shown in figure 27. It is clear that favorable vortex interference is present for $0 \leq \phi < 20^\circ$. It is interesting to note that for both cases the magnitude of the favorable interaction seems to be a function of the distance of the body vortex from the fin. In fact, when the fin is at 20° bank (second quadrant), the favorable interaction is lost. The mechanism here appears to be similar to that encountered for strake-wing interference. The phenomenon will be investigated in the second year of the present effort.

4.2.3 Windward fins.— Comparisons between data and theory for fins 3 and 4 of body-tail configuration no. 2 at $M_\infty = 0.8$ are given in figure 28. Note that the trends are similar to those of figure 14 as they should be since the fins are nearly identical in planform. The chief difference is the size of the fins relative to the body. In section 3.2, the possibility was discussed of improving the prediction for fin 3 by taking into account the dependence of vortex lift on leading-edge sweep changes due to pitch and roll.

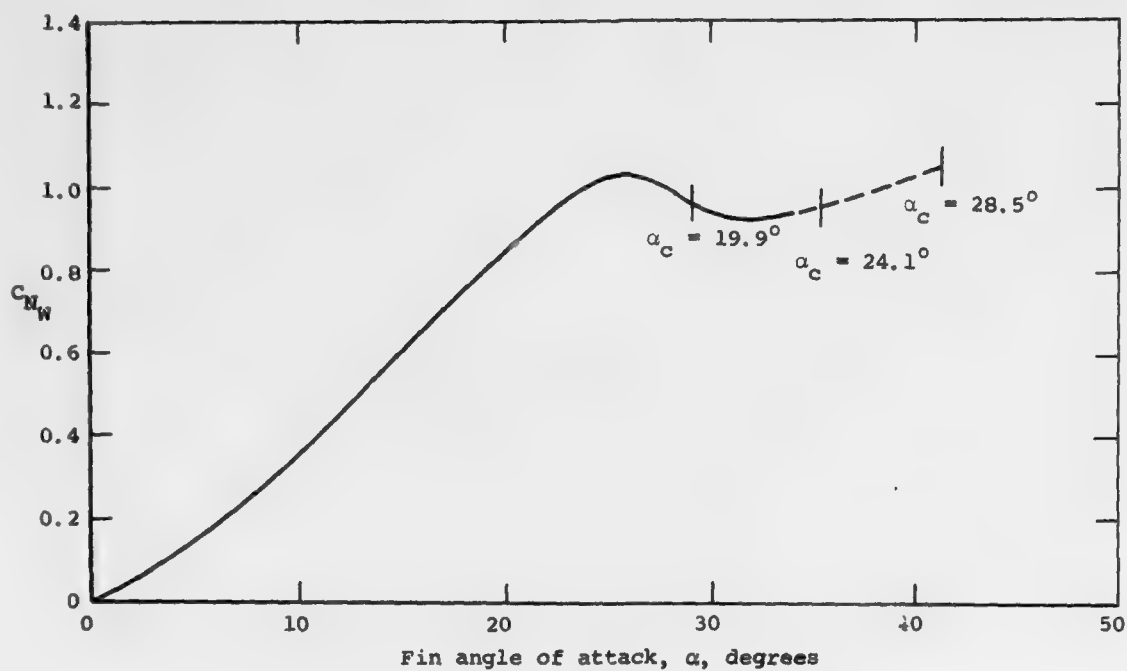


Figure 26. Wing-alone normal-force coefficient for low-aspect-ratio fins (T_{15}), $M_\infty = 0.8$; $R = 1.0$, S_R = planform area.

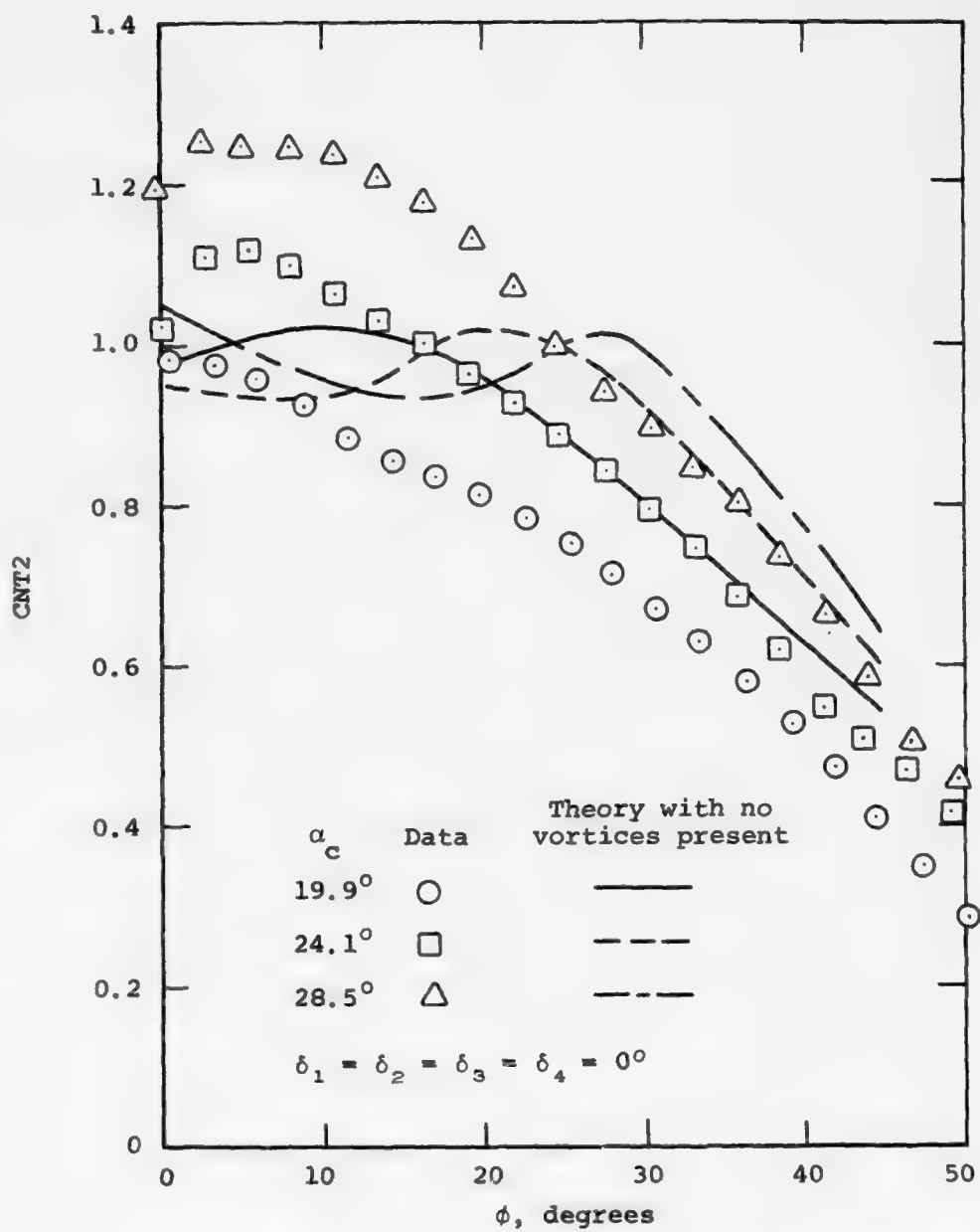
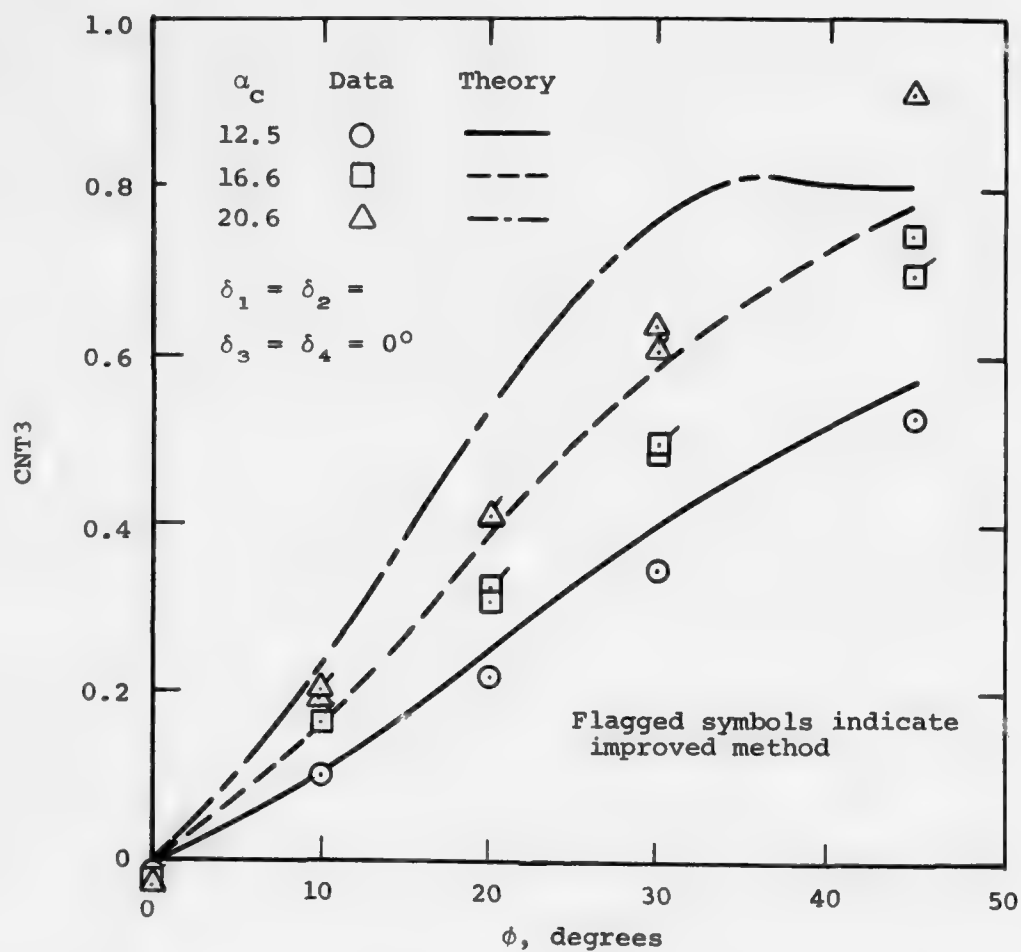
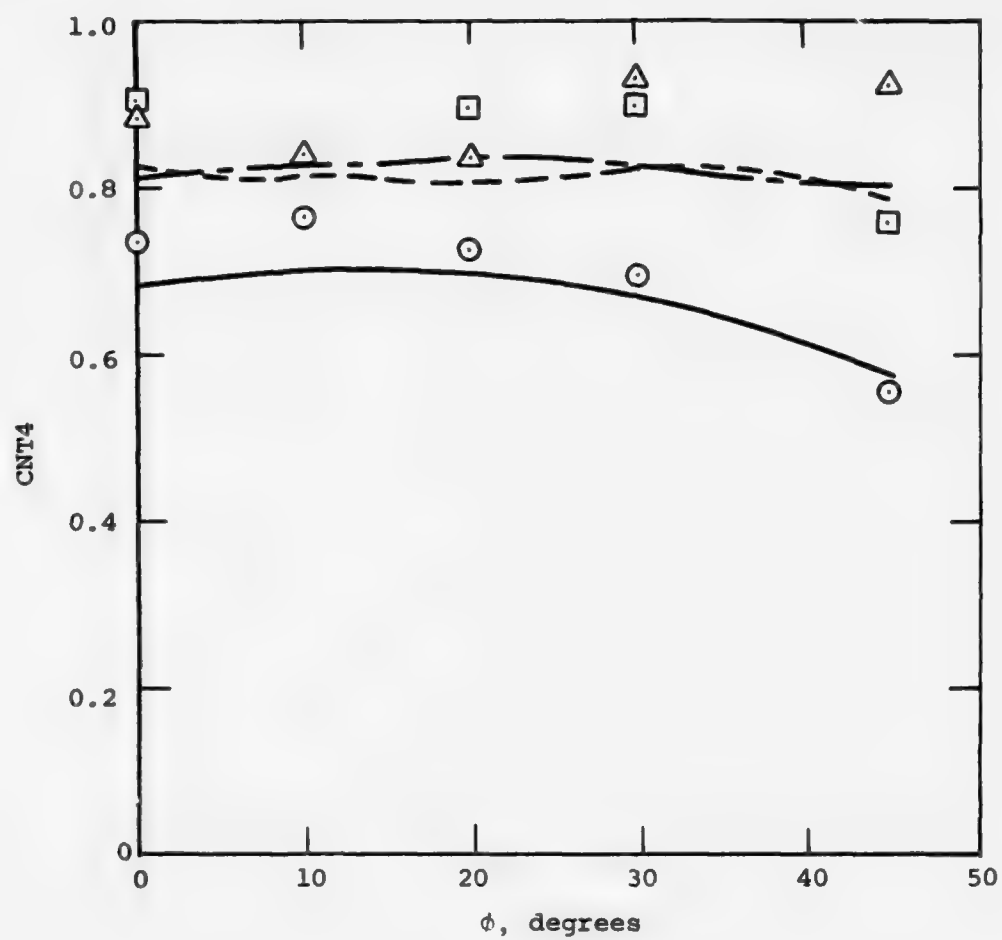


Figure 27. Comparison of data and theory for fin 2
normal force, BT 3, $M_\infty = 0.8$;
 S_R = fin planform area.



(a) Fin 3.

Figure 28. Comparison of data and theory for fin 3
 normal force, BT 2, $M_\infty = 0.8$, $V_{\max}/V_\infty = 0.1$;
 S_R = model base area.



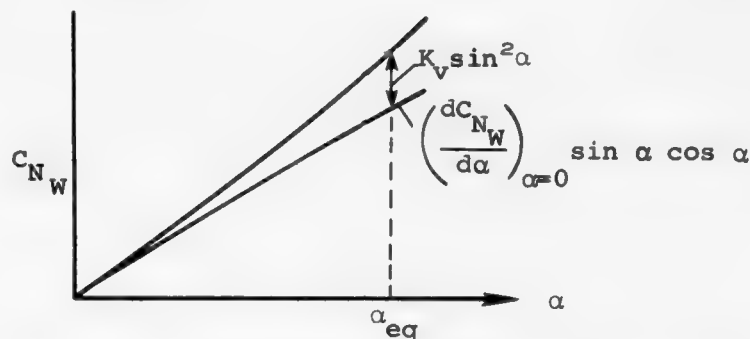
(b) Fin 4.

Figure 28. Concluded.

These improvements are based on an approximate method now described. For clarity the discussion will be made initially for triangular wings. The normal-force curve for a wing alone which develops vortex lift can be approximated by the following formula.

$$C_{N_W} = \left(\frac{dC_{N_W}}{d\alpha} \right)_{\alpha=0} \sin \alpha \cos \alpha + K_V \sin^2 \alpha \quad (34)$$

The corresponding normal-force curve has the following characteristic shape :



Sketch 3. Normal-force curve for a wing alone which develops vortex lift.

where

$$\left(\frac{dC_{N_W}}{d\alpha} \right)_{\alpha=0} = \text{normal-force curve slope at } \alpha = 0$$

$$K_V = \text{"vortex lift" constant}$$

The constant K_V can be obtained from an experimental normal-force curve. It can also be estimated theoretically by assuming that all the leading-edge suction is converted into vortex lift (Polhamus analogy). For delta wings at subsonic speeds theoretical values of K_V depend only on leading-edge sweep angle or its equivalent, aspect ratio. For supersonic speeds, the theoretical value of K_V depends on the ratio of the tangent of the leading-edge sweep angle to the tangent of the Mach angle, or βAR . For supersonic edges, K_V is zero. Generally, not all the leading-edge suction is converted to vortex lift. The parameter K^* is defined to represent this fraction.

$$K^* = \frac{(K_v)_{\text{exp}}}{(K_v)_{\text{theory}}} \quad (35)$$

Correlations of K^* for delta wings are included in reference 12.

For a cruciform missile at included angle of attack, α_c , and roll angle, ϕ , the sweep angle of a delta wing is changed from its nominal angle at $\alpha_c = 0$. This changes both the potential normal force and the vortex normal force. The change in normal force is handled in the present method by the change in equivalent angle of attack determined using the interference factor, $K_{\alpha\beta}$. This is correct for the normal force due to potential flow. However, special consideration must be given to the vortex normal force because not only is the leading-edge suction changed by change in sideslip angle but so also is the fraction of it converted to vortex lift.

Consider first the changes in sweep angle of a delta fin leading edge as influenced by pitch and roll. For zero pitch and roll, we have

$$\Lambda_0 = \cot^{-1} \left(\frac{4}{R} \right) \quad (36)$$

For combined pitch and roll, the sweep angle, Λ_{eff} , is now

$$\Lambda_{\text{eff}} = \cot^{-1} \left(\frac{4}{R} \right) - \alpha_c \cos \phi \quad (37)$$

From the results of reference 12, values of K^* corresponding to Λ_0 and Λ_{eff} can be obtained and are designated K_0^* and K_{eff}^* .

In estimating the change in vortex normal force, we determine α_{eq} in the usual way. The curve, $(dC_{N_w}/d\alpha)_{\alpha=0} \sin \cos \alpha$, is constructed on the normal-force curve of the wing alone as shown in the preceding sketch. A "vortex normal force" is determined by subtracting the potential normal force from the experimental normal force. This vortex normal force is then scaled by the ratio, K_{eff}^*/K_0^* . This method assumes that the leading-edge suction is a constant fraction of the potential normal force as sweep angle changes. Using vortex-lattice or panel methods, we can determine the actual change in leading-edge suction with sweep angle before applying the K^* factors but have not done so in the approximate method.

An application of the above improvement in the present method has been made to fin 1 for the conditions of figure 28(a). The fin is a clipped delta fin, and it has been approximated by a delta fin with the same aspect ratio for obtaining values of K^* . In determining the potential normal force, $\sin \alpha$ was taken as α and $\cos \alpha$ as unity in equation (34). The pertinent wing normal-force curve is given in figure 12(a). The numerical results obtained by this "improved method" are shown in figure 28(a) by the flagged symbols. Much improved agreement with data is exhibited. It seems clear from the improvement shown in figure 28(a) that an important phenomenon not now included in the present method has been identified. Furthermore, a means for accounting for its effects has been found. Further refinement to account separately for the effects of leading edges and side edges seems desirable.

4.3 Total Loads for Body-Tail Configurations

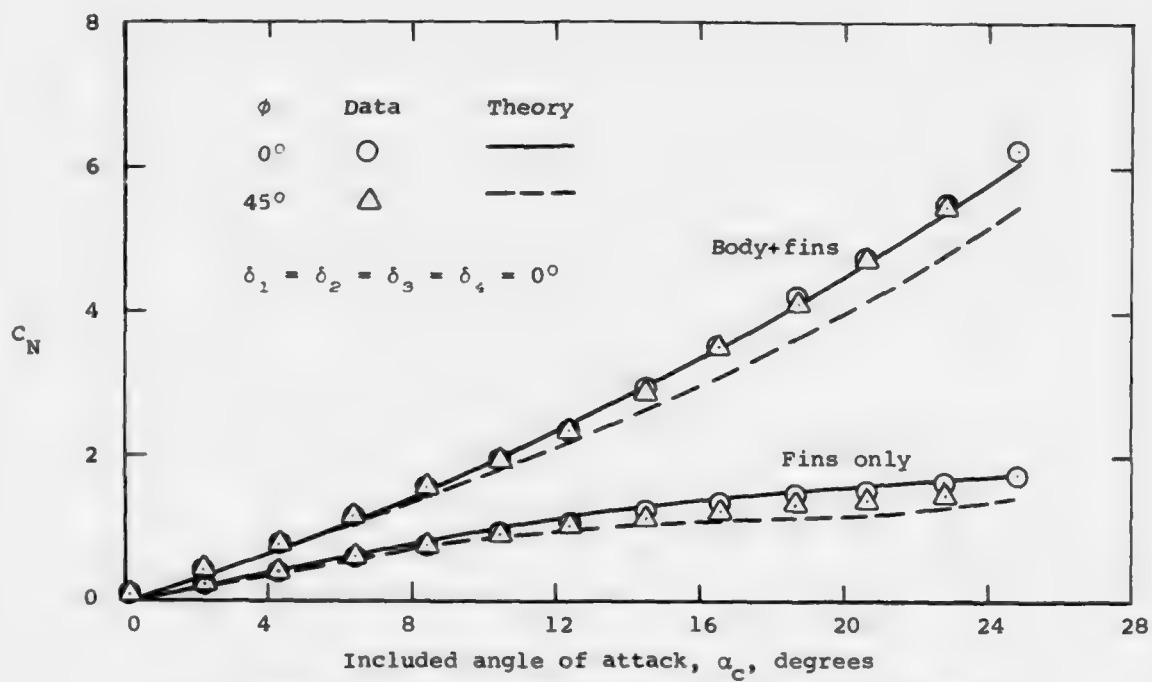
We have made comparisons of data for complete body-tail configurations with the present theory without the improvements discussed above. The results shown in figures 29-31 are typical. We will discuss the normal-force results first and then rolling moment and side force.

Generally, the agreement for total normal force is good at low α_c and fair at high α_c . Let us first consider the results for body-tail configuration no. 2 at $M_\infty = 1.75$. Note that the contribution of the tail fin loads to the normal force is well predicted. Results not presented show that the body-alone normal force for this case is also well predicted. Consideration of the axial location of the center of pressure (fig. 29(b)) also suggests that the predicted contribution to the normal force for the tail region at $\phi = 45^\circ$ is slightly low since the predicted center of pressure location is slightly forward.

For the $M_\infty = 0.8$ case, it is clear from figure 30(a) that the calculated contribution of the tail fins to normal force is somewhat low at high angles of attack. As discussed above in section 4.2.2, the discrepancy appears to be due to favorable vortex-fin interaction which is not accounted for in the present method.

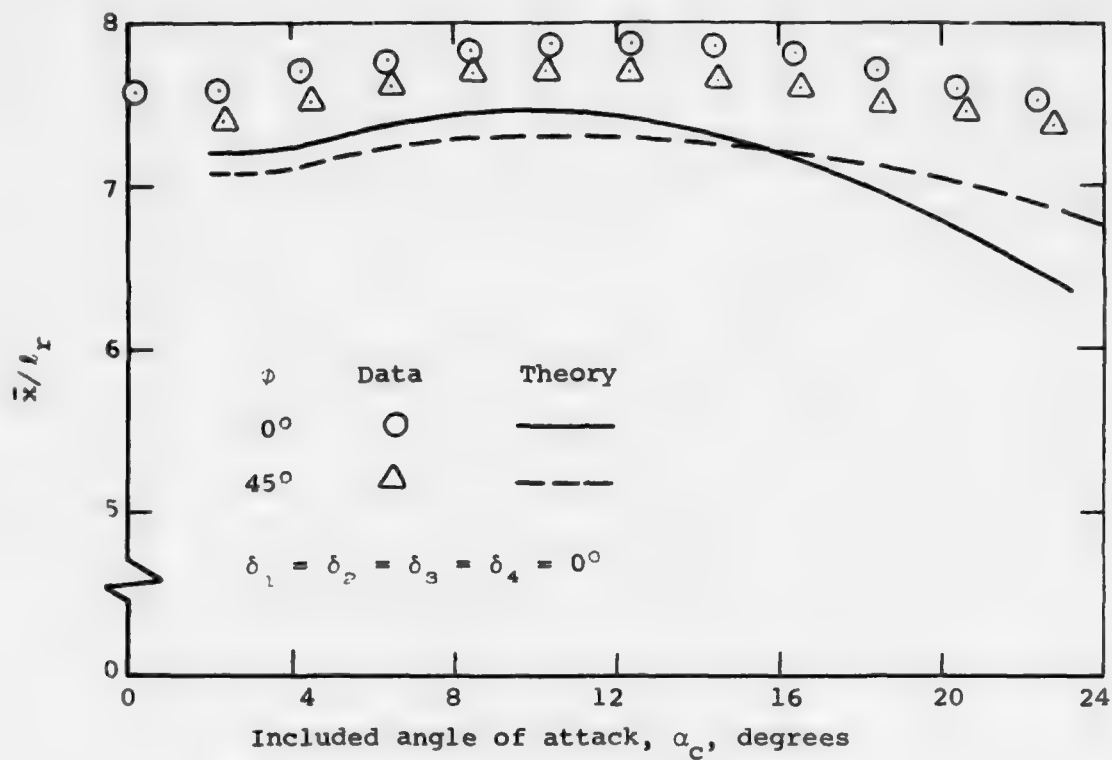
Results for the AIM-9L body and tail (body-tail configuration no. 4) are shown in figure 31 for $M_\infty = 0.8$ and a bank angle of 22.5° . The fins were undeflected. The agreement between data and theory for normal force is very good.

The induced rolling moments for the body-tail cases presented in figures 29(c) and 30(c) and 31(b) are interesting since the rolling moment is a second-order quantity (linear theory with no vortices would give zero rolling moment). The rolling moments shown correspond roughly to 2° of aileron control. The agreement between data and theory is only fair. The agreement should improve considerably if the phenomena discussed in sections 3 and 4.2 are incorporated into the method.

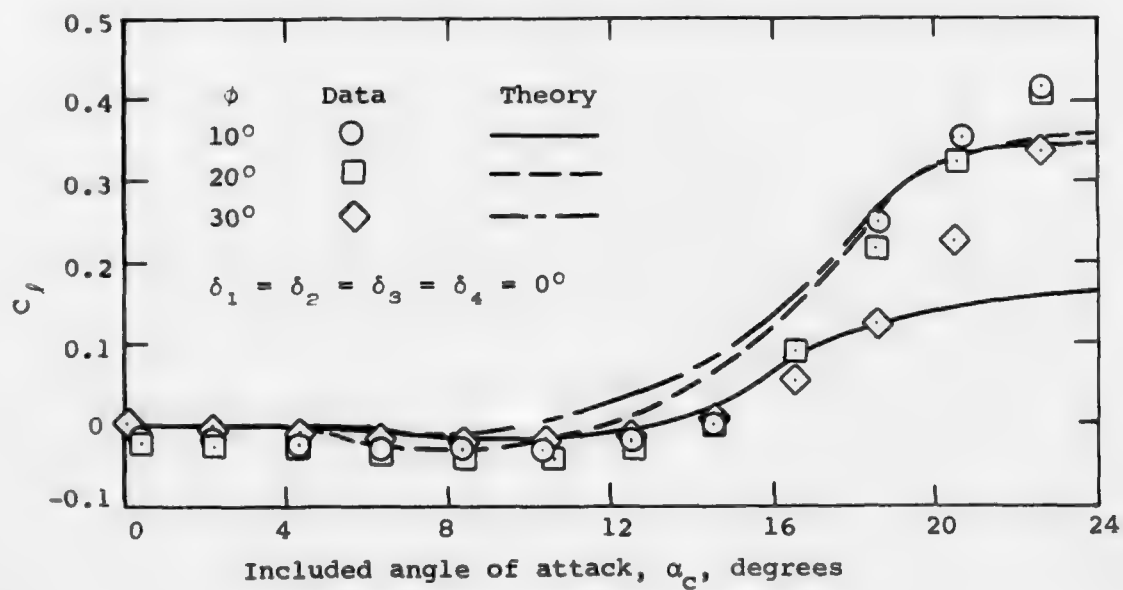


(a) Normal-force coefficient in unrolled body coordinates.

Figure 29. Comparison of data and theory for BT 2, $M_\infty = 1.75$,
 $V_{\max}/V_\infty = 0.4$; S_R = model base area,
 l_r = model base diameter.

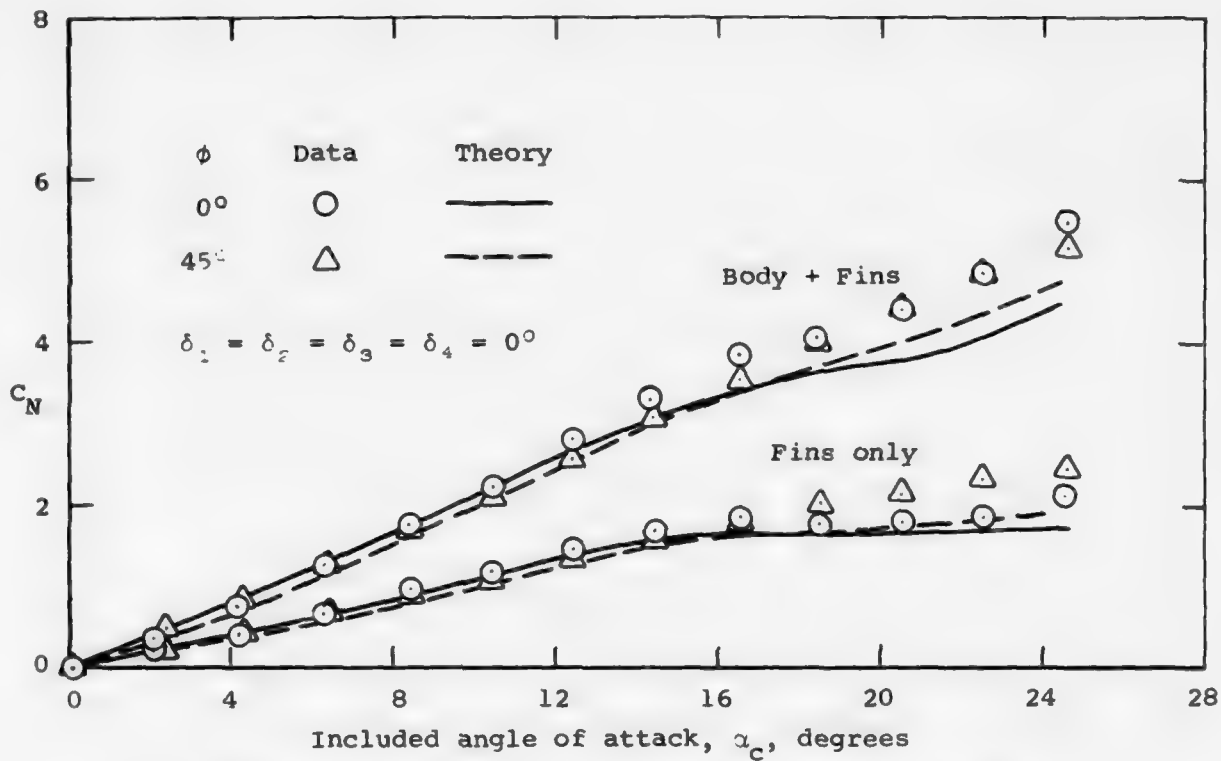


(b) Axial location of center of pressure for normal force, measured from MS 0.



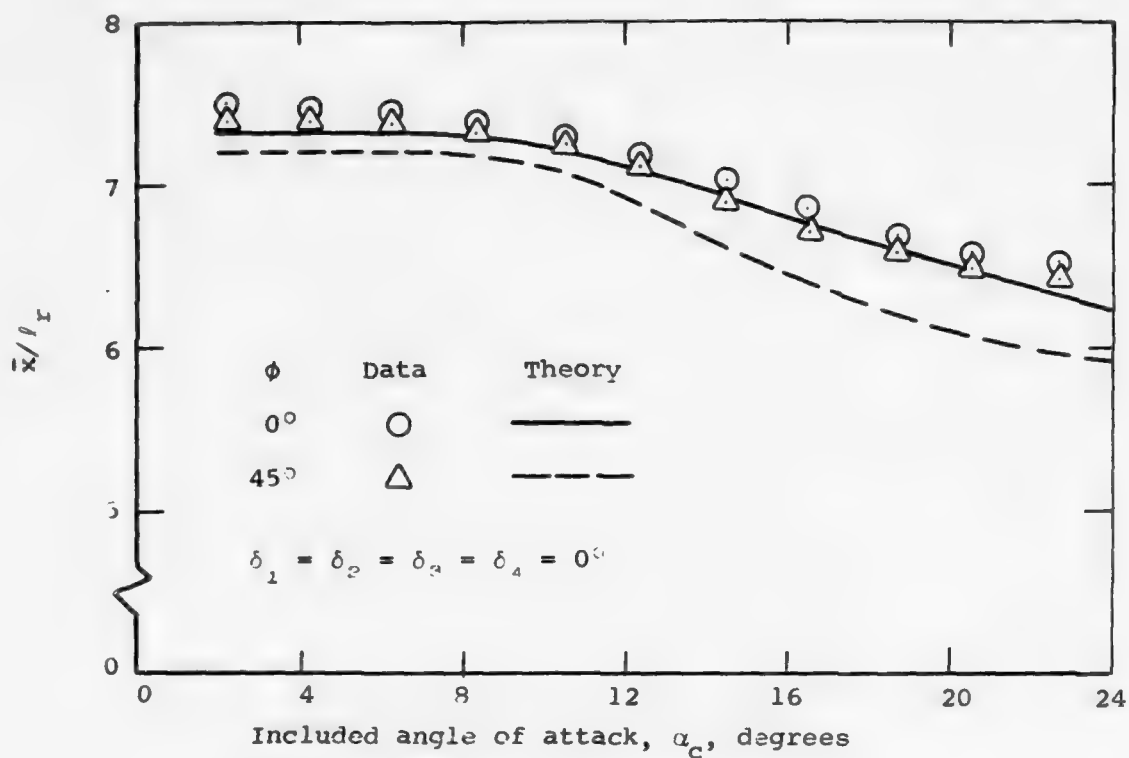
(c) Rolling-moment coefficient.

Figure 29. Concluded.

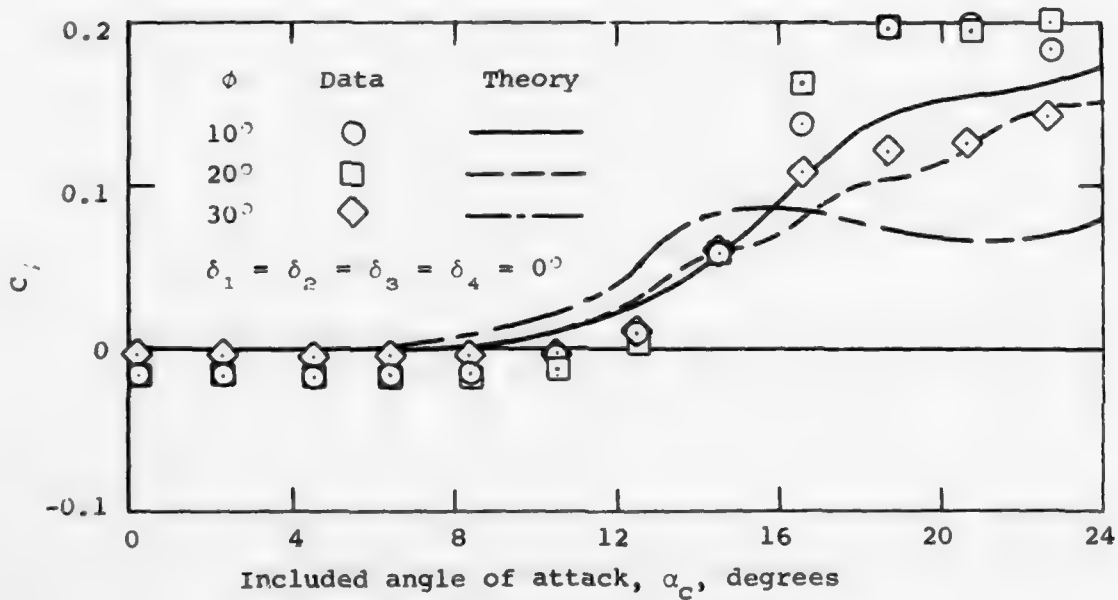


(a) Normal-force coefficient in unrolled body coordinates.

Figure 30. Comparison of data and theory for BT 2, $M_\infty = 0.8$,
 $V_{\max}/V_\infty = 0.1$; S_R = model base area,
 l_r = model base diameter.

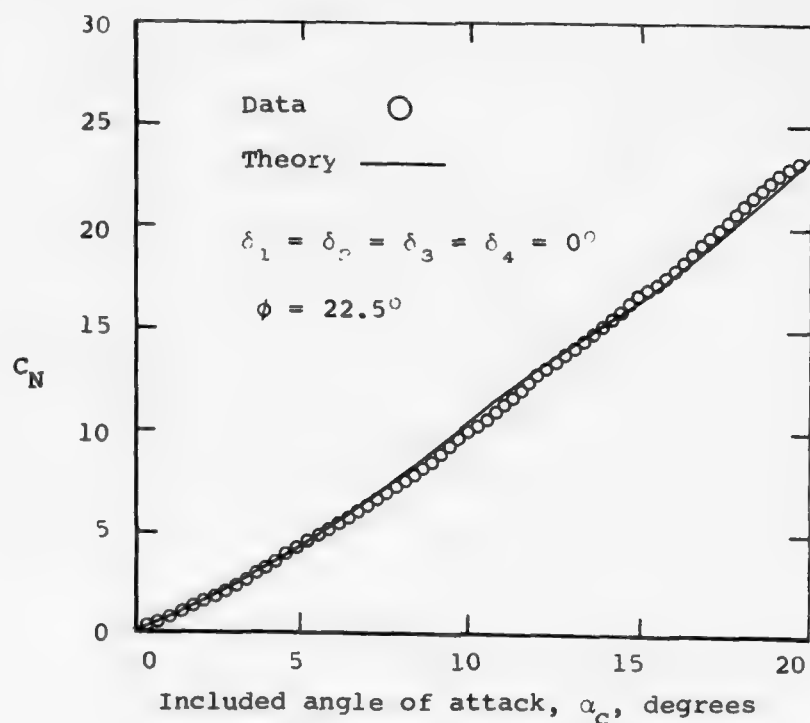


(b) Axial location of center of pressure for normal force, measured from MS 0.

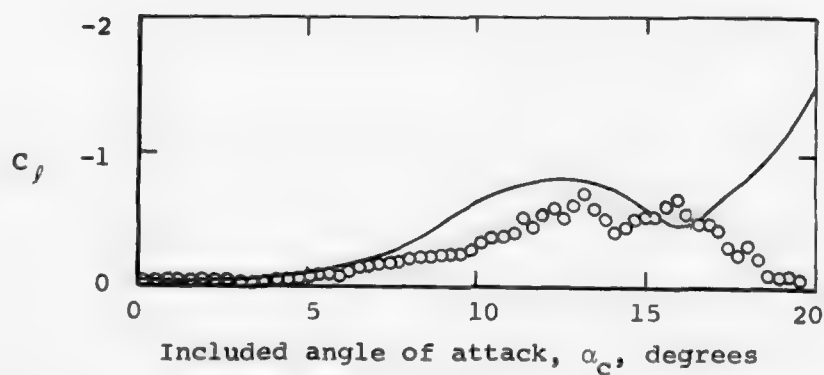


(c) Rolling-moment coefficient.

Figure 30. Concluded.



(a) Normal-force coefficient in unrolled body coordinates.



(b) Rolling-moment coefficient.

Figure 31. Comparison of data and theory for BT 4, $M_\alpha = 0.8$, $v_{\max}/v_\infty = 0.4$; S_R = model base area, l_r = model base diameter.

5. COMPARISONS WITH DATA FOR BODY-CANARD AND BODY-CANARD-TAIL CONFIGURATIONS

This section is concerned with body-canard and body-canard-tail configurations which require vortex tracking for the calculation of forces and moments. The method used to obtain the vortex system behind the canard fins is heuristic, and its validity can best be determined by comparing its predictions with data. The method, as described in Appendix D, represents any body-generated vorticity which may form aft of the canard trailing edge as discrete vortices which change strength and position as a function of their axial positions. The first subsection below contains results for body-canard configurations (see fig. 3). Since no tail fins are present, these results are a sensitive indication of the ability of the tracking method to reproduce actual body loads in the presence of the wake over the afterbody. The second subsection below is concerned with body-canard-tail configurations (see fig. 3). These results are good tests of the ability of the tracking method to locate the vortices of the afterbody wake properly with respect to the tail fins.

5.1 Results for Body-Canard Configurations

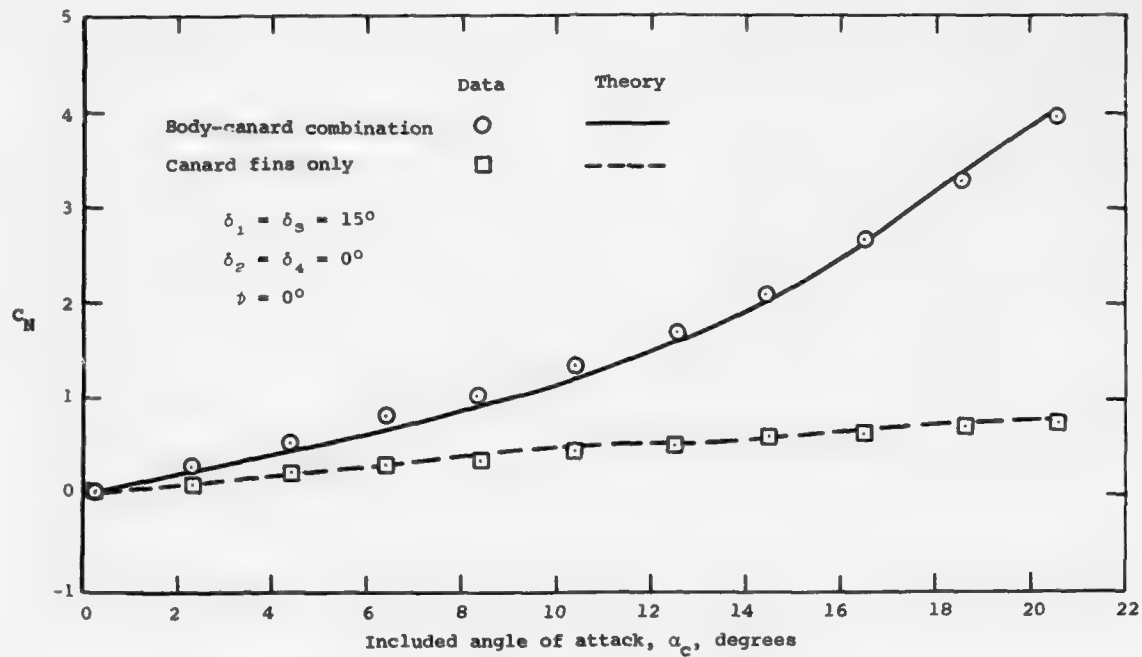
One of the features of the present method is that all vorticity is regarded as discrete and all the vorticity generated from a separation line on the body is represented by a single vortex. For example, the nose vorticity on the port side, the trailing-edge vorticity from canard fin 1 and the afterbody vorticity on the port side are each represented by a single vortex. Vapor screen (ref. 5) and laser anemometer (ref. 20) studies of the development of such vorticity indicate that more than one vortex may at times be required to represent the shed vorticity from each of these sources. It is known, for example, from the work of reference 5 that for $\alpha_c \leq 20^\circ$ the vorticity formed ahead of the canard fins of body-canard configuration no. 1 is dispersed as it moves over the fins and is no longer rolled up by the time it reaches the canard trailing edge. The present model represents such a vorticity field by a concentrated vortex which cannot disperse. The user of the code does have the option, however, of eliminating the nose vortices at the canard leading or trailing edges if he feels that they have dispersed in the actual flow. The vapor screen study of reference 5 also implied that vorticity shed from one of the windward fins can travel up and around the body and

strongly interact with the body boundary layer. The method used herein does not include this effect.

During the tests of reference 4, individual fin load data were obtained for body-canard configuration nos. 1 and 2 shown in figure 3. These data enable us to investigate the effects of afterbody wake asymmetry on total body loads. Results for body-canard configuration no. 1 are presented in figure 32 for $M_\infty = 1.75$ and zero bank. The moderate-aspect-ratio C_6 fins are deflected 15° in yaw and 0° in pitch. The comparisons show that total normal force is accurately predicted. However, side force is poorly predicted although the trend is correct. Note that the contributions of the fins to the total normal and side forces are well predicted. Hence, any discrepancies present must be attributed to the afterbody wake model.

Results for body-canard configuration no. 2 are presented in figure 33 for $M_\infty = 1.75$ and 20° bank. The low-aspect-ratio C_7 fins were undeflected. Note that the C_7 fins are considerably smaller relative to the body than the C_6 fins, yet similar results were obtained. Again, the contribution of the fins to total loads is well predicted. The agreement for total normal force is satisfactory though not quite so good as for the previous case. The results for total side force are interesting since, as in the previous case, the trend (for $\alpha_c < 24^\circ$) is represented correctly although the magnitude is not. In this case, the side force is a second-order quantity being generally less than 10 percent of the normal force.

Another set of comparisons are presented in figure 34 for body-canard configuration no. 3 for $M_\infty = 0.8$ and zero bank. This configuration represents the AIM-9L. Note that the canards (see fig. 3(g)) are considerably larger relative to the body than the fins of body-canard configuration no. 1. Note also that the leading edge of each canard fin has a break in sweep. Although the present version of the code cannot handle breaks in leading-edge sweep, the fins can be adequately modeled with a straight leading edge running from the actual location of the leading edge of the root chord to the actual location of the tip chord. For the results of figure 34, the fins were deflected 20° in yaw and 0° in pitch. The agreement is fair for normal force and poor for side force. (Note that the side-force scale is 50 times the normal-force scale.) If more accurate side-force calculations on a percentage basis are to be made, some improvement in the afterbody vortex model is



(a) Normal-force coefficient in unrolled body coordinates.

Figure 32. Comparison of data and theory for BC 1, $M_\infty = 1.75$, $V_{\max}/V_\infty = 0.4$; S_R = model base area.

AD-A034 722

NIELSEN ENGINEERING AND RESEARCH INC MOUNTAIN VIEW CALIF F/G 16/4
CALCULATION OF COMPONENT FORCES AND MOMENTS OF ARBITRARILY BANK--ETC(U)
NOV 76 M J HEMSCH, C A SMITH, J N NIELSEN N00014-74-C-0050

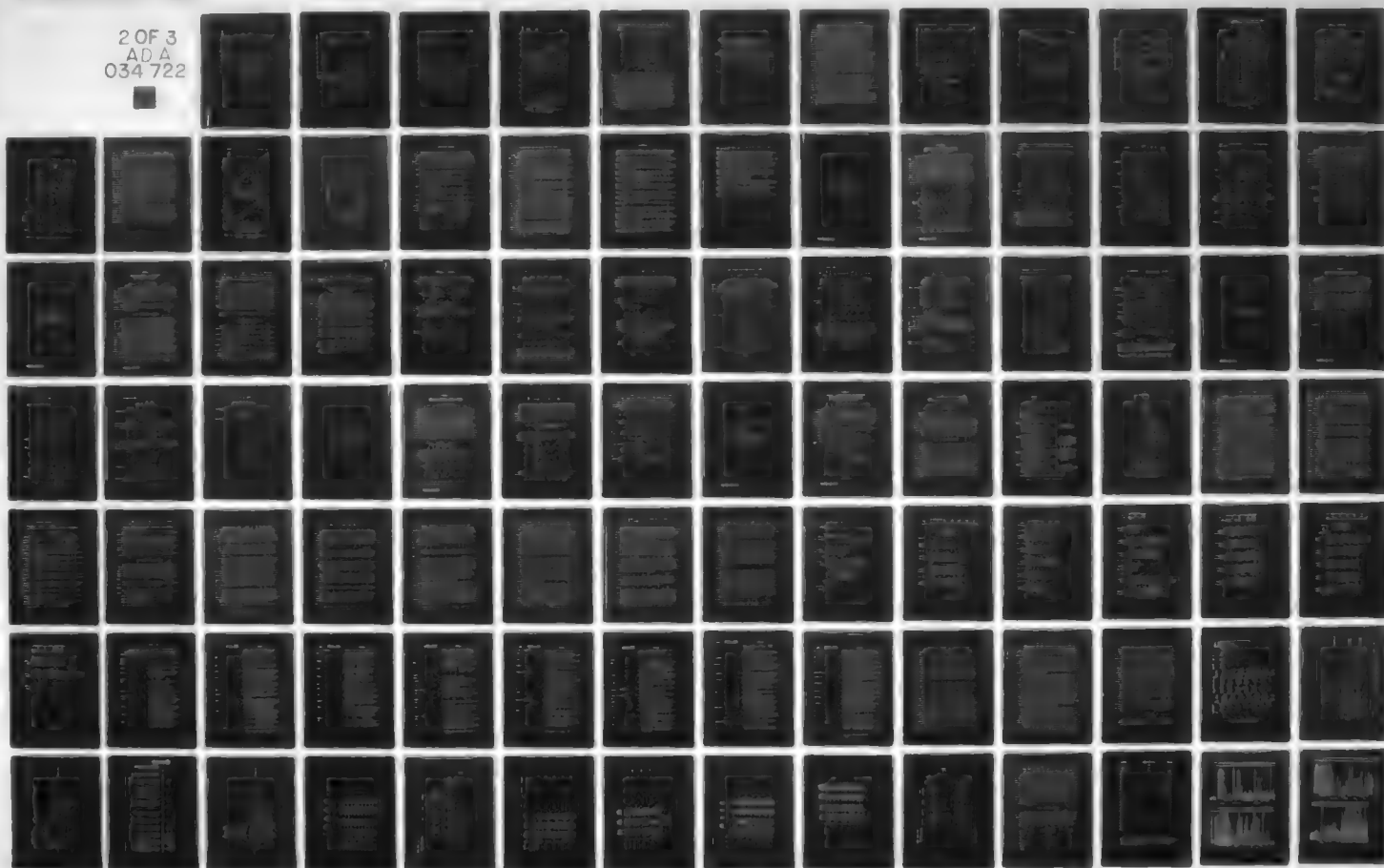
UNCLASSIFIED

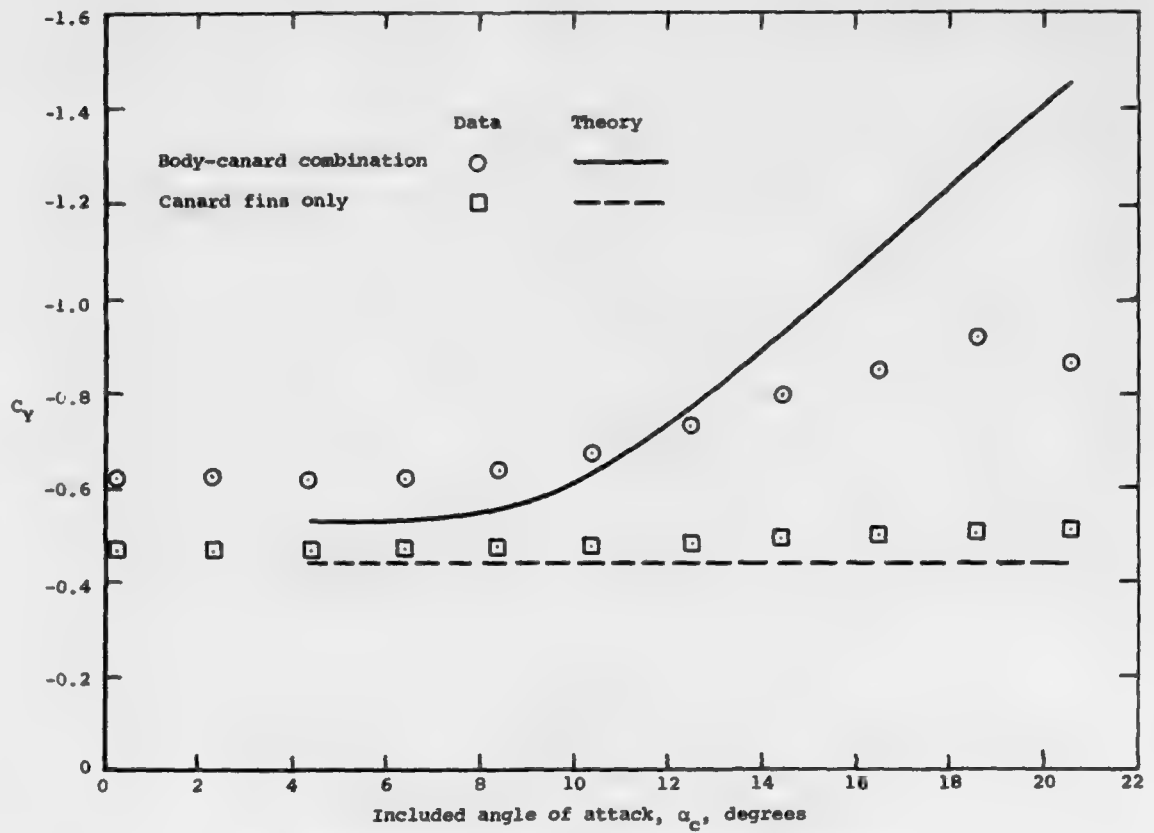
NEAR-TR-125

ONR-CR215-226-3

NL

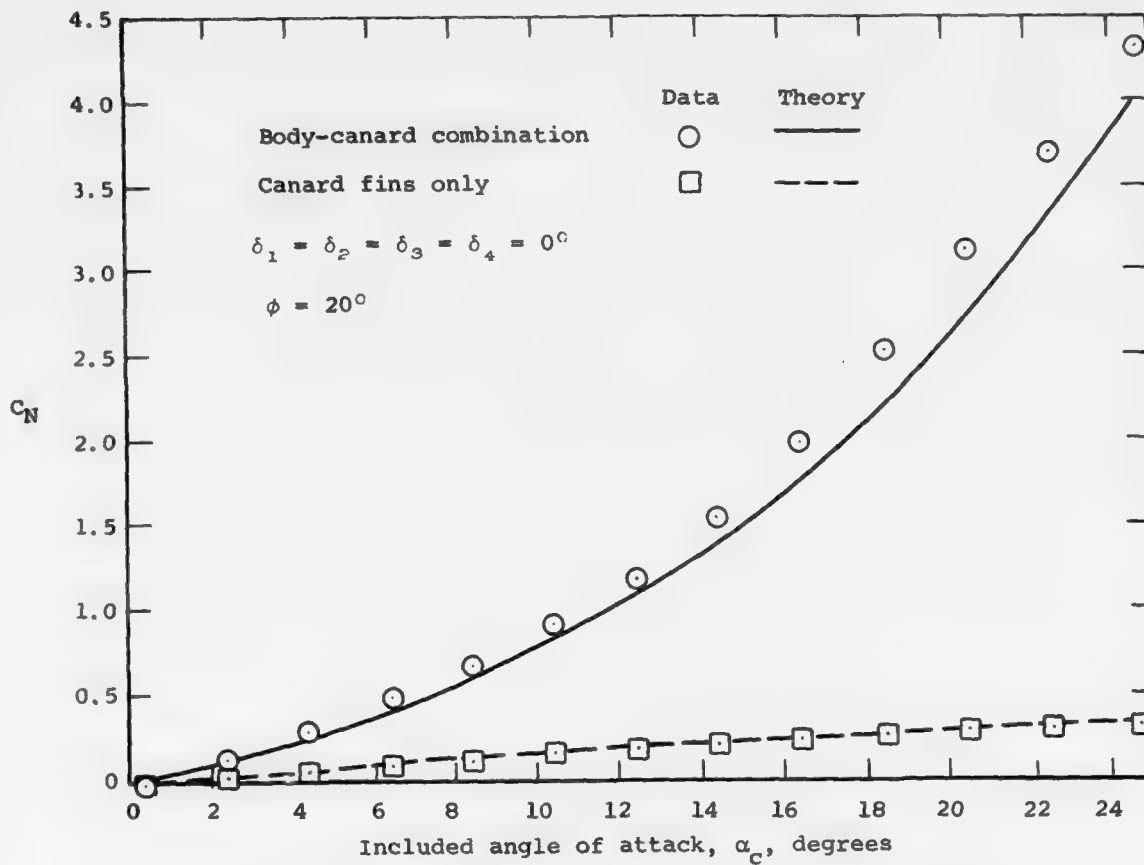
2 OF 3
ADA
034 722





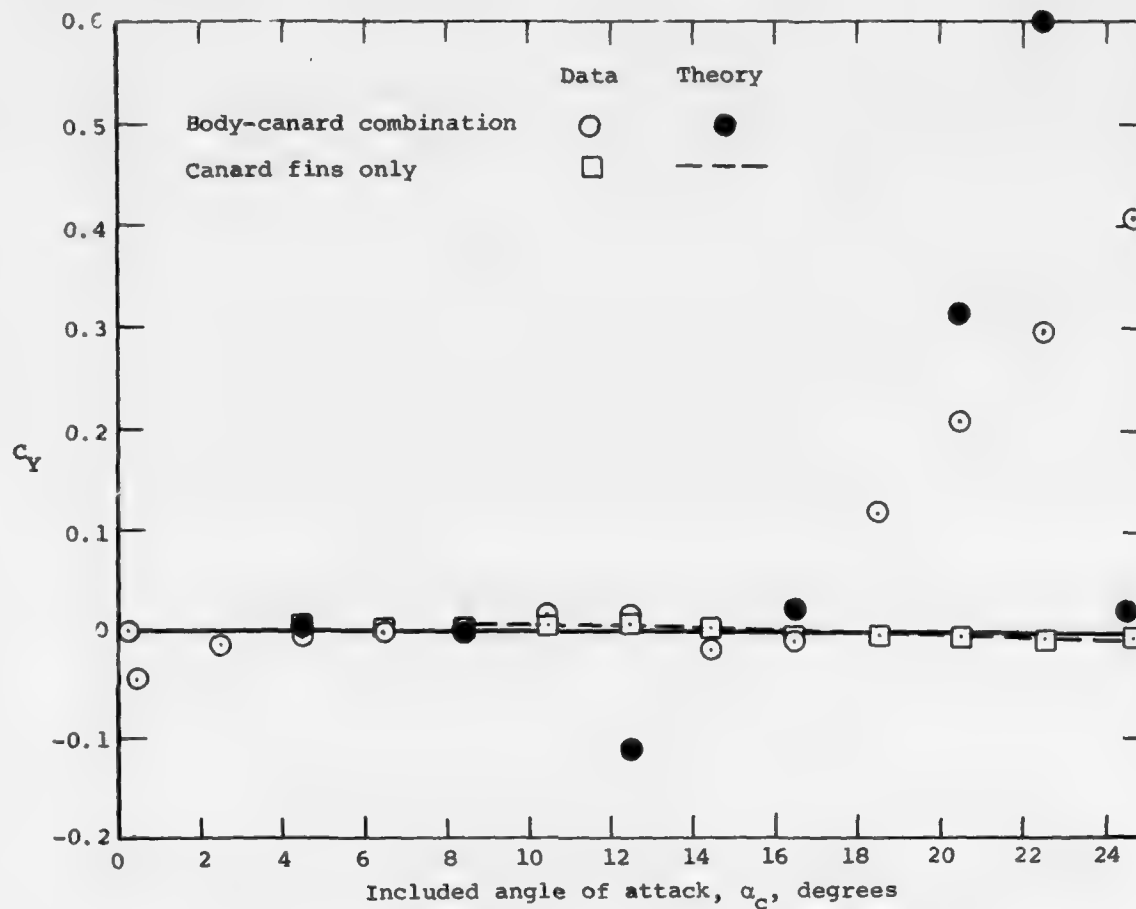
(b) Side-force coefficient in unrolled body coordinates.

Figure 32. Concluded.



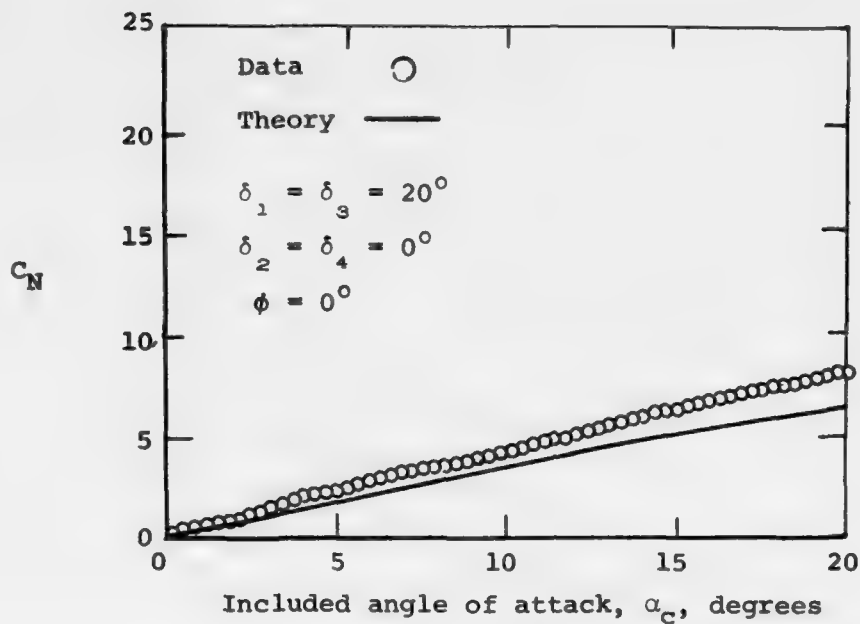
(a) Normal-force coefficient in unrolled body coordinates.

Figure 33. Comparison of data and theory for BC 2, $M_\infty = 1.75$, $V_{\max}/V_\infty = 0.4$; S_R = model base area.

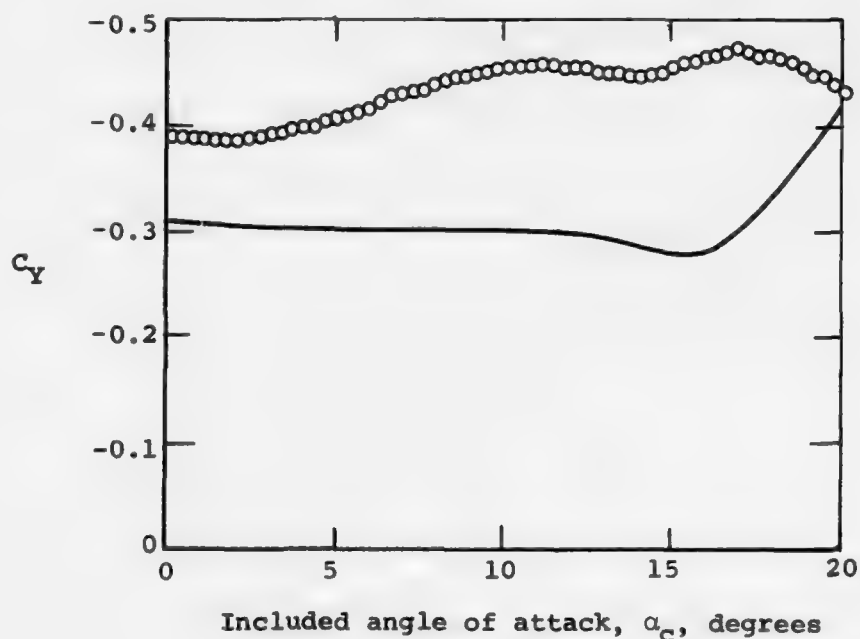


(b) Side-force coefficient in unrolled body coordinates.

Figure 33. Concluded.



(a) Normal-force coefficient in unrolled body coordinates.



(b) Side-force coefficient in unrolled body coordinates.

Figure 34. Comparison of data and theory for BC 3, $M_\infty = 0.8$, $V_{\max}/V_\infty = 0.1$; S_R = model base diameter.

indicated. The sources of side force can be found by examining the vortex impulse theorem (eq. (28)) which is used to compute them. If we take the real and imaginary parts of equation (28) and integrate over the afterbody section, we obtain

$$C_N = \frac{4\pi a^2}{S_R} \sum_{j=1}^{NV(x)} \left\{ \left[\Gamma'_j y_{v,j} \left(1 - \frac{1}{r_{v,j}^2} \right) \right]_{\text{body base}} - \left[\Gamma'_j y_{v,j} \left(1 - \frac{1}{r_{v,j}^2} \right) \right]_{\text{trailing edge of canard section}} \right\} \quad (38)$$

$$C_Y = - \frac{4\pi a^2}{S_R} \sum_{j=1}^{NV(x)} \left\{ \left[\Gamma'_j z_{v,j} \left(1 - \frac{1}{r_{v,j}^2} \right) \right]_{\text{body base}} - \left[\Gamma'_j z_{v,j} \left(1 - \frac{1}{r_{v,j}^2} \right) \right]_{\text{trailing edge of canard section}} \right\} \quad (39)$$

where Γ' is nondimensionalized by $2\pi V_\infty a$ and y_v and z_v are nondimensionalized by a . If a vortex is free, its strength is constant, and its contribution to the normal force and side force depend on its movement in the y_0 and z_0 directions, respectively. The initial strength of an afterbody vortex is zero and its contribution to the forces depends only on its strength and position in the crossflow plane at the body base.

We have computed the predicted effect of each vortex present on the afterbody loads for the case shown in figure 32 at $\alpha_c = 20.6^\circ$. The results are given in Table 1. Note that a 5- to 10-percent change in the vertical position relative to the body axis of any of the vortices could make a large difference in the predicted side force for the afterbody section. Also large side-force contributions of alternating sign occur. The results of Table 1 clarify the need for accurate vortex tracking past the afterbody section. While the present model is capable of reproducing most of the physics, further improvement is needed if accurate results for side force are to be obtained.

TABLE 1. PREDICTED CONTRIBUTION OF VORTICES TO AFTERBODY LOADING
 FOR BODY-CANARD CONFIGURATION NO. 1; $M_\infty = 1.75$, $\phi = 0^\circ$,
 $\delta_1 = \delta_3 = 15^\circ$, $\delta_2 = \delta_4 = 0^\circ$, $\alpha_c = 20.6^\circ$,
 S_R = model base area.

Vortex	CANARD TRAILING EDGE			BODY BASE			C_N	C_Y
	Γ'	y_v/a	z_v/a	Γ'	y_v/a	z_v/a		
C1	0.053	0.18	1.93	0.053	0.52	3.43	0.07	-0.37
C2	-0.111	-1.87	0.	-0.111	-0.68	4.16	-0.31	1.74
C3	-0.072	0.18	-1.91	-0.072	1.22	3.59	-0.29	1.36
C4	0.115	1.87	0.	0.115	0.96	4.01	-0.20	-1.74
A_L	0.	-0.68	0.99	-0.397	-0.09	1.98	0.11	2.34
A_R	0.	1.09	0.50	0.411	1.76	2.85	2.64	-4.27
TOTAL							2.02	-0.94

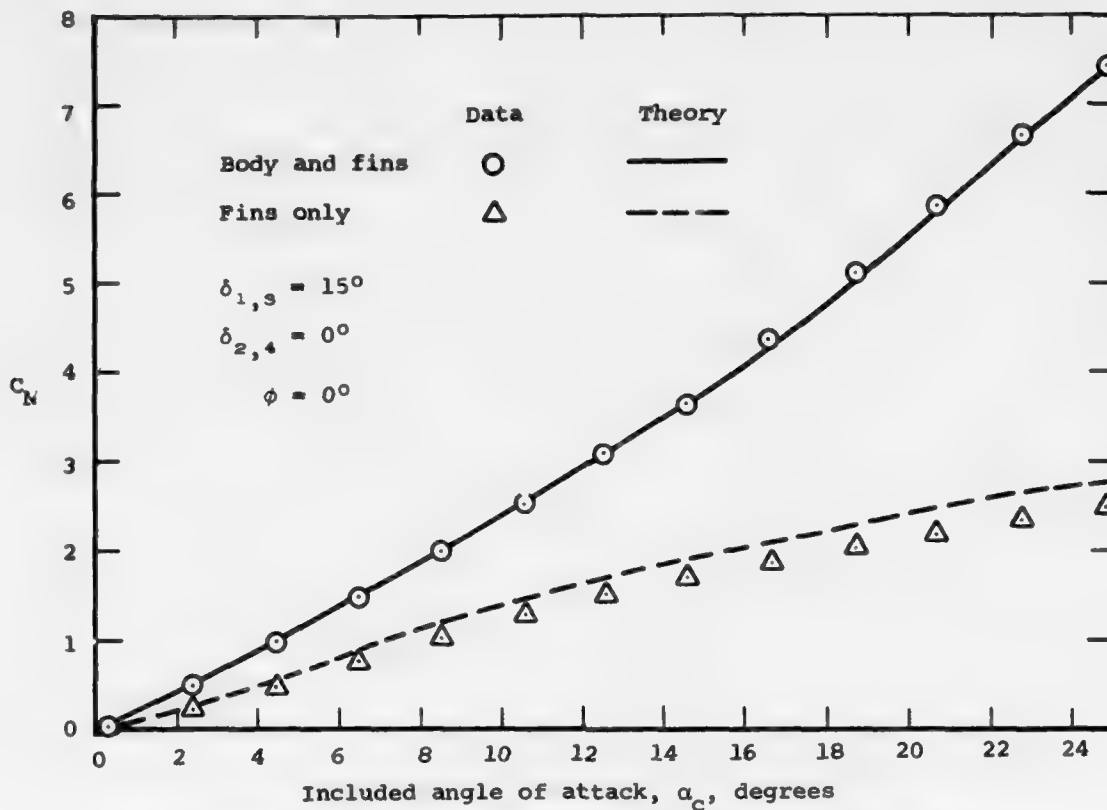
5.2 Results for Body-Canard-Tail Configurations

Comparisons between data and theory for two different body-canard-tail configurations are given in this section. The configurations are unrolled but have large yaw control deflections. Figure 35 presents results for body-canard-tail configuration no. 1 at $M_\infty = 1.75$ with zero bank. The fins are deflected 15° in yaw and 0° in pitch. The normal force is well predicted. However, the theory for side force departs increasingly from data for angles of attack above 18° . Since the contribution of the fins to the total side force is fairly well predicted, the procedure for obtaining the afterbody vortex positions and strengths on the afterbody section is the likely source of the discrepancy. The results for rolling moment are only fair.

Since the body cannot support a rolling moment, an analysis of the individual contributions of the fins to the total rolling moment should be of interest. The results are given in Table 2 for $\alpha_c = 8.5^\circ$ and 20.6° . It is interesting to note that both the canard section and the tail section contribute substantially to the rolling moment but for different reasons. The canard section does not have significant body vorticity present. Hence, the only source of rolling moment for the canard section is differential fin loading due to sideslip. Canard fins 2 and 4 are not sideslipping as α_c increases. Therefore, fins 1 and 3 contribute most to the total rolling moment.

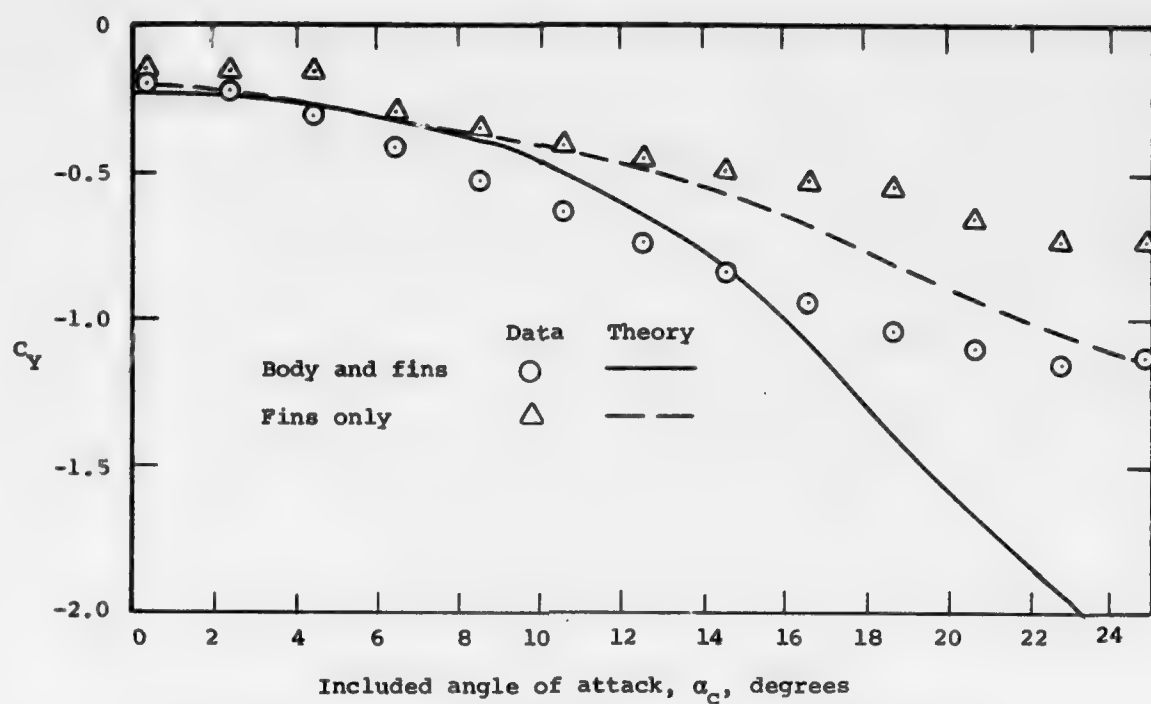
In the absence of vorticity shed by the body and canard fins, the tail section for $\phi = 0$ cannot support a rolling moment. Hence, the only source of rolling moment for the tail section is vortex-fin interference. This is clearly evident in the data for fins 1, 2, and 4. Note that the discrepancies between data and theory for individual fins are not large compared to the size of the loads seen. Yet those same discrepancies create large percentage errors in the overall rolling moment.

It is interesting to see which of the vortices present in the wake influence each fin. Calculated and measured vortex positions for several angles of attack at the leading edge of the tail root chord are presented in figure 36. Note that the predictions of the present method place the left afterbody vortex too far to the right and the right afterbody vortex too high.



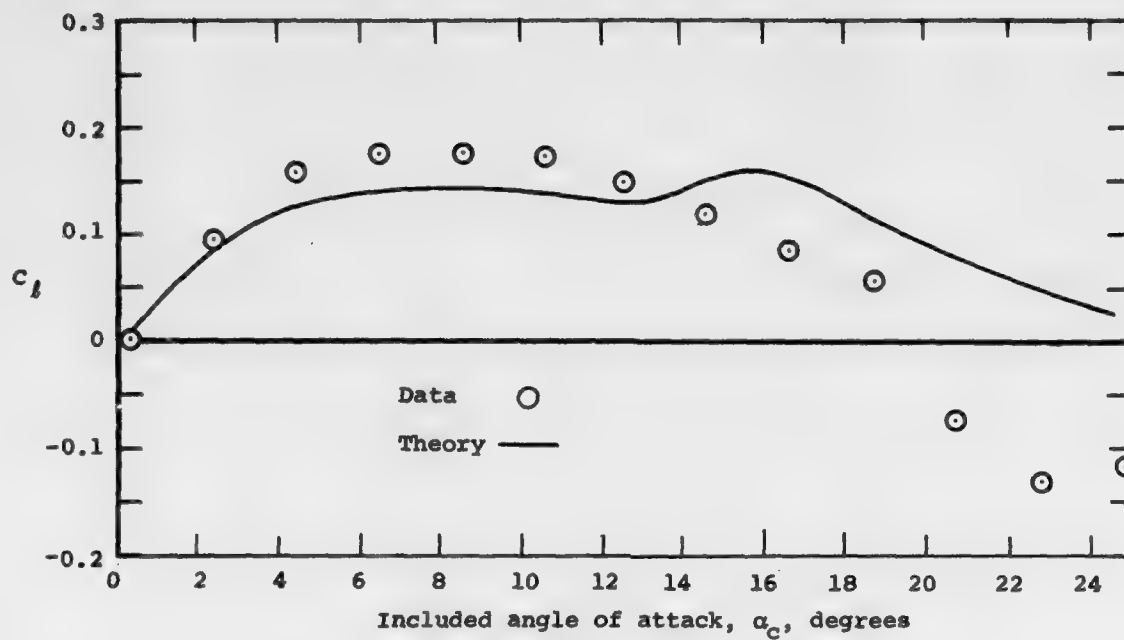
(a) Normal-force coefficient in unrolled body coordinates.

Figure 35. Comparison of data and theory for BCT 1, $M_\infty = 1.75$,
 $V_{\max}/V_\infty = 0.4$; S_R = model base area,
 l_r = model base diameter.



(b) Side-force coefficient in unrolled body coordinates.

Figure 35. Continued.



(c) Rolling-moment coefficient.

Figure 35. Concluded.

TABLE 2. ANALYSIS OF ERROR IN ROLLING MOMENT FOR
BODY-CANARD-TAIL CONFIGURATION NO. 1;

$M_\infty = 1.75$, $\phi = 0$, $\delta_1 = \delta_3 = 15^\circ$,
 $\delta_2 = \delta_4 = 0^\circ$, S_R = model base area,
 ℓ_r = model base diameter.

(a) $\alpha_c = 8.5^\circ$.

$\epsilon_i \equiv (\text{CRMi})_{\text{theory}} - (\text{CRMi})_{\text{data}}$ $\epsilon_T \equiv [(C_\ell)_{\text{theory}} - (C_\ell)_{\text{data}}]_{\text{all fins}}$				
	Data	Theory	ϵ_i	$\epsilon_i/ \epsilon_T $
CRMC1	0.1605	0.1634	0.0029	0.06
CRMC2	0.1423	0.1504	0.0081	0.17
CRMC3	0.1974	0.1829	-0.0145	-0.30
CRMC4	0.1392	0.1545	0.0153	0.32
CRMT1	-0.0747	-0.0575	0.0172	0.36
CRMT2	0.3170	0.3454	0.0284	0.59
CRMT3	-0.0001	0.0118	0.0119	0.25
CRMT4	0.2457	0.2924	0.0467	0.97
$(C_\ell)_{\text{canard fins}}$	0.0400	0.0154		
$(C_\ell)_{\text{tail fins}}$	0.1459	0.1223		
$(C_\ell)_{\text{all fins}}$	0.1859	0.1377		
$\frac{[(C_\ell)_{\text{theory}} - (C_\ell)_{\text{data}}]_{\text{canard fins}}}{[(C_\ell)_{\text{theory}} - (C_\ell)_{\text{data}}]_{\text{all fins}}} = 0.51$ $\frac{[(C_\ell)_{\text{theory}} - (C_\ell)_{\text{data}}]_{\text{tail fins}}}{[(C_\ell)_{\text{theory}} - (C_\ell)_{\text{data}}]_{\text{all fins}}} = 0.49$				

TABLE 2. CONCLUDED

(b) $\alpha_c = 20.6^\circ$.

	Data	Theory	ϵ_i	$\epsilon_i/ \epsilon_T $
CRMC1	0.1512	0.1494	-0.0018	-0.01
CRMC2	0.2775	0.3018	0.0243	0.16
CRMC3	0.2395	0.1968	-0.0427	-0.29
CRMC4	0.2854	0.3102	0.0248	0.17
CRMT1	0.1446	0.1272	-0.0174	-0.12
CRMT2	0.6094	0.7496	0.1402	0.95
CRMT3	-0.0044	0.0434	0.0478	0.32
CRMT4	0.6083	0.6250	0.0167	0.11
(C_ℓ) canard fins	0.0804	0.0391		
(C_ℓ) tail fins	-0.1479	0.0408		
(C_ℓ) all fins	-0.0675	0.0799		
$\frac{[(C_\ell) \text{ theory} - (C_\ell) \text{ data}]_{\text{canard fins}}}{[(C_\ell) \text{ theory} - (C_\ell) \text{ data}]_{\text{all fins}}} = -0.28$				
$\frac{[(C_\ell) \text{ theory} - (C_\ell) \text{ data}]_{\text{tail fins}}}{[(C_\ell) \text{ theory} - (C_\ell) \text{ data}]_{\text{all fins}}} = 1.28$				

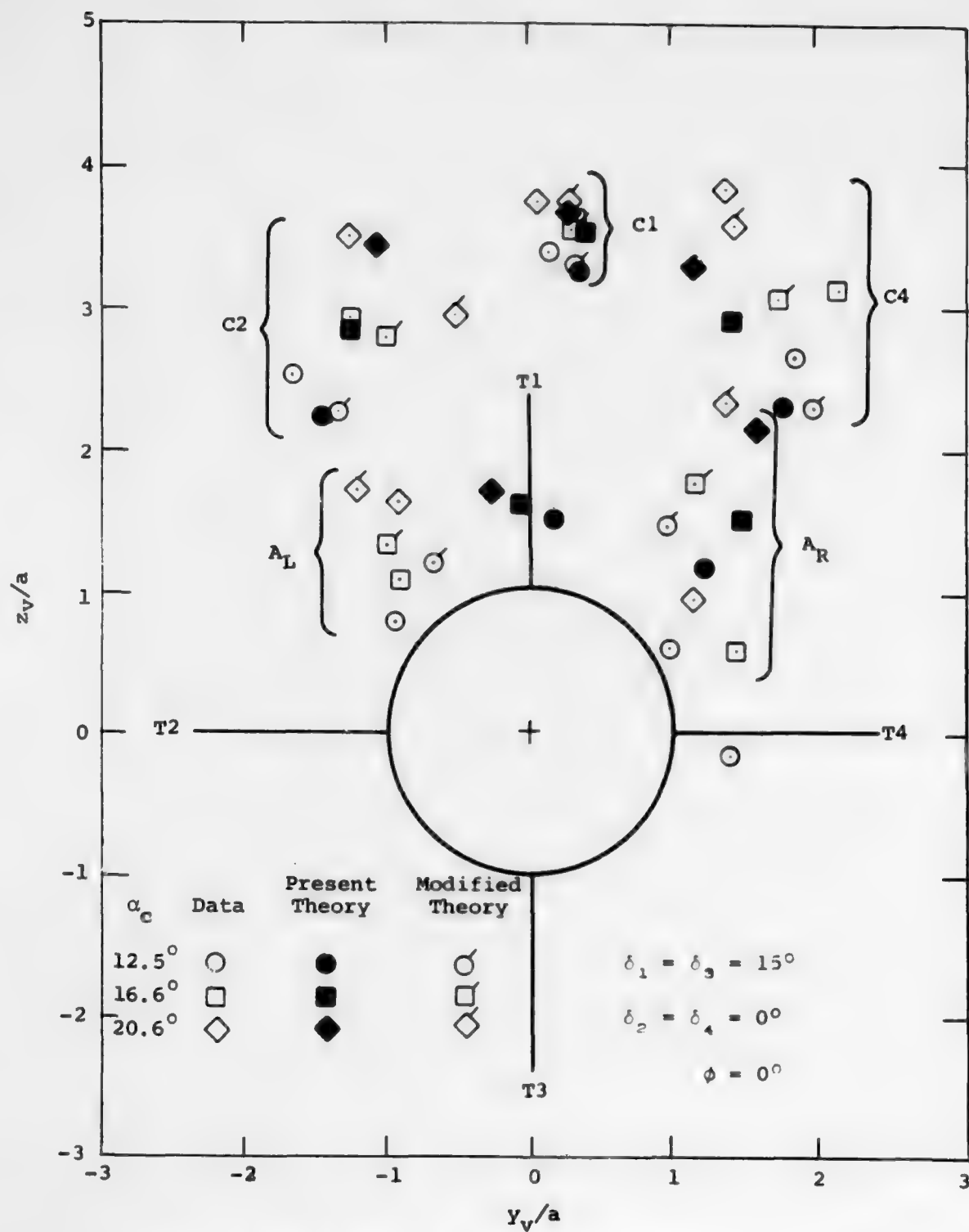


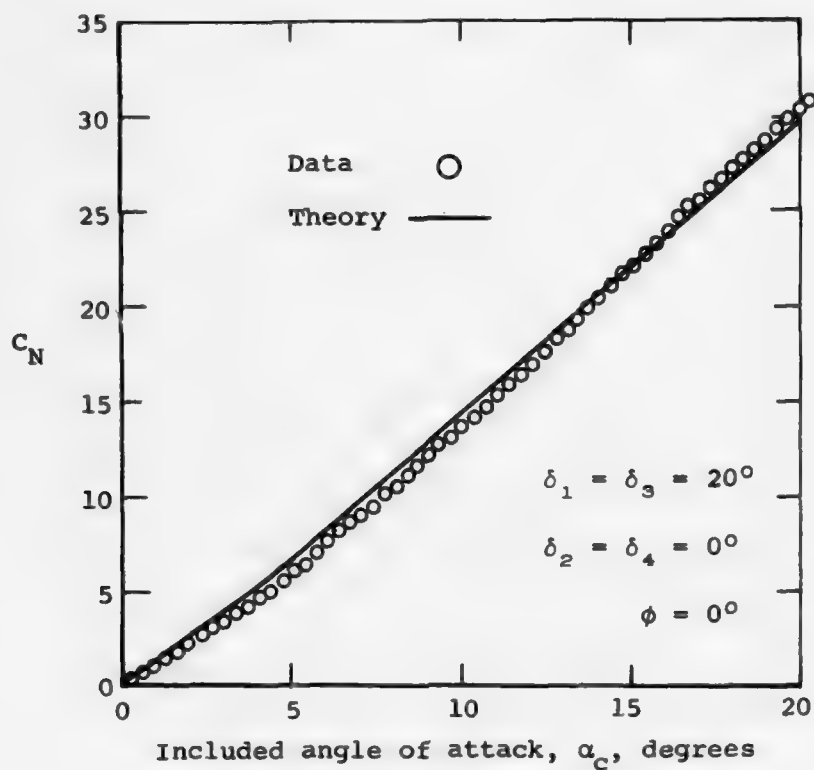
Figure 36. Measured and predicted vortex positions at $x/a = 17.2$ for BCT 1, $M_\infty = 1.75$.

In the present method, the afterbody vortices are assumed to be initially located 50° on either side of the crossflow velocity vector given by the free-stream flow and by the vorticity shed by the canard section. For the case presented in figure 36, the crossflow velocity vector at the trailing edge of the canard fins points to the right 25° , 19° , and 15° from the vertical for $\alpha_c = 12.5^\circ$, 16.6° , and 20.6° , respectively. This means that the left afterbody vortex would be started in the second quadrant at 65° , 59° , and 55° measured clockwise from fin T2. However, the vapor screen results of reference 5* indicate that the left afterbody vorticity actually separates from the body much lower in the second quadrant. Furthermore, the angular location of the separation line does not vary significantly with α_c .

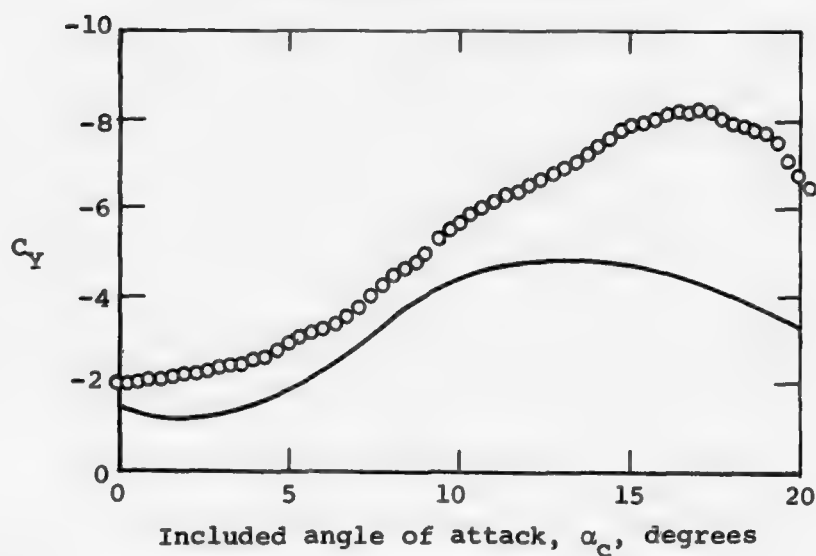
An attempt was made to represent more accurately the physics for this case by assuming the afterbody vorticity to separate 60° on either side of the vertical. The results for the modified theory are presented in figure 36 as flagged symbols. Note that the agreement between data and theory for A_L is considerably better. No improvement was obtained for A_R , however. The data of reference 5 showed that the C3 vortex moved up and to the right as it moved downstream. At some point along the body depending upon α_c , it came close enough to the body surface to interact with the body boundary layer. From that point aft, it was combined with the right afterbody vortex. That behavior is not accounted for in the present method.

In order to show that the results discussed above were not limited to an isolated case, comparisons between data and theory were made for another configuration and are presented in figure 37. The model is the AIM-9L of reference 14 (body-canard-tail configuration no. 2, fig. 3(i)). The model is unrolled and has 20° of yaw control and 0° of pitch control. The free-stream Mach number is 0.8. As in the case previously discussed, the agreement is good for normal force but only fair for side force and rolling moment.

* See also figure 20 of reference 4.

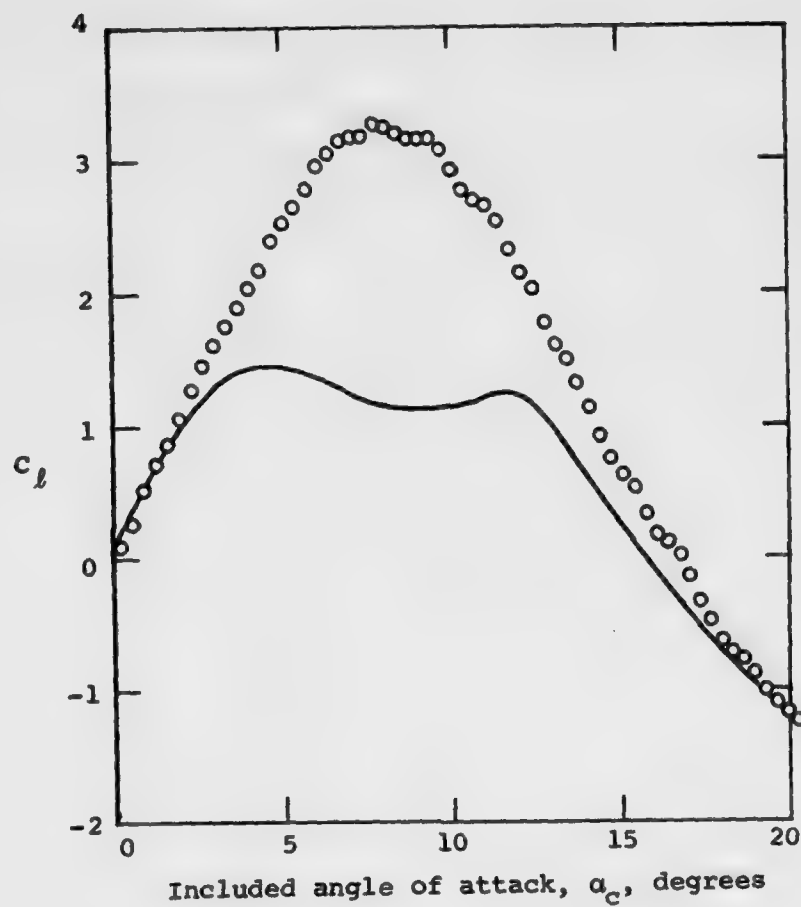


(a) Normal-force coefficient in unrolled body coordinates.



(b) Side-force coefficient in unrolled body coordinates.

Figure 37. Comparison of data and theory for BCT 2,
 $M_\infty = 0.8$, $V_{\max}/V_\infty = 0.1$; S_R = model base area,
 l_r = model base diameter.



(c) Rolling-moment coefficient.

Figure 37. Concluded.

6. CONCLUDING REMARKS

This report covers the first year's work in a two-year effort to develop a computer program for determining the forces and moments on the individual components of cruciform missiles at high angles of attack. The program is intended for use at subsonic, transonic, and supersonic speeds. It presently accommodates arbitrary roll angles, pitch control, and yaw control. It is, however, subject to the following limitations.

1. The fins in each finned section must be identical, uncambered, and untwisted.
2. Opposing fins must be symmetrically deflected; the program does not accommodate roll control at this time.
3. The wake from each fin is represented by a single vortex.
4. The trailing set of fins may not be deflected.
5. The leading edges of the fins must not be sweptforward, and the trailing edges must be unswept.
6. The small angle definitions of α and β are used.
7. The body wake upstream of the first finned section is represented by two discrete symmetric vortices.
8. The vorticity shed from the afterbody section is represented by two discrete vortices.

As part of this effort, a comprehensive comparison between data and predictions of the computer program has been made for bodies alone, body-tail combinations, body-canard combinations, and body-canard-tail combinations. The following ranges of parameters were covered:

Angle of Attack:	0° - 24°	for finned missiles
	0° - 47°	for bodies alone
Mach Number:	0.8 - 2.0	
Roll Angle:	0° - 45°	
Control Deflection:	0° - 20°	
Fin Aspect Ratio:	0.87 - 4.2	

The following conclusions can be drawn from the study:

1. For the bodies alone, accurate results were obtained except when the crossflow Mach number was near unity. The two-dimensional crossflow drag coefficients used in the procedure are too large under these circumstances.
2. For computing individual fin loads, the equivalent angle of attack concept is generally adequate except for two new vortical effects not included in the method as described in the next two items.
3. As a missile rolls, its fin leading and trailing edges undergo sweep changes. These sweep changes cause changes in the leading-edge and side-edge suction as well as the fractions of these suction converted to vortex lift. This effect, not included in the computer program, can cause significant changes in panel normal force particularly for low-aspect-ratio fins.
4. Increased panel normal force can result under certain conditions as a result of possible favorable vortex interference. This occurred for the left horizontal fin (T2) in the 16° to 29° range for angles of roll between 0° and 30° with low-aspect-ratio fins.
5. In general, normal force and axial location of center of pressure were well predicted by the method for complete configurations.
6. For no control deflections, a cruciform configuration can develop side forces and rolling moments principally as a result of nose, afterbody, or canard vortices. In the range of angle of attack considered here, the side force is typically about 10 percent of the normal force, and the rolling moment corresponds to 2° of roll control on all four fins. The errors in predicting these quantities are of the order of 50 percent. Improving the accuracy of these predictions will depend to a considerable degree on developing a better model for predicting the vortex path over the afterbody and the afterbody vortex strengths and predictions.

In the second year's work we plan to compare the theory with additional diagnostic data, particularly that which will be obtained to angles of attack of about 50° in the Ames Research Center 11-Foot Wind Tunnel under a NASA/Ames Research Center contract. Changes in the computer program to improve its accuracy at high angles of attack are contemplated, and certain of the limitations and shortcomings discussed above will be removed.

REFERENCES

1. Dillenius, M. F. E. and Nielsen, J. N.: Supersonic Lifting-Surface Computer Program for Cruciform Wing-Body Combinations in Combined Pitch and Sideslip. NEAR TR 74, ONR Contract N00014-74-C-0050, Dec. 1974.
2. Dillenius, M. F. E. and Nielsen, J. N.: Prediction of Aerodynamics of Missiles at High Angles of Attack in Supersonic Flow. NEAR TR 99, ONR Contract N00014-74-C-0050, Oct. 1975.
3. Hemsch, M. J., Nielsen, J. N., and Dillenius, M. F. E.: Method for Calculating Induced Rolling Moments for Cruciform Canard Missiles at Angles of Attack up to 20 Deg. NWC TP 5761, NWC Contract N00123-74-C-0829, May 1975.
4. Hemsch, M. J. and Nielsen, J. N.: Test Report for Canard Missile Tests in Ames 6- by 6-Foot Supersonic Wind Tunnel. NEAR TR 72, NWC Contract N00123-74-C-0829, Aug. 1974.
5. Hemsch, M. J.: Reduced Vapor Screen Data from Canard Missile Tests in Ames 6- by 6-Foot Supersonic Wind Tunnel. NEAR TR 81, NWC Contract N00123-74-C-0829, Feb. 1975.
6. Nielsen, J. N., Hemsch, M. J., and Dillenius, M. F. E.: The Induced Rolling Moments of Cruciform Wing-Body Combinations as Influenced by Panel-Panel Interference. NEAR TR 75, NWC Contract N00123-74-C-0829, Nov. 1974.
7. Fidler, J. E. and Bateman, M. C.: Aerodynamic Methodology (Isolated Fins and Bodies). Martin Marietta Corporation OR 12,339, Mar. 1973.
8. Jorgensen, L. H.: Prediction of Static Aerodynamic Characteristics for Space-Shuttle-Like and Other Bodies at Angles of Attack From 0° to 180° . NASA TN D-6996, Jan. 1973.
9. Nielsen, J. N.: Missile Aerodynamics. McGraw-Hill Book Co., New York, 1960.
10. Pitts, W. C., Nielsen, J. N., and Kaattari, G. E.: Lift and Center of Pressure of Wing-Body-Tail Combinations at Subsonic, Transonic, and Supersonic Speeds. NACA Rept. 1307, 1957.
11. Nielsen, J. N., Hemsch, M. J., and Dillenius, M. F. E.: Further Studies of the Induced Rolling Moments of Canard-Cruciform Missiles as Influenced by Canard and Body Vortices. NEAR TR 79, NWC Contract N00123-74-C-0829, Jan. 1975.
12. Mendenhall, M. R. and Nielsen, J. N.: Effect of Symmetrical Vortex Shedding on the Longitudinal Aerodynamic Characteristics of Wing-Body-Tail Combinations. NEAR TR 69, NASA/Ames Research Center Contract NAS2-7347, May 1974.
13. Aiello, G. F.: Aerodynamic Methodology (Bodies with Tails at Arbitrary Roll Angles, Transonic and Supersonic). Martin Marietta Corporation OR 14,145, Apr. 1976.

14. Piper, E. M. and Brown, A. E.: AIM-9L Wind Tunnel Test Report. NWC TN 4063-233, Oct. 1972.
15. Emerson, H. F.: Wind Tunnel Investigation of the Effect of Clipping the Tips of Triangular Wings of Different Thicknesses, Camber, and Aspect Ratio-Transonic Bump Method. NACA TN 3671, June 1956.
16. Spring, D. J.: Wind Tunnel Data for Body-Tail Configurations. Army Missile Command, Huntsville, AL. Private Communication, June 1976.
17. Gomillion, G. R.: A Compilation of Static Stability and Fin Loads Data for Slender Body Missile Models with and without Tail Fins and Wings. Arnold Engineering Development Center, AEDC-TR-75-125 (Vol. I-V). Also, AFATL-TR-76-23, Mar. 1976.
18. Jorgensen, L. H. and Nelson, E. R.: Experimental Aerodynamic Characteristics for a Cylindrical Body of Revolution with Various Noses at Angles of Attack from 0° to 58° and Mach Numbers from 0.6 to 2.0. NASA TM X-3128, Dec. 1974.
19. Chapman, Gary: Private Communication.
20. Fidler, J. E., Schwind, R. G., and Nielsen, J. N.: An Investigation of Slender-Body Wake Vortices. NEAR TR 108, MICOM Contract DAAH01-75-C-0008, Feb. 1976.
21. Patel, M. H. and Hancock, G. J.: Some Experimental Results of the Effect of a Streamwise Vortex on a Two-Dimensional Wing. Aeronautical Journal, vol. 78, 1974, pp. 151-155.
22. Fidler, J. E. and Bateman, M. C.: Aerodynamic Methodology (Bodies with Tails at Arbitrary Roll Angle). Martin Marietta Corporation OR 13,375-1, Dec. 1974.

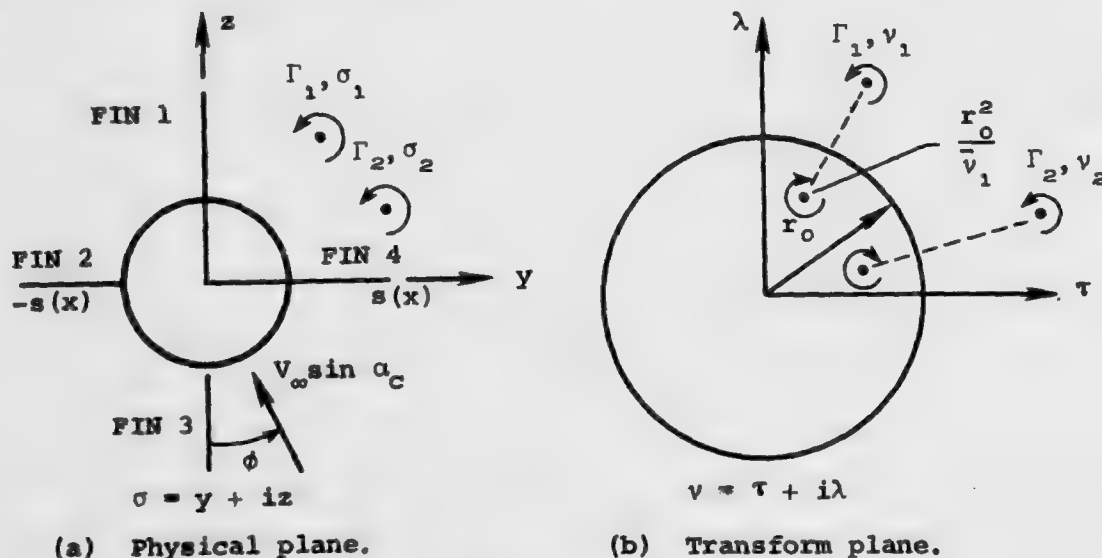
APPENDIX A

PROCEDURE FOR COMPUTATION OF VORTEX
PATHS IN THE PRESENCE OF A CRUCIFORM
WING-BODY COMBINATION

APPENDIX A

PROCEDURE FOR COMPUTATION OF VORTEX PATHS IN THE PRESENCE OF A CRUCIFORM WING-BODY COMBINATION

The determination of the loading on a finned section of a missile due to the presence of a set of vortices requires that the paths of the vortices be known. A procedure for computing those paths has been previously derived (refs. 9, 12, and A.1) and is repeated below. It is based on slender-body theory and assumes that the vortices can be "tracked" in a crossflow plane which is perpendicular to the body axis and which moves downstream at $V_\infty \cos \alpha_c$. The body boundary conditions are properly handled by imaging the external vortices. Since the image system for a cruciform wing-body combination would be quite complex, the actual configuration in the crossflow plane is transformed into a circle as shown in the sketch below. The sketch shows two asymmetrical vortices in the presence of a cruciform wing-body combination at combined pitch and roll.



Sketch A.1 Computational planes for
vortex tracking.

The vortices are assumed to be discrete potential vortices moving as Lagrangian fluid particles. We will derive the equation of motion of Γ_1 with Γ_2 present, and then generalize the results to many vortices.

The fin semispan, s , will be considered to be a function of the distance along the body axis, x . No effects of fin deflection on vortex paths are included.

Consider first the transformation and its derivatives of the cruciform wing-body combination in the σ plane into the circle of radius, r_0 in the v plane.

$$\sigma^2 \left(1 + \frac{a^4}{\sigma^4} \right) = v^2 \left(1 + \frac{r_0^4}{v^4} \right) \quad (\text{A.1})$$

$$r_0^2 = \frac{1}{2} s^2 \left(1 + \frac{a^4}{s^4} \right) \quad (\text{A.2})$$

$$\frac{dv}{d\sigma} = \frac{\sigma}{v} \left(\frac{1 - a^4/\sigma^4}{1 - r_0^4/v^4} \right) \quad (\text{A.3})$$

$$\frac{d^2v}{d\sigma^2} = \frac{dv}{d\sigma} \left[\frac{1}{v} \left(3 - \frac{4}{1 - r_0^4/v^4} \right) \left(\frac{dv}{d\sigma} \right) - \frac{1}{\sigma} \left(3 - \frac{4}{1 - a^4/\sigma^4} \right) \right] \quad (\text{A.4})$$

These expressions are given by Spahr, reference A.1, on page 10.

The complex potential for the flow in the v plane is given by

$$W(v) = -iv_\infty \sin \alpha_c e^{-i\phi} \left(v - \frac{r_0^2 e^{2i\phi}}{v} \right) - \frac{i\Gamma_1}{2\pi} \ln \left(\frac{v - v_1}{v - r_0^2/\bar{v}_1} \right) - \frac{i\Gamma_2}{2\pi} \ln \left(\frac{v - v_2}{v - r_0^2/\bar{v}_2} \right) \quad (\text{A.5})$$

We have assumed that the body is of uniform radius and have put no image vortices at the center of the body. The direction of the flow at infinity is unchanged under the transformation.

The complex potential $W_1[v(\sigma)]$ for the complex velocity $v_1 - iw_1$ of vortex, Γ_1 , in the σ plane is the total complex potential $W(v)$ for the flow including the vortices minus the singularity at vortex, Γ_1 .

$$\begin{aligned}
W_1[v(\sigma)] = & -iv_\infty \sin \alpha_c e^{-i\phi} \left(v - \frac{r_o^2 e^{2i\phi}}{v} \right) - \frac{i\Gamma_1}{2\pi} \ln \left(\frac{1}{v - r_o^2/\bar{v}_1} \right) \\
& - \frac{i\Gamma_2}{2\pi} \ln \left(\frac{v - v_2}{v - r_o^2/\bar{v}_2} \right) + \frac{i\Gamma_1}{2\pi} \ln \left(\frac{\sigma - \sigma_1}{v - v_1} \right)
\end{aligned} \quad (A.6)$$

The complex velocity of vortex, Γ_1 , in the σ plane is given by

$$v_1 - iw_1 = \left. \frac{dw_1}{d\sigma} \right|_{\sigma=\sigma_1} \quad (A.7)$$

In reference 9 it is shown that

$$\lim_{\substack{v \rightarrow v_1 \\ \sigma \rightarrow \sigma_1}} \frac{d}{d\sigma} \ln \left(\frac{\sigma - \sigma_1}{v - v_1} \right) = -\frac{1}{2} \left(\frac{d\sigma}{dv} \right) \left(\frac{d^2 v}{d\sigma^2} \right)_{\sigma=\sigma_1} \quad (A.8)$$

The velocity $v_1 - iw_1$ is thus given by

$$\begin{aligned}
v_1 - iw_1 = & \frac{d}{d\sigma} \left[-iv_\infty \sin \alpha_c e^{-i\phi} \left(v - \frac{r_o^2 e^{2i\phi}}{v} \right) + \frac{i\Gamma_1}{2\pi} \ln \left(v - \frac{r_o^2}{\bar{v}_1} \right) \right. \\
& \left. - \frac{i\Gamma_2}{2\pi} \ln \left(\frac{v - v_2}{v - r_o^2/\bar{v}_2} \right) \right] - \frac{i\Gamma_1}{2\pi} \left(\frac{d\sigma}{dv} \right) \left(\frac{d^2 v}{d\sigma^2} \right)
\end{aligned} \quad (A.9)$$

all evaluated at $\sigma = \sigma_1$. Carrying out the operation yields

$$\begin{aligned}
v_1 - iw_1 = & \left[-iv_\infty \sin \alpha_c e^{-i\phi} \left(1 + \frac{r_o^2 e^{2i\phi}}{v_1^2} \right) + \frac{i\Gamma_1}{2\pi} \left(\frac{1}{v_1 - r_o^2/\bar{v}_1} \right) \right. \\
& \left. - \frac{i\Gamma_2}{2\pi} \left(\frac{1}{v_1 - v_2} - \frac{1}{v_1 - r_o^2/\bar{v}_2} \right) \right] \left(\frac{dv}{d\sigma} \right)_{\sigma=\sigma_1} - \frac{i\Gamma_1}{2\pi} \left(\frac{d\sigma}{dv} \right) \left(\frac{d^2 v}{d\sigma^2} \right)_{\sigma=\sigma_1}
\end{aligned} \quad (A.10)$$

If there are n external vortices, $\Gamma_1, \Gamma_2, \dots, \Gamma_n$, then equation (A.10) will have the form

$$v_1 - iw_1 = \left[-iv_\infty \sin \alpha_c e^{-i\phi} \left(1 + \frac{r_o^2 e^{2i\phi}}{v_1^2} \right) + \frac{i\Gamma_1}{2\pi} \left(\frac{1}{v_1 - r_o^2/\bar{v}_1} \right) \right. \\ \left. - i \sum_{k=1}^n \frac{\Gamma_k}{2\pi} \left(\frac{1}{v_1 - v_k} - \frac{1}{v_1 - r_o^2/\bar{v}_k} \right) \right] \left(\frac{dv}{d\sigma} \right)_{\sigma=\sigma_1} - \frac{i\Gamma_1}{4\pi} \left(\frac{d\sigma}{dv} \right) \left(\frac{d^2 v}{d\sigma^2} \right)_{\sigma=\sigma_1} \quad (\text{A.11})$$

For the j^{th} vortex, we can write

$$v_j - iw_j = \left[-iv_\infty \sin \alpha_c e^{-i\phi} \left(1 + \frac{r_o^2 e^{2i\phi}}{v_j^2} \right) + \frac{i\Gamma_j}{2\pi} \left(\frac{1}{v_j - r_o^2/\bar{v}_j} \right) \right. \\ \left. - i \sum_{\substack{k=1 \\ k \neq j}}^n \frac{\Gamma_k}{2\pi} \left(\frac{1}{v_j - v_k} - \frac{1}{v_j - r_o^2/\bar{v}_k} \right) \right] \left(\frac{dv}{d\sigma} \right)_{\sigma=\sigma_j} - \frac{i\Gamma_j}{2\pi} \left(\frac{d\sigma}{dv} \right) \left(\frac{d^2 v}{d\sigma^2} \right)_{\sigma=\sigma_j} \quad (\text{A.12})$$

In determining the trajectories of vortices passing by a cruciform finned section of a missile, the positions and strengths of the vortices must be given at some initial value of x . Then the appropriate equations of motion for the vortices are

$$\frac{dy_j}{dt} = v_j \quad \text{and} \quad \frac{dz_j}{dt} = w_j \quad (\text{A.13})$$

Since the crossflow plane is moving downstream with the speed, $v_\infty \cos \alpha_c$, we have

$$\frac{dx}{dt} = v_\infty \cos \alpha_c \quad (\text{A.14})$$

Substituting equation (A.14) into (A.13) gives

$$\frac{dy_j}{dx} = \frac{v_j}{v_\infty \cos \alpha_c} \quad \text{and} \quad \frac{dz_j}{dx} = \frac{w_j}{v_\infty \cos \alpha_c} \quad (\text{A.15})$$

The set of differential equations (A.15) together with the initial conditions and the set of algebraic relations (A.12) form a system of ordinary first-order initial value differential equations which can be solved by standard integration routines.

The present method uses small angle approximations throughout. Hence, the quantity $\cos \alpha_c$ in equations (A.15) is set equal to one. When the influence of the fins is to be ignored, the code sets $s(x) = a$.

The following relationships can be used to go back and forth between the σ and v planes:

$$\sigma^2 = \frac{(v^2 + r_o^4/v^2) + \sqrt{(v^2 + r_o^4/v^2)^2 - 4a^4}}{2} \quad (A.16)$$

$$v^2 = \frac{(\sigma^2 + a^4/\sigma^2) + \sqrt{(\sigma^2 + a^4/\sigma^2)^2 - 4r_o^4}}{2} \quad (A.17)$$

The roots are to be chosen such that corresponding points are always in corresponding quadrants.

REFERENCE

- A.1. Spahr, J. R.: Theoretical Prediction of the Effects of Vortex Flows on the Loading, Forces and Moments of Slender Aircraft. NASA TR-R-101, 1961.

APPENDIX B

REVERSE FLOW METHOD FOR COMPUTATION
OF FIN FORCES AND MOMENTS IN
THE PRESENCE OF VORTICES

APPENDIX B

REVERSE FLOW METHOD FOR COMPUTATION OF FIN FORCES AND MOMENTS IN THE PRESENCE OF VORTICES

B.1. INTRODUCTION

The purpose of this appendix is to present the procedure used in the code MLOADS to compute the effects of vortices on the loading experienced by a cruciform wing-body combination. The reverse flow method used herein was originally developed for the calculation of forces and moments on an external store in a nonuniform flow field and was presented in reference B.1. The development below closely follows that of Appendix I of reference B.1.

In the procedure under discussion the body is at zero angle of attack and the fins are undeflected so that only the loading due to vortices will be computed.

B.2. DISCUSSION OF METHOD

Our problem is to determine the fin normal forces and rolling moments due to an external vortex passing a cruciform fin-body combination. The first step is to determine the changes in fin twists due to the vortex. The vortex is assumed to be rectilinear and parallel to the fin, and it induces an angle of attack normal to the i 'th fin, $\alpha_{v,i}(t)$, which can be established by methods which will be discussed. It is possible using a reverse flow theorem to determine the force which is normal to the fin planform and acts on the fin-body combination. We then multiply the fin-body normal force by the ratio, $K_W/(K_W + K_B)$, to obtain an estimate of the normal force acting on the fin. We divide the normal force acting on the fin by the fin-alone normal force for unit angle of attack and obtain an equivalent angle of attack $(\Delta\alpha_{eq})_{v,i}$ on the i 'th fin due to the vortex. This procedure can be carried out using either linear theory or slender-body theory provided the same theory is used throughout. Any bias is minimized since a normal-force ratio is utilized to obtain an equivalent angle of attack.

The next step is to use the nonlinear normal-force curve for the fin alone to determine the fin force associated with $(\Delta\alpha_{eq})_{v,i}$. This fin force depends at what point on the normal-force curve the fin is

operating before account is taken of $(\Delta\alpha_{eq})_{v,i}$. The associated force acting on the body is then obtained by multiplying the fin normal force by the ratio, K_B/K_W . The procedure can be applied to all four fins to obtain the normal-force and side-force components of the fin-body combination.

With respect to rolling moment, it is possible to obtain the rolling moment acting on the wing-body due to the fin twist associated with a vortex using reverse flow theorems. This rolling moment is due in part to direct roll associated with the fin in question and by reverse roll associated with the other fins. If the rolling moment (about the body axis) is divided by the fin-alone normal force calculated by the same theory as the rolling moment, then an effective lever arm for the fin is established. This lever arm includes the effects of reverse roll and is thus closer to the body axis than if reverse roll had been neglected. The nonlinear rolling moment due to the fin can then be calculated by multiplying the nonlinear fin normal force by this lever arm.

The detailed derivations of the equations based on this method are now given.

B.3. BOUNDARY CONDITIONS INDUCED ON FINS BY VORTICES

The procedure for calculating the distribution of induced angle of attack normal to the fins is as follows:

1. Specify the spanwise fin coordinates at which the induced angle of attack is to be calculated.
2. Calculate the velocities induced at those coordinates by the Biot-Savart law for all the vortices present.
3. From the velocities computed for each point, determine the component normal to the fin.
4. Depending upon the option of the user, limit the velocity which may be induced on the fin.

The code gives the user a number of options concerning the induced angle of attack. The options are: (1) impose no limit on the angle of attack which may be induced on the fin; (2) assume that each vortex has a viscous core; or (3) limit the maximum velocity which may be induced on

a fin to a specified fraction of V_∞ . If either option (1) or (2) is selected, $\alpha_{v,i}$ is set equal to the arc tangent of the ratio of the induced velocity to V_∞ . If option (3) is selected, $\alpha_{v,i}$ is set equal to the ratio of the induced velocity to V_∞ or V_{\max}/V_∞ , whichever is smaller.

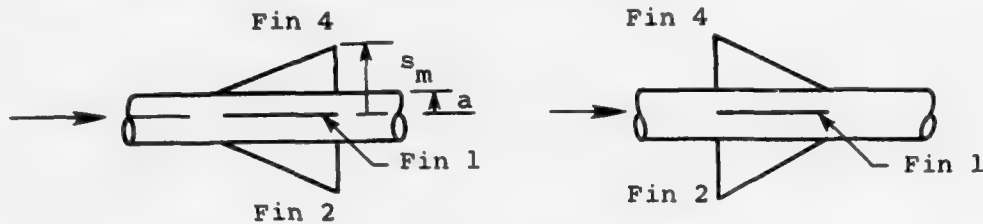
B.4. DETERMINATION OF LOADING ACTING ON FINNED SECTION

Since it is based on integral theorems, the reverse flow method cannot give the loading on individual fins. Rather, it gives the overall loading on the finned section due to the flow field seen by each fin. This is sufficient for small angles of attack for which the fin loading characteristics are linear. However, when the fin loading characteristics are nonlinear, an extension to the reverse flow method is required. The extension used in the present method is based on the equivalent angle of attack concept. The procedure we will use is as follows:

1. Compute the normal force or side force acting on the fin-body configuration due to the fin twist associated with the vortices using a combination of reverse flow theory and slender-body theory.
2. Estimate the fraction of the normal force or side force acting on the fin by multiplying the quantity calculated in (1) by the ratio, $K_W/(K_W + K_B)$.
3. Divide the fin force of (2) by the slope of the slender-body theory fin-alone normal-force curve to obtain an equivalent angle of attack, $(\Delta\alpha_{eq})_v$. Using this quantity with the fin-alone nonlinear normal-force curve will give the nonlinear fin normal force in the presence of the body.
4. Using the same theory as in (2) above, calculate the total rolling moment acting on the finned section due to the fin twist associated with the vortex.
5. Divide the result of (4) by the result of (2) to get a moment arm for the force due to $(\Delta\alpha_{eq})_v$.

B.4.1 Computation of Equivalent Angle of Attack for Each Fin

Consider now a cruciform finned section with a circular body in direct flow and in reverse flow as shown. We will consider the force normal to the plane of fins 2 and 4 first and generalize the results to an arbitrary fin. The fins are undeflected.



Sketch B.1. Direct and reverse flow.

Let S_B be the body planform area and let S_1 , S_2 , S_3 , and S_4 be the planform areas for the fins. Let P_d and α_d be the fin loading coefficient and the local angle of attack in direct flow, and let P_r and α_r be the corresponding quantities in reverse flow. Then, the reverse flow theorem (ref. 9, p. 221) gives

$$\iint_{\substack{S_B + S_1 + S_2 \\ + S_3, S_4}} P_r \alpha_d dS = \iint_{\substack{S_B + S_1 + S_2 \\ + S_3 + S_4}} P_d \alpha_r dS \quad (B.1)$$

Choose the following specific values of angles of attack and pressure coefficients

<u>Direct</u>	<u>Reverse</u>
$\alpha_d = 0$ on S_B, S_1, S_3	$\alpha_r = 1$ on S_B
$\alpha_d = \alpha_{v,i}$ on S_2, S_4	$\alpha_r = 1$ on S_2, S_4
$P_d = P_d$	$\alpha_r = 0$ on S_1, S_3
	$P_r = P_3$

Then, (B.1) becomes

$$\iint_{\substack{S_B + S_1 + S_2 \\ + S_3 + S_4}} P_d dS = \iint_{S_2} \alpha_{V,2} P_3 dS + \iint_{S_4} \alpha_{V,4} P_3 dS \quad (B.2)$$

where P_3 is the loading for a wing-body combination at unit angle of attack and no yaw or pitch control. The force normal to the plane of fins 2 and 4 acting on the finned section is

$$N = q_\infty \iint_{S_B + S_2 + S_4} P_d dS \quad (B.3)$$

Substituting (B.2) into (B.3) gives

$$N = q_\infty \int_a^m \int_{l.e.}^{t.e.} \alpha_{V,2}(x,t) P_3 dx dt + q_\infty \int_a^m \int_{l.e.}^{t.e.} \alpha_{V,4}(x,t) P_3 dx dt \quad (B.4)$$

where the dummy variable t refers to integration along the span of the fins. Let the span-load distribution associated with P_3 be $(cc_\ell)_3$ such that

$$(cc_\ell)_3 = \int_{l.e.}^{t.e.} P_3 dx \quad (B.5)$$

Now we assume that $\alpha_{V,i}$ varies slowly in the chordwise x -direction so that substitution of (B.5) into (B.4) gives

$$N = q_\infty \int_a^m \bar{\alpha}_{V,2} (cc_\ell)_3 dt + q_\infty \int_a^m \bar{\alpha}_{V,4} (cc_\ell)_3 dt \quad (B.6)$$

The normal forces acting on S_2 and S_4 are not given by this result since part of the load due to each integral can appear on the body and the opposing fin. Here $(cc_\ell)_3$ is the span loading on the fins for the configuration in reverse flow with both body and panels at unit angle of attack with no yaw or pitch control. From reference 9, equation (5-15), we have the slender-body theory expression for the span loading:

$$(cc_\ell)_3 = 4 \left[\left(s_m + \frac{a^2}{s_m} \right)^2 - \left(y + \frac{a^2}{y} \right)^2 \right]^{1/2} \quad (B.7)$$

In order to obtain the normal force on each individual fin and thereby carry out item 2 of the procedure described above, we multiply equation (B.6) by $K_W/(K_W + K_B)$ and consider each term to be the force acting on the fin over which the integration is taking place. We can follow the same procedure for fins 1 and 3 with the following result for fin i:

$$N_{fin\ i} = \frac{q_\infty K_W}{K_W + K_B} \int_a^{s_m} \bar{\alpha}_{v,i}(t) (cc_\ell)_3 dt \quad (B.8)$$

The slender-body normal-force slope for the fin is $\pi q_\infty (s_m - a)^2$. Hence, carrying out item 3 of the procedure described at the beginning of this section, we find

$$\begin{aligned} (\Delta \alpha_{eq})_v &= \frac{F_{fin\ i}}{\pi q_\infty (s_m - a)^2} \\ &= \frac{K_W}{\pi (K_W + K_B) (s_m - a)^2} \int_a^{s_m} \bar{\alpha}_{v,i}(t) (cc_\ell)_3 dt \end{aligned} \quad (B.9)$$

Without the vortex present, the i'th fin operates at $(\alpha_{eq,p})_i$. The difference in normal force at $[\alpha_{eq,p} + \Delta(\alpha_{eq})_v]_i$ and at $(\alpha_{eq,p})_i$ in the fin-alone nonlinear normal-force curve is the nonlinear normal force on the fin associated with the vortex. It must be multiplied by (K_B/K_W) to obtain the nonlinear contribution due to body carryover.

B.4.2 Computation of the Moment Arm for the Rolling Moment Associated with Each Fin due to the Vortex

The reverse-flow theorem for all the fins with the body aligned in the free-stream direction (i.e., $\alpha = 0$ on body) is

$$\int_{S_1+S_2+S_3+S_4} \int \alpha_d P_r dS = \int_{S_1+S_2+S_3+S_4} \int \alpha_r P_d dS \quad (B.10)$$

Choose the direct and reverse flow conditions as follows:

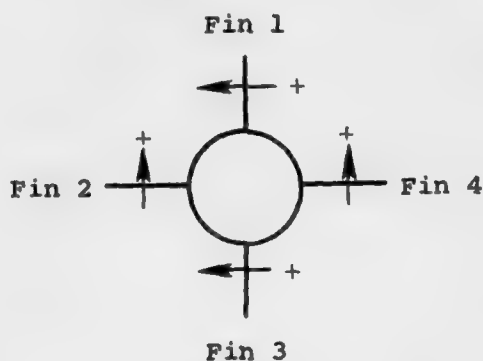
$$\alpha_d = \alpha_{v,i}(x,t) \quad \alpha_r = \omega t / V_\infty$$

$$P_d = P_d \quad P_r = P_e$$

where t is the spanwise coordinate for each fin measured from the body axis. Note that α_r corresponds to the distribution of angle of attack which would be seen by a configuration rolling at the rate of ω radians per second clockwise. Then, (B.10) becomes

$$\begin{aligned} \frac{\omega}{V_\infty} \iint_{\substack{S_1+S_2 \\ +S_3+S_4}} t P_d dS = & - \iint_{S_1} \alpha_{v,1}(x,t) P_e dS + \iint_{S_2} \alpha_{v,2}(x,t) P_e dS \\ & + \iint_{S_3} \alpha_{v,3}(x,t) P_e dS - \iint_{S_4} \alpha_{v,4}(x,t) P_e dS \quad (B.11) \end{aligned}$$

where $\alpha_{v,i}$ has the sign convention shown in the sketch below.



Sketch B.2. Sign convention for $\alpha_{v,i}$.

The total rolling moment for the finned section is:

$$M_\ell = \alpha_\infty \iint_{\substack{S_1+S_2 \\ +S_3+S_4}} t P_d dS \quad (B.12)$$

Substituting (B.11) into (B.12) gives

$$M_l = \frac{q_\infty V_\infty}{\omega} \left[- \int_a^m \int_{l.e.}^{t.e.} \alpha_{v,1}(x,t) P_e dx dt + \int_a^m \int_{l.e.}^{t.e.} \alpha_{v,2}(x,t) P_e dx dt \right. \\ \left. + \int_a^m \int_{l.e.}^{t.e.} \alpha_{v,3}(x,t) P_e dx dt - \int_a^m \int_{l.e.}^{t.e.} \alpha_{v,4}(x,t) P_e dx dt \right] \quad (B.13)$$

Let the span loading for the reverse flow case above be

$$(cc_l)_e = \frac{V_\infty}{\omega} \int_{l.e.}^{t.e.} P_e dx \quad (B.14)$$

Recall our original assumption that $\alpha_{v,i}$ is constant in the chordwise direction, and substitute (B.14) into (B.13). The result is

$$M_l = q_\infty \left[- \int_a^m \bar{\alpha}_{v,1}(t) (cc_l)_e dt + \int_a^m \bar{\alpha}_{v,2}(t) (cc_l)_e dt \right. \\ \left. + \int_a^m \bar{\alpha}_{v,3}(t) (cc_l)_e dt - \int_a^m \bar{\alpha}_{v,4}(t) (cc_l)_e dt \right] \quad (B.15)$$

The integrals in equation (B.15) do not represent the actual rolling moments exerted on the individual fins. Rather, they represent the contribution to the total rolling moment due to the distribution of angle of attack induced on each fin. To determine the actual rolling moment for each fin, we must determine the effect of each fin on every other fin. Let us define the following quantities.

$$M_{l_{fin i}} \equiv \text{rolling moment induced on fin } i \quad (B.16)$$

$$I_i \equiv \mu q_\infty \int_a^m \bar{\alpha}_{v,i}(t) (cc_l)_e dt \quad (B.17)$$

$$\mu \equiv \begin{cases} -1, & i = 1 \\ +1, & i = 2 \\ +1, & i = 3 \\ -1, & i = 4 \end{cases} \quad (\text{B.18})$$

$$k_{ij} \equiv \text{fraction of } I_j \text{ contributing to rolling moment of fin } i \quad (\text{B.19})$$

Using the above definitions, we can write

$$\begin{bmatrix} M_{l,1} \\ M_{l,2} \\ M_{l,3} \\ M_{l,4} \end{bmatrix} = \begin{bmatrix} k_{11} & k_{12} & k_{13} & k_{14} \\ k_{21} & k_{22} & k_{23} & k_{24} \\ k_{31} & k_{32} & k_{33} & k_{34} \\ k_{41} & k_{42} & k_{43} & k_{44} \end{bmatrix} \begin{bmatrix} I_1 \\ I_2 \\ I_3 \\ I_4 \end{bmatrix} \quad (\text{B.20})$$

Note that

$$k_{1i} + k_{2i} + k_{3i} + k_{4i} = 1$$

so that equation (B.15) is recovered.

In principle, the k_{ij} can be computed by slender-body theory or by linear theory computer codes such as CRFWBD (Appendix F). However, for $i \neq j$, the coefficients are generally considerably less than one although not negligible. However, we neglect them in the present approximate method for calculating the individual fin rolling moments and assume that

$$k_{ij} = \begin{cases} 1, & i = j \\ 0, & i \neq j \end{cases} \quad (\text{B.21})$$

Substituting the approximation of (B.21) into (B.20) gives the following rolling moment for each fin:

$$M_{l, \text{fin } i} = \mu q_{\infty} \int_a^m \alpha_{v,i}(t) (cc)_l s dt \quad (\text{B.22})$$

The slender-body theory expression for $(cc_\ell)_e$ is given by Adams and Dugan (ref. B.2, eq. (18)):

$$(cc_\ell)_e = \frac{8R^2}{\pi} \left[\cos 2\theta \tanh^{-1} \left(\frac{\sin 2\theta}{\sin 2\gamma} \right) - \cos 2\gamma \tanh^{-1} \left(\frac{\tan 2\theta}{\tan 2\gamma} \right) \right] + \frac{4R^2}{\pi} [K(k_1) \sin 4\theta - 2k_1 \cos A_1 K(k_1) Z(A_1, k_1)] \quad (B.23)$$

where

$$R = \frac{1}{2} \sqrt{s_m^2 + \frac{a^4}{s_m^2}} \quad (B.24)$$

$$\cos 2\theta = \frac{1}{4R^2} \left(t^2 + \frac{a^4}{t^2} \right) = \frac{s^2}{t^2} \left(\frac{a^4}{a^4 + s_m^4} \right) \quad (B.25)$$

$$\cos 2\gamma = \frac{a^2}{2R^2} \quad (B.26)$$

$$k_1 = \sin 2\gamma \quad (B.27)$$

$$K(k_1) = \int_0^{\pi/2} \frac{d\bar{z}}{1 - k_1^2 \sin^2 \bar{z}} = \text{complete elliptic integral of first kind with modulus } k_1 \quad (B.28)$$

$$A_1 = \sin^{-1} \left(\frac{\sin 2\theta}{\sin 2\gamma} \right) \quad (B.29)$$

$$Z(A_1, k_1) = \text{Jacobi zeta function} \quad (B.30)$$

$$K(k_1) Z(A_1, k_1) = K(k_1) E(A_1, k_1) - E(\pi/2, k_1) F(A_1, k_1) \quad (B.31)$$

$$F(A_1, k_1) = \int_0^{A_1} \frac{d\bar{z}}{\sqrt{1 - k_1^2 \sin^2 \bar{z}}} = \text{incomplete elliptic integral of the first kind} \quad (B.32)$$

$$E(\pi/2, k_1) = \int_0^{\pi/2} \sqrt{1 - k_1^2 \sin^2 \bar{z}} \, d\bar{z} = \begin{array}{l} \text{complete elliptic integral} \\ \text{of second kind} \end{array} \quad (\text{B.33})$$

$$E(A_1, k_1) = \int_0^{A_1} \sqrt{1 - k_1^2 \sin^2 \bar{z}} \, d\bar{z} = \begin{array}{l} \text{incomplete elliptic integral} \\ \text{of second kind} \end{array} \quad (\text{B.34})$$

In equation (B.23) as $\theta \rightarrow \gamma$; that is, as $t \rightarrow a$, the first of the two principal terms becomes indeterminate. It is possible to show that

$$\begin{aligned} \lim_{\theta \rightarrow \gamma} \left[\cos 2\theta \tanh^{-1} \left(\frac{\sin 2\theta}{\sin 2\gamma} \right) - \cos 2\gamma \tanh^{-1} \left(\frac{\tan 2\theta}{\tan 2\gamma} \right) \right] \\ = -\cos 2\gamma \log(\cos 2\gamma) \end{aligned} \quad (\text{B.35})$$

Thus, the span loading at the juncture between the fin and body, $t = a$, is

$$(cc_\ell)_e = \frac{8R^2}{\pi} \left[-\cos 2\gamma \log(\cos 2\gamma) + 0.5 K(k_1) \sin 4\theta \right] \quad (\text{B.36})$$

To obtain the moment arm for the fin load represented by $(\Delta\alpha_{eq})_v$, we divide $M_{\ell_{fin i}}$ by $N_{fin i}$; that is,

$$\bar{y}_{v_i} = \frac{M_{\ell_{fin i}}}{N_{fin i}} \quad (\text{B.37})$$

The total rolling moment is then obtained by multiplying \bar{y}_{v_i} by each corresponding fin nonlinear normal force as obtained in item 3 of the procedure described above.

REFERENCES

- B.1. Goodwin, F. K., Dillenius, M. F. E., and Nielsen, J. N.: Prediction of Six-Degree-of-Freedom Store Separation Trajectories at Speeds up to the Critical Speed. Volume I - Theoretical Methods and Comparisons with Experiment. Nielsen Engineering & Research, Inc., AFFDL-TR-72-83, Vol. I, Oct. 1974.
- B.2. Adams, G. J. and Dugan, D. W.: Theoretical Damping in Roll and Rolling Moment Due to Differential Wing Incidence for Slender Cruciform Wings and Wing-Body Combinations. NACA Rept. 1088, 1952.

APPENDIX C

PROCEDURE FOR COMPUTING STRENGTHS AND
POSITIONS OF FIN TRAILING VORTICES

APPENDIX C

PROCEDURE FOR COMPUTING STRENGTHS AND POSITIONS OF FIN TRAILING VORTICES

In setting up a model of a single vortex per fin we must specify the vortex strengths and the lateral position of the center of vorticity. Using the equivalent angle of attack concept, we can obtain a good estimation of the fin normal force and lateral center of pressure position. The single-vortex-per-panel model is compatible with this input data. To go to more vortices per fin requires knowledge of the span-load distribution.

At low angles of attack, the span-load distribution of slender wings tends to be elliptical. At high angles of attack, the wing loading tends to be uniform, and for a delta wing the span loading tends to be linear. As an approximation to actual span loadings consider a superposition of an elliptical loading plus a linear loading. We will now derive expressions for the normal force and rolling moment associated with elliptic and linear span loadings.

$$(cc_\ell)_L = a_L(1 - \eta) ; \eta = \frac{y - a}{s_m - a} \quad (C.1)$$

$$(cc_\ell)_e = a_e \sqrt{1 - \eta^2} \quad (C.2)$$

By definition,

$$CN = \frac{\int_a^{s_m} (cc_\ell) dy}{S_R} \quad (C.3)$$

$$CRM = \frac{\int_a^{s_m} y(cc_\ell) dy}{S_R \ell_r} \quad (C.4)$$

Now the first integral can be written as

$$\begin{aligned} \int_a^{s_m} (cc_\ell) dy &= (s_m - a) \int_0^1 (cc_\ell) d\eta \\ &= (s_m - a) \left[a_L \int_0^1 (1 - \eta) d\eta + a_e \int_0^1 \sqrt{1 - \eta^2} d\eta \right] \end{aligned} \quad (C.5)$$

$$\int_a^{s_m} (cc_\ell) dy = (s_m - a) \left[\frac{a_L}{2} + a_e \left(\frac{\pi}{4} \right) \right] \quad (C.6)$$

Thus

$$CN = \frac{s_m - a}{s_R} \left[\frac{a_L}{2} + a_e \left(\frac{\pi}{4} \right) \right] \quad (C.7)$$

For the rolling moment, we obtain

$$\begin{aligned} CRM &= \frac{a \int_a^{s_m} (cc_\ell) dy + (s_m - a) \int_a^{s_m} \eta (cc_\ell) dy}{s_R \ell_r} \\ &= \frac{a(s_m - a)}{s_R \ell_r} \left(\frac{a_L}{2} + \frac{\pi}{4} a_e \right) \\ &\quad + \frac{(s_m - a)^2}{s_R \ell_r} \left[a_L \int_0^1 \eta (1 - \eta) d\eta + a_L \int_0^1 \eta \sqrt{1 - \eta^2} d\eta \right] \\ &= \frac{a(s_m - a)}{s_R \ell_r} \left(\frac{a_L}{2} + \frac{\pi}{4} a_e \right) + \frac{(s_m - a)^2}{s_R \ell_r} \left(\frac{a_L}{6} + \frac{a_e}{3} \right) \end{aligned} \quad (C.8)$$

The lateral location of the center of pressure is simply given by

$$\bar{y} = \frac{\ell_r CRM}{CN} = a + (s_m - a) \frac{\left(\frac{a_L}{6} + \frac{a_e}{3} \right)}{\left(\frac{a_L}{2} + \frac{\pi}{4} a_e \right)} \quad (C.9)$$

or in nondimensional form

$$\bar{\eta} = \frac{\bar{y} - a}{s_m - a} = \frac{\left(\frac{a_L}{6} + \frac{a_e}{3}\right)}{\left(\frac{a_L}{2} + \frac{\pi}{4} a_e\right)} \quad (C.10)$$

Solving for a_e/a_L , we find

$$\frac{a_e}{a_L} = \frac{\frac{1}{2} \bar{\eta} - \frac{1}{6}}{\frac{1}{3} - \frac{\pi}{4} \bar{\eta}} \quad (C.11)$$

This gives the ratio a_e/a_L in terms of the lateral location of the center of pressure. The fin normal-force coefficient, C_N , then permits us to obtain a_L from equation (C.7) as follows:

$$a_L = \frac{S_R C_N}{(s_m - a) \left(\frac{1}{2} + \frac{\pi}{4} \frac{a_e}{a_L} \right)} \quad (C.12)$$

Having a_e and a_L corresponding to the data, we now must find the vortex strength, Γ , and its lateral position, y_v^* . The lateral position, y_v^* , is at the centroid of the trailing vorticity given by the following expression (see ref. 9, pp. 144-153):

$$y_v^* = a + \frac{\int_a^{s_m} y \frac{d(cc)_l}{dy} dy}{\int_a^{s_m} \frac{d(cc)_l}{dy} dy} \quad (C.13)$$

Carrying out the indicated operations yields

$$\frac{y_v^* - a}{s_m - a} = \frac{\frac{a_L}{2} + \frac{\pi}{4} a_e}{a_L + a_e} \quad (C.14)$$

Assuming that the part of the bound vortex outside the body represents the fin normal force, we can write

$$\rho_\infty V_\infty \Gamma (y_v^* - a) = \frac{1}{2} \rho_\infty V_\infty^2 S_R C_N \quad (C.15)$$

Substituting (C.7) into (C.15), we obtain

$$\frac{\Gamma}{V_{\infty}} = \frac{1}{2} \frac{s_m - a}{y_v^* - a} \left(\frac{a_L}{2} + \frac{\pi}{4} a_e \right) \quad (C.16)$$

Substituting (C.14) into (C.16) gives

$$\Gamma' \equiv \frac{\Gamma}{2\pi V_{\infty} a} = \frac{1}{4\pi a} (a_L + a_e) \quad (C.17)$$

Equations (C.14) and (C.17) give the desired vortex strength and position.

APPENDIX D

METHOD FOR COMPUTING VORTEX POSITIONS
AND STRENGTHS OVER AFTERBODY SECTION

APPENDIX D

METHOD FOR COMPUTING VORTEX POSITIONS AND STRENGTHS OVER AFTERBODY SECTION

D.1. INTRODUCTION

The purpose of this appendix is to describe the method used by the code MLOADS to track vortices downstream of the first finned section. The method consists of three procedures: (1) determination of the starting positions of the afterbody vortices; (2) tracking of all the vortices present over the afterbody section; and (3) determination of the strengths of the two afterbody vortices as functions of axial location. The code MLOADS uses the method described in reference 3 for procedure (1) with one exception. In the method of reference 3, afterbody vortices are not started unless the direction of the crossflow velocity vector is within 90° of the vertical axis, z_0 . In the present version of the code, the user selects an angle OMEGA. If the crossflow velocity vector is not within $\pm\text{OMEGA}$ of z_0 , afterbody vortices are not allowed to form. Procedures (2) and (3) are described in the sections below.

D.2. TRACKING OF VORTICES OVER THE AFTERBODY SECTION

We assume that the vortex centers move as Lagrangian fluid points in a crossflow plane moving with the speed $V_\infty \cos \alpha_c$. The complex velocity for vortex j in the presence of a circular body and the other vortices may be obtained from equation (A.10) by setting $dv/d\sigma \equiv 1$ and $r_0 = a$. The result is

$$v_j - iw_j = -iV_\infty \sin \alpha_c \left(1 + \frac{a^2}{\sigma_j^2}\right) - \frac{i}{2\pi} \sum_{\substack{k=1 \\ k \neq j}}^n \Gamma_k \left(\frac{1}{\sigma_j - \sigma_k} - \frac{1}{\sigma_j - a^2/\bar{\sigma}_k} \right) + \frac{i}{2\pi} \frac{\Gamma_j}{\sigma_j - a^2/\bar{\sigma}_j} \quad (\text{D.1})$$

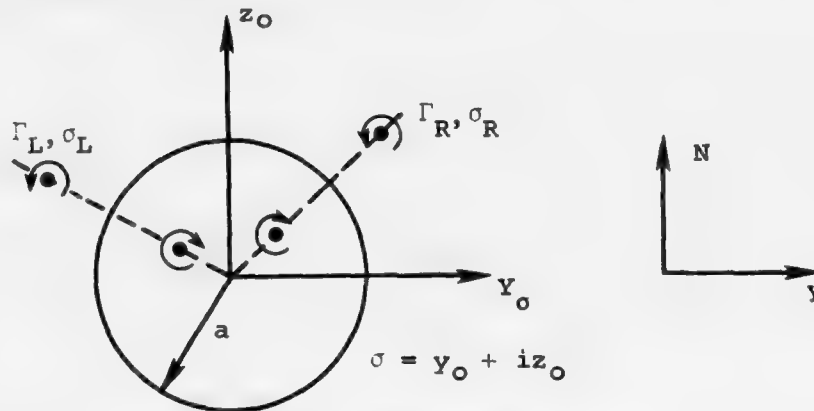
where n is the number of vortices present. We may now repeat the development following equation (A.12) to get

$$\frac{dy_j}{dx} = \frac{v_j}{V_\infty} \frac{1}{\cos \alpha_c} \quad \text{and} \quad \frac{dz_j}{dx} = \frac{w_j}{V_\infty} \frac{1}{\cos \alpha_c} \quad (\text{D.2})$$

Again, the present version of the code uses small angle approximations and $\cos \alpha_c$ in (D.2) is set equal to one. The differential equations (D.2) and the algebraic relations (D.1) provide a system of ordinary first-order initial value differential equations which can be solved by standard integration routines. The system is complete if no afterbody vortices are present. If afterbody vortices are present, two of the Γ_k are unknown functions of x . Differential equations for the afterbody vortex strengths are derived in the next section.

D.3. DERIVATION OF DIFFERENTIAL EQUATIONS FOR THE STRENGTHS OF THE AFTERBODY VORTICES

Consider a crossflow plane, shown in sketch D.1, containing the afterbody cross section, and let afterbody vortices Γ_L and Γ_R appear at stations σ_L and σ_R in the crossflow plane. The other vortices are not shown for simplicity.



Sketch D.1. Computational plane.

In a small axial distance, dx , the afterbody increments in normal force and side force are given by the vortex impulse theorem (eq. (28)).

$$dN - i dY = \rho_\infty V_\infty d \left[\Gamma_L \left(\sigma_L - \frac{a^2}{\bar{\sigma}_L} \right) + \Gamma_R \left(\sigma_R - \frac{a^2}{\bar{\sigma}_R} \right) \right] \quad (\text{D.3})$$

If Γ_L and Γ_R are constant, then the resulting terms on the right-hand side of equation (D.2) are differentials of vortex position and are associated with inviscid forces on the afterbody. If Γ_L and Γ_R are not constant because of vortex feeding sheets, then additional terms containing differentials of Γ_L and Γ_R appear which are associated with crossflow drag. If we use the subscript v to indicate that part of $dN - i dY$ due to viscous crossflow, then

$$dN_v - i dY_v = \rho_\infty V_\infty \left[\left(\sigma_L - \frac{a^2}{\bar{\sigma}_L} \right) d\Gamma_L + \left(\sigma_R - \frac{a^2}{\bar{\sigma}_R} \right) d\Gamma_R \right] \quad (D.4)$$

Now we will assume that the crossflow drag is in the same direction as the crossflow velocity vector, θ . Then,

$$dN_v - i dY_v = D_v (\sin \theta - i \cos \theta) \quad (D.5)$$

where D_v is the crossflow drag force on the elemental length of cylinder, Δx . In terms of the crossflow drag coefficient, D_v is

$$D_v = c_{d_c} q_\infty \sin^2 \alpha_{cr} 2a dx \quad (D.6)$$

Substitution of (D.5) and (D.6) into (D.4) gives

$$\rho_\infty V_\infty \left[\left(\sigma_L - \frac{a^2}{\bar{\sigma}_L} \right) \frac{d\Gamma_L}{dx} + \left(\sigma_R - \frac{a^2}{\bar{\sigma}_R} \right) \frac{d\Gamma_R}{dx} \right] = 2a c_{d_c} q_\infty \sin^2 \alpha_{cr} (\sin \theta - i \cos \theta) \quad (D.7)$$

Equation (D.7) gives two scalar first-order initial value ordinary differential equations which can be solved simultaneously with equation (D.2).

APPENDIX E

MLOADS, A COMPUTER PROGRAM FOR CALCULATING
THE COMPONENT FORCES AND MOMENTS OF
ARBITRARILY BANKED CRUCIFORM MISSILES
WITH CONTROL DEFLECTIONS

APPENDIX E

MLOADS, A COMPUTER PROGRAM FOR CALCULATING THE COMPONENT FORCES AND MOMENTS OF ARBITRARILY BANKED CRUCIFORM MISSILES WITH CONTROL DEFLECTIONS

E.1. INTRODUCTION

The purpose of this appendix is to describe the operation of the computer code MLOADS in sufficient detail to permit understanding and use of the program. The program computes forces and moments for each fin, for each section of the configuration, and for the complete configuration. Minimum drag is not computed. Intermediate output gives vortex strengths and positions along the body. The code, through the integer control variable, NFIN, is capable of handling the following missile configurations:

NFIN = 1: body-alone consisting of nose and cylindrical afterbody

NFIN = 2: body-tail combination (finner)

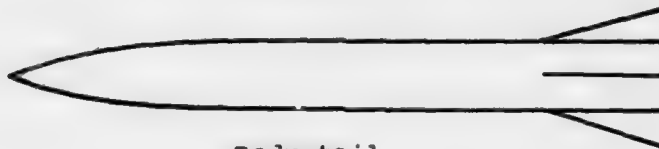
NFIN = 3: body-canard combination (body-wing)

NFIN = 4: body-canard-tail combination (body-wing-tail)

Typical examples of the above configurations are given in the sketch below.



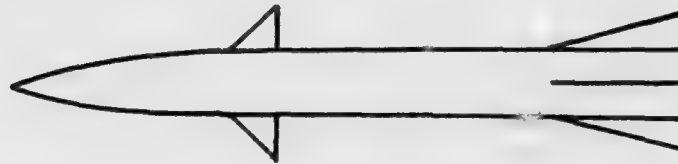
Body-alone



Body-tail



Body-canard



Body-canard-tail

Sketch E.1. Examples of missile configurations.

A description of the engineering method used is given in reference 3 and in the main text and Appendices A through D of this report.

The program is written in FORTRAN IV (029 punch) and has been run on the CDC 6600 and 7600 machines. No files other than INPUT and OUTPUT are required. The program conforms to the ANSI standard Fortran language except for the program definition statement and for several DATA statements. For a body-tail combination, the running time is roughly 0.08 CPU second per data point on the CDC 7600. For a body-canard-tail combination, the running time is about 0.5 CPU second per data point on the CDC 7600. Run times on the CDC 6600 are about six times those for the CDC 7600.

E.2. PROGRAM DESCRIPTION

For computational purposes, the missile to be studied is divided into four sections as shown in figure 1 of the main text. The nose section is defined to be from the nose tip to the leading edge of the root chord of the first finned section. The canard section (first finned section) is defined to be from the end of the nose section to the trailing edge of the first set of fins. The afterbody section is defined to be from the end of the canard section to the leading edge of the root chord of the second finned section. The tail section (second finned section) is defined to be from the end of the afterbody section to the trailing edge of the second set of fins. The computations proceed as shown in figure E.1. The branching for the four possible configurations is shown in figure E.2. The main program MLOADS controls the flow of operations. It calls the routines which control the operations for each section of the missile. A more complete description of the program operation is given below.

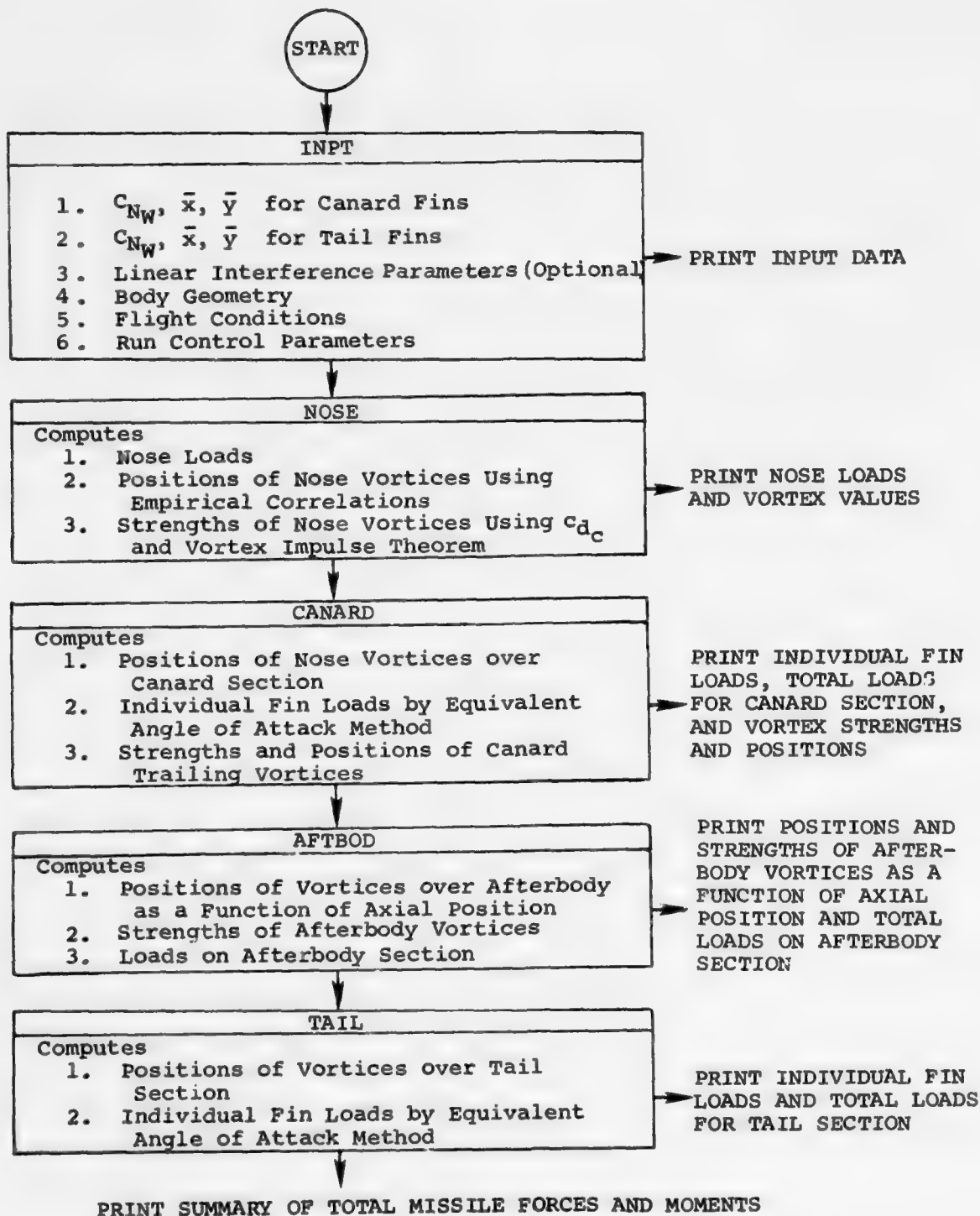


Figure E.1. Flow of program computations.

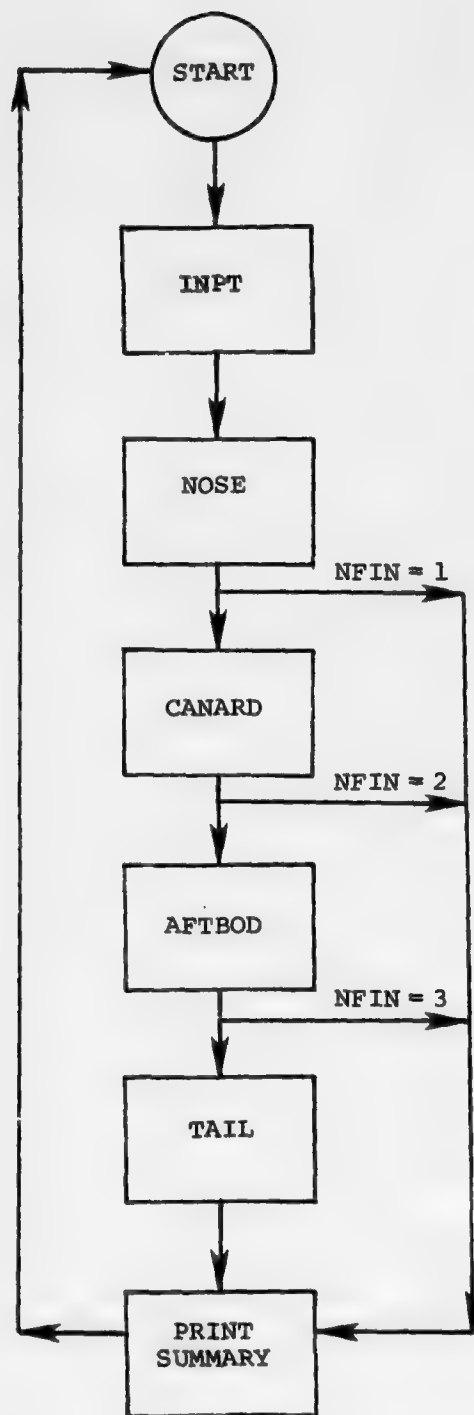


Figure E.2. Schematic description of control of MLOADS operations by NFIN.

E.2.1 Calculation Procedure

After reading in the run identification information, the subprogram INPT reads in body geometry, run control parameters, flow conditions, and any required empirical information not built into the program. All length quantities are then normalized by the body radius and all areas are normalized by the square of the body radius. The user has the option of allowing the code to compute the necessary interference parameters or of reading them in. If the user selects the former option, the methods of slender-body theory and reference 10 are employed. The user may read in any or all of the interference parameters.

The user must read in the wing-alone characteristics for each set of fins. These characteristics include the normal-force coefficient, spanwise location of the fin center of pressure and chordwise location of the fin center of pressure as functions of angle of attack.

After all the input has been read in and all required interference factors have been computed, the main program MLOADS calls subroutine NOSE. This routine first computes the axial starting location of the nose vortices (if present). The locations and strengths of the nose vortices in the crossflow plane at the leading edge of the root chord of the first finned (canard) section are computed next. The subroutine then computes the forces and moments on the nose and returns control to MLOADS.

If $NFIN = 1$, the driver program prints a summary of the overall forces and moments and reads in a new data set. If $NFIN \geq 2$, subroutine CANARD is called. This routine computes the fin and body loadings for the first set of fins downstream of the nose.* The individual fin forces and moments in the absence of nose vortices are computed first. The routine then calls the routine CRUTRJ which computes the positions of the nose vortices over the canard section. The discrete vortex model used to represent the nose vorticity may not adequately represent the flow when the separated flow from the nose is diffuse or when a vortex is close to a fin. With the present model, it is possible for a vortex to be captured by its image and to travel completely around the body. Such behavior has not been observed in flow visualization studies and the predicted loads obtained when a vortex is "captured" do not agree

*Note that if the configuration is a body-tail combination, the tail section results are computed by subroutine CANARD and are output under the headings for "CANARD SECTION."

with experiment. We have found that the present model gives best results when the presence of the fins is ignored during the vortex tracking procedure. The user can exercise this option by setting the logical variable NEARC equal to .TRUE. This option is recommended. The user may also choose to ignore the nose vortices over all or part of the missile if he believes they have dispersed. This control is achieved through the parameter NVORT.

When CRUTRJ has finished tracking the nose vortices, it stores their locations in the crossflow planes at the fin area centroid and at the fin trailing edge and returns control to CANARD. Subroutine CANARD then calls REVFLO which computes the equivalent angle of attack and spanwise location of the center of pressure for the loading due to the nose vortices. Subroutine REVFLO assumes the vortices to be infinite line vortices parallel to the body axis. The vortex locations at the fin area centroid are used.

When REVFLO returns control to CANARD, the total fin forces and moments and body forces and moments (for the canard section) are computed. The strengths and positions of the vortices shed from each fin are calculated next. After the above information has been printed out, control is returned to MLOADS.

If NFIN = 2, the driver program prints a summary of the overall forces and moments and reads in a new data set. If $NFIN \geq 3$, subroutine AFTBOD is called. This routine tracks the trailing vortices from the first set of fins and the nose vortices (if present) over the afterbody section. The routine also decides if afterbody vortices should be shed and computes their starting locations. If afterbody vortices are formed, they are tracked along with the other vortices present. The strengths of the afterbody vortices as functions of axial position are also computed. Once the vortex trajectories have been computed for the afterbody section, the forces and moments on the afterbody section are computed and control is returned to MLOADS.

If NFIN = 3, MLOADS prints a summary of the overall forces and moments and reads in a new data set. If NFIN = 4, subroutine TAIL is called. This routine proceeds in a manner similar to CANARD except that the trailing vortices of the tail fins are ignored. When TAIL has finished, it returns control to MLOADS. Subroutine MLOADS then computes and prints out the total forces and moments for the configuration and reads in a new data set.

E.2.2 Program Limitations and Precautions

The program makes a number of assumptions about the missile configuration and the flow field which are listed in section 6 of the main text.

E.2.3. Description of Subroutines

Subroutine INPT reads in all input and nondimensionalizes it.

Subroutine NOSE computes nose vortex positions and strengths and nose forces and moments.

Subroutine CANARD controls the subroutines which compute vortex strengths and positions, individual fin forces and moments, body forces and moments and total forces and moments for the canard section.

Subroutine ALFAQ computes equivalent angles of attack for individual fins in the absence of vortices.

Subroutine VORTEX computes the strengths and positions of the vortices shed from the trailing edges of the canard fins.

Subroutine CRUTRJ computes the paths of free vortices in the presence of a cruciform wing-cylindrical body section.

Subroutine FCT computes derivatives needed by the differential equation solver of CRUTRJ.

Subroutine SHAPE provides the body and fin coordinates needed by FCT.

Subroutine DASCUR is the differential equation solver used by CRUTRJ and AFTBOD.

Subroutine REVFLO computes the equivalent angles of attack and span-wise locations of the centers of pressure for a set of fins due to the presence of vortices.

Subroutine SIMSON is a Simpson's rule integration package used by REVFLO.

Subroutine VEL computes the velocities induced on a set of fins by the vortices present for use by REVFLO.

Subroutines CEL1, CEL2, ELI1, and ELI2 are IBM SSP subroutines for computing elliptic integrals. They are called by REVFLO.

Subroutine LNTRP is a linear interpolation routine.

Subroutine CURVES is a BLOCK DATA routine for initializing a number of empirical tables used in the program.

Subroutine AFTBOD computes vortex positions and strengths and body loading for the afterbody section.

Subroutine DERIV computes derivatives needed by the differential equation solver of AFTBOD.

Subroutine TAIL controls the subroutines which compute vortex strengths and positions, individual fin forces and moments, body forces and moments and total forces and moments for the tail section.

Subroutines CHRT8, EQ24, EQ26, EQ30, EQ31, and CH1416 are used to compute K_B and \bar{x}_B based on the methods of reference 10. These subroutines are described in reference E.1.

Subroutine INTFAC calculates any interference parameters which have not been input.

E.3. DESCRIPTION OF INPUT

This section describes the input for the program MLOADS. In the following discussion, the contents of all input cards are specified. All possible input variables are listed at the end of this section in the order of appearance in the input deck. The input format for all cards is shown in figure E.3 and the item numbers also refer to that figure. A sample input is described in section E.6 which discusses a sample case.

Item 1

These cards provide identification of the run. The information on them is printed on the first page of the output.

Item 2

This item includes the variable NFIN which specifies the configuration. The following configurations may be studied:

NFIN = 1: body-alone configuration

NFIN = 2: body-tail configuration

NFIN = 3: body-canard configuration

NFIN = 4: body-canard-tail configuration

Item 3

This optional item is read if $NFIN \geq 2$ and includes integer control parameters for the first set of fins. The first six specify whether the various interference parameters are to be input by the user or are to be determined by the program. The quantities NCNC, NCPXC, and NCPYC specify the number of entries in the tables which describe the wing-alone characteristics. Since the fins are assumed to be uncambered and untwisted, the wing-alone characteristics should be input for positive α_{eq} only.

Also in this item is NI, the number of integration intervals plus one, used in the Simpson's rule integration routine called by REVFLO. The value of NI must be odd. A suitable value for NI depends on how close a vortex is to a fin. If a vortex is close to a fin, NI should be at least 51.

The quantity NXOUTC is the number of stations for which vortex positions are to be output. A value between 5 and 10 should be sufficient to monitor the vortex trajectories over the canard (first finned) section.

The quantity NAFTC is used if NFKBC and/or NFXBC are zero and $M_\infty > 1$; that is, K_B and/or \bar{x}_B are to be determined by the code. For supersonic speeds, lift on the body due to the presence of the fins can be generated downstream of the fin trailing edges. If NAFTC = 1, the code will assume that there is sufficient body surface downstream of the fin trailing edges to fully develop that lift. If NAFTC = 2, it is assumed that there is no body after the fins. If $NFIN \geq 3$, always use NAFTC = 1. If $NFIN = 2$, the user should input NAFTC = 2 unless it is clear that significant lift carryover will be developed downstream of the fins.

The last integer variable on this card is NVORT. This variable is used to control the influence of the nose vortices. It has been observed (refs. 4 and 5) that nose vorticity for $\alpha_c \leq 20^\circ$ may disperse over the canard section. Since the present model for nose vorticity is incapable of representing such a situation, the user has the option of ignoring the influence of nose vorticity downstream. The options are:

NVORT = 0: nose vortices, if present, are tracked over entire configuration

NVORT = 1: nose vortices are ignored downstream of the leading edge of the canard root chord

NVORT = 2: nose vortices are ignored downstream of the trailing edge of the canard root chord

Item 4

This optional item is read if $NFIN \geq 3$. The quantity NXOUTB is equal to the number of integration intervals used in the calculations of afterbody loading. It is also the number of axial stations at which vortex positions and strengths are output. As a rule of thumb, use a value of NXOUTB greater than the length of the afterbody in body diameters. If the vortex positions change drastically between output stations, KXOUTB should be increased.

Item 5

This optional item is read if $NFIN = 4$. The parameters have the same function as those in Item 3. For example, NXOUTT has the same purpose for the tail section as NXOUTC has for the canard section.

Item 6

The logical quantity TURB is used to determine which branch of the crossflow drag coefficient table is to be used in NOSE and AFTBOD. For crossflow Mach numbers below 0.6, the laminar and turbulent values of c_{d_c} differ. If there is doubt about which type of flow separation is present, use $TURB = .TRUE.$

The logical variables NEARC and NEART are used to control the influence of the fins on vortex trajectories over a finned section. If these variables are set equal to $.TRUE.$, the influence of the fins is ignored. This option has given the best agreement with experiment.

Item 7

This item contains flight conditions and fin deflection angles.

Item 8

This optional item is read if $NFIN \geq 2$. It is possible that an indefinite condition may result if Φ is zero and the fins are undeflected. It is recommended that $\Phi = 0.01$ be used for an unbanked configuration with undeflected fins.

Item 9

This item contains some required reference information. The variable XMC is the moment center measured from MS 0.

Item 10

This optional information for the first set of fins is input if $NFIN \geq 2$. The variable CPXRC is the reference length which was used to nondimensionalize the chordwise location of the fin center of pressure for the wing-alone tables. Typically, this length is equal to the root chord of the fin. Similarly, CPYRC is the reference length for the lateral location of the fin center of pressure. This value is usually the exposed semispan of the fin. The last variable is SRCAN which is the reference area used for the fin normal-force table. It is usually the wing-alone planform area.

Item 11

This optional information is input if $NFIN = 4$. It is similar to Item 10 and is the corresponding information for the second set of fins.

Item 12

This information is input if $NFIN \geq 2$. It is concerned with control of vortex trajectory calculations and with the influence a vortex may have on a fin. The first variable, RO, enables the user to approximate the effects of viscous cores for the vortices in determining the velocities which may be induced on the fins. If RO is positive, it is interpreted as the ratio of the vortex core radius to the body radius. If RO is negative, its magnitude is interpreted as the maximum allowed fraction of the free-stream velocity which can be induced normal to the fins. The best agreement with experiment has been obtained with $RO = -0.1$ for $M_\infty < 1$ and $RO = -0.4$ for $M_\infty > 1$.

Subroutine CRUTRJ calculates the trajectories of the vortices in the presence of fins. It uses a differential equation solver, DASCURU, to solve the equations of motion of the vortices. The input variable, DXI, is the initial integration interval required by DASCURU for the trajectory calculations. It is nondimensionalized by the body radius. The initial interval can be automatically reduced by DASCURU by as much as a factor of 100 in an attempt to provide the desired accuracy. A value of DXI between 0.02 and 0.05 should work for most cases. When two vortices get very close together, or when a vortex gets very near the wing or body, a smaller value of DXI may be required.

The desired accuracy in the vortex trajectory calculations, referred to in the previous paragraph, is controlled through the input variable

EPS. This variable also controls the vortex strength calculations of the afterbody vortices. The value of EPS should be set equal to one half the desired accuracy. For instance, if EPS is set to 5×10^{-4} , this usually results in a solution accurate to three significant figures.

Experimental observations show that when two vortices of like sign become very close to one another they often combine or coalesce to form one vortex. This situation is included in the program through the variable RVORT. If vortices are not combined and they get too close, then computation time can increase dramatically. The variable RVORT is entered as a separation distance in terms of body radii. When two vortices of like sign are within this distance of each other, they are combined to form one vortex of strength equal to the two original strengths and at a position between the two proportional to the original strengths. A value of 0.5 for RVORT has been found to be satisfactory.

Item 13

This item is also optional and contains the last of the program control information. The first two variables in this item govern the shedding of the afterbody vortices. Hence, this item must be entered if an afterbody is present behind the first set of fins (i.e., if $NFIN \geq 3$).

The first variable in this item is RVOA, which is the radial distance from the body centerline in body radii at which the afterbody vortices are to be placed initially. The suggested range of values for RVOA is 1.2 to 1.5. The results presented in this report were computed with $RVOA = 1.2$. If RVOA is too small, the afterbody vortices tend to be captured by their own images.

The second control variable in this item is OMEGA. This is an angle, measured from the z_0 axis within which the crossflow velocity vector must lie in order for afterbody vortices to be formed. This crossflow velocity vector is determined by first computing the upwash and sidewash at the body axis due to the external vortices. The quantity $\sin \alpha_c$ is then added to the upwash to account for the flow of the free stream around the cylindrical body. The resultant vector is the crossflow velocity vector. If OMEGA is set equal to zero, no afterbody vortices will form unless the flow is perfectly symmetrical about the plane containing the wind and body axes. If OMEGA is set equal to 180° , afterbody vortices may form regardless of the strength and direction of the crossflow velocity. A value of $OMEGA = 45^\circ$ is recommended.

The last variable on this card is XTLE which is the axial location of the end of the afterbody section.

Item 14

This item describes the nose section back to the first set of fins. The first card contains the number of entries, NNOSE, in the table of nose coordinates and an integer variable, NCA, indicating whether the slope of the linear normal-force curve, $C_{N\alpha}$, is to be read in. If NCA equals zero, then $C_{N\alpha}$ is assigned the value 2.0 by the program. Otherwise, a value for $C_{N\alpha}$ is to be read in two cards later.

Following NNOSE and NCA, the two variables TIPRAD and ETAN are entered. The variable TIPRAD is the radius of the spherical nose tip. For the case of a pointed nose, this value is zero. If the nose is pointed, then ETAN is the nose half-angle. If the nose is blunted, then ETAN is the angle between the body axis and the tangent to the nose at the juncture of the spherical cap and the rest of the nose (see ref. 3, p. 11).

If NCA is not equal to zero, the linear normal-force coefficient slope (DCNDA) is read in next. Following this optional input, the nose coordinates are entered, first the axial coordinates, then the corresponding radial coordinates. All axial locations are to be measured from missile station zero (MS 0). Thus, the value of XNOSE(1) is the axial location of the nose tip measured from MS 0.

Item 15

If NFIN = 1, then the body length is entered in this item. The program defines the nose as extending to the leading edge of the root chord of the first set of fins, XCLE. Thus, for the body-alone case, the body length is entered as XCLE in this item.

Item 16

This optional item is entered if NFIN \geq 2. This item contains information describing the first set of fins. On the first card of this item are the relevant geometric parameters that describe the fins. If a fin with a rectangular planform is to be specified, the user must set the leading-edge sweep to some small positive value. This should be accomplished by making XCTIPL > XCLE by a small number, say 0.01. Following this geometric information are three empirical curves that describe the fin wing-alone characteristics. The first curve is the

normal-force curve, entered as corresponding values of angle of attack (ALFCNC) and normal-force coefficient (CNWC). There are NCNC pairs of values. The second empirical curve is the chordwise center of pressure location as a function of angle of attack. These axial locations are measured from the leading edge of the root chord. The NCPXC values are entered in the same fashion as the normal-force curve. Next, the table for the spanwise location of the wing-alone center of pressure is entered. The spanwise distance is measured from the root chord. There are NCPYC pairs of values.

Following these empirical curves, any or all of the interference factors for this set of fins may be entered. As discussed previously, the method of calculation of each interference factor is controlled by an integer flag. If the value of the flag is zero, then the corresponding interference factor is not entered but is calculated internally. If the value of the flag is one, then the interference parameter is entered here for the first set of fins and at the end of Item 17 for the second set of fins. The integer flags corresponding to the interference factors for the set of fins of Item 16 were entered in Item 3. Each card is read if any of the information on it is needed. The quantities which are not needed are ignored.

Item 17

This item is similar to Item 16 in that it contains the corresponding information for the second set of fins. Hence, this item is entered only when $NFIN = 4$. In addition to geometrical information, the first card contains the interdigitation angle. This is the angle by which the tail fins are rolled with respect to the canard fins. The axial location of the tail fin root chord leading edge was entered in Item 13. Just as in Item 16, the three empirical curves describing the wing-alone characteristics are entered next. The last two cards, if they are entered, contain the fin interference factors. The integer flags that determine whether or not the interference factors for this fin are entered are in Item 5. Each card is read if any of the information on it is needed. The quantities which are not needed are ignored.

Item 18

This card ends the process of entering data. It should be the last card and follow all the data cards for the case(s) to be run. The computer program stops the search for more data and the run is finished.

Item No. 1:

(1) Format (16I5), 1 card

Column Number	5
Program Variable	NCARDS

(2) Format (20A4), NCARDS cards

Column Number	1-80
Program Variable	HEAD

Item No. 2:

(1) Format (16I5)

Column Number	5	10
Program Variable	NFIN	NALFA

Item No. 3: Optional

(1) Format (16I5)

Column Number	5	10	15	20	25	30	35	40	45
Program Variable	NFKWC	NFLKW	NFKABC	NFKD	NFKBC	NFXBC	NCNC	NCPXC	NCPYC

50	55	60	65	70
NI	NPHI	NXOUTC	NAPTC	NVORT

Item No. 4: Optional

(1) Format (16I5)

Column Number	5
Program Variable	NXOUTB

Figure E.3(a). Input formats for computer program MLOADS.

Item No. 5: Optional

(1) Format (16I5)

Column Number	5	10	15	20	25	30	35
Program Variable	NFKWT	NFKABT	NFKBT	NFKBT	NCNT	NCPXT	NCPYT

40	45
NKOUTT	NAFTT

Item No. 6:

(1) Format (16L5)

Column Number	5	10	15
Program Variable	TURB	NEARC	NEART

Item No. 7:

(1) Format (8F10.5), 1 card

Column Number	10	20	30	40	50
Program Variable	FMACH	DELTA(1)	DELTA(2)	DELTA(3)	DELTA(4)

(2) Format (8F10.5), 8 values of ALFAC per card

Column Number	10	20		10 × NALFA
Program Variable	ALFAC(1)	ALFAC(2)	. . .	ALFAC(NALFA)

Item No. 8: Optional

(1) Format (8F10.5), 8 values of PHI per card

Column Number	10	20	. . .	10 × NPHI
Program Variable	PHI(1)	PHI(2)	. . .	PHI(NPHI)

Figure E.3(b). Continued.

Item No. 9:

	(1) Format (8F10.5)			
Column Number	10	20	30	40
Program Variable	LROUT	SROUT	XMC	A

Item No. 10: Optional

	(1) Format (8F10.5)		
Column Number	10	20	30
Program Variable	CPXRC	CPYRC	SRCAN

Item No. 11: Optional

	(1) Format (8F10.5)		
Column Number	10	20	30
Program Variable	CPXRT	CPYRT	SRTAIL

Item No. 12: Optional

	(1) Format (8F10.5)			
Column Number	10	20	30	40
Program Variable	RO	DXI	EPS	RVORT

Item No. 13: Optional

	(1) Format (8F10.5)		
Column Number	10	20	30
Program Variable	RVOA	OMEGA	XTLE

Item No. 14:

	(1) Format (16I5), 1 card	
Column Number	5	10
Program Variable	NNOSE	NCA

Figure E.3(c). Continued.

(2) Format (8F10.5), 1 card

Column Number	10	20
Program Variable	TIPRAD	ETAN

(3) Optional, Format (8F10.5), 1 card

Column Number	10
Program Variable	DCNDA

(4) Format (8F10.5), 8 values of XNOSE per card

Column Number	10	20	...	10 × NNOSE
Program Variable	XNOSE(1)	XNOSE(2)	...	XNOSE(NNOSE)

(5) Format (8F10.5), 8 values of RNOSE per card

Column Number	10	20	...	10 × NNOSE
Program Variable	RNOSE(1)	RNOSE(2)	...	RNOSE(NNOSE)

Item No. 15: Optional

(1) Format (8F10.5)

Column Number	10
Program Variable	XCLE

Item No. 16: Optional

(1) Format (8F10.5), 1 card

Column Number	10	20	30	40	50	60	70
Program Variable	ARC	SPANC	XCHL	XCLE	XCTIPL	XCTE	XFC

(2) Format (8F10.5), 8 values of ALFCNC per card

Column Number	10	20	...	10 × NCNC
Program Variable	ALFCNC(1)	ALFCNC(2)	...	ALFCNC(NCNC)

Figure E.3(d). Continued.

(3) Format (8F10.5), 8 values of CNWC per card

Column Number	10	20	. . .	$10 \times \text{NCNC}$
Program Variable	CNWC(1)	CNWC(2)	. . .	CNWC(NCNC)

(4) Format (8F10.5), 8 values of ACPXC per card

Column Number	10	20	. . .	$10 \times \text{NCPXC}$
Program Variable	ACPXC(1)	ACPXC(2)	. . .	ACPXC(NCPXC)

(5) Format (8F10.5), 8 values of CPXC per card

Column Number	10	20	. . .	$10 \times \text{NCPXC}$
Program Variable	CPXC(1)	CPXC(2)	. . .	CPXC(NCPXC)

(6) Format (8F10.5), 8 values of ACPYC per card

Column Number	10	20	. . .	$10 \times \text{NCPYC}$
Program Variable	ACPYC(1)	ACPYC(2)	. . .	ACPYC(NCPYC)

(7) Format (8F10.5), 8 values of CPYC per card

Column Number	10	20	. . .	$10 \times \text{NCPYC}$
Program Variable	CPYC(1)	CPYC(2)	. . .	CPYC(NCPYC)

(8) Optional, Format (8F10.5), 1 card

Column Number	10	20	30	40
Program Variable	KWC	LKW	KBC	XBC

Figure E.3(e). Continued.

(9) Optional, Format (8F10.5), 1 card

Column Number	10	20	30	40	50	60
Program Variable	KABC(1)	KABC(2)	KABC(3)	KABC(4)	KD(1)	KD(2)

70	80
KD(3)	KD(4)

Item No. 17: Optional

(1) Format (8F10.5), 1 card

Column Number	10	20	30	40	50	60
Program Variable	ART	SPANT	XTTIPL	XTTE	XFT	PHIT

(2) Format (8F10.5), 8 values of ALFNCT per card

Column Number	10	20	. . .	10 × NCNT
Program Variable	ALFCNT(1)	ALFCNT(2)	. . .	ALFCNT(NCNT)

(3) Format (8F10.5), 8 values of CNWT per card

Column Number	10	20	. . .	10 × NCNT
Program Variable	CNWT(1)	CNWT(2)	. . .	CNWT(NCNT)

(4) Format (8F10.5), 8 values of ACPXT per card

Column Number	10	20	. . .	10 × NCPXT
Program Variable	ACPXT(1)	ACPXT(2)	. . .	ACPXT(NCPXT)

(5) Format (8F10.5), 8 values of CPXT per card

Column Number	10	20	. . .	10 × NCPXT
Program Variable	CPXT(1)	CPXT(2)	. . .	CPXT(NCPXT)

Figure E.3(f). Continued.

(6) Format (8F10.5), 8 values of ACPYT per card

Column Number	10	20	. . .	10×NCPYT	
Program Variable	ACPYT(1)	ACPYT(2)	. . .	ACPYT(NCPYT)	

(7) Format (8F10.5), 8 values of CPYT per card

Column Number	10	20	. . .	10 × NCPYT	
Program Variable	CPYT(1)	CPYT(2)	. . .	CPYT(NCPYT)	

(8) Optional, Format (8F10.5), 1 card

Column Number	10	20	30	40	50	60	70	
Program Variable	KWT	KBT	XBT	KABT(1)	KABT(2)	KABT(3)	KABT(4)	

Item No. 18:

(1) Format (16I5)

Column Number	5	
Program Variable	999	

Figure E.3(g). Concluded.

E.4. SYMBOL LISTING

This section lists all input variables in the order in which they are entered, gives the algebraic symbol if one exists, and a brief definition. Refer to figure E.3 for the proper input format.

<u>Program Variable</u>	<u>Algebraic Symbol (If Applicable)</u>	<u>Comments</u>
<u>Item 1</u>		
		Alphanumeric information to identify the run.
NCARDS		Number of cards used to identify the run; $\text{NCARDS} \geq 1$.
HEAD(I)		(NCARDS) cards of alphanumeric information for identification of the run; $1 \leq I \leq \text{NCARDS}$.
<u>Item 2</u>		
NFIN		Integer specifying type of configuration. NFIN = 1 Body-alone. NFIN = 2 Body-tail. NFIN = 3 Body-canard. NFIN = 4 Body-canard-tail.
NALFA		Number of angles of attack for which calculations are to be made; $1 \leq \text{NALFA} \leq 10$.
<u>Item 3 (optional)</u>		
NFKWC		Integer flag indicating how K_W for canard section is to be determined. NFKWC = 0 Determined by code. NFKWC = 1 K_W is input.
NFLKW		Integer flag indicating how k_W for canard section is to be determined. NFLKW = 0 Determined by code. NFLKW = 1 k_W is input.
NFKABC		Integer flag indicating how $K_{\alpha\beta}$ for canard section is to be determined. NFKABC = 0 Determined by code. NFKABC = 1 $K_{\alpha\beta}$ is input.
NFKD		Integer flag indicating how $K_{\alpha\delta}$ for canard section is to be determined. NFKD = 0 Determined by code. NFKD = 1 $K_{\alpha\delta}$ is input.

<u>Program Variable</u>	<u>Algebraic Symbol (If Applicable)</u>	<u>Comments</u>
NFKBC		Integer flag indicating how K_B for canard section is to be determined. NFKBC = 0 Determined by code. NFKBC = 1 K_B is input.
NFXBC		Integer flag indicating how \bar{x}_B for canard section is to be determined. NFXBC = 0 Determined by code. NFXBC = 1 \bar{x}_B is input.
NCNC		Number of entries in table for canard wing-alone normal force coefficient; $2 \leq NCNC \leq 20$.
NCPXC		Number of entries in table for the chord-wise location of the canard wing-alone center of pressure; $2 \leq NCPXC \leq 20$.
NCPYC		Number of entries in table for the span-wise location of the canard wing-alone center of pressure; $2 \leq NCPYC \leq 20$.
NI		One plus the number of intervals to be used in the Simpson's rule integration package in REVFLO; must be odd; $1 \leq NI \leq 99$.
NPHI		Number of roll angles for which calculations are to be made; $1 \leq NPHI \leq 10$.
NXOUTC		Number of axial stations along the canard at which vortex locations are to be output.
NAFTC		Integer flag indicating whether afterbody is present downstream of the first set of fins for computation of body carryover lift; ignored if NFKBC and NFXBC \neq 0. NAFTC = 1 Afterbody present. NAFTC = 2 No afterbody present.
NVORT		Integer flag indicating how far along body influence of nose vortices is to be felt. NVORT = 0 Influence of nose vortices felt along entire body. NVORT = 1 Influence of nose vortices felt up to leading edge of canard root chord. NVORT = 2 Influence of nose vortices felt up to trailing edge of canard root chord.
<u>Item 4 (optional)</u>		Optional input to be read in if NFIN \geq 3.
NXOUTB		Number of axial stations along the afterbody at which vortex locations are to be output (see Item 4 of section E.3).

<u>Program Variable</u>	<u>Algebraic Symbol (If Applicable)</u>	<u>Comments</u>
<u>Item 5 (optional)</u>		
Optional input to be read in if NFIN = 4.		
NFKWT		Integer flag indicating how K_W for tail section is to be determined. NFKWT = 0 Determined by code. NFKWT = 1 K_W is input.
NFKABT		Integer flag indicating how $K_{\alpha\beta}$ for tail section is to be determined. NFKABT = 0 Determined by code. NFKABT = 1 $K_{\alpha\beta}$ is input.
NFKBT		Integer flag indicating how K_B for tail section is to be determined. NFKBT = 0 Determined by code. NFKBT = 1 K_B is input.
NFXBT		Integer flag indicating how \bar{x}_B for tail section is to be determined. NFXBT = 0 Determined by code. NFXBT = 1 \bar{x}_B is input.
NCNT		Number of entries in table for tail wing-alone normal force; $2 \leq \text{NCNT} \leq 20$.
NCPXT		Number of entries in table for the chord-wise location of the tail wing-alone center of pressure; $2 \leq \text{NCPXT} \leq 20$.
NCPYT		Number of entries in table for the span-wise location of the tail wing-alone center of pressure; $2 \leq \text{NCPYT} \leq 20$.
NXOUTT		Number of axial stations along the tail at which vortex locations are to be output.
NAFTT		Integer flag indicating whether afterbody is present downstream of second set of fins for calculation of body carryover lift; ignored if NFKBT and NFXBT \neq 0. NAFTT = 1 Afterbody present. NAFTT = 2 No afterbody present.
<u>Item 6</u>		
TURB		Logical variable stating whether crossflow on body is laminar or turbulent. TURB = .TRUE. Crossflow is turbulent. TURB = .FALSE. Crossflow is laminar.

<u>Program Variable</u>	<u>Algebraic Symbol (If Applicable)</u>	<u>Comments</u>
NEARC		Logical variable stating whether canard fins are to be ignored for vortex tracking over canard section; NEARC is ignored if $NFIN < 2$. NEARC = .TRUE. Ignore fins. NEARC = .FALSE. Include influence of fins.
NEART		Logical variable stating whether tail fins are to be ignored for vortex tracking over tail section; NEART is ignored if $NFIN < 4$. NEART = .TRUE. Ignore fins. NEART = .FALSE. Include influence of fins.
<u>Item 7</u>		
FMACH	M_{∞}	Free-stream Mach number.
DELTA(J)	$\delta(J)$	Deflection angles in degrees of canard fins; $1 \leq J \leq 4$; J = number of canard fin.
ALFAC(K)	$\alpha_c(K)$	Body angle of attack in degrees; $1 \leq K \leq NALFA$.
<u>Item 8 (optional)</u>		
PHI(L)	$\phi(L)$	Bank angle in degrees; angle between z and z_0 axes; positive measured clockwise viewed from rear; $1 \leq L \leq NPHI$.
<u>Item 9</u>		
LROUT	l_r	Reference length used in center of pressure calculations.
SROUT	S_R	Reference area used in force calculations.
XMC	x_{MC}	Moment center of missile, dimensional.
A	a	Radius of missile, dimensional.
<u>Item 10 (optional)</u>		
CPXRC		Reference length used in table for chord-wise location of canard wing-alone center of pressure, dimensional.
CPYRC		Reference length used in table for span-wise location of canard wing-alone center of pressure, dimensional.
SRCAN		Reference area used in table for canard wing-alone normal-force coefficient, dimensional.

<u>Program Variable</u>	<u>Algebraic Symbol (If Applicable)</u>	<u>Comments</u>
<u>Item 11</u> (optional)		
		Optional input to be read in if NFIN = 4.
CPXRT		Reference length used in table for chord-wise location of tail wing-alone center of pressure, dimensional.
CPYRT		Reference length used in table for span-wise location of tail wing-alone center of pressure, dimensional.
SRTAIL		Reference area used in table for tail wing-alone normal-force coefficient, dimensional.
<u>Item 12</u> (optional)		
		Optional input to be read in if NFIN \geq 2.
RO		If $RO \geq 0$, RO is the ratio of the vortex core radius to the body radius; if $RO \leq 0$, RO is the negative of the maximum fraction of the free-stream velocity which may be induced normal to the fins.
DXI		Maximum value of integration interval in body radii for vortex tracking.
EPS		Accuracy criterion used in DASCUR.
RVORT		If the separation distance in body radii between vortices of like sign is less than RVORT, vortices are combined (afterbody section only).
<u>Item 13</u> (optional)		
		Optional input to be read in if NFIN \geq 3.
RVOA	r_v/a	Distance from body centerline at which afterbody vortices are positioned initially, nondimensionalized by body radius.
OMEGA		Angle measured from z_0 axis within which the crossflow velocity vector must lie in order for afterbody vortices to be formed, degrees.
XTLE		Location of end of afterbody section; position of leading edge of tail root chord if second set of fins are present and axial position of body base if only one set of fins present.
<u>Item 14</u>		
NNOSE		Number of entries in the table of nose coordinates; $2 \leq$ NNOSE \leq 20.

<u>Program Variable</u>	<u>Algebraic Symbol (If Applicable)</u>	<u>Comments</u>
NCA		Integer flag specifying whether C_{N_α} of nose is to be entered. NCA = 0 C_{N_α} not entered. NCA \neq 0 C_{N_α} entered.
TIPRAD		Nose tip radius, dimensional.
ETAN	η	Half angle of body nose for pointed body; or angle between tangent to nose at juncture of spherical cap and rest of nose and the body axis, degrees.
DCNDA	C_{N_α}	Slope of nose normal-force coefficient at $\alpha_c = 0$; entered if NCA \neq 0.
XNOSE (M)		Axial location entries in nose coordinate table from a nose tip; $1 \leq M \leq \text{NNOSE}$; XNOSE(1) is axial location of nose tip from MS 0, dimensional.
RNOSE (M)		Corresponding radial location entries in nose coordinate table; $1 \leq M \leq \text{NNOSE}$, dimensional.
<u>Item 15 (optional)</u>		Optional input to be read in if NFIN = 1.
XCLE		Length of body, dimensional.
<u>Item 16 (optional)</u>		Optional input to be read in if NFIN \geq 2.
ARC	AR	Aspect ratio of canard fins.
SPANC	s_m	Maximum semispan, measured from body centerline, of canard fins, dimensional.
XCHL	x_{HL}	Axial distance to canard hinge line, measured from MS 0, dimensional.
XCLE		Axial distance to leading edge of canard root chord, measured from MS 0, dimensional.
XCTIPL		Axial distance to leading edge of canard tip chord, measured from MS 0, dimensional; XCTIPL > XCLE (see Item 16 of section D.3).
XCTE		Axial distance to canard trailing edge, measured from MS 0, dimensional.
XFC		Axial distance to area centroid of canard fin planform, measured from MS 0, dimensional.

<u>Program Variable</u>	<u>Algebraic Symbol (If Applicable)</u>	<u>Comments</u>
ALFCNC (N)		Angle of attack entries in canard wing-alone normal-force table, degrees; $2 \leq N \leq \text{NCNC}$.
CNWC (N)		Corresponding normal-force coefficient entries in canard wing-alone normal-force table; $2 \leq N \leq \text{NCNC}$.
ACPXC (II)		Angle of attack entries in canard wing-alone table for chordwise location of center of pressure, degrees, $2 \leq \text{II} \leq \text{NCPXC}$.
CPXC (II)		Corresponding entries for chordwise locations of center of pressure in canard wing-alone table, nondimensional; $2 \leq \text{II} \leq \text{NCPXC}$, measured from leading edge of canard root chord.
ACPYC (IJ)		Angle of attack entries in canard wing-alone table for spanwise location of center of pressure, degrees; $2 \leq \text{IJ} \leq \text{NCPYC}$.
CPYC (IJ)		Corresponding entries for spanwise locations of center of pressure in canard wing-alone table, nondimensional; $2 \leq \text{IJ} \leq \text{NCPYC}$, measured from fin root chord.
KWC	K_W	Wing-body interference factor for canard normal force.
LKW	k_W	Wing-body interference factor for canard fin deflection.
KBC	K_B	Wing-body interference factor for lift carryover from canard fins to body.
XBC	\bar{x}_B	Center of pressure for K_B load based on fraction of root chord measured from leading edge of canard root chord.
KABC (IK)		Wing-body interference factor associated with $\alpha\beta$ coupling on canard fins; $1 \leq \text{IK} \leq 4$; IK = number of canard fin.
KD (IL)	$K_D(\text{IL})$	Wing-body interference factor associated with $\alpha\delta_V$ and $\beta\delta_H$ coupling on canard fins; $1 \leq \text{IL} \leq 4$; IL = number of canard fin.
<u>Item 17 (optional)</u>		Optional input to be read in if NFIN = 4.
ART	$\mathcal{A}R$	Aspect ratio of tail fins.
SPANT	s_m	Maximum semispan, measured from body centerline, of tail fins, dimensional.

<u>Program Variable</u>	<u>Algebraic Symbol (If Applicable)</u>	<u>Comments</u>
XTTIPL		Axial distance to leading edge of tail tip chord, measured from MS 0, dimensional; XTTIPL > XTLE (see Item 16 of section E.3).
XTTE		Axial distance to tail fin trailing edge, measured from MS 0, dimensional.
XFT		Axial distance to area centroid of tail fin planform, measured from MS 0, dimensional.
PHIT	ϕ_T	Interdigitation angle between tail fins and canard fins, measured clockwise from canard fin no. 1 to tail fin no. 1, degrees
ALFCNT(IM)		Angle of attack entries in tail wing-alone normal-force table, degrees; $2 \leq IM \leq NCNT$.
CNWT(IM)		Corresponding normal-force coefficient entries in tail wing-alone normal-force table; $2 \leq IM \leq NCNT$.
ACPXT(IN)		Angle of attack entries in tail wing-alone table for chordwise location of center of pressure, degrees; $2 \leq IN \leq NCPXT$, measured from leading edge of tail root chord.
CPXT(IN)		Corresponding entries for chordwise locations of center of pressure in tail wing-alone table, nondimensional; $2 \leq IN \leq NCPXT$.
ACPYT(KI)		Angle of attack entries in tail wing-alone table for spanwise location of center of pressure, degrees; $2 \leq KI \leq NCPYT$.
CPYT(KI)		Corresponding entries for spanwise locations of center of pressure in tail wing-alone table, nondimensional; $2 \leq KI \leq NCPYT$, measured from fin root chord.
KWT	K_W	Wing-body interference factor for tail normal force.
KBT	K_B	Wing-body interference factor for lift carryover from tail fin to body.
KBT	\bar{x}_B	Center of pressure for K_B based on percentage of root chord measured from leading edge of tail root chord.
KABT(KK)		Wing-body interference factor associated with $\alpha\beta$ coupling on tail fins; $1 \leq KK \leq 4$; KK = number of tail fin.
<u>Item 18</u>		
999		This card causes the program to stop searching for more data and the run is stopped.

E.5. DESCRIPTION OF OUTPUT

This section describes the output of the computer program. The contents of each of the output items is specified and discussed. A sample output is included in the next section which discusses the sample case.

The output consists of a minimum of four items and a maximum of seven, depending upon the type of configuration. The first item consists of the input data and takes up the first three pages. The run identification and missile geometry appear on the first page. The second page contains reference lengths, reference areas, and flight conditions. Included with the flight conditions are the values of TURB, NEARC, and NEART listed under the headings, "turbulent flow," "vortices are near canard," and "vortices are near tail," respectively. The third and last page of this item contains the tables for the wing-alone characteristics for both sets of fins. The program operation variables are also given on this page.

The second output item appears on page four and is a listing of all interference parameters used in the program and their source. The number zero for the source of an interference parameter indicates that that particular parameter was calculated by the code. If the value for the source is one, the interference parameter was input by the user.

Page five marks the beginning of the force and moment results. Three items of information are given at the beginning of the output for each of the individual sections: (1) the name of the particular section (e.g., nose); (2) the value of α_c ; and (3) the bank angle, ϕ . Following the output for the last section of the configuration is a summary giving total forces and moments. The forces and moments are all presented in coefficient form with SROUT as the reference area and LROUT as the reference length. In addition, the force and moment coefficients are listed as components along the appropriate Cartesian axes. The coefficients in unrolled coordinates are listed as CZO, normal force; CYO, side force, CXO, axial force; CMZO, yawing moment; CMYO, pitching moment; and CMXO, rolling moment. The same convention is used for the values in rolled coordinates. Note that $CZO = C_N$, $CYO = C_Y$, $CXO = C_A$, $CMXO = -C_l$, $CMYO = C_m$, and $CMZO = -C_n$. Also printed is the contribution to the lift and drag coefficient from each section.

The loads on the nose section are reported on the fifth page of the output beginning with the axial starting position of the nose vortices, if any. If nose vortices have formed, their nondimensional strength (normalized by $2\pi V_\infty a$) and their positions in the crossflow plane at the end of the nose section are presented next. Then the nose forces and moments are printed.

The results from the canard section (or first finned section) start on page six. Presented first are results for the individual fins in the absence of vortices. For each fin the following information is given: (1) the equivalent angle of attack; (2) the fin normal-force coefficient; and (3) the location of the fin center of pressure normalized by LROUT. The value CPX is measured from the root chord leading edge, and CPY is measured from the body centerline.

If nose vortices have formed and if their influence over the canard section is to be calculated (i.e., if NVORT is not equal to one), the results from CRUTRJ giving the trajectory of the vortices over the fin section are presented next. Positions in the crossflow plane in both rolled and unrolled coordinates are given at NXOUTC+2 axial locations, the first one being the root chord leading edge. Other output locations are at intervals of $(XCTE - XCLE)/NXOUTC$ with the positions at the axial location of the area centroid also given. It is the vortex positions at the fin area centroid that are used in computing the vortex induced effects. Immediately following the vortex trajectory information are the vortex induced equivalent angles of attack and corresponding spanwise locations of the centers of pressure for each fin. The spanwise locations of the centers of pressure are measured from the body centerline and are nondimensionalized by the body radius.

Next are listed the strengths and positions of the canard fin trailing vortices in the crossflow plane at the canard fin trailing edge. One vortex is generated per fin. Total individual fin loads are presented next. For each fin the total equivalent angle of attack is used to determine the force normal to the fin (CN), the location of the normal-force center of pressure (CPX and CPY), the fin rolling moment (CRM), bending moment about the root chord (CBM), and hinge moment (CHM). These individual fin loads are then summed and added to the forces and moments acting on the body in the presence of the fins. The totals are given in both rolled and unrolled coordinates. If a body-tail missile

is being run, the results from the tail section, being the first set of fins, appear here.

Following the canard section results are the load contributions from the afterbody section. These results are presented in the form of vortex, flow field, and force information for each of the NXOUTB axial stations specified. From left to right the printout reads: X/A , the axial station, nondimensionalized by the body radius; I , the identification number of the vortices; $GAMMA(I)$, the nondimensional strength of the vortices at X/A ; $Y(I)/A$, the nondimensional y_0 -coordinate of the vortices; $Z(I)/A$, the nondimensional z_0 -coordinate of the vortices; $FLOANG$, the inverse sine in degrees of the magnitude of the crossflow velocity vector nondimensionalized by V_∞ ; $THETA$, the polar angle in degrees of the crossflow velocity vector measured from the positive y_0 -axis counterclockwise; $NORMAL\ FORCE$, the increment of normal force acting on the afterbody over the preceding interval; and $SIDE\ FORCE$, the increment of side force acting on the afterbody over the preceding interval. If two vortices are combined (i.e., if two vortices of like sign come within a distance of $RVORT$ of each other), then their strengths are added and the indexing of the vortices is rearranged as described in the output. The contribution of the afterbody section to the total loads in the unrolled body coordinate system is presented after the trajectory information.

Results for the tail section appear next. The format is the same as for the canard section with the exception of hinge moment. The contribution of the tail section to the axial force is always zero because the tail panels do not deflect.

The final item of output is the summary of the total forces and moments on the configuration in both rolled and unrolled coordinates. Included in this section is the axial center of pressure due to the total normal force (CPX) and the axial center of pressure due to the total side force (CPY).

E.6. SAMPLE CASE

In this section we describe a sample case to illustrate the use of the computer program. The case consists of a body-canard-tail configuration at supersonic speed, unrolled, at an angle of attack, and with yaw control.

[illegible]

183

CALCULATION OF AERODYNAMIC LOADS ON A CRUCIFORM MISSILE

WICOM-NAC BODY-CANARD-TAIL CASE WITH 26 AND 12 FINS
 MACH NUMBER IS 1.75
 BANK ANGLE IS 7.740 DEGREES
 YAW ANGLE IS 1.0 DEGREES
 PITCH ANGLE IS ZERO DEGREES

***** MISSILE BODY GEOMETRY *****

MISSILE IS A CANARD-TAIL COMBINATION

*** NOSE GEOMETRY ***

NOSE TIP RADIUS NOSE HALF ANGLE
 .56000 16.7230

NOSE COORDINATES

XNOSE 1.274 1.324 1.424 1.524 1.673 2.000 2.300 3.000 4.000 5.000 6.000 7.000 8.000 9.000 10.000 11.000 12.000 13.000 14.000
 YNOSE 0.000 .231 .381 .537 .635 .779 .926 1.173 1.426 1.615 1.803 1.967 2.109 2.229 2.327 2.423 2.457 2.500
 LINEAR NORMAL FORCE COEFFICIENT SLOPE IS 2.440

*** CANARD GEOMETRY ***

ASPECT RATIO SPAN CHINGE LINE ROOT LEADING EDGE TIP LEADING EDGE TRAILING EDGE X POS. CENTROID
 3.53000 6.25000 15.00000 12.72300 16.47300 15.72300 15.36000

*** BODY GEOMETRY ***

BODY RADIUS 2.50000 CENTER OF ADJUSTMENTS 25.00000

*** TAIL GEOMETRY ***

ASPECT RATIO SPAN NOSE LEADING EDGE TIP LEADING EDGE TRAILING EDGE X POS. CENTROID PMIT
 1.33000 6.00000 43.00000 45.00000 50.00000 47.20000 6.000

Figure 2.5(a). Output for sample case;
 body-canard-tail configuration.

***** REFERENCE LENGTHS AND AREAS *****

REFERENCE LENGTHS

OUTPUT LENGTH = 5.0000
 CPXRC = 4.00000 CPYRC = 5.75000
 CPXRT = 7.00000 CPYRT = 3.50000

REFERENCE AREAS

OUTPUT AREA = 19.63495
 CANARD WING-ALONE REF. AREA = 15.94000
 TAIL WING-ALONE REF. AREA = 35.75000

***** FLIGHT CONDITIONS *****

MACH NUMBER 1.750
 TURBULENT FLOW Y
 CANARD DEFLECTION ANGLES
 PANEL ANGLE
 1 15.000
 2 0.000
 3 15.000
 4 0.000

ANGLES OF ATTACK 16.60
 ROLL ANGLES 0.00

Figure E.5(b). Continued.



***** CYLINDRICAL INPUT *****

CANARD WING-ALONE DATA

NORMAL FORCE				CENTER OF PRESSURE				TAIL FING-ALONE DATA				CENTER OF PRESSURE			
ANGLE	CNWC	ANGLE	CPX	ANGLE	CPY	ANGLE	CPY	ANGLE	CNWT	ANGLE	CPX	ANGLE	CPY	ANGLE	CPY
0.00	7.000	1.00	.630	3.00	.433	0.00	.433	0.00	0.000	0.00	.214	0.00	.444	0.00	.444
10.00	.429	45.00	.659	3.00	.433	3.10	.433	3.10	.090	5.00	.214	30.00	.444	30.00	.444
20.00	.762	90.00	.667	3.00	.383	5.81	.383	5.81	.294	10.00	.333	60.00	.444	60.00	.444
30.00	1.048	0.00	0.000	15.00	.378	6.41	.378	6.41	.304	20.00	.354	90.00	.444	90.00	.444
35.00	1.100	0.00	0.000	20.00	.374	11.08	.374	11.08	.409	30.00	.377	0.00	0.000	0.00	0.000
40.00	1.100	0.00	0.000	25.00	.373	13.73	.373	13.73	.511	40.00	.382	0.00	0.000	0.00	0.000
45.00	1.250	0.00	0.000	30.00	.365	16.39	.365	16.39	.614	50.00	.385	0.00	0.000	0.00	0.000
50.00	1.340	0.00	0.000	35.00	.351	19.07	.351	19.07	.695	60.00	.394	0.00	0.000	0.00	0.000
55.00	1.380	0.00	0.000	40.00	.358	24.45	.358	24.45	.855	70.00	.393	0.00	0.000	0.00	0.000
60.00	1.430	0.00	0.000	45.00	.353	29.83	.353	29.83	.984	80.00	.387	0.00	0.000	0.00	0.000
65.00	1.530	0.00	0.000	50.00	.350	35.00	.350	35.00	1.105	90.00	.515	0.00	0.000	0.00	0.000
70.00	1.530	0.00	0.000	55.00	.345	40.00	.345	40.00	1.195	0.00	.000	0.00	0.000	0.00	0.000
80.00	1.580	0.00	0.000	60.00	.340	45.00	.340	45.00	1.268	0.00	.000	0.00	0.000	0.00	0.000
90.00	1.580	0.00	0.000	65.00	.333	50.00	.333	50.00	1.360	0.00	.000	0.00	0.000	0.00	0.000
0.00	0.000	0.00	0.000	70.00	.333	55.00	.333	55.00	1.407	0.00	.000	0.00	0.000	0.00	0.000
0.00	0.000	0.00	0.000	75.00	.333	60.00	.333	60.00	1.451	0.00	.000	0.00	0.000	0.00	0.000
0.00	0.000	0.00	0.000	80.00	.333	70.00	.333	70.00	1.546	0.00	.000	0.00	0.000	0.00	0.000
0.00	0.000	0.00	0.000	85.00	.333	80.00	.333	80.00	1.588	0.00	.000	0.00	0.000	0.00	0.000
0.00	0.000	0.00	0.000	90.00	.333	90.00	.333	90.00	1.593	0.00	.000	0.00	0.000	0.00	0.000
0.00	0.000	0.00	0.000	0.00	.333	0.00	.333	0.00	1.593	0.00	.000	0.00	0.000	0.00	0.000
0.00	0.000	0.00	0.000	0.00	.333	0.00	.333	0.00	1.593	0.00	.000	0.00	0.000	0.00	0.000

***** PROGRAM OPERATION *****

RJ	RVCA	RXOUTC	RYDUTA	YXOUTT	NI	DXI	EPS	OMEGA	RJURT
-0.430	1.200	10	10	10	51	.050	.00010	45.000	.33

NOSE VORTICES ARE RUN TO CANARD TRAILING EDGE

VORTICES ARE NEAR CANARD
VORTICES ARE NEAR TAIL

Figure E.5(c). Continued.

INTERPOLATED FACTORS

SUJAL

KBC = 1.2443
 LKB = .9332
 KABC(1) = .5121
 KABC(2) = .5020
 KABC(3) = .5121
 KABC(4) = .5121
 KBI(1) = .7794
 KBI(2) = .3850
 KBI(3) = .5790
 KBI(4) = .2850
 KBC = .3671
 XBC = .9546
 KBT = 1.4342
 KBT(1) = .4950
 KBT(2) = .4950
 KBT(3) = .4950
 KBT(4) = .4950
 KBT = .4838
 XBT = .7877

THE FOLLOWING LOAD CALCULATIONS ARE FOR ALPHA = 15.600 AND PHI = 0.030

***** CONTRIBUTION OF NOSE SECTION TO TOTAL LOADS *****

NOSE VORTICES HAVE FORMED AT X/A = 3.30325

STRENGTHS AND POSITIONS OF VORTICES AT LEADING EDGE OF CANARD ROOT CHORD

I	GAMMA/2PIVA	Y/A	Z/A
1	.25317	.6241	1.0869
2	-.05317	-.6241	1.0869

NORMAL FORCE COEFFICIENT AND PITCHING MOMENT COEFFICIENT
IN UNROLLED BODY COORDINATES

C/D	CMY'
.03242	2.77754
CL = .749	
CU = .229	

Figure E.5(d). Continued.

***** CAVAR) SECTION RESULTS FOR ALPHA = 16.630 AND PHE = 0.33) *****

RESULTS FOR T) PANEL-PANEL INFORMATION:

PANEL	ALPHA	CN	CPX	CPY
1	2.1315	.2024	.5474	.7657
2	24.0735	.3326	.5133	.7793
3	15.9235	.2542	.2414	.7629
4	22.7872	.3417	.5241	.7798

*** VORTEX TRACKING RESULTS OVER FINS ***

X	VORTEX	Y	Z	Y3	Z3
.5388E+01	1	.6041E+00	.1387E+01	.5041E+00	.1097E+01
	2	-.6041E+00	.1387E+01	-.5041E+00	.1097E+01
.5248E+01	1	.5957E+00	.1106E+01	.5957E+00	.1106E+01
	2	-.5957E+00	.1106E+01	-.5957E+00	.1106E+01
.5408E+01	1	.5872E+00	.1126E+01	.5872E+00	.1126E+01
	2	-.5872E+00	.1126E+01	-.5872E+00	.1126E+01
.5568E+01	1	.5784E+00	.1147E+01	.5784E+00	.1147E+01
	2	-.5784E+00	.1147E+01	-.5784E+00	.1147E+01
.5728E+01	1	.5696E+00	.1167E+01	.5696E+00	.1167E+01
	2	-.5696E+00	.1167E+01	-.5696E+00	.1167E+01
.5888E+01	1	.5608E+00	.1188E+01	.5608E+00	.1188E+01
	2	-.5608E+00	.1188E+01	-.5608E+00	.1188E+01
.6048E+01	1	.5521E+00	.1208E+01	.5521E+00	.1208E+01
	2	-.5521E+00	.1208E+01	-.5521E+00	.1208E+01
.6152E+01	1	.5464E+00	.1222E+01	.5464E+00	.1222E+01
	2	-.5464E+00	.1222E+01	-.5464E+00	.1222E+01
.6312E+01	1	.5375E+00	.1243E+01	.5375E+00	.1243E+01
	2	-.5375E+00	.1243E+01	-.5375E+00	.1243E+01
.6472E+01	1	.5287E+00	.1264E+01	.5287E+00	.1264E+01
	2	-.5287E+00	.1264E+01	-.5287E+00	.1264E+01
.6632E+01	1	.5202E+00	.1285E+01	.5202E+00	.1285E+01
	2	-.5202E+00	.1285E+01	-.5202E+00	.1285E+01
.6868E+01	1	.5122E+00	.1306E+01	.5122E+00	.1306E+01
	2	-.5122E+00	.1306E+01	-.5122E+00	.1306E+01

Figure E.5(e) Continued.

VORTEX INDUCED EQUIVALENT
 ANGLE OF ATTACK, DEGREES
 FIN 1 FIN 2 FIN 3 FIN 4
 .0742E+13 -.4773E+00 -.8141E-14 -.4007E+00
 CENTER OF PRESSURE I/A
 VORTEX INDUCED LOADS
 .3294E+00 .0137E+00 .0720E+00 .0137E+00

STRENGTHS AND POSITIONS OF CANARD VORTICES AT CANARD TRAILING EDGE

PANEL	CANARD/PIVA	Y/A	Z/A	Y/A	Z/A
1	.0548	.1781	.0225	.1781	1.9255
2	-.0921	-1.3898	-0.0333	-1.8898	0.0000
3	-.0699	.1781	-1.9394	.1781	-1.9394
4	.0423	1.8872	-0.0333	1.8872	0.0000

*** TOTAL CANARD FIN LOADS INCLUDING VORTEX EFFECTS ***

PANEL	ALPHAEO	CX	CPX	CPY	CRM	CB4	CM4
1	12.1316	.2029	.5394	.7337	.1540	.0593	-.0128
2	21.0381	.3280	.5136	.7793	.2573	.0333	-.0189
3	15.9234	.2542	.9111	.7459	.1922	.0719	-.0140
4	22.3862	.3373	.5139	.7788	.2642	.0457	-.0193

*** CONTRIBUTION OF CANARD SECTION TO TOTAL LOADS ***

UNROLLED COORDINATES				ROLLED COORDINATES			
CX0 =	.1193	CY0 =	-.0314	CX =	.1183	CXK =	-.0314
CY0 =	-.5594	CMY0 =	1.7567	CY =	-.5594	CYK =	1.7567
CZ0 =	.5424	CMZ0 =	1.1546	CZ =	.5424	CZK =	1.1696
CL =	.7735						
CU =	.1241						

Figure E.5(f). Continued.

***** AFTERBODY SECTION RESULTS FOR ALPHA = 16.00 AND PHI = 0.000 *****

***** VORTEX TRACKING RESULTS OVER AFTERBODY *****							
X/A	I	GAMMA(I)	Y(I)/A	Z(I)/A	FLDANG	THETA	SIDE FORCE
.6689E+01	1	.5482E-01	.1725E+01	.1726E+01	11.43	71.00	
	2	-.9215E-01	-.1130E+01	0.			
	3	-.6988E-01	.1732E+00	-.1109E+01			
	4	.9496E-01	.1337E+01	0.			

*** AFTERBODY VORTICES HAVE FORMED AT X/A = 5.69

THE LEFT VORTEX POSITION IS Y3/A = -.018 AND Z3/A = 1.129
 THE RIGHT VORTEX POSITION IS Y0/A = 1.120 AND Z0/A = .433

.7739E+01	1	.5482E-01	.1932E+01	.2124E+01	11.74	71.20	.0313	.0233
	2	-.9215E-01	-.1365E+01	.3256E+00				
	3	-.6988E-01	.2433E+00	-.1715E+01				
	4	.9496E-01	.8999E+01	.3276E+00				
	5	-.1522E-01	-.4295E+00	.1166E+01				
	6	.1611E-01	.1018E+01	.6423E+00				
.8793E+01	1	.5482E-01	.2195E+00	.2314E+01	12.37	71.92	.0390	.0248
	2	-.9215E-01	-.1855E+01	.6476E+00				
	3	-.6988E-01	.3378E+00	-.1526E+01				
	4	.9496E-01	.1900E+01	.6494E+00				
	5	-.3144E-01	-.2993E+00	.1262E+01				
	6	.3715E-01	.9532E+00	.7555E+00				
.9842E+01	1	.5482E-01	.2395E+00	.2504E+01	13.29	73.16	.0503	.0245
	2	-.9215E-01	-.1779E+01	.9594E+00				
	3	-.6988E-01	.4799E+00	-.1341E+01				
	4	.9496E-01	.1832E+01	.9685E+00				
	5	-.4516E-01	-.2143E+00	.1340E+01				
	6	.6144E-01	.9410E+00	.8277E+00				
.1089E+02	1	.5482E-01	.2556E+00	.2689E+01	14.48	75.19	.0642	.0192
	2	-.9215E-01	-.1799E+01	.1261E+01				
	3	-.6988E-01	.6755E+00	-.1225E+01				
	4	.9496E-01	.1571E+01	.2372E+01				
	5	-.6758E-01	-.1576E+00	.1437E+01				
	6	.8871E-01	.9711E+00	.6517E+00				
.1194E+02	1	.5482E-01	.2757E+00	.2872E+01	15.83	78.04	.0817	.0070
	2	-.9215E-01	-.1585E+01	.1553E+01				
	3	-.6988E-01	.9340E+00	-.0132E+00				
	4	.9496E-01	.1333E+01	.2392E+01				
	5	-.8662E-01	-.1256E+00	.1433E+01				
	6	.1178E+01	.1526E+01	.9478E+00				

Figure B.5(g). Continued.

.1300E+02	1	.5482E-01	.3342E+00	.3435E+01	10.31	83.59	.0991	-.0140
	2	-.9215E-01	-.1346E+01	.1347E+01				
	3	-.6988E-01	.1123E+01	-.3586E+02				
	4	.9496E-01	.1779E+01	.1966E+01				
	5	-.1064E+00	-.1355E+00	.1355E+01				
	6	.1472E+01	.1593E+01	.9548E+00				
.1405E+02	1	.5482E-01	.3215E+00	.3466E+01	17.28	87.98	.1310	-.0464
	2	-.9215E-01	-.1346E+01	.2122E+01				
	3	-.6988E-01	.1272E+01	.1263E+00				
	4	.9496E-01	.1716E+01	.2176E+01				
	5	-.1254E+00	-.9483E-01	.1356E+01				
	6	.1745E+00	.1167E+01	.1343E+01				
.1510E+02	1	.5482E-01	.3344E+00	.3466E+01	17.11	89.89	.2041	-.0780
	2	-.9215E-01	-.1346E+01	.2395E+01				
	3	-.6988E-01	.1413E+01	.4377E+00				
	4	.9496E-01	.1521E+01	.2439E+01				
	5	-.1433E+00	-.8397E-01	.1360E+01				
	6	.1975E+00	.1265E+01	.1169E+01				
.1615E+02	1	.5482E-01	.3335E+00	.3484E+01	16.81	90.32	.3769	-.0958
	2	-.9215E-01	-.1346E+01	.2556E+01				
	3	-.6988E-01	.1572E+01	.7609E+00				
	4	.9496E-01	.1588E+01	.2687E+01				
	5	-.1613E+00	-.8420E-01	.1585E+01				
	6	.2159E+00	.1394E+01	.1335E+01				
.1723E+02	1	.5482E-01	.3344E+00	.3508E+01	16.55	91.37	.5844	-.1045
	2	-.9215E-01	-.1346E+01	.2933E+01				
	3	-.6988E-01	.1582E+01	.1215E+01				
	4	.9496E-01	.1524E+01	.2923E+01				
	5	-.1769E+00	-.7665E-01	.1616E+01				
	6	.2317E+00	.1537E+01	.1567E+01				

*** CONTRIBUTION OF AFTERBODY SECTION TO TOTAL LOADS IN UNROLLLED BODY COORDINATES **

CVJ = -.240
 CMYD = -.824
 CZJ = .712
 CMZD = .991
 CL = .633
 CD = .234

Figure E.5(h). Continued.

DATA ALPHAS 24 2PA 2PV

1	0.0000	0.000	0.000	0.000
2	0.0000	0.000	0.000	0.000
3	0.0000	0.000	0.000	0.000
4	0.0000	0.000	0.000	0.000

*** WINTER TRACKING RESULTS OVER FINS ***

X	VORTEX	Y	Z	Y0	Z0
.1720E+02	1	.3644E+00	.360E+01	.3644E+00	.360E+01
	2	-.1258E+01	.271E+01	-.1258E+01	.271E+01
	3	.1622E+01	.215E+01	.1622E+01	.215E+01
	4	.1244E+01	.223E+01	.1244E+01	.223E+01
	5	-.7665E-01	.124E+01	-.7665E-01	.124E+01
	6	.1237E+01	.1567E+01	.1237E+01	.1567E+01
.1749E+02	1	.3609E+00	.338E+01	.3609E+00	.338E+01
	2	-.1233E+01	.266E+01	-.1233E+01	.266E+01
	3	.2254E+01	.136E+01	.2254E+01	.136E+01
	4	.1507E+01	.298E+01	.1507E+01	.298E+01
	5	-.7343E-01	.126E+01	-.7343E-01	.126E+01
	6	.1272E+01	.1539E+01	.1272E+01	.1539E+01
.1776E+02	1	.3609E+00	.367E+01	.3609E+00	.367E+01
	2	-.1209E+01	.302E+01	-.1209E+01	.302E+01
	3	.2113E+01	.153E+01	.2113E+01	.153E+01
	4	.2493E+01	.334E+01	.2493E+01	.334E+01
	5	-.5917E-01	.163E+01	-.5917E-01	.163E+01
	6	.1264E+01	.1717E+01	.1264E+01	.1717E+01
.1804E+02	1	.3759E+00	.369E+01	.3759E+00	.369E+01
	2	-.1186E+01	.308E+01	-.1186E+01	.308E+01
	3	.2156E+01	.156E+01	.2156E+01	.156E+01
	4	.2474E+01	.310E+01	.2474E+01	.310E+01
	5	-.5395E-01	.158E+01	-.5395E-01	.158E+01
	6	.1233E+01	.1749E+01	.1233E+01	.1749E+01
.1832E+02	1	.3725E+00	.372E+01	.3725E+00	.372E+01
	2	-.1162E+01	.314E+01	-.1162E+01	.314E+01
	3	.2179E+01	.159E+01	.2179E+01	.159E+01
	4	.2475E+01	.310E+01	.2475E+01	.310E+01
	5	-.5746E-01	.160E+01	-.5746E-01	.160E+01
	6	.1230E+01	.1749E+01	.1230E+01	.1749E+01
.1860E+02	1	.3741E+00	.374E+01	.3741E+00	.374E+01
	2	-.1128E+01	.310E+01	-.1128E+01	.310E+01
	3	.2182E+01	.162E+01	.2182E+01	.162E+01
	4	.2441E+01	.322E+01	.2441E+01	.322E+01
	5	-.5921E-01	.157E+01	-.5921E-01	.157E+01
	6	.1273E+01	.177E+01	.1273E+01	.177E+01

Figure E.5(1) Continued.

.1844E+02	1	.377E+01	.377E+01	.377E+01	.377E+01
	2	.377E+01	.377E+01	.377E+01	.377E+01
	3	.377E+01	.377E+01	.377E+01	.377E+01
	4	.377E+01	.377E+01	.377E+01	.377E+01
	5	.377E+01	.377E+01	.377E+01	.377E+01
	6	.377E+01	.377E+01	.377E+01	.377E+01
.1894E+02	1	.377E+01	.377E+01	.377E+01	.377E+01
	2	.377E+01	.377E+01	.377E+01	.377E+01
	3	.377E+01	.377E+01	.377E+01	.377E+01
	4	.377E+01	.377E+01	.377E+01	.377E+01
	5	.377E+01	.377E+01	.377E+01	.377E+01
	6	.377E+01	.377E+01	.377E+01	.377E+01
.1919E+02	1	.377E+01	.377E+01	.377E+01	.377E+01
	2	.377E+01	.377E+01	.377E+01	.377E+01
	3	.377E+01	.377E+01	.377E+01	.377E+01
	4	.377E+01	.377E+01	.377E+01	.377E+01
	5	.377E+01	.377E+01	.377E+01	.377E+01
	6	.377E+01	.377E+01	.377E+01	.377E+01
.1947E+02	1	.377E+01	.377E+01	.377E+01	.377E+01
	2	.377E+01	.377E+01	.377E+01	.377E+01
	3	.377E+01	.377E+01	.377E+01	.377E+01
	4	.377E+01	.377E+01	.377E+01	.377E+01
	5	.377E+01	.377E+01	.377E+01	.377E+01
	6	.377E+01	.377E+01	.377E+01	.377E+01
.1975E+02	1	.377E+01	.377E+01	.377E+01	.377E+01
	2	.377E+01	.377E+01	.377E+01	.377E+01
	3	.377E+01	.377E+01	.377E+01	.377E+01
	4	.377E+01	.377E+01	.377E+01	.377E+01
	5	.377E+01	.377E+01	.377E+01	.377E+01
	6	.377E+01	.377E+01	.377E+01	.377E+01
.2000E+02	1	.377E+01	.377E+01	.377E+01	.377E+01
	2	.377E+01	.377E+01	.377E+01	.377E+01
	3	.377E+01	.377E+01	.377E+01	.377E+01
	4	.377E+01	.377E+01	.377E+01	.377E+01
	5	.377E+01	.377E+01	.377E+01	.377E+01
	6	.377E+01	.377E+01	.377E+01	.377E+01

Figure E.5(j). Continued.

VORTEX INDUCED EQUIVALENT
ANGLE OF ATTACK, DEGREES

CENTER OF PRESSURE FOR
VORTEX INDUCED LOADS

FIN 1 FIN 2 FIN 3 FIN 4

.4475E+01 .0150E+01 .2610E+01 -.7271E+01

.1635E+00 .1323E+01 .9325E+00 .9387E+00

*** TOTAL TAIL FIN LOADS INCLUDING VORTEX EFF=CTS ***

PANEL	ALPHA	CM	CPX	CPY	CM
1	4.4758	.1337	.7196	.8124	.0199
2	24.5576	.8029	.7364	.8138	.6448
3	2.4134	.0656	.7196	.8138	.0313
4	16.4859	.5775	.7964	.8138	.5378

*** CONTRIBUTION OF TAIL SECTION TO TOTAL LOADS ***

UNROLLED COORDINATES

CX0 = 0.0000	CY0 = -.1270	CZ0 = 1.8470	CMX = -.1270	CMY = -.7.8938	CMZ = -1.1245
CL = 1.7720	CD = .5277				

ROLLED COORDINATES

CX = 0.0000	CY = -.2667	CZ = 1.8470	CMX = -.15838	CMY = -3.98339	CMZ = .94644
-------------	-------------	-------------	---------------	----------------	--------------

*** SUMMARY OF TOTAL LOADS IN BODY COORDINATES ***

ALPHA = 16.600 PHI = 3.020

UNROLLED COORDINATES

CX0 = .11932	CY0 = -.15838	CZ0 = -3.98339	CMX = .11832	CMY = -3.98339	CMZ = .94644
CL = 3.99550	CPX = 0.14745	CD = 1.31451			

ROLLED COORDINATES

CX = .11832	CY = -1.06615	CZ = 4.20433	CMX = -.15838	CMY = -3.98339	CMZ = .94644
-------------	---------------	--------------	---------------	----------------	--------------

END OF CALCULATIONS FOR ALPHA SLEEP AT PHI = 3.000

END OF CALCULATIONS FOR THIS CASE

Figure E.5(k). Concluded.

The configuration is shown in figure 3(h) of the main text and is the MICOM-NWC model of reference 4 with the N_3 nose, the C_e canard fins, and the T_2 tail fins. The angle of attack is 16.6° , the model is at a bank angle of 0° , and the yaw panels (canard panels 1 and 3) are deflected 15° . The pitch panels are not deflected. Mach number is 1.75 and the crossflow is considered turbulent. The values of five interference factors (KBC,XBC,KWT,KBT,XBT) were input. These values were obtained from running the wing-body computer program CRFWBD described in Appendix F and reference 3. The influence of nose vortices is calculated to the canard trailing edge (NVORT = 2). Both NEARC and NEART are set equal to .TRUE. The maximum vortex induced velocity on the fins is limited to $0.4 V_\infty$ (RO = -0.4). Afterbody vortices (if they form) are initially positioned at 1.2 radii from the body axis (RVOA = 1.2). Finally, vortices of like sign are combined along the afterbody if they come within a distance of 0.5 body radii of one another (RVORT = 0.5). The input deck for this case is shown in figure E.4. The output is presented in figure E.5.

E.7. PROGRAM LISTING

The program is written in FORTRAN IV computer language (029 punch). The program consists of a main program, MLOADS, and twenty-eight subprograms. Each source deck is identified in columns 73 through 80 by a three-character identification and a three-digit number sequencing the cards within that deck. The program listing is given on the following pages. The table below will act as a table of contents for the listing.

<u>PROGRAM</u>	<u>IDENTIFICATION</u>	<u>PAGE NO.</u>
MLOADS	M01	197
INPT	M02	198
NOSE	M03	200
CANARD	M04	202
ALFAQ	M05	203
VORTEX	M06	203
CRUTRJ	M07	204

<u>PROGRAM</u>	<u>IDENTIFICATION</u>	<u>PAGE NO.</u>
FCT	M08	205
SHAPE	M09	205
DASCRU	M10	205
REVFLO	M11	206
SIMSON	M12	207
VEL	M13	207
CEL1	M14	208
CEL2	M15	208
ELI1	M16	208
ELI2	M17	208
LNTRP	M18	209
CURVES	M19	209
AFTBOD	M20	210
DERIV	M21	212
TAIL	M22	212
CHRT8	M23	213
EQ24	M24	214
EQ26	M25	214
EQ30	M26	214
EQ31	M27	214
CH1416	M28	214
INTFAC	M29	216

REFERENCE

- E.1. Mendenhall, M. R., Goodwin, F. K., Dillenius, M. F. E., and Kline, D. M.: Computer Programs for Calculating the Static Longitudinal Aerodynamic Characteristics of Wing-Body-Tail Configurations. NASA CR-2474, Jan. 1975.

AD-A034 722

NIELSEN ENGINEERING AND RESEARCH INC MOUNTAIN VIEW CALIF F/G 16/4
CALCULATION OF COMPONENT FORCES AND MOMENTS OF ARBITRARILY BANK--ETC(U)
NOV 76 M J HEMSCH, C A SMITH, J N NIELSEN N00014-74-C-0050

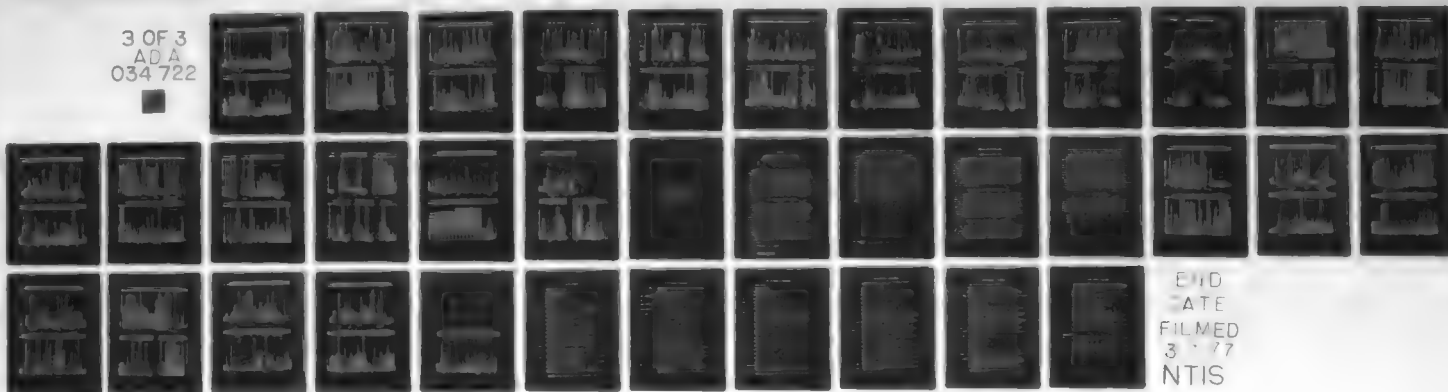
UNCLASSIFIED

NEAR-TR-125

ONR-CR215-226-3

NL

3 OF 3
ADA
034 722




```

C 3450 CANDECO=8ALFACOT/SHOUT
C
C 3460 IN ORDER TO DETERMINE THE CENTER OF PRESSURE OF THE POTENTIAL
C 3470 NORMAL FORCE, MUST FIRST CALCULATE THE NOSE VOLUME BACK TO THE
C 3480 SHOULDER
C
C 3490 VOLUME=0
C 3500 DO 20 I=2,NNOSE
C 3510 VOLUME=VOLUME+XNOSE(I)*XNOSE(I-1)+XNOSE(I)*XNOSE(I+1)+XNOSE(I)*XNOSE(I+2)
C 3520 CONTINUE
C 3530 VOLUME=VOLUME*PI/3
C 3540 XBAR=VOLUME/PI
C 3550 XBAR=XBAR+XNOSE(1)*XNOSE(1)/XNOSE(1)
C 3560 XBAR=XBAR+XNOSE(2)*XNOSE(2)/XNOSE(2)
C 3570 XBAR=XBAR+XNOSE(3)*XNOSE(3)/XNOSE(3)
C 3580 XBAR=XBAR+XNOSE(4)*XNOSE(4)/XNOSE(4)
C 3590 XBAR=XBAR+XNOSE(5)*XNOSE(5)/XNOSE(5)
C 3600 XBAR=XBAR+XNOSE(6)*XNOSE(6)/XNOSE(6)
C 3610 XBAR=XBAR+XNOSE(7)*XNOSE(7)/XNOSE(7)
C 3620 XBAR=XBAR+XNOSE(8)*XNOSE(8)/XNOSE(8)
C 3630 XBAR=XBAR+XNOSE(9)*XNOSE(9)/XNOSE(9)
C 3640 XBAR=XBAR+XNOSE(10)*XNOSE(10)/XNOSE(10)
C 3650 XBAR=XBAR+XNOSE(11)*XNOSE(11)/XNOSE(11)
C 3660 XBAR=XBAR+XNOSE(12)*XNOSE(12)/XNOSE(12)
C 3670 XBAR=XBAR+XNOSE(13)*XNOSE(13)/XNOSE(13)
C 3680 XBAR=XBAR+XNOSE(14)*XNOSE(14)/XNOSE(14)
C 3690 XBAR=XBAR+XNOSE(15)*XNOSE(15)/XNOSE(15)
C 3700 XBAR=XBAR+XNOSE(16)*XNOSE(16)/XNOSE(16)
C 3710 XBAR=XBAR+XNOSE(17)*XNOSE(17)/XNOSE(17)
C 3720 XBAR=XBAR+XNOSE(18)*XNOSE(18)/XNOSE(18)
C 3730 XBAR=XBAR+XNOSE(19)*XNOSE(19)/XNOSE(19)
C 3740 XBAR=XBAR+XNOSE(20)*XNOSE(20)/XNOSE(20)
C 3750 XBAR=XBAR+XNOSE(21)*XNOSE(21)/XNOSE(21)
C 3760 XBAR=XBAR+XNOSE(22)*XNOSE(22)/XNOSE(22)
C 3770 XBAR=XBAR+XNOSE(23)*XNOSE(23)/XNOSE(23)
C 3780 XBAR=XBAR+XNOSE(24)*XNOSE(24)/XNOSE(24)
C 3790 XBAR=XBAR+XNOSE(25)*XNOSE(25)/XNOSE(25)
C 3800 XBAR=XBAR+XNOSE(26)*XNOSE(26)/XNOSE(26)
C 3810 XBAR=XBAR+XNOSE(27)*XNOSE(27)/XNOSE(27)
C 3820 XBAR=XBAR+XNOSE(28)*XNOSE(28)/XNOSE(28)
C 3830 XBAR=XBAR+XNOSE(29)*XNOSE(29)/XNOSE(29)
C 3840 XBAR=XBAR+XNOSE(30)*XNOSE(30)/XNOSE(30)
C 3850 XBAR=XBAR+XNOSE(31)*XNOSE(31)/XNOSE(31)
C 3860 XBAR=XBAR+XNOSE(32)*XNOSE(32)/XNOSE(32)
C 3870 XBAR=XBAR+XNOSE(33)*XNOSE(33)/XNOSE(33)
C 3880 XBAR=XBAR+XNOSE(34)*XNOSE(34)/XNOSE(34)
C 3890 XBAR=XBAR+XNOSE(35)*XNOSE(35)/XNOSE(35)
C 3900 XBAR=XBAR+XNOSE(36)*XNOSE(36)/XNOSE(36)
C 3910 XBAR=XBAR+XNOSE(37)*XNOSE(37)/XNOSE(37)
C 3920 XBAR=XBAR+XNOSE(38)*XNOSE(38)/XNOSE(38)
C 3930 XBAR=XBAR+XNOSE(39)*XNOSE(39)/XNOSE(39)
C 3940 XBAR=XBAR+XNOSE(40)*XNOSE(40)/XNOSE(40)
C 3950 XBAR=XBAR+XNOSE(41)*XNOSE(41)/XNOSE(41)
C 3960 XBAR=XBAR+XNOSE(42)*XNOSE(42)/XNOSE(42)
C 3970 XBAR=XBAR+XNOSE(43)*XNOSE(43)/XNOSE(43)
C 3980 XBAR=XBAR+XNOSE(44)*XNOSE(44)/XNOSE(44)
C 3990 XBAR=XBAR+XNOSE(45)*XNOSE(45)/XNOSE(45)
C 4000 XBAR=XBAR+XNOSE(46)*XNOSE(46)/XNOSE(46)
C 4010 XBAR=XBAR+XNOSE(47)*XNOSE(47)/XNOSE(47)
C 4020 XBAR=XBAR+XNOSE(48)*XNOSE(48)/XNOSE(48)
C 4030 XBAR=XBAR+XNOSE(49)*XNOSE(49)/XNOSE(49)
C 4040 XBAR=XBAR+XNOSE(50)*XNOSE(50)/XNOSE(50)
C 4050 XBAR=XBAR+XNOSE(51)*XNOSE(51)/XNOSE(51)
C 4060 XBAR=XBAR+XNOSE(52)*XNOSE(52)/XNOSE(52)
C 4070 XBAR=XBAR+XNOSE(53)*XNOSE(53)/XNOSE(53)
C 4080 XBAR=XBAR+XNOSE(54)*XNOSE(54)/XNOSE(54)
C 4090 XBAR=XBAR+XNOSE(55)*XNOSE(55)/XNOSE(55)
C 4100 XBAR=XBAR+XNOSE(56)*XNOSE(56)/XNOSE(56)
C 4110 XBAR=XBAR+XNOSE(57)*XNOSE(57)/XNOSE(57)
C 4120 XBAR=XBAR+XNOSE(58)*XNOSE(58)/XNOSE(58)
C 4130 XBAR=XBAR+XNOSE(59)*XNOSE(59)/XNOSE(59)
C 4140 XBAR=XBAR+XNOSE(60)*XNOSE(60)/XNOSE(60)
C 4150 XBAR=XBAR+XNOSE(61)*XNOSE(61)/XNOSE(61)
C 4160 XBAR=XBAR+XNOSE(62)*XNOSE(62)/XNOSE(62)
C 4170 XBAR=XBAR+XNOSE(63)*XNOSE(63)/XNOSE(63)
C 4180 XBAR=XBAR+XNOSE(64)*XNOSE(64)/XNOSE(64)
C 4190 XBAR=XBAR+XNOSE(65)*XNOSE(65)/XNOSE(65)
C 4200 XBAR=XBAR+XNOSE(66)*XNOSE(66)/XNOSE(66)
C 4210 XBAR=XBAR+XNOSE(67)*XNOSE(67)/XNOSE(67)
C 4220 XBAR=XBAR+XNOSE(68)*XNOSE(68)/XNOSE(68)
C 4230 XBAR=XBAR+XNOSE(69)*XNOSE(69)/XNOSE(69)
C 4240 XBAR=XBAR+XNOSE(70)*XNOSE(70)/XNOSE(70)
C 4250 XBAR=XBAR+XNOSE(71)*XNOSE(71)/XNOSE(71)
C 4260 XBAR=XBAR+XNOSE(72)*XNOSE(72)/XNOSE(72)
C 4270 XBAR=XBAR+XNOSE(73)*XNOSE(73)/XNOSE(73)
C 4280 XBAR=XBAR+XNOSE(74)*XNOSE(74)/XNOSE(74)
C 4290 XBAR=XBAR+XNOSE(75)*XNOSE(75)/XNOSE(75)
C 4300 XBAR=XBAR+XNOSE(76)*XNOSE(76)/XNOSE(76)
C 4310 XBAR=XBAR+XNOSE(77)*XNOSE(77)/XNOSE(77)
C 4320 XBAR=XBAR+XNOSE(78)*XNOSE(78)/XNOSE(78)
C 4330 XBAR=XBAR+XNOSE(79)*XNOSE(79)/XNOSE(79)
C 4340 XBAR=XBAR+XNOSE(80)*XNOSE(80)/XNOSE(80)
C 4350 XBAR=XBAR+XNOSE(81)*XNOSE(81)/XNOSE(81)
C 4360 XBAR=XBAR+XNOSE(82)*XNOSE(82)/XNOSE(82)
C 4370 XBAR=XBAR+XNOSE(83)*XNOSE(83)/XNOSE(83)
C 4380 XBAR=XBAR+XNOSE(84)*XNOSE(84)/XNOSE(84)
C 4390 XBAR=XBAR+XNOSE(85)*XNOSE(85)/XNOSE(85)
C 4400 XBAR=XBAR+XNOSE(86)*XNOSE(86)/XNOSE(86)
C 4410 XBAR=XBAR+XNOSE(87)*XNOSE(87)/XNOSE(87)
C 4420 XBAR=XBAR+XNOSE(88)*XNOSE(88)/XNOSE(88)
C 4430 XBAR=XBAR+XNOSE(89)*XNOSE(89)/XNOSE(89)
C 4440 XBAR=XBAR+XNOSE(90)*XNOSE(90)/XNOSE(90)
C 4450 XBAR=XBAR+XNOSE(91)*XNOSE(91)/XNOSE(91)
C 4460 XBAR=XBAR+XNOSE(92)*XNOSE(92)/XNOSE(92)
C 4470 XBAR=XBAR+XNOSE(93)*XNOSE(93)/XNOSE(93)
C 4480 XBAR=XBAR+XNOSE(94)*XNOSE(94)/XNOSE(94)
C 4490 XBAR=XBAR+XNOSE(95)*XNOSE(95)/XNOSE(95)
C 4500 XBAR=XBAR+XNOSE(96)*XNOSE(96)/XNOSE(96)
C 4510 XBAR=XBAR+XNOSE(97)*XNOSE(97)/XNOSE(97)
C 4520 XBAR=XBAR+XNOSE(98)*XNOSE(98)/XNOSE(98)
C 4530 XBAR=XBAR+XNOSE(99)*XNOSE(99)/XNOSE(99)
C 4540 XBAR=XBAR+XNOSE(100)*XNOSE(100)/XNOSE(100)
C 4550 XBAR=XBAR+XNOSE(101)*XNOSE(101)/XNOSE(101)
C 4560 XBAR=XBAR+XNOSE(102)*XNOSE(102)/XNOSE(102)
C 4570 XBAR=XBAR+XNOSE(103)*XNOSE(103)/XNOSE(103)
C 4580 XBAR=XBAR+XNOSE(104)*XNOSE(104)/XNOSE(104)
C 4590 XBAR=XBAR+XNOSE(105)*XNOSE(105)/XNOSE(105)
C 4600 XBAR=XBAR+XNOSE(106)*XNOSE(106)/XNOSE(106)
C 4610 XBAR=XBAR+XNOSE(107)*XNOSE(107)/XNOSE(107)
C 4620 XBAR=XBAR+XNOSE(108)*XNOSE(108)/XNOSE(108)
C 4630 XBAR=XBAR+XNOSE(109)*XNOSE(109)/XNOSE(109)
C 4640 XBAR=XBAR+XNOSE(110)*XNOSE(110)/XNOSE(110)
C 4650 XBAR=XBAR+XNOSE(111)*XNOSE(111)/XNOSE(111)
C 4660 XBAR=XBAR+XNOSE(112)*XNOSE(112)/XNOSE(112)
C 4670 XBAR=XBAR+XNOSE(113)*XNOSE(113)/XNOSE(113)
C 4680 XBAR=XBAR+XNOSE(114)*XNOSE(114)/XNOSE(114)
C 4690 XBAR=XBAR+XNOSE(115)*XNOSE(115)/XNOSE(115)
C 4700 XBAR=XBAR+XNOSE(116)*XNOSE(116)/XNOSE(116)
C 4710 XBAR=XBAR+XNOSE(117)*XNOSE(117)/XNOSE(117)
C 4720 XBAR=XBAR+
```


SUBROUTINE CELL(RES,AK,IER)

```

C      IERR=0
C      TEST MODULUS
C      SECD=1.0E+08
C      IF(ABS(RES))
C      1 RETURN
C      SET RESULT VALUE = OVFLOW
C      2 RES=1.0E+30
C      RETURN
C      3 IF(ABS(RES))
C      4 IERR=1
C      TEST(RES)=1.0E+08
C      AR=1.0E+08
C      AR=1.0E+08
C      TEST OF ACCURACY
C      IF(ABS(RES)-TEST)0.0,5
C      5 SECD=1.0E+08
C      IF(ABS(RES))
C      6 RES=1.0E+30
C      RETURN
C      END

```

M14 2
M14 3
M14 4
M14 5
M14 6
M14 7
M14 8
M14 9
M14 10
M14 11
M14 12
M14 13
M14 14
M14 15
M14 16
M14 17
M14 18
M14 19
M14 20
M14 21
M14 22
M14 23
M14 24
M14 25
M14 26
M14 27
M14 28
M14 29
M14 30
M14 31

M19 30
M19 31
M19 32
M19 33
M19 34
M19 35
M19 36
M19 37
M19 38
M19 39
M19 40
M19 41
M19 42
M19 43
M19 44
M19 45

```

C      TEST OF ACCURACY
C      IF(ABS(RES)-TEST)0.0,5
C      5 SECD=1.0E+08
C      IF(ABS(RES))
C      6 RES=1.0E+30
C      RETURN
C      END

```

M14 2
M14 3
M14 4
M14 5
M14 6
M14 7
M14 8
M14 9
M14 10
M14 11
M14 12
M14 13
M14 14
M14 15
M14 16
M14 17
M14 18
M14 19
M14 20
M14 21
M14 22
M14 23
M14 24
M14 25
M14 26
M14 27
M14 28
M14 29
M14 30
M14 31

SUBROUTINE EL11(RES,X,CK)

```

C      IF(X)2,1,2
C      1 RES=0
C      RETURN
C      2 IF(CK)3,4,3,6
C      3 RES=ALOG(ABS(X)+SORT(1,X,X))
C      4 RES=ALOG(1/X)
C      5 RES=0
C      6 RES=0
C      7 RES=0
C      8 RES=0
C      9 RES=0
C      10 RES=0
C      11 RES=0
C      12 RES=0
C      13 RES=0
C      14 RES=0
C      15 RES=0
C      16 RES=0
C      17 RES=0
C      18 RES=0
C      19 RES=0
C      20 RES=0
C      21 RES=0
C      22 RES=0
C      23 RES=0
C      24 RES=0
C      25 RES=0
C      26 RES=0
C      27 RES=0
C      28 RES=0
C      29 RES=0
C      30 RES=0
C      31 RES=0

```

M10 2
M10 3
M10 4
M10 5
M10 6
M10 7
M10 8
M10 9
M10 10
M10 11
M10 12
M10 13
M10 14
M10 15
M10 16
M10 17
M10 18
M10 19
M10 20
M10 21
M10 22
M10 23
M10 24
M10 25
M10 26
M10 27
M10 28
M10 29
M10 30
M10 31

SUBROUTINE CELL(RES,AK,IER)

```

C      IERR=0
C      TEST MODULUS
C      SECD=1.0E+08
C      IF(ABS(RES))
C      1 RETURN
C      SET RESULT VALUE = OVFLOW
C      2 RES=1.0E+30
C      RETURN
C      3 IF(ABS(RES))
C      4 IERR=1
C      TEST(RES)=1.0E+08
C      AR=1.0E+08
C      AR=1.0E+08
C      TEST OF ACCURACY
C      IF(ABS(RES)-TEST)0.0,5
C      5 SECD=1.0E+08
C      IF(ABS(RES))
C      6 RES=1.0E+30
C      RETURN
C      END

```

M15 2
M15 3
M15 4
M15 5
M15 6
M15 7
M15 8
M15 9
M15 10
M15 11
M15 12
M15 13
M15 14
M15 15
M15 16
M15 17
M15 18
M15 19
M15 20
M15 21
M15 22
M15 23
M15 24
M15 25
M15 26
M15 27
M15 28
M15 29
M15 30
M15 31

M16 30
M16 31
M16 32
M16 33
M16 34
M16 35
M16 36
M16 37
M16 38
M16 39
M16 40
M16 41
M16 42
M16 43
M16 44
M16 45

```

C      TEST OF ACCURACY
C      IF(ABS(RES)-TEST)0.0,5
C      5 SECD=1.0E+08
C      IF(ABS(RES))
C      6 RES=1.0E+30
C      RETURN
C      END

```

M17 30
M17 31
M17 32
M17 33
M17 34
M17 35
M17 36
M17 37
M17 38
M17 39
M17 40
M17 41
M17 42
M17 43
M17 44
M17 45

```

C RETURN
C 7 INITIALIZATION
C 8 ANGLE=PI/180
C 9
C 10
C 11
C 12
C 13
C 14
C 15
C 16
C 17
C 18
C 19
C 20
C 21
C 22
C 23
C 24
C 25
C 26
C 27
C 28
C 29
C 30
C 31
C 32
C 33
C 34
C 35
C 36
C 37
C 38
C 39
C 40
C 41
C 42
C 43
C 44
C 45
C 46
C 47
C 48
C 49
C 50
C 51
C 52
C 53
C 54
C 55
C 56
C 57
C 58
C 59
C 60
C 61
C 62
C 63
C 64
C 65
C 66
C 67
C 68
C 69
C 70
C 71
C 72
C 73
C 74
C 75
C 76
C 77
C 78
C 79
C 80
C 81
C 82
C 83
C 84
C 85
C 86
C 87
C 88
C 89
C 90
C 91
C 92
C 93
C 94
C 95
C 96
C 97
C 98
C 99
C 100
C 101
C 102
C 103
C 104
C 105
C 106
C 107
C 108
C 109
C 110
C 111
C 112
C 113
C 114
C 115
C 116
C 117
C 118
C 119
C 120
C 121
C 122
C 123
C 124
C 125
C 126
C 127
C 128
C 129
C 130
C 131
C 132
C 133
C 134
C 135
C 136
C 137
C 138
C 139
C 140
C 141
C 142
C 143
C 144
C 145
C 146
C 147
C 148
C 149
C 150
C 151
C 152
C 153
C 154
C 155
C 156
C 157
C 158
C 159
C 160
C 161
C 162
C 163
C 164
C 165
C 166
C 167
C 168
C 169
C 170
C 171
C 172
C 173
C 174
C 175
C 176
C 177
C 178
C 179
C 180
C 181
C 182
C 183
C 184
C 185
C 186
C 187
C 188
C 189
C 190
C 191
C 192
C 193
C 194
C 195
C 196
C 197
C 198
C 199
C 200
C 201
C 202
C 203
C 204
C 205
C 206
C 207
C 208
C 209
C 210
C 211
C 212
C 213
C 214
C 215
C 216
C 217
C 218
C 219
C 220
C 221
C 222
C 223
C 224
C 225
C 226
C 227
C 228
C 229
C 230
C 231
C 232
C 233
C 234
C 235
C 236
C 237
C 238
C 239
C 240
C 241
C 242
C 243
C 244
C 245
C 246
C 247
C 248
C 249
C 250
C 251
C 252
C 253
C 254
C 255
C 256
C 257
C 258
C 259
C 260
C 261
C 262
C 263
C 264
C 265
C 266
C 267
C 268
C 269
C 270
C 271
C 272
C 273
C 274
C 275
C 276
C 277
C 278
C 279
C 280
C 281
C 282
C 283
C 284
C 285
C 286
C 287
C 288
C 289
C 290
C 291
C 292
C 293
C 294
C 295
C 296
C 297
C 298
C 299
C 300
C 301
C 302
C 303
C 304
C 305
C 306
C 307
C 308
C 309
C 310
C 311
C 312
C 313
C 314
C 315
C 316
C 317
C 318
C 319
C 320
C 321
C 322
C 323
C 324
C 325
C 326
C 327
C 328
C 329
C 330
C 331
C 332
C 333
C 334
C 335
C 336
C 337
C 338
C 339
C 340
C 341
C 342
C 343
C 344
C 345
C 346
C 347
C 348
C 349
C 350
C 351
C 352
C 353
C 354
C 355
C 356
C 357
C 358
C 359
C 360
C 361
C 362
C 363
C 364
C 365
C 366
C 367
C 368
C 369
C 370
C 371
C 372
C 373
C 374
C 375
C 376
C 377
C 378
C 379
C 380
C 381
C 382
C 383
C 384
C 385
C 386
C 387
C 388
C 389
C 390
C 391
C 392
C 393
C 394
C 395
C 396
C 397
C 398
C 399
C 400
C 401
C 402
C 403
C 404
C 405
C 406
C 407
C 408
C 409
C 410
C 411
C 412
C 413
C 414
C 415
C 416
C 417
C 418
C 419
C 420
C 421
C 422
C 423
C 424
C 425
C 426
C 427
C 428
C 429
C 430
C 431
C 432
C 433
C 434
C 435
C 436
C 437
C 438
C 439
C 440
C 441
C 442
C 443
C 444
C 445
C 446
C 447
C 448
C 449
C 450
C 451
C 452
C 453
C 454
C 455
C 456
C 457
C 458
C 459
C 460
C 461
C 462
C 463
C 464
C 465
C 466
C 467
C 468
C 469
C 470
C 471
C 472
C 473
C 474
C 475
C 476
C 477
C 478
C 479
C 480
C 481
C 482
C 483
C 484
C 485
C 486
C 487
C 488
C 489
C 490
C 491
C 492
C 493
C 494
C 495
C 496
C 497
C 498
C 499
C 500
C 501
C 502
C 503
C 504
C 505
C 506
C 507
C 508
C 509
C 510
C 511
C 512
C 513
C 514
C 515
C 516
C 517
C 518
C 519
C 520
C 521
C 522
C 523
C 524
C 525
C 526
C 527
C 528
C 529
C 530
C 531
C 532
C 533
C 534
C 535
C 536
C 537
C 538
C 539
C 540
C 541
C 542
C 543
C 544
C 545
C 546
C 547
C 548
C 549
C 550
C 551
C 552
C 553
C 554
C 555
C 556
C 557
C 558
C 559
C 560
C 561
C 562
C 563
C 564
C 565
C 566
C 567
C 568
C 569
C 570
C 571
C 572
C 573
C 574
C 575
C 576
C 577
C 578
C 579
C 580
C 581
C 582
C 583
C 584
C 585
C 586
C 587
C 588
C 589
C 590
C 591
C 592
C 593
C 594
C 595
C 596
C 597
C 598
C 599
C 600
C 601
C 602
C 603
C 604
C 605
C 606
C 607
C 608
C 609
C 610
C 611
C 612
C 613
C 614
C 615
C 616
C 617
C 618
C 619
C 620
C 621
C 622
C 623
C 624
C 625
C 626
C 627
C 628
C 629
C 630
C 631
C 632
C 633
C 634
C 635
C 636
C 637
C 638
C 639
C 640
C 641
C 642
C 643
C 644
C 645
C 646
C 647
C 648
C 649
C 650
C 651
C 652
C 653
C 654
C 655
C 656
C 657
C 658
C 659
C 660
C 661
C 662
C 663
C 664
C 665
C 666
C 667
C 668
C 669
C 670
C 671
C 672
C 673
C 674
C 675
C 676
C 677
C 678
C 679
C 680
C 681
C 682
C 683
C 684
C 685
C 686
C 687
C 688
C 689
C 690
C 691
C 692
C 693
C 694
C 695
C 696
C 697
C 698
C 699
C 700
C 701
C 702
C 703
C 704
C 705
C 706
C 707
C 708
C 709
C 710
C 711
C 712
C 713
C 714
C 715
C 716
C 717
C 718
C 719
C 720
C 721
C 722
C 723
C 724
C 725
C 726
C 727
C 728
C 729
C 730
C 731
C 732
C 733
C 734
C 735
C 736
C 737
C 738
C 739
C 740
C 741
C 742
C 743
C 744
C 745
C 746
C 747
C 748
C 749
C 750
C 751
C 752
C 753
C 754
C 755
C 756
C 757
C 758
C 759
C 760
C 761
C 762
C 763
C 764
C 765
C 766
C 767
C 768
C 769
C 770
C 771
C 772
C 773
C 774
C 775
C 776
C 777
C 778
C 779
C 780
C 781
C 782
C 783
C 784
C 785
C 786
C 787
C 788
C 789
C 790
C 791
C 792
C 793
C 794
C 795
C 796
C 797
C 798
C 799
C 800
C 801
C 802
C 803
C 804
C 805
C 806
C 807
C 808
C 809
C 810
C 811
C 812
C 813
C 814
C 815
C 816
C 817
C 818
C 819
C 820
C 821
C 822
C 823
C 824
C 825
C 826
C 827
C 828
C 829
C 830
C 831
C 832
C 833
C 834
C 835
C 836
C 837
C 838
C 839
C 840
C 841
C 842
C 843
C 844
C 845
C 846
C 847
C 848
C 849
C 850
C 851
C 852
C 853
C 854
C 855
C 856
C 857
C 858
C 859
C 860
C 861
C 862
C 863
C 864
C 865
C 866
C 867
C 868
C 869
C 870
C 871
C 872
C 873
C 874
C 875
C 876
C 877
C 878
C 879
C 880
C 881
C 882
C 883
C 884
C 885
C 886
C 887
C 888
C 889
C 890
C 891
C 892
C 893
C 894
C 895
C 896
C 897
C 898
C 899
C 900
C 901
C 902
C 903
C 904
C 905
C 906
C 907
C 908
C 909
C 910
C 911
C 912
C 913
C 914
C 915
C 916
C 917
C 918
C 919
C 920
C 921
C 922
C 923
C 924
C 925
C 926
C 927
C 928
C 929
C 930
C 931
C 932
C 933
C 934
C 935
C 936
C 937
C 938
C 939
C 940
C 941
C 942
C 943
C 944
C 945
C 946
C 947
C 948
C 949
C 950
C 951
C 952
C 953
C 954
C 955
C 956
C 957
C 958
C 959
C 960
C 961
C 962
C 963
C 964
C 965
C 966
C 967
C 968
C 969
C 970
C 971
C 972
C 973
C 974
C 975
C 976
C 977
C 978
C 979
C 980
C 981
C 982
C 983
C 984
C 985
C 986
C 987
C 988
C 989
C 990
C 991
C 992
C 993
C 994
C 995
C 996
C 997
C 998
C 999
C 1000

```


218


```

100 C=7941.08/(C-999*(V-C=1.0))
101 S=S+DCC*E/(1.1+1997*(1+282+1.0)*((1.0/NB=1.0)+NB))
102 RETURN
103 GO TO 60
104 RETURN
105 GO TO 20
106 RETURN
107 END

```

```

2
3
4
5
6
7
8
9
10
11
12
13
14
15
16
17
18
19
20
21
22
23
24
25
26
27
28
29
30
31
32
33
34
35
36
37
38
39
40
41
42
43
44
45
46
47
48
49
50
51
52
53
54
55
56
57
58
59
60
61
62
63
64
65
66
67
68
69
70
71
72
73
74
75
76
77
78
79
80
81
82
83
84
85
86
87
88
89
90
91
92
93
94
95
96
97
98
99
100
101
102
103
104
105
106
107
108
109
110
111
112
113
114
115
116
117
118
119
120
121
122
123
124
125
126
127
128
129
130
131
132
133
134
135
136
137
138
139
140
141
142
143
144
145
146
147
148
149
150
151
152
153
154
155
156
157
158
159
160
161
162
163
164
165
166
167
168
169
170
171
172
173
174
175
176
177
178
179
180
181
182
183
184
185
186
187
188
189
190
191
192
193
194
195
196
197
198
199
200
201
202
203
204
205
206
207
208
209
210
211
212
213
214
215
216
217
218
219
220
221
222
223
224
225
226
227
228
229
230
231
232
233
234
235
236
237
238
239
240
241
242
243
244
245
246
247
248
249
250
251
252
253
254
255
256
257
258
259
260
261
262
263
264
265
266
267
268
269
270
271
272
273
274
275
276
277
278
279
280
281
282
283
284
285
286
287
288
289
290
291
292
293
294
295
296
297
298
299
300
301
302
303
304
305
306
307
308
309
310
311
312
313
314
315
316
317
318
319
320
321
322
323
324
325
326
327
328
329
330
331
332
333
334
335
336
337
338
339
340
341
342
343
344
345
346
347
348
349
350
351
352
353
354
355
356
357
358
359
360
361
362
363
364
365
366
367
368
369
370
371
372
373
374
375
376
377
378
379
380
381
382
383
384
385
386
387
388
389
390
391
392
393
394
395
396
397
398
399
400
401
402
403
404
405
406
407
408
409
410
411
412
413
414
415
416
417
418
419
420
421
422
423
424
425
426
427
428
429
430
431
432
433
434
435
436
437
438
439
440
441
442
443
444
445
446
447
448
449
450
451
452
453
454
455
456
457
458
459
460
461
462
463
464
465
466
467
468
469
470
471
472
473
474
475
476
477
478
479
480
481
482
483
484
485
486
487
488
489
490
491
492
493
494
495
496
497
498
499
500
501
502
503
504
505
506
507
508
509
510
511
512
513
514
515
516
517
518
519
520
521
522
523
524
525
526
527
528
529
530
531
532
533
534
535
536
537
538
539
540
541
542
543
544
545
546
547
548
549
550
551
552
553
554
555
556
557
558
559
560
561
562
563
564
565
566
567
568
569
570
571
572
573
574
575
576
577
578
579
580
581
582
583
584
585
586
587
588
589
590
591
592
593
594
595
596
597
598
599
600
601
602
603
604
605
606
607
608
609
610
611
612
613
614
615
616
617
618
619
620
621
622
623
624
625
626
627
628
629
630
631
632
633
634
635
636
637
638
639
640
641
642
643
644
645
646
647
648
649
650
651
652
653
654
655
656
657
658
659
660
661
662
663
664
665
666
667
668
669
670
671
672
673
674
675
676
677
678
679
680
681
682
683
684
685
686
687
688
689
690
691
692
693
694
695
696
697
698
699
700
701
702
703
704
705
706
707
708
709
710
711
712
713
714
715
716
717
718
719
720
721
722
723
724
725
726
727
728
729
730
731
732
733
734
735
736
737
738
739
740
741
742
743
744
745
746
747
748
749
750
751
752
753
754
755
756
757
758
759
760
761
762
763
764
765
766
767
768
769
770
771
772
773
774
775
776
777
778
779
780
781
782
783
784
785
786
787
788
789
790
791
792
793
794
795
796
797
798
799
800
801
802
803
804
805
806
807
808
809
810
811
812
813
814
815
816
817
818
819
820
821
822
823
824
825
826
827
828
829
830
831
832
833
834
835
836
837
838
839
840
841
842
843
844
845
846
847
848
849
850
851
852
853
854
855
856
857
858
859
860
861
862
863
864
865
866
867
868
869
870
871
872
873
874
875
876
877
878
879
880
881
882
883
884
885
886
887
888
889
890
891
892
893
894
895
896
897
898
899
900
901
902
903
904
905
906
907
908
909
910
911
912
913
914
915
916
917
918
919
920
921
922
923
924
925
926
927
928
929
930
931
932
933
934
935
936
937
938
939
940
941
942
943
944
945
946
947
948
949
950
951
952
953
954
955
956
957
958
959
960
961
962
963
964
965
966
967
968
969
970
971
972
973
974
975
976
977
978
979
980
981
982
983
984
985
986
987
988
989
990
991
992
993
994
995
996
997
998
999
1000
1001
1002
1003
1004
1005
1006
1007
1008
1009
1010
1011
1012
1013
1014
1015
1016
1017
1018
1019
1020
1021
1022
1023
1024
1025
1026
1027
1028
1029
1030
1031
1032
1033
1034
1035
1036
1037
1038
1039
1040
10
```

[illegible][illegible][illegible]

```

FUNCTION E02=(BM,TAPER,BDCR,R03)
  1
  2
  3
  4
  5
  6
  7
  8
  9
  10
  11
  12
  13
  14
  15
  16
  17
  18
  19
  20
  21
  22
  23
  24
  25
  26
  27
  28
  29
  30
  31
  32
  33
  34
  35
  36
  37
  38
  39
  40
  41
  42
  43
  44
  45
  46
  47
  48
  49
  50
  51
  52
  53
  54
  55
  56
  57
  58
  59
  60
  61
  62
  63
  64
  65
  66
  67
  68
  69
  70
  71
  72
  73
  74
  75
  76
  77
  78
  79
  80
  81
  82
  83
  84
  85
  86
  87
  88
  89
  90
  91
  92
  93
  94
  95
  96
  97
  98
  99
  100
  101
  102
  103
  104
  105
  106
  107
  108
  109
  110
  111
  112
  113
  114
  115
  116
  117
  118
  119
  120
  121
  122
  123
  124
  125
  126
  127
  128
  129
  130
  131
  132
  133
  134
  135
  136
  137
  138
  139
  140
  141
  142
  143
  144
  145
  146
  147
  148
  149
  150
  151
  152
  153
  154
  155
  156
  157
  158
  159
  160
  161
  162
  163
  164
  165
  166
  167
  168
  169
  170
  171
  172
  173
  174
  175
  176
  177
  178
  179
  180
  181
  182
  183
  184
  185
  186
  187
  188
  189
  190
  191
  192
  193
  194
  195
  196
  197
  198
  199
  200
  201
  202
  203
  204
  205
  206
  207
  208
  209
  210
  211
  212
  213
  214
  215
  216
  217
  218
  219
  220
  221
  222
  223
  224
  225
  226
  227
  228
  229
  230
  231
  232
  233
  234
  235
  236
  237
  238
  239
  240
  241
  242
  243
  244
  245
  246
  247
  248
  249
  250
  251
  252
  253
  254
  255
  256
  257
  258
  259
  260
  261
  262
  263
  264
  265
  266
  267
  268
  269
  270
  271
  272
  273
  274
  275
  276
  277
  278
  279
  280
  281
  282
  283
  284
  285
  286
  287
  288
  289
  290
  291
  292
  293
  294
  295
  296
  297
  298
  299
  300
  301
  302
  303
  304
  305
  306
  307
  308
  309
  310
  311
  312
  313
  314
  315
  316
  317
  318
  319
  320
  321
  322
  323
  324
  325
  326
  327
  328
  329
  330
  331
  332
  333
  334
  335
  336
  337
  338
  339
  340
  341
  342
  343
  344
  345
  346
  347
  348
  349
  350
  351
  352
  353
  354
  355
  356
  357
  358
  359
  360
  361
  362
  363
  364
  365
  366
  367
  368
  369
  370
  371
  372
  373
  374
  375
  376
  377
  378
  379
  380
  381
  382
  383
  384
  385
  386
  387
  388
  389
  390
  391
  392
  393
  394
  395
  396
  397
  398
  399
  400
  401
  402
  403
  404
  405
  406
  407
  408
  409
  410
  411
  412
  413
  414
  415
  416
  417
  418
  419
  420
  421
  422
  423
  424
  425
  426
  427
  428
  429
  430
  431
  432
  433
  434
  435
  436
  437
  438
  439
  440
  441
  442
  443
  444
  445
  446
  447
  448
  449
  450
  451
  452
  453
  454
  455
  456
  457
  458
  459
  460
  461
  462
  463
  464
  465
  466
  467
  468
  469
  470
  471
  472
  473
  474
  475
  476
  477
  478
  479
  480
  481
  482
  483
  484
  485
  486
  487
  488
  489
  490
  491
  492
  493
  494
  495
  496
  497
  498
  499
  500
  501
  502
  503
  504
  505
  506
  507
  508
  509
  510
  511
  512
  513
  514
  515
  516
  517
  518
  519
  520
  521
  522
  523
  524
  525
  526
  527
  528
  529
  530
  531
  532
  533
  534
  535
  536
  537
  538
  539
  540
  541
  542
  543
  544
  545
  546
  547
  548
  549
  550
  551
  552
  553
  554
  555
  556
  557
  558
  559
  560
  561
  562
  563
  564
  565
  566
  567
  568
  569
  570
  571
  572
  573
  574
  575
  576
  577
  578
  579
  580
  581
  582
  583
  584
  585
  586
  587
  588
  589
  590
  591
  592
  593
  594
  595
  596
  597
  598
  599
  600
  601
  602
  603
  604
  605
  606
  607
  608
  609
  610
  611
  612
  613
  614
  615
  616
  617
  618
  619
  620
  621
  622
  623
  624
  625
  626
  627
  628
  629
  630
  631
  632
  633
  634
  635
  636
  637
  638
  639
  640
  641
  642
  643
  644
  645
  646
  647
  648
  649
  650
  651
  652
  653
  654
  655
  656
  657
  658
  659
  660
  661
  662
  663
  664
  665
  666
  667
  668
  669
  670
  671
  672
  673
  674
  675
  676
  677
  678
  679
  680
  681
  682
  683
  684
  685
  686
  687
  688
  689
  690
  691
  692
  693
  694
  695
  696
  697
  6
```

```

FUNCTION E202(EM,TAPER,RDCR,R02)
      CALCULATE RECD=RECLAN OR HNTV=RECLAT FROM E20 20, FOR H GREATER THAN
      1.0, VALUE OF ASPECT RATIO PARAMETER GREATER THAN 2, AND
      NB LESS THAN OR EQUAL TO 1
      IF (R02-LE-0.0) 50 TO 10
      IF (R02-GE-0.0) 60 TO 80
      TAPBN/1.0=NB
      TAPERDCR/2
      TCR=0.078
      TAPBNCR/1.0=TCR
      TAPBNCR*(TCR-1.0)=2.0-TAPBNCR*(0.0+LOG(1.0-TCR))-3.0*LOG(1.0-TCR)
      E202=1.0+TAPBNCR*TCR/2.0+TAPBNCR*(1.0+TCR)*RDCR*(1.0/R02-1.0)
      RETURN
      10 E202=0
      RETURN
      20 E202=0
      RETURN
      END

```

[illegible]

APPENDIX F

MODIFICATIONS TO CRFWBD, A COMPUTER
PROGRAM FOR CALCULATING AERODYNAMIC
CHARACTERISTICS OF CRUCIFORM WING-BODY
COMBINATIONS IN SUPERSONIC FLOW

APPENDIX F

MODIFICATIONS TO CRFWBD, A COMPUTER PROGRAM FOR CALCULATING AERODYNAMIC CHARACTERISTICS OF CRUCIFORM WING-BODY COMBINATIONS IN SUPERSONIC FLOW*

F.1. INTRODUCTION

This appendix describes several changes and extensions to the computer program CRFWBD first discussed in Appendix A of reference 3. In addition, a study was made to determine the effect on fin loading of various panel sizes used to cover the fin planform and body interference shell. The results of this investigation are also included. Only the modifications to the program CRFWBD which were made during the course of the present study will be discussed in this appendix. The user should consult Appendix A of reference 3 for a complete description of the original code. The modified program is written in the FORTRAN IV language for the CDC 7600 machine. The modified routines are punched in 029. The user should note that the original routines are all punched in 026.

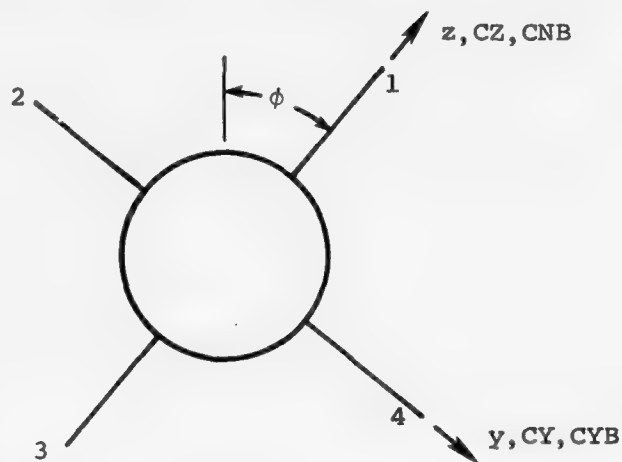
F.2. MODIFICATIONS TO CRFWBD

The first change to the program was to remove all calls to the previously system-supplied subroutine REQFL. This subroutine computed the actual dimension requirement for the aerodynamic coefficient matrix FVN. In the current version this matrix is given the fixed dimension corresponding to the maximum number of constant u-velocity panels allowed and is placed in large core memory. The maximum number of constant u-velocity panels available has been increased from 250 to 350. Thus, the dimension of FVN is 350x350 or 122,500.

Several modifications were made to subroutine LOADS to compute the lift carryover onto the body. In addition, the variable FIL (for body interference length) has been added to namelist INPUT to allow the user to select the length (measured from the leading edge of the fin root chord) over which the wing exerts lift carryover onto the body. In general, the minimum length that should be chosen is determined by the intersection of the Mach cone from the trailing edge of the root chord with the body centerline.

*The work described in this appendix was performed by Dr. M.F.E. Dillenius of Nielsen Engineering & Research, Inc.

Certain output has been added to allow calculation of the distribution of lift carryover onto the body and, specifically, to aid in the determination of the K_B and \bar{x}_B factors described in the main text of this report. Loading information for each body ring has been added to the section of the code concerned with the properties of the body influence panels. This information includes: (1) the contribution from each ring to the force in the z-direction (i.e., along fin 1), CZ, (2) the force in the y-direction (i.e., along fin 4), CY, and (3) the moments about the z and y axes taken with the root chord leading edge as moment center.* The moments are designated CZMOM and CYMOM respectively. In addition, the accumulated normal and side forces due to lift carryover (CNB and CYB) and the locations of the axial centers of pressure (XCP,CZ and XCP,CY) are given as a function of the number of rings in the axial direction. To determine lift carryover, the user should look at the contribution to CZ and CY from each ring. In general, these quantities will increase for each successive ring in the axial direction to a maximum and then decrease. The ring experiencing maximum CZ and/or CY is then the last ring over which lift carryover is dominant (in successive rings wake effects become dominant). The lift carryover is then determined from the accumulated CZ and CY over the affected body rings by vectorial addition and XCP,CZ and XCP,CY are the corresponding centers of pressure.



Sketch F.1. Coordinate system used for body loading due to lift.

*Note that the x,y,z coordinate system used here is for rolled body coordinates. See sketch F.1.

F.3. LOADING CONVERGENCE STUDY

F.3.1 Modeling of Missile Body

A study was undertaken to investigate the effect on the fin loading of the number of line sources/sinks and doublets distributed along the body centerline to model the missile body. Specifically, the magnitude of the velocity component normal to the fin surfaces was calculated for different numbers of body singularities. It was found that for cross-flow planes aft of the shoulder of an ogive-cylinder at angle of attack, the computed upwash varied smoothly with distance away from the body. At every point, the magnitude of the upwash appeared to converge rapidly with increasing numbers of body singularities. As a rule of thumb, the number of body singularities over the length spanned by the fins should be at least equal to the number of constant u-velocity panels laid in a chordwise row on the fins.

F.3.2 Modeling of Fins for Wing-Alone Case

The effect of the number of constant u-velocity panels distributed over the fins and body interference shell were studied in a systematic manner. First a wing-alone was considered. The normal force was computed for many combinations of chordwise and spanwise numbers of panels. It was concluded that the normal force approaches a definite limit as the number of chordwise rows is increased while the number of panels in each row is kept constant. For typical missile fin planforms, a layout of 9 panels spanwise and 4 panels chordwise should give good results. This recommendation is based both on the findings from the convergence studies for a wing alone and on comparison with experimental data.

F.3.3 Modeling of Fins and Body Interference Shell for Wing-Body Case

Next, the effect of the number of panels on the fins and interference shell for a cruciform fin-body combination was investigated. Based on the results of many calculations of the normal forces acting on the fins, it was concluded that the size of the panels in the interference shell should be comparable to the size of the panels on the fins in the chordwise row at the fin-body junction. Thus, the number of panels in the

interference shell in the axial direction should equal the number of panels in a chordwise row on the fins. The number of panels on the circumference of the interference shell should be selected such that the panel width is comparable to the span of the chordwise row of panels on the fin at the fin-body junction.

For the case of an unrolled, cruciform fin-body configuration at angle of attack and with the vertical panels deflected for yaw control, the contribution to rolling moment from the deflected fins (termed direct roll) can be determined with good accuracy using 12 panels on the circumference and 4 along the body length spanned by the fins. In accordance with the above recommendations, each fin should be covered with 3 or 4 chordwise rows with 4 panels in each row. In contrast, the contribution to the rolling moment from the undeflected, horizontal fins (termed reverse roll) was very small for the case considered. Furthermore, the convergence was not monotonic. In this instance, the number of panels required to reach a limiting value exceeded the maximum number allowed by the computer program.

F.4. PROGRAM LISTING

A listing is given below of the two subroutines affected by the modifications discussed above. Other subroutines were changed only to make COMMON statements compatible or to remove calls to the system-supplied subroutine REQFL and to place the aerodynamic coefficient matrix FVN in large core memory. The following subroutines have been written in the FORTRAN IV language (029 punch) for the CDC 7600 computer.

<u>PROGRAM</u>	<u>IDENTIFICATION</u>	<u>PAGE NO.</u>
CRFWBD	WB01	223
LOADS	WB03	227

LIST OF SYMBOLS

A_L	left afterbody vortex
A_R	right afterbody vortex
AR	wing-alone aspect ratio
A_1	see equation (B.29)
a	body radius
a_e	proportionality coefficient for elliptic span loading; see equation (C.2)
a_L	proportionality coefficient for linear span loading; see equation (C.1)
C_A	axial-force coefficient; axial force/ $q_\infty S_R$
C_D	drag coefficient; drag/ $q_\infty S_R$
C_L	lift coefficient; lift/ $q_\infty S_R$
C_l	rolling-moment coefficient; rolling moment/ $q_\infty S_R l_r$
C_m	pitching-moment coefficient; pitching moment/ $q_\infty S_R l_r$
C_N	normal-force coefficient; normal force/ $q_\infty S_R$
C_n	yawing-moment coefficient; yawing moment/ $q_\infty S_R l_r$
$C_{N_{B(W)}}$	normal-force coefficient for body in the presence of fins; normal force/ $q_\infty S_R$
C_{N_W}	normal-force coefficient of "wing alone" formed by joining two opposing fins; normal force/ $q_\infty S_R$
$C_{N_{W(B)}}$	normal-force coefficient for two opposing fins in the presence of a body; normal force/ $q_\infty S_R$
C_{N_α}	slope of nose normal-force coefficient at $\alpha_c = 0$; reference area is the base area of the nose
C_Y	side-force coefficient; side force/ $q_\infty S_R$
C_6	moderate-aspect-ratio canard fins used in MICOM-NWC tests; see reference 4 and figure 3(a)
C_7	low-aspect-ratio canard fins used in MICOM-NWC tests; see reference 4 and figure 3(b)

LIST OF SYMBOLS (CONTINUED)

CNC1,CNC2,etc.	normal-force coefficients associated with fins C1, C2, etc.
CNi	normal-force coefficient for fin i
CNT1,CNT2,etc.	normal-force coefficients associated with fins T1, T2, etc.
CRMi	rolling-moment coefficient for fin i
CRMCl,CRMC2,etc.	rolling-moment coefficients associated with fins C1, C2, etc.
CRMT1,CRMT2,etc.	rolling-moment coefficients associated with fins T1, T2, etc.
C1,C2,etc.	canard fins; also vortices associated with canard fins
c_{d_c}	two-dimensional crossflow drag coefficient
c_r	length of fin root chord
$(cc)_e$	elliptic span loading; see equation (C.2)
$(cc)_L$	linear span loading; see equation (C.1)
$(cc)_s$	span loading; see equation (B.5)
$(cc)_e$	span loading; see equation (B.14)
D_V	crossflow drag force on an elemental length of cylinder; see equation (D.5)
K^*	fraction of fin leading-edge or side-edge suction which is converted to vortex lift
K_B	wing-body interference factor for body normal force for $\delta = 0, \alpha_c \neq 0$
K_W	wing-body interference factor for fin normal force for $\delta = 0, \alpha_c \neq 0$
K_V	vortex lift parameter; see equation (34)
$K_{\alpha\beta}$	wing-body interference factor for bank, $\delta = 0, \alpha_c \neq 0$
k_B	wing-body interference factor for body normal force for $\delta \neq 0, \alpha_c = 0$
k_W	wing-body interference factor for fin normal force for $\delta \neq 0, \alpha_c = 0$
k_1	see equation (B.27)

LIST OF SYMBOLS (CONTINUED)

$l.e.$	leading edge
l_r	reference length
M_c	crossflow Mach number, $M_\infty \sin \alpha_c$
M_l	rolling moment
M_∞	free-stream Mach number
MS 0	missile station zero; origin of coordinate system
N	normal force
N_v	normal force due to viscous crossflow
NV(x)	number of vortices in the crossflow plane located at axial position x
P	difference between pressure coefficient on suction side of fin (or body) and pressure coefficient on impact side of fin (or body)
q_∞	dynamic pressure of free stream
R	see equation (B.24)
r_o	radius of circle in transform plane; see equation (A.2)
r_v	$\sqrt{y_v^2 + z_v^2}$
$r(x)$	radius of nose at axial position x
S_B	body planform area in finned section
S_C	crossflow area upstream of first set of fins
S_i	planform area of fin i
S_R	reference area
s_m	semispan of fin on body
$s(x)$	fin semispan at axial location x
T1, T2, etc.	tail fins
T_2	low-aspect-ratio tail fins used in MICOM-NWC tests; see reference 4 and figure 3(d)
T_{14}	low-aspect-ratio tail fins used in MICOM tests; see reference 16 and figure 3(c)

LIST OF SYMBOLS (CONTINUED)

T_{1s}	low-aspect-ratio tail fins used in MICOM tests; see reference 16 and figure 3(e)
t	fin spanwise coordinate
$t.e.$	trailing edge
V_{max}	maximum normal velocity which can be induced on a fin
V_N	volume of nose from tip to shoulder
V_{∞}	free-stream velocity
v	velocity component in y-direction
w	velocity component in z-direction
x,y,z	missile body axes; x measured positive downstream along body rotational axis, y measured positive to right in the plane of C4, and z measured positive upward in the plane of C1; origin is located at MS 0
x_o, y_o, z_o	special set of x,y,z axes for $\phi = 0$; also called unrolled body coordinates
$XCTE$	axial position of the canard trailing edge
$XTLE$	axial position of the leading edge of the tail root chord
x_{HL}	axial position of fin hinge line measured from MS 0
x_{MC}	axial location of reference for moments acting on missile measured from MS 0
x_N	length of nose from tip to shoulder
x_s	axial location of initial separation of body nose vorticity
\bar{x}	axial position of center of pressure
\bar{x}_B	axial position of center of pressure for body normal force due to presence of fins measured from MS 0
\bar{x}_i	axial position of the center of pressure for fin i measured from MS 0
\bar{x}_{linear}	axial position of center of pressure for nose normal force due to potential flow
$\bar{x}_{viscous}$	axial location of center of pressure for nose normal force due to viscous flow
Y	side force

LIST OF SYMBOLS (CONTINUED)

y_v	side force due to viscous crossflow
y_v, z_v	coordinates of vortex in the crossflow plane
y_v^*	spanwise location of centroid of fin trailing vorticity
\bar{y}_i or \bar{z}_i	lateral location of the center of pressure for fin i measured from body centerline
\bar{y}_v	moment arm for normal force induced by vortices
α	fin angle of attack
α_c	included angle of attack; angle between x axis and free-stream velocity
α_{cr}	resultant angle of crossflow at body centerline due to free-stream flow and external vortices exclusion of afterbody vortices
α_{eq}	equivalent angle of attack; that angle of attack of the wing alone for which its normal force is twice that of the fin; the wing alone is formed by joining two opposing fins together
$\alpha_{eq,p}$	equivalent angle of attack when no vortices are present
$\alpha_{v,i}(x,t)$	local angle of attack induced at x,t on fin i by presence of vortices
$\bar{\alpha}_{v,i}(t)$	average of $\alpha_{v,i}(x,t)$ over chord
β	fin angle of sideslip
γ	see equation (B.26)
Γ	vortex strength
Γ'	nondimensional vortex strength; vortex strength/ $2\pi V_\infty a$
$(\Delta\alpha_{eq})_v$	change in α_{eq} due to a collection of external vortices and their images
$\delta_1, \delta_2, \text{etc.}$	incidence angles associated with fins $C_1, C_2, \text{etc.}$, for $\phi = 0$, δ_1 and δ_3 are positive for trailing edges to the right viewed from the rear, and δ_2 and δ_4 are positive for trailing edges down
η	nondimensional spanwise coordinate; see equation (C.1)
$\bar{\eta}$	nondimensional spanwise position of fin center of pressure; see equation (C.10)

LIST OF SYMBOLS (CONCLUDED)

θ	direction of resultant crossflow velocity at body centerline due to free-stream flow and external vortices exclusive of afterbody vortices; measured counterclockwise from position y_0 -axis; also see equation (B.25)
Λ	fin leading-edge sweep
λ	ratio of fin tip chord to root chord; also complex position in the transform plane
μ	interaction coefficient for fin rolling moment due to presence of vortices; see equation (B.18)
v	complex position in the transform plane
ρ_∞	density of fluid in free stream
ζ	complex position in the crossflow plane
ζ'	complex distance between a vortex and its image inside a cylinder nondimensionalized by the cylinder radius
ϕ	roll angle, angle between z axis and z_0 axis; positive measured clockwise viewed from rear
ϕ_T	interdigitation angle, angle between canard fin C1 and tail fin T1 measured clockwise from fin C1
ω	angular rate of rotation of wing-body combination

Subscripts

body	contribution to total forces and moments due to loading seen by body in finned section
d	direct flow
fins	contribution to total forces and moments due to loading seen by all four fins in a finned section
L	left afterbody vortex; in Appendix C, refers to linear span loading
R	right afterbody vortex
r	reverse flow